



HAL
open science

Vers de nouvelles approches pour la description des propriétés des états excités et de la réactivité: une approche basée sur la densité

Anna Perfetto

► **To cite this version:**

Anna Perfetto. Vers de nouvelles approches pour la description des propriétés des états excités et de la réactivité: une approche basée sur la densité. Chimie théorique et/ou physique. Université Paris sciences et lettres, 2020. Français. NNT: 2020UPSLC028 . tel-03557763

HAL Id: tel-03557763

<https://pastel.hal.science/tel-03557763>

Submitted on 4 Feb 2022

HAL is a multi-disciplinary open access archive for the deposit and dissemination of scientific research documents, whether they are published or not. The documents may come from teaching and research institutions in France or abroad, or from public or private research centers.

L'archive ouverte pluridisciplinaire **HAL**, est destinée au dépôt et à la diffusion de documents scientifiques de niveau recherche, publiés ou non, émanant des établissements d'enseignement et de recherche français ou étrangers, des laboratoires publics ou privés.



THÈSE DE DOCTORAT
DE L'UNIVERSITÉ PSL

Préparée à Chimie ParisTech

**Towards new theoretical approaches for the description
of excited state properties and reactivity:
a Density Based Approach**

Soutenue par

Anna PERFETTO

Le 22 10 2020

Ecole doctorale n° ED388

**Chimie physique et chimie
analytique de Paris Centre**

Spécialité

Chimie physique

Composition du jury :

Professeur Alexis MARKOVITS Sorbonne Université	<i>Président</i>
Assistant Professeur Daniel ESCUDERO Chemistry Department Ku Leuven	<i>Rapporteur</i>
Professeur Masahiro EHARA Institute for Molecular Science	<i>Rapporteur</i>
Professeur Nadia REGA Università degli Studi di Napoli	<i>Examineur</i>
Directeur de recherche Ilaria CIOFINI Chimie ParisTech	<i>Directeur de thèse</i>

Contents

1	Introduction and Thesis Framework	4
2	Theoretical Background	7
2.1	The Schrödinger Equation	8
2.2	The Hartree-Fock Method (HF)	10
2.2.1	Spin-Orbital Approximation	10
2.2.2	The Slater Determinant	11
2.2.3	The Hartree-Fock Energy	12
2.2.4	Introduction of atomic orbitals basis	13
2.2.5	The Secular Equation	14
2.2.6	The Self-Consistent Field procedure	15
2.2.7	Different types of atomic orbitals basis	17
2.2.8	Electron Correlation	19
2.3	Density Functional Theory (DFT)	21
2.3.1	Existence and variational theorems	21
2.3.2	The Kohn-Sham method	23
2.3.3	The Exchange-Correlation energy	26
2.3.4	Self-interaction energy and different types of hybrid functionals	30
2.4	Time-Dependent Density Functional Theory (TD-DFT)	33
2.4.1	Fundamental theorems in TD-DFT	33
2.4.2	Linear Response approach	34
2.4.3	Excitation energy calculation	36
2.4.4	The adiabatic approximation	39
2.4.5	Charge transfer excitations	40
2.5	Modeling Solvent Effect	42
2.5.1	The polarizable continuum model (PCM)	42
3	How can we explore excited states?	45
3.1	Interpreting electronic transitions through descriptors: excited states indexes	47
3.1.1	Luzanov (1975)	47
3.1.2	Head Gordon (1995)	48
3.1.3	Tozer (2008)	48

3.1.4 Tarantelli (2010)	49
3.1.5 Plasser (2012)	50
3.1.6 Adamo (2013)	51
3.1.7 Etienne (2014)	52
3.1.8 Plasser (2014)	53
3.1.9 D _{CT} Index (2011)	53
3.2 The problematic description of excited states by (TD)-DFT	57
3.2.1 The problem of Charge-Transfer in TD-DFT	57
3.2.2 The problem of conical intersections in TD-DFT	59
4 A new metric to study charge-transfer excitations in symmetric systems	64
4.1 Context	64
4.2 Introduction	65
4.3 Computational Methods and Details	67
4.4 Results and Discussion	69
4.5 Conclusions	76
5 A new general index for the analysis of charge-transfer in symmetric and non-symmetric compounds	77
5.1 Context	77
5.2 Introduction	78
5.3 Computational Methods and Details	80
5.4 Results and Discussion	83
5.5 Conclusions	97
6 Investigating excited states via the analysis of electron density rearrangement	99
6.1 Context	99
6.2 Introduction	100
6.3 Computational Methods and Details	103
6.4 Results and Discussion	104
6.4.1 An excursion through the excited states	104
6.4.2 Simulation of the observed absorption spectrum	107

6.4.3 Interpretation of the dual emission through the Π index	109
6.5 Conclusions	112
7 Understanding the mechanism of a reaction by the use of density-based indexes	114
7.1 Context	114
7.2 Introduction	115
7.3 Computational Methods and Details	117
7.4 Results and Discussion	119
7.4.1 Experimental results	119
7.4.2 Computational results	122
7.5 Conclusions	132
8 How can the environment affect optical properties?	134
8.1 Context	134
8.2 Introduction	135
8.3 Computational Methods and Details	136
8.3.1 Solvent/vacuum calculations	136
8.3.2 Crystal-embedded calculations	137
8.4 Results and Discussion	138
8.4.1 UV-Vis response to mechanical drawing	144
8.4.2 NIR response to mechanical drawing	150
8.5 Conclusions	153
9 General conclusions and Perspectives	154
Appendix	158
Appendix to Chapter 6	158
Appendix to Chapter 8	164
Bibliography	167
Résumé en français	178

Chapter 1

Introduction and Thesis Framework

During recent years there has been growing interest in the application of theoretical methods for the study of phenomena happening at the excited state. Such interest is mostly due to a huge request of new classes of compounds to apply in different fields, such as biological and medical [1,2], of optoelectronics and energy storage [3,4], whose performances imply light-matter interaction. Indeed, upon interaction with light these materials are able to elicit an observable response in the form of color change, luminescence, alteration of magnetic properties, induced chemical reaction or several of these, thus the reason why they are called “photoactive molecules” [5]. So, raising technologies require the synthesis of molecules with very specific target functions, but the lack of knowledge about the molecular mechanism of photoinduced phenomena constitutes a severe drawback for the design of such systems. This research work shows how the implementation of new computational approaches may provide a solution to handle this issue.

Upon the absorption of a quantum of light, a molecule basically moves from the ground state to an excited state, which on turn takes part into a photochemical reaction. The intermediates of this preliminary process are very high in energy compared to those accessible via the normal thermally intermediates and may undergo to various secondary “dark” reactions, yielding at the end the final products. Understanding these processes at the molecular level requires an accurate description of the excited states. Due to the complexity of the experimental characterization of photochemical processes and the requirement for a detailed picture of the states concerned, theoretical methods may play an increasingly important role in this context, especially for complex molecular systems. Recent developments in density functional theory (DFT), and in particular in time-dependent density functional theory (TD-DFT) allow nowadays to obtain a complete description of a photoinduced phenomenon, from the absorption up to the formation of final photoproducts [6-8]. The simplest methodology to study a photochemical process consists in sequencing

the entire course into different reaction steps over potential energy surfaces along with a representative reaction coordinate. In this way, it is possible to identify the relevant step connecting the Frank Condon region, which is basically where the system absorbs light, to the zone where photoproducts are formed. Nonetheless the identification of minima and transition states along the potential energy surfaces (PES)s, and therefore the mere energetic analysis results to be unsatisfying. In particular, the presence of electron donating and acceptor groups in the molecular structure strongly affects the nature of the excited state, which may acquire charge-transfer (CT) character, and consequently the photophysical properties of the system. For this reason, an additional fundamental quantity that can be also viewed is the electron density and its reorganization throughout the entire process. In this manner the energetic analysis provides the local properties along the PES, such as saddle points, minima and maxima, through which then it is possible to calculate energy barriers, activation energies and so on. On the other hand, the electron density analysis can give a clear picture of the redistribution of electron density during the process, making possible to characterize the nature of the electronic states, and thus gaining further insights into the light induced phenomena.

In this context, DFT and TD-DFT lend themselves well for this twofold analysis. The main advantage lies in their favorable cost-accuracy ratio and their capability to integrate environmental effects in a computationally cheap way. Nevertheless, it is well documented in literature that the density functionals used to evaluate the exchange and correlation energy contribution, basically the only approximate term in the expression of the total energy, suffer from various disadvantages [9-13]. Some of these are the incorrect description of long-range electronic interaction and erroneous calculated energies associated to a charge-transfer, leading to the prediction of unphysical low-lying excited states with CT character, also known as "ghost states" [10,11]. Furthermore, TD-DFT is unable to replicate the crossing points between two or more excited states, due to the intrinsically multi-determinantal nature of this type of phenomenon. Consequently, in the context of the DFT and TD-DFT, there is a meaningful need of developing new tools to treat or correct the disadvantages of the density functional, and at the same time to explore the complete excited state PES, thus giving a better description of the light induced phenomena. Indeed, the purpose of this research work is developing and test innovative *ad hoc* theoretical descriptors based on electronic density to deal with these drawbacks. These descriptors actually provide information on important physical properties, translating computational results into simple chemical and physical concepts. In this way it is possible to effectively define the most important photophysical pathways for complex processes taking place simultaneously at the excited state (electronic reorganization, radiative and non-radiative decay). The ultimate aim is then determining and predicting new interesting photoactive molecular systems with target properties.

After a brief overview of DFT and TD-DFT in Chapter 2, Chapter 3 contains a temporal excursus of existing tools developed in the last decades to explore excited states

properties via quantification of charge density redistribution involved in the excitation, thus offering a concise description of the electronic transition, not only in the Franck Condon region. Indeed, the intention is extending the investigation from the vertical absorption up to the emissive phenomenon. Chapter 4 and Chapter 5 present our contribution in revising an existing density-based descriptor enabling to quantify the extension of a CT excitation, trying to overcome its limitations when applied in symmetric molecules. In Chapter 4, indeed, we propose an expedient to exploit the original mathematical definition to compute the CT extent associated only to the contribution of a selected asymmetric fragment of the symmetric molecule. In Chapter 5 instead we modify the mathematical definition and suggest a general density-based index enabling to measure the particle - hole distance for whatever molecules. Chapter 6 and 7 extend the use of density-based descriptors to obtain an exhaustive portrayal of excited state evolution, within and outside the Franck Condon region by visualizing the electron density reorganization. In light of this descriptor we are able to qualitatively identify the regions of PES involved in radiative or non-radiative decay, helpful to interpret the emission behavior of a phenanthroline derivative (Chapter 6) and the mechanism of the deoxygenation reaction of heteroaromatic *N*-oxides occurring at excited state (Chapter 7). Finally, Chapter 9 raises the question of modeling photophysical processes including the environmental influence in form of surrounding solvent molecules, in the case of solution, or other molecules in the case of crystalline or amorphous-phase materials.

Chapter 2

Theoretical Background

Quantum chemistry aims at describing atomic, molecular and extended systems in order to predict their properties starting from 'first principles' solving the Schrödinger equation (SE) (2.1). Nevertheless, the SE can be analytically solved only for an extremely restricted number of cases, such as the hydrogen atom, the hydrogen molecular ion or hydrogenoid systems. For real systems, different *ab-initio* methods have been implemented to provide approximate solutions to the Schrödinger differential equation, including the Hartree-Fock (HF) method and the Density Functional Theory (DFT). The first based on the use of wave functions while the latter on electron density and they both allow to access to the ground state (GS) of the system.

Other methods are available to describe systems subjected to an external time-dependent potential, thus enabling the prediction of light-matter interaction. The time-dependent DFT methods (TD-DFT) is among allowing to compute the electron density of the excited state (ES) and the corresponding electronic excitation energy [14]. In this Chapter we will provide a short and non-exhaustive overview of these methods focusing on those used in the thesis.

The HF method will be briefly presented in paragraph 2.2 along with its limitations, followed by an introduction to the DFT and TD-DFT, which are basically the theoretical approaches used throughout this work (Paragraph 2.3 and 2.4).

Generally, the environment is also able to influence the geometrical and electronic structure of a system. Therefore, in the context of this thesis it was necessary to use an approach to take into account the presence of the solvent, which is illustrated in Paragraph 2.5. Starting from classical physics principles, the peripheral zone of the core quantum region can be treated using continuum dielectric medium models, such as the polarizable continuum model (PCM). The basic principles of PCM for the description of solvent effects at ground and the excited state will be briefly reviewed

2.1 The Schrödinger Equation

The aim of quantum methods is to solve the Schrödinger equation, which in its time-independent form is an eigenvalues problem:

$$\widehat{H} |\Psi(x_1, \dots, x_N)\rangle = E |\Psi(x_1, \dots, x_N)\rangle \quad (2.1.1)$$

Solving exactly the SE for a many-body system implies the use of a complete Hilbert space (infinite) to describe the eigenstates. One can basically truncate it using restricted spaces related to the electronic freedom degrees of the system, and thus calculate an approximate solution to the resulting eigenvalues problem. \widehat{H} is the quantum mechanical Hamiltonian operator and $|\Psi(x_1, \dots, x_N)\rangle$ is the many body wave function corresponding to the eigenstate, which is described as an elementary tensor in the Hilbert space. The main feature of the wave function (eigenfunction) is that it contains all necessary information about the quantum state of the system, while E is the total system energy (eigenvalue). For a polyelectronic system of N nuclei and n electrons, the non-relativistic Hamiltonian can be written as a sum of five terms:

$$\widehat{H} = \widehat{T}_e + \widehat{T}_N + \widehat{V}_{Ne} + \widehat{V}_{ee} + \widehat{V}_{NN} \quad (2.1.2)$$

\widehat{T}_e and \widehat{T}_N are the operators for the kinetic energy of electrons and nuclei, respectively. \widehat{V}_{Ne} is the operator for the electron-nuclei Coulomb attraction, \widehat{V}_{ee} and \widehat{V}_{NN} are the operators for the inter-electronic and inter-nuclei repulsion energy. If we assume the nuclei and electron to be point masses and neglect spin-orbit and other relativistic interactions, then the molecular Hamiltonian can be written as:

$$\widehat{H} = \sum_i^n \frac{-\hbar^2}{2m_e} \nabla_i^2 + \sum_\alpha^N \frac{-\hbar^2}{2M_\alpha} \nabla_\alpha^2 - \sum_\alpha^N \sum_i^n \frac{eZ_\alpha}{4\pi\epsilon_0 r_{i\alpha}} + \sum_i^n \sum_{j>i}^n \frac{e^2}{4\pi\epsilon_0 r_{ij}} + \sum_\alpha^N \sum_{\beta>\alpha}^N \frac{Z_\alpha Z_\beta}{4\pi\epsilon_0 r_{\alpha\beta}} \quad (2.1.3)$$

where indexes i and j (α and β) run over all electrons (nuclei); r is the inter-particle distance, e and m (Z and M) are the charge and mass of an electron (nucleus). \hbar is the reduced Planck's constant and ∇^2 is the Laplacian. The restriction $j > i$ ($\beta > \alpha$) avoids the double counting of the same interelectronic (internuclear) repulsion and the counting of the self-repulsion. A such defined wave-function contains information about all the nuclei and electrons, and it is then defined as a function of $3(n + N)$ coordinates. One can rewrite (2.1.3) in a more condensed form, and using atomic units:

$$\widehat{H} = -\frac{1}{2} \sum_{i=1}^n \nabla_i^2 - \frac{1}{2} \sum_{\alpha}^N \frac{1}{2M_\alpha} \nabla_\alpha^2 - \sum_{\alpha}^N \sum_i^n \frac{Z_\alpha}{r_{i\alpha}} + \sum_i^n \sum_{j>i}^n \frac{1}{r_{ij}} + \sum_{\alpha}^N \sum_{\beta>\alpha}^N \frac{Z_\alpha Z_\beta}{r_{\alpha\beta}} \quad (2.1.4)$$

A widely used approximation to streamline the SE is the **Born-Oppenheimer approximation** (BOA) [15]. Since the mass of any given nuclei is far greater than that of the electrons and the nuclei move about three orders of magnitude slower than electrons. In the classical vision, during the time of a cycle of electronic motion, the change in nuclear configuration is negligible. Hence, we can separate the electronic and nuclear degree of freedom considering instantaneously that the nuclei are fixed and the electrons moving in the static nuclear potential field. The first consequence of this approximation is that the nuclear kinetic energy can be neglected, and as the nuclear repulsion term has become a constant quantity that can be added to the electronic energy to obtain the total system energy E_{tot} . Under the constrain of the BOA, the movement of nuclei and electrons are decoupled, and the electronic properties of the system can be calculated at a fixed nuclear geometry. This nuclear position dependency means that a unique electronic wave-function exists for each possible nuclear arrangement (molecular geometry). The many-body Schrödinger electronic equation can thus be written as follow:

$$\widehat{H}_{el} | \Psi_{el} \rangle = E_{el} | \Psi_{el} \rangle \quad (2.1.5)$$

Therefore, the Hamiltonian to be solved reduces to the electronic Hamiltonian, here expressed as:

$$\widehat{H} = -\frac{1}{2} \sum_i^n \nabla_i^2 - \sum_\alpha^N \sum_i^n \frac{Z_\alpha}{r_{i\alpha}} + \sum_i^n \sum_{j>i}^n \frac{1}{r_{ij}} \quad (2.1.6)$$

Within the Born-Oppenheimer framework, the total potential energy of the system can be written as the sum of electronic energy E_{el} and the constant nuclear repulsion V_{NN} :

$$E_{tot} = E_{el} + V_{NN} \quad (2.1.7)$$

It is an eigenvalue equation that returns the Ψ_{el} eigenstate and the corresponding pure electronic energy E_{el} . It is convenient rewriting the purely electronic Hamiltonian \widehat{H}_{el} as the sum of mono- and bi-electronic terms:

$$\widehat{H}_{el} = \sum_i^n \left(\widehat{h}_1(i) + \sum_{j>i}^n \widehat{h}_{12}(i,j) \right) \quad (2.1.8)$$

Because of the bi-electronic term, which is the electron-electron interaction the last term of (2.1.6), the solution of electronic SE cannot be analytically found for systems with more than one electron (hydrogen, hydrogen molecular ion and hydrogenoid system). Indeed, for many-electrons systems it is necessary to implement approximate methods to easily deal with the Schrödinger equation.

2.2 The Hartree-Fock Method (HF)

Because of the presence of the interelectronic repulsion term in the electronic Hamiltonian (2.1.9), the Schrödinger equation cannot be solved analytically for systems with more complexity than a hydrogenic system. The first effort to solve the Schrödinger equation for a many electrons system (within the BOA) was proposed by Douglas Rayner Hartree in 1928. The Hartree method aims at approximating the exact wave function implying an average field potential and the neglecting of instantaneous electronic movement. The theory consists of simplifying the overall many-body problem into a series of non-interacting hydrogenlike equations. Hence, one may transform a N -electron unsolvable problem into N -monoelectronic readily solvable problems.

2.2.1 Spin-Orbital Approximation

As an initial approach, it is possible to represent the overall electronic wave function ψ_{el} as the Hartree product of N -monoelectronic eigenfunctions (orbitals) [16]:

$$\psi_{el} = \varphi_1(r_1)\varphi_2(r_2) \dots \varphi_n(r_n) \quad (2.2.1)$$

If we assume that there is no interaction between the electrons of the system, one may rewrite the multielectronic Hamiltonian as a sum of mono-electronic operators $\hat{h}(i)$ resulting in the following eigenvalue equation:

$$\hat{h}(i) \varphi_i(r_i) = e_i \varphi_i(r_i) \quad (2.2.2)$$

where r_i is the position vector of the electron i , φ_i are the one-electron eigenfunctions called *orbitals* and e_i the eigenvalues correspond to the orbital energies, the product of which constitutes the multielectronic wave function ψ_{el} (2.2.1). Thus, the total system electronic energy of the system is written as sum of the orbital energies e_i :

$$E_{el} = \sum_i^n e_i \quad (2.2.3)$$

Orbitals can be defined as a product of space (φ_i) and spin (σ_i) functions, yielding the so-called *spin-orbitals* (χ_i).

$$\chi_i(r_i; s_i) = \varphi_i(r_i)\sigma_i(s_i) \quad (2.2.4)$$

As in the Hamiltonian the spin-orbit interaction is neglected (non-relativistic), there is no coupling between spin and space functions comprising a given spin-orbital. Within the **spin-orbital approximation** (SOA), the multielectronic wave function (ψ_{el}) can be written as the product of monoelectronic spin-orbit wave functions (χ_i):

$$\psi_{el} = \chi_1(x_1)\chi_2(x_2) \dots \chi_n(x_n) \quad (2.2.5)$$

where x_i is the vector containing the spatial and spin coordinates of the electron ($\chi_i(r; s)$). The spin function describes the intrinsic angular momentum of an electron, which may assume two values: $\pm \frac{1}{2}$, generally denoted by α and β . Equation (2.2.5) is well known as the Hartree Product.

2.2.2 The Slater Determinant

Electrons are fermion particles and *Pauli's exclusion principle* implies that a wave function describing an ensemble of fermions must be antisymmetric with respect to the permutation of two electrons. This means the sign of the wave function must be inverted when exchanging the coordinates of two electrons. As the Hartree Product wave function does not fulfill this criterion, in 1930 Vladimir Aleksandrovich Fock and John Clark Slater gave a solution to this drawback substituting the Hartree Product with the **Slater Determinant**, Φ_k :

$$\Phi_k = \frac{1}{\sqrt{n!}} \begin{vmatrix} \varphi_1(r_1)\sigma_1(s_1) & \varphi_2(r_1)\sigma_2(s_1) & \dots & \varphi_n(r_1)\sigma_n(s_1) \\ \varphi_1(r_2)\sigma_2(s_2) & \varphi_2(r_2)\sigma_2(s_i) & \dots & \varphi_n(r_2)\sigma_n(s_2) \\ \vdots & \vdots & \ddots & \vdots \\ \varphi_1(r_n)\sigma_2(s_n) & \varphi_2(r_n)\sigma_2(s_n) & \dots & \varphi_n(r_n)\sigma_n(s_n) \end{vmatrix} \quad (2.2.6)$$

where the pre-factor is the normalization constant of the wave function and the space functions of the spin-orbitals functions are orthonormal:

$$\langle \varphi_i | \varphi_j \rangle = \delta_{ij} \quad (2.2.7)$$

Here we use the Dirac notation to represent the overlap of two space functions, with δ_{ij} corresponding to the Kronecker delta. All the elements of a column involve the same spin-orbital, while elements in the same row all involve the same electron. In the Slater Determinant N spin-orbitals are occupied by N electrons with no specific position (indistinguishable electrons). If two columns are identical, it means that two electrons are in the same spin-orbital, which is impossible according to the Pauli's exclusion principle (two electrons cannot have the same four quantum numbers). In this case the determinant is equal to zero. If we interchange two columns or rows in a determinant, this latter changes its sign. Permuting two columns of the Slater determinant corresponds to interchanging the coordinates of two electrons, hence the wave function is antisymmetric.

It is worth to noticing that the HF determinant is composed by a single Slater Determinant. Thus, the resolution of the overall wave function requires a single electronic configuration. Moreover, the introduction of the antisymmetric Slater

determinant makes appear a new term, namely the exchange energy K , which have not a classical analogue, but it is due to the fermion nature of electrons.

2.2.3 The Hartree-Fock Energy

The variational principle tells us that for any trial function

$$\tilde{E} = \frac{\langle \tilde{\Phi} | \widehat{H}_{el} | \tilde{\Phi} \rangle}{\langle \tilde{\Phi} | \tilde{\Phi} \rangle} \geq E^{Exact} \quad (2.2.8)$$

So, assuming the stationary ground state of a system, whose normalized wave function Φ_0 and the corresponding energy satisfy the Schrödinger equation, the expectation value of the energy should be at least greater than or equal to the lowest possible energy of the system. For a given set of space functions $\{\varphi_i\}$, the minimal energy for a given nuclear configuration can be found by varying the form of each space function under the orthonormality constraint (2.2.7).

In a closed-shell system the molecular orbitals are doubly occupied, and all electrons of opposite spin are paired. The Hartree-Fock energy can be calculated by utilizing the \widehat{H}_{el} operator, which corresponds to the sum of a mono- (h_{ii}) and bi-electrons (J_{ij} and K_{ij}) terms:

$$E_0^{HF} = \langle \Phi_0 | \widehat{H}_{el} | \Phi_0 \rangle = 2 \sum_i^{n/2} h_{ii} + \sum_i^{n/2} \sum_j^{n/2} (2J_{ij} - K_{ij}) \quad (2.2.9)$$

h_{ii} is the one electron operator given by the following integral:

$$h_{ii} = \int \chi_i^*(1) \widehat{h}_1 \chi_i(1) dr_1 = \langle i | \widehat{h}_1 | i \rangle \quad (2.2.10)$$

while J_{ij} and K_{ij} , are the Coulomb and exchange integrals, respectively:

$$J_{ij} = \int \chi_i^*(1) \chi_j^*(2) \widehat{h}_{12} \chi_i(1) \chi_j(2) dr_1 dr_2 = \langle ij | \widehat{h}_{12} | ij \rangle \quad (2.2.11)$$

$$K_{ij} = \int \chi_i^*(1) \chi_j^*(2) \widehat{h}_{12} \chi_j(1) \chi_i(2) dr_1 dr_2 = \langle ij | \widehat{h}_{12} | ji \rangle \quad (2.2.12)$$

Each integral is calculated over a finite volume element r_i in three dimensions. J_{ij} represents the mean-field Coulombic repulsion term related to the repulsion among all pairs of electrons. On the other hand, K_{ij} is rather a *non-local* term because it explicitly depends on the function on which it acts, and moreover it is necessary to know the value of the function on which it acts in each point of the space. It reflects the Fermi correlation principle between two electrons with parallel spin and arises from the anti-symmetric nature of the wave function described as a Slater Determinant.

In order to obtain the set of orbitals $\{\chi_i\}$, which constitute the HF wave function, we have to include approximatively the interaction of a given electron i with the other electrons as well as with the nuclei. The potential felt by the electron i can be approximated as a mean-field created by the remaining electrons. Within this approximation, each orbital χ_i is an eigenvector of an effective operator, called the Fock operator \hat{F} and the i energy levels of the systems (e_i) correspond to the eigenvalues of the eigenvalue equations, known as Hartree-Fock equations:

$$\hat{F}\chi_i = e_i \chi_i \quad (2.2.13)$$

Therefore, the minimization of the energy associated with the determinant describing the wave function Φ_0 is nothing more than a series of $n/2$ eigenvalue problems to solve, where $n/2$ corresponds to the number of occupied molecular orbitals of the system. The Fock operator is defined as:

$$\hat{F}(1) = \widehat{h}_1(1) + \sum_j^{n/2} [2\widehat{J}_j(1) - \widehat{K}_j(1)] \quad (2.2.14)$$

where:

$$\widehat{J}_j(1) \chi_i(1) = \int \chi_j^*(2) \widehat{h}_{12} \chi_j dr_2 \chi_i(1) \quad (2.2.15)$$

$$\widehat{K}_j(1) \chi_i(1) = \int \chi_j^*(2) \widehat{h}_{12} \chi_j dr_2 \chi_j(1) \quad (2.2.16)$$

As the Coulomb and the exchange operators depend on χ_i , the Hartree Fock equations are *non-linear*, more precisely these equations are defined as *coupled non-linear integro-differential equations*. An electron moving in the mean-field created by all other electrons and nuclei feels an effective potential that is included in the Hamiltonian to take into account the interelectronic repulsion term:

$$v_i^{HF} = \sum_j^{n/2} [2\widehat{J}_j - \widehat{K}_j] \quad (2.2.17)$$

This expression represents the average potential felt by the i electron occupying the i molecular orbital. The subtraction of the double sum avoids to counting each interelectronic repulsion twice.

2.2.4 Introduction of atomic orbitals basis

In order to solve the HF equations, it is possible to convert the canonical differential equations into algebraic equations introducing a known basis set (spatial functions), which define the space that our wave function can occupy. The equations coming from the above-mentioned transformation are called **Roothaan equations** and can be solved by classical techniques of numerical calculus (matrix algebra). So, starting from a set of K known basis functions (atomic orbitals) $\{\phi_\mu | \mu = 1, 2 \dots K\}$, one can rewrite the

unknown molecular orbitals as a linear expansion of atomic orbitals centered on each atom [17]:

$$\chi_i = \sum_{\mu=1}^K (C)_{\mu i} \phi_{\mu i} \quad i = 1, \dots, L \quad (2.2.18)$$

This approximation is well known as **Linear Combination of Atomic Orbitals** (LCAO). If the basis set $\{\phi_{\mu}\}$ is complete (infinite), one can use whatever set of variable functions and the expansion will be exact. But, practically, calculation methods use finite basis set: K basis set producing L canonical spin-orbitals, whose N are the occupied orbitals, while $(L - N)$ are the non-occupied ones (virtual). Consequently, in order to perfectly describe the occupied orbitals in Φ_k and determine as best as possible the energy of ground state e_0 it is necessary to choose correctly the basis set. The larger the basis set, the more one can theoretically approximate the exact representation. In other words, one can converge to the eigenfunctions of the exact Fock operator. $(C)_{\mu i}$ are the expansion coefficients, which have to be varied following an iterative procedure self-consistent field type to optimize the wave function. Hence, the problem of calculation of canonical spin-orbitals may be transform into the evaluation of coefficients by using matrix algebra.

2.2.5 The Secular Equation

Within the LCAO approximation the eigenvalue Hartree-Fock problem can be written as a matrix equation by introducing the linear expansion [17]:

$$\sum_{\mu} F_{\mu v} C_{\mu i} = e_i \sum_{\mu} S_{\mu v} C_{\mu i} \quad (2.2.19)$$

$$\mathbf{FC} = \mathbf{SCe} \quad (2.2.20)$$

Where S ($K \times K$) is the overlap Hermitian matrix, generally real and symmetric:

$$(S)_{\mu\nu} = \int \phi_{\mu}^*(1) \phi_{\nu}(1) dr_1 \quad (2.2.21)$$

The existence of the overlap matrix stems from the fact that although the basis functions are generally considered normal and linear independent, they generally are not orthogonal. Since the overlap matrix is a Hermitian, it can be diagonalized by a unitary transformation. As concern the Fock matrix F ($K \times K$), it corresponds to the matrix representation of the one -electron Fock operator (involves the coordinates of only one electron) in the basis set $\{\phi_{\mu}\}$, defined as follows:

$$(2.2.22)$$

$$(F)_{\mu\nu} = H_{\mu\nu} + \sum_{\rho} \sum_{\sigma} P_{\rho\sigma} \left[(\mu\nu|\rho\sigma) - \frac{1}{2}(\mu\sigma|\rho\nu) \right]$$

Where $(\mu\nu|\rho\sigma)$ is the Coulomb integral, $(\mu\sigma|\rho\nu)$ is the exchange integral and $P_{\rho\sigma}$ are the elements of the *density matrix*:

(2.2.23)

$$P_{\rho\sigma} = 2 \sum_i^{n/2} c_{\rho i} c_{\sigma i}$$

$H_{\mu\nu}$ are the mono-electronic integrals defined as:

$$H_{\mu\nu} = \int \phi_{\mu}^*(1) \widehat{h}_1 \phi_{\nu}(1) dr_1 \quad (2.2.24)$$

which remain fixed for a given basis set. The Fock matrix is a Hermitian as well and generally real and symmetric as the overlap matrix. \mathbf{C} is a $(K \times L)$ matrix containing the expansion coefficients C_{vi} that relate the molecular orbitals to the orthonormal basis functions, while \mathbf{e} is the diagonal matrix of orbital energies e_i :

$$\mathbf{C} = \begin{bmatrix} C_{11} & C_{12} & \dots & C_{1L} \\ C_{21} & C_{22} & \dots & C_{2L} \\ \vdots & \vdots & \ddots & \vdots \\ C_{K1} & C_{K2} & \dots & C_{KL} \end{bmatrix} \quad \mathbf{e} = \begin{bmatrix} e_1 & 0 & 0 & 0 \\ 0 & e_2 & 0 & 0 \\ \vdots & \vdots & \ddots & \vdots \\ 0 & 0 & \dots & e_L \end{bmatrix} \quad (2.2.25)$$

One can demonstrate that

$$\mathbf{C}^{\dagger} \mathbf{S} \mathbf{C} = \mathbf{1} \quad (2.2.26)$$

Comparing the \mathbf{C} matrix with equation (2.2.18), one may note that the columns describe the canonical spin-orbitals, namely the coefficients describing the spatial part φ_1 are in the first column of \mathbf{C} , the ones describing φ_2 are in the second column of \mathbf{C} , and so on.

In order to obtain the molecular orbitals $\{\psi_i\}$ and e_i energies, it is necessary to solve equation (2.2.20). But as said before, the Fock matrix F depends on the density matrix P , which in turn depends on the expansion coefficient matrix \mathbf{C} . Hence, as the eigenvalue problem is non-linear one has to use an iterative process called **Self Consistent Field** (SCF) procedure, which will be discussed in the next paragraph.

2.2.6. The Self-Consistent Field procedure

The variational problem in equation 2.2.8 can be solved starting from an initial guess of spin-orbitals and performing an iterative minimization procedure to find the best

ensemble of orbitals, which minimize the energy of the system (variational principle). The mathematical procedure used to perform the iterative minimization is the above mentioned SCF procedure, whose flowchart is represented in Figure 1.

The procedure starts with the selection of the basis set and the molecular geometry to compute the overlap matrix S (2.2.21), and the one- and two-electrons integrals. From the overlap integral and an orthogonalization procedure one can obtain the initial guess of coefficients, producing orthonormal basis functions. One can then estimate the guess density matrix P (2.2.23) and calculate the Fock matrix F to construct and solve the eigenvalue equation 2.2.20. By F matrix diagonalization one can obtain the eigenvalue and eigenvector matrices ϵ and C . Using the last calculated coefficients, one can compute an improved density matrix. At this point a convergence test should be performed. If all density matrix elements of the k^{th} and $(k - 1)^{th}$ cycles differ by less than a defined threshold, the calculation has converged, and one can use the SCF wave function to calculate molecular properties. Otherwise the procedure is repeated calculating an improved Fock matrix from the current density matrix until the self-consistency is reached. Thus, it is common to fix the threshold on the variation of the density matrix elements as convergence criteria. It is worth noticing that the iterative procedure is repeated by varying the nuclear coordinates to find the wave function at a given geometry, which minimizes the total energy. This is nothing more than a geometry optimization procedure.

From a physical point of view, the basic idea behind the SCF procedure is performing multiple evaluation and refinement of the average field felt by each electron. In other words, the mean-field produced by the guess charge density should correspond to the field produced from the same density.

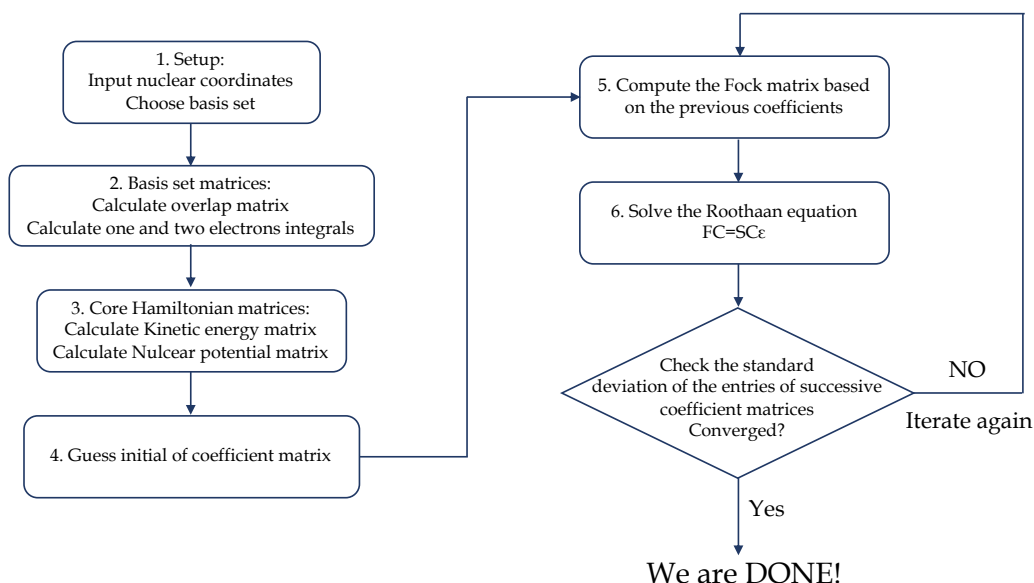


Figure 1 Flowchart of the SCF procedure within the HF approach.

2.2.7 Different types of atomic orbitals basis

At the time of performing a molecular calculation a meaningful step is the choice of the basis set to construct the wave function. The study of the chemical reactivity, for example, requires a fine representation of the valence electrons, while to predict the nuclear magnetic resonance (NMR) chemical shifts one has to properly describe the behavior of the core electrons. More generally, larger basis sets accurately approximate the orbitals by imposing fewer restrictions on the location of the electrons in the space. But evidently, one has to reach a compromise between the computational cost of a too large basis set and the inefficiency of a too small basis set.

Within the LCOA approximation, the general functions constituting the basis set are generally of two types: Slater-type orbital (STO) and Gaussian-type orbital (GTO). The STOs introduce a simplification, since they transform hydrogenoids functions into functions, whose radial part depends only on quantum numbers. The normalized form of the STOs is the following:

$$\phi^{STO} = \frac{[(2\zeta/a_0)!]^{n+1/2}}{[(2n)!]^{1/2}} r^{n-1} e^{-\zeta r/a_0} Y_l^m(\theta, \Pi) \quad (2.2.27)$$

The set of all such functions form a complete set, where n , l , and m are the quantum numbers, while $Y_l^m(\theta, \Pi)$ are the spherical harmonics as a function of radial coordinates. The parameter ζ is called the *orbital exponent* and corresponds to the exponent of the function controlling its 'diffuseness' with respect to the nuclear center. The STOs well represent the exponential decrease of the electron-nuclei interaction amplitude as a function of the nuclei distance, moreover they accurately describe the cusp at the origin, and eventually their use allows a fast basis convergence. Nevertheless, if the one- and two-centers integral is analytical, the three- and four-centers integral is not as well. Indeed, the STOs are basis used to describe simple systems. For more complex systems, it is usual to reproduce the overall form of a STO by using a linear combination of GTOs, that are rather simpler to integrate. The general form of a GTO is represented as the product of a Cartesian factor and an exponential:

$$\phi^{GTO} = \left(\frac{2\alpha}{\pi}\right)^{3/4} \left[\frac{(8\alpha)^{i+j+k} i! j! k!}{(2i)!(2j)!(2k)!}\right]^{1/2} x^i y^j z^k e^{-\alpha r^2} \quad (2.2.28)$$

Since the exponent term decays more rapidly, the GTOs do not present a likeness to the hydrogen 1s orbital. x , y , and z are the Cartesian coordinates, while α controls the width of the Gaussian function. i , j , and k are non-zero integers represent the type of atomic orbital according to their value:

- $i = j = k = 0$ ($i + j + k = 0$) Spherical symmetry \rightarrow orbital s
- $i = 1$ and $j = k = 0$ ($i + j + k = 1$) Axial symmetry \rightarrow orbital p
- $i + j + k = 2 \rightarrow$ orbital d

Although all types of integrals have an analytical solution, since the product of two different centered-atom gaussians gives back a third gaussian, the GTOs present some disadvantages. As concerns the radial part of the orbital, the GTOs have a zero derivative at the origin, unlike the STOs that faithfully reproduce the above-mentioned point effect (cusp). Meanwhile, the GTOs do not closely reproduce the exponential decrease at long distance.

Practically, it is typically used to retain some of the Gaussian *primitives* (PGTO) in fixed linear combinations, and this procedure is called *contraction*. Hence, the resulting *contracted* Gaussian functions (CGTO) is a linear combination of *primitive* Gaussian-type orbitals written as follows:

$$\phi^{CGTO} = \sum_{\mu} d_{\mu} \phi_{\mu}^{GTO} \quad (2.2.29)$$

d_{μ} are the coefficients of each primitive function and control the overall shape of the CGTO. Each primitive function differs only in the width (the exponent α), while it conserves its character (i.e. i , j , and k remain identical). Different contraction procedures exist: a *segmented contraction*, if a set of PGTOs is divided in such a way that each one defines a CGTO. Or a *general contraction* when all primitives – for each atom and angular moment – contribute to the composition of CGTOs. In any case, the price to be paid for the contraction is the loss of variational flexibility. Indeed, during the optimization of the overall wavefunction, one can solely optimize the linear combination coefficients of the basis functions and not the coefficients attributed to each primitive.

The smallest possible basis set is called the *minimal basis set*, and it contains a function to represent every orbital necessary for the description of the atom electrons (simple- ζ). For example, the hydrogen atom has just one orbital, but carbon has 5 (1s, 2s, 2p_x, 2p_y, and 2p_z), even though one of the p orbitals for carbon atom will be unoccupied. These basis sets are the *STO-MG*, namely *Slater Type Orbitals* approximated by M Gaussian functions. M is the contraction length and can vary from 2 to 6. The most common is the *STO-3G*, which accounts three Gaussian primitives per basis function. Moreover, there is the possibility to double, to triple (to quadruple, to quintuple, ...) the number of basis functions for each atomic orbital (double- ζ , triple- ζ ...). For example, in the *split-valence basis set* the core electrons are described by simple- ζ with more primitives, while the valence electrons are represented by triple- ζ by utilizing less primitives. They can be schematically referred as $k - nlmG$, where k corresponds to the number of PGTOs summed to describe the inner shell orbitals, while n , l , and m are referred to the number of basis function used to represent the valence electrons. For example, in the *3-21G* basis set for the carbon atom, the 1s orbital is described by simple- ζ with $k=3$ Gaussian primitives, while 2s, 2p_x, 2p_y, and 2p_z orbitals are described by $n=2$ Gaussian primitives, which comprise the first STO of the double- ζ , and $l=1$ Gaussian function in the second STO double- ζ .

The split valence basis set allows orbitals to change size but not the shape. *Polarized basis sets* remove this limitation by adding functions presenting a higher angular momentum than valence electrons (p for H, d for elements of the second row, f functions for transition metals). These functions are schematically noted after the “G” with the corresponding letter or by asterisks: $k - nlmG$ (d,p,f) or $k - nlmG^{***}$.

In order to allow orbitals occupying larger regions of the space one can use *diffuse functions*, which are functions with lower α exponent. These functions are useful to describe systems with electrons relatively far from the nucleus: lone pairs, systems with negative charge, system at the excited state, system with low ionization potential and so on. They are schematized as “plus” before the “G”: $k - nlm++G$.

In order to reduce computational cost, it is possible to separate the valence electrons (active) and core electrons (spectators). The latter ones can be represented by a pseudopotential operator added to the core Hamiltonian and optimized to better reproduce an all electron calculation, as in the case of LANL2DZ. Moreover, the employment of this method permits to include at least indirectly some relativistic effects.

2.2.8 Electron Correlation

The Hartree-Fock theory is an approximated method developed to solve the stationary eigenvalue Schrödinger equation. As said before, it stems on a mean-field approximation, namely each electron moves in a static electric field generated by all the other electrons. It obviously does not represent the real behavior of the system where the electron movements are correlated. The Hartree-Fock theory actually results a higher total energy than the exact one, which misses the electronic correlation energy. Indeed, contrary to the Hamiltonian operator \hat{H} returning the electronic energy for a many-body system, the Fock operator \hat{F} is an ensemble of one-electron operators, which compute the energy for the wave function described by a single Slater determinant. Within the limit of a complete basis set, Per-Olov Löwdin thus defined the correlation energy as the difference between the exact non-relativistic energy and the HF energy:

$$\varepsilon_{correlation} = \varepsilon_{exact} - \varepsilon_{HF} \quad (2.2.30)$$

Nevertheless, the Hartree-Fock method in a certain way includes the electronic correlation through the Fermi correlation. Excluding the possibility to find two electrons with the same spin in the same orbital, the Fermi correlation is actually a direct consequence of the antisymmetric character of the fermion wave function, included by using the Slater determinant. The Hartree-Fock method cannot be defined properly no-correlated, since it considers the effect of the electron correlation in an average sense - each electron sees and reacts to an average electron density. Nevertheless, the approach does not include the correlation of electronic instantaneous movement. Indeed, it is the Coulomb hole (repulsion among electrons,) that defines the electronic correlation, which reduces the probability to find electrons close each

other's. Generally, two types of electronic correlation are missed in the HF approach: *static* and *dynamic*. The missing static electronic correlation arises from the mono-determinantal nature of the wave function. But multiconfigurational and post-HF methods are able to recover the static correlation using multiple Slater determinants. While, the dynamic electronic correlation arises from the substitution of the interelectronic repulsion term in the Hamiltonian for the average potential and can be recovered by post-HF methods. It is worth to notice that the density functional theory (DFT) is able not only to recover the dynamic correlation, but in some extend may recover also part of the static electronic correlation.

2.3 Density Functional Theory (DFT)

The Density Functional Theory (DFT) is a quantum method developed to study the electronic structure of a system. Rather than HF and Post-HF methods, which are based on a complex multielectronic wave function, the DFT stems on the simple electron density of the system. Indeed, the electronic wave function of an n -electrons molecule not only depends on $3n$ spatial and n spin coordinates, but also it lacks a direct physical significance. On the other hand, the electronic density is a real observable (e.g. X-ray spectroscopy), which can be defined by only three spatial coordinates (x,y,z) , linked to the WF as follows [18]:

$$\rho(r) = \Psi^*(r)\Psi(r) = |\Psi^2(r)| \quad (2.3.1)$$

The N - electrons are directly correlated to the electron density by the integration of the density over all space:

$$N = \int \rho(r) dr \quad (2.3.2)$$

The main advantage of this theory is the simplification of the N -electron problem into a unique electron density problem. This is the reason why DFT is the most utilized approach over the WF based methods to provide an efficient and accurate description of *ground state properties*, especially for large molecules. Furthermore, DFT is able to produce quite accurate results comparable with experimental data with relatively small basis sets and low computational costs.

DFT is generally defined as a formally exact method for systems of interacting particles, which uses the basic approach of solving the eigenvalue Schrödinger equation. The rigorous modern formulation of DFT is due to Hohenberg and Kohn, authors of the two most important foundation theorems [19].

2.3.1 Existence and variational theorems

The enunciate of the first Hohenberg and Kohn theorem, also known as the **existence theorem**, is the following:

Theorem 1: *“Two N -electron systems defined by two Hamiltonians with external potentials differing by more than one constant cannot have ground states with the same electronic density, i.e. the external potential is defined by the electron density of the ground state.”*

This theorem proves that the ground electron density $\rho_0(r)$ can replace, within a trivial additive constant, the external potential $v_{ext}(r)$. As the integration of the electron density yields the number of electrons (2.3.2), consequently $\rho_0(r)$ determines the ground state wave function. Therefore, according to this theorem the ground state

energy of a quantum mechanical system is a *functional* of the electron density. (Contrary to a *function*, which maps one number to another, a *functional* assigns a number to a function). Hence, a unique relationship exists between the ground state energy and the ground state electron density. Within the BOA approximation, one can express the ground state electronic energy as follows:

$$E_0(\rho) = \langle T_e(\rho) \rangle + \langle V_{ee}(\rho) \rangle + \langle V_{Ne}(\rho) \rangle \quad (2.3.3)$$

It is easy to see the correspondence between this relation and (2.1.2).

$\langle T_e(\rho) \rangle$, $\langle V_{ee}(\rho) \rangle$ $\langle V_{Ne}(\rho) \rangle$ are respectively the kinetic energy, the electron-electron repulsion and the nucleus-electron attraction potential energies (the expectation values of the corresponding operators). The potential generated by the nuclei can be considered as an external potential felt by the electrons. Generalizing (2.3.3), one can write

$$\langle F_{HK}(\rho) \rangle = \langle T_e(\rho) \rangle + \langle V_{ee}(\rho) \rangle \quad (2.3.4)$$

$F_{HK}(\rho)$ contains the kinetic energy of the electrons and their interactions. This functional is independent to the form of the external potential and depends only on the electrons. One can rewrite (2.3.3) as:

$$E_0(\rho) = \langle F_{HK}(\rho) \rangle + \int \rho(r) v_{ext}(r) dr \quad (2.3.5)$$

Moreover, $\rho_0(r)$ also defines the expectation values of any ground state observable. This means that in principle one can find all other properties for all electron systems, which are functionals of $\rho_0(r)$.

The second Hohenberg and Kohn theorem, called **variational theorem**, enunciates that:

Theorem 2: “Any approximate trial electronic density $\rho(r)$, which defines completely the v_{ext} and a trial wave function Ψ , can be used to determine variationally the electronic density that minimizes the energy of the ground state”.

The second theorem introduces the possibility to use the variational method as a resolution procedure to calculate the energy of the ground state:

$$E(\rho) = \langle \Psi(\rho) | \hat{H} | \Psi(\rho) \rangle \geq E_0 \quad (2.3.6)$$

It means that any trial electronic density will give an upper bound on the true ground state density. To reassume, according to the existence theorem there is an exact functional relationship, which is a *universal* functional, between the ground state energy and the electron density. This latter can be optimized variationally according to the second theorem. Nevertheless, in order to use the variational optimization

procedure, one has to exactly know the relationship between E and ρ . But it is not possible to know the analytic formula of the universal functional, as the exact formula of the electronic kinetic energy $\langle T_e(\rho) \rangle$ and interelectronic interaction $V_{ee}(\rho)$ are not known.

2.3.2 The Kohn-Sham method

In order to overcome the principal drawback of expressing the universal functional, Kohn and Sham proposed an exact method to determine the ground state electron density of a system, and consequently the energy. In principle the method is exact, but actually the Kohn Sham (KS) equations contain an unknown functionals that has to be approximated. Therefore, the results yield by DFT in the KS formulation are approximated. The starting point of the theory is considering a fictitious reference system of N non-interacting electrons, which feel the same external potential $v_{ext}(r)$. The external potential is such that the ground state electron density of the reference system ρ_r is equal to the exact electron density of the system of interest $\rho_r = \rho_0$. One can introduce two quantities $\Delta\langle T(\rho) \rangle$ and $\Delta\langle V_{ee}(\rho) \rangle$. The first corresponds to the deviation of the real kinetic energy from that of the reference system and contains the correlation kinetic energy:

$$\Delta\langle T(\rho) \rangle = \langle T_e(\rho) - T_r(\rho) \rangle \quad (2.3.7)$$

While $\Delta\langle V_{ee}(\rho) \rangle$ is the deviation of the real electron-electron repulsion energy from that of the reference system. It can be expressed as the difference between the true electron-electron coulombic repulsion and a classical term that accounts only for average electronic repulsion.

$$\Delta\langle V_{ee}(\rho) \rangle = \langle V_{ee}(\rho) \rangle - \frac{1}{2} \int \int \frac{\rho(r_1)\rho(r_2)}{r_{12}} dr_1 dr_2 \quad (2.3.8)$$

Therefore, the deviation includes all electron-electron interactions not contained in the classical term, namely the exchange and instantaneous electronic correlation.

Using (2.3.7) and (2.3.8), one may rewrite (2.3.3) as:

$$E(\rho) = \langle T_r(\rho) \rangle + \frac{1}{2} \int \int \frac{\rho(r_1)\rho(r_2)}{r_{12}} dr_1 dr_2 + \int \rho(r) v_{ext}(r) dr + \Delta\langle T(\rho) \rangle + \Delta\langle V_{ee}(\rho) \rangle \quad (2.3.9)$$

The sum of the last two terms is the so-called *exchange correlation energy functional*:

$$E_{xc} = \Delta\langle T(\rho) \rangle + \Delta\langle V_{ee}(\rho) \rangle \quad (2.3.10)$$

Using (2.3.10) and (2.3.9), the resultant KS - total energy functional can be written as:

(2.3.11)

$$E(\rho) = \langle T_r(\rho) \rangle + \frac{1}{2} \iint \frac{\rho(r_1)\rho(r_2)}{r_{12}} dr_1 dr_2 + \int \rho(r) v_{ext}(r) dr + E_{xc}$$

The first three terms can be explicitly expressed by KS orbitals, while the last term contains all information that one does not know how to calculate exactly.

1. The first term $\langle T_r(\rho) \rangle$ is the electronic kinetic energy of the non-interacting system. It can be calculated as the expectation value of the summation of the one electron kinetic energy operators over the ground state multielectron wave function of the reference system Ψ_r :

(2.3.12)

$$\langle T_r(\rho) \rangle = \langle \Psi_r \left| \sum_{i=1}^N -\frac{1}{2} \nabla_i^2 \right| \Psi_r \rangle$$

As the reference system is non-interacting, Ψ_r can be written as a Slater determinant wavefunction built up from a set of one-electron orbitals, the *Kohn-Sham orbitals* χ :

(2.3.13)

$$\langle T_r(\rho) \rangle = -\frac{1}{2} \sum_{i=1}^N \langle \chi_i | \nabla_i^2 | \chi_i \rangle$$

Moreover, the KS-orbitals give an easy way to construct the density:

(2.3.14)

$$\rho(r) = \sum_{i=1}^N \chi_i^*(r) \chi_i(r) = \sum_{i=1}^N |\chi_i(r)|^2$$

2. The second term corresponds to the classical electrostatic repulsion energy, which can be readily calculated knowing ρ .
3. The third term corresponds to the integral of the density times the external potential and can be expressed as:

(2.3.15)

$$\int \rho(r) v_{ext}(r) dr = \int \left[\rho(r) \sum_{\text{nuclei } A} -\frac{Z_A}{|r-R|} \right] dr = - \sum_{\text{nuclei } A} Z_A \int \frac{\rho(r)}{|r-R|} dr$$

Once the density ρ is known, the integral to be summed are readily calculated.

4. The fourth term is the above-mentioned exchange-correlation functional, whose exact formulation is not known. E_{xc} is the term most affected to error and it is negative. If one knows exactly its values, the total energy functional calculated by the DFT method would be exact. Consequently, the accuracy of

DFT calculations depends on the accuracy of exchange-correlation functional. But compared to the other energetic terms it is relatively small, thus yielding quite realistic results.

Using (2.3.13), (2.3.14) and (2.3.15), one can obtain a new definition of the energy functional able to connect the KS orbitals, the electron density and the energy:

$$E(\rho) = \sum_{i=1}^N \chi_i^*(r) \left(-\frac{\nabla_i^2}{2} \right) \chi_i(r) dr + \frac{1}{2} \sum_{i=1}^N \chi_i^*(r_1) \left(\int \frac{\rho(r_2)}{r_{12}} \right) \chi_i(r_1) dr_1 - \sum_{\text{nuclei } A} \int \chi_i^*(r) \left(\frac{Z_A}{|r-R|} \right) \chi_i(r) dr + E_{xc} \quad (2.3.16)$$

With the constrain that the KS orbitals remain orthonormal:

$$\int \chi_i^* \chi_j d\tau = \delta_{ij} \quad (2.3.17)$$

the KS orbitals are eigenfunctions of the KS operator and solving the eigenvalue equation it is possible to obtain the energy levels of the KS orbitals ε_i :

$$\left(-\frac{\nabla_i^2}{2} + \int \frac{\rho(r_2)}{r_{12}} - \sum_{\text{nuclei } A} \left(\frac{Z_A}{|r_1-R|} \right) + V_{xc}(1) \right) \chi_i(r) = \varepsilon_i \chi_i(r) \quad (2.3.18)$$

The first three terms of the KS operator account respectively for the kinetic energy of the electron in χ_i , the Coulombic attraction between the electron in χ_i and the total electron density, and finally the static coulombic repulsion between the nuclei and the electron in χ_i .

The last term V_{xc} is the exchange correlation potential and accounts for the exchange repulsion, the electron correlation, the self-interaction energy and the kinetic energy correction associated with the electron in χ_i . It can be defined as the exchange correlation energy functional derivative respect to the electron density:

$$V_{xc}[\rho(r)] = \frac{\partial E_{xc}[\rho(r)]}{\partial \rho(r)} \quad (2.3.19)$$

The KS equation can be thus written as:

$$\widehat{h}^{KS} \chi_i(r) = \varepsilon_i \chi_i(r) \quad (2.3.20)$$

It is possible to glimpse a similarity with the HF equation. However, in the Fock operator only exchange interactions are accounted. Therefore, it does not properly consider the electron correlation as the KS operator. The HF method aims to solve the SE using a trial approximated WF consisting of a single Slater determinant. Thus, it

computes an exact solution to an approximate problem, unlike the DFT that yields an approximated solution to an exact description due to the E_{xc} term.

Nonetheless, the standard procedure to solve the KS eigenvalue problems reflects the resolution variational approach for the HF eigenvalue equations. Indeed, one can expand the KS orbitals as linear combination of atomic basis functions centered on each atom:

$$\chi_i = \sum_{v=1}^m c_{vi} \phi_v(r) \quad i = 1, 2, 3 \dots, m \quad (2.3.21)$$

c_{vi} are the coefficients that have to be optimized variationally to obtain the ground state wave function. As a result, the KS equations can be solved by the iterative SCF procedure as explained in 2.2.6. Paragraph. In this case, the optimization procedure starts with the guess of the electron density to obtain the external potential v_{ext} and obtain the expression of the KS equations. From the diagonalization of the set of N eigenvalues equations it is possible to calculate the coefficients and replicate the same procedure until the density matrix elements are sufficiently similar. The consistency condition requires that the calculated charge density corresponds to the field produced by the same density.

2.3.3 The Exchange-Correlation energy

The exchange correlation functional contains all information about the many body system of interacting electrons. In order to calculate the DFT energy of the system one has to make approximation of this term. Nevertheless, a systematic procedure to improve the E_{xc} (thus improving the calculated molecular properties) does not exist and this represents the main weakness of the DFT method. Perdew proposed a general classification of the different approximation, namely the well known "*Jacob's ladder of density functional approximation*". Climbing the rungs of this ladder, which in mathematical terms means by inclusion of additive terms, one may access to more accurate approximations, but on the backs of computational cost.

According to the specific system to study, the best approximation has to be chosen in order to describe as well as possible the molecular properties. In this section various approximation of the V_{xc} will be discussed, along with their implications on the corresponding calculated energy of the system.

The local density approximation (LDA)

The local density approximation is the easiest approach to approximate E_{xc} , based on a model problem, namely the homogeneous electron gas. The adjective *local* indicates that the energy density for a given point in the system is computed exclusively considering the value of the electron density ρ at that point. Within the LDA, the ρ

varies very slowly with the position r , and thus the fluctuations in ρ away from r do not affect the value of E_{xc} at r [20]. Moreover, the exchange and correlation contributions are separated in two terms:

$$E_{XC}^{LDA} = \int \rho(r) \varepsilon_{xc}[\rho(r)] dr = \int \rho(r) \{ \varepsilon_x[\rho(r)] + \varepsilon_c[\rho(r)] \} dr \quad (2.3.22)$$

The exchange term can be computed analytically:

$$\varepsilon_x^{LDA}[\rho(r)] = C_x \rho(r)^{1/3} \quad (2.3.23)$$

For the correlation term, in turn, there is not an analytical formulation. Therefore, its analytical expression may be approximated through a complex function depending on parameters fitted by values coming from accurate simulations for the energy (as quantum Monte-Carlo) of the uniform electron gas as reference.

The local spin density approximation (LSDA)

The local spin density approximation can be considered as an extension of the LDA where the electrons of the uniform gas are treated differently according to their spin projection α and β . Particularly, the KS orbitals are separated in χ_α and χ_β from which different electron density functions ρ_α and ρ_β are calculated.

This approximation has the advantage of handling system with one or more unpaired electrons, such as radical, or non-equilibrium geometries becoming unpaired. Anyhow, both LDA and LSDA functionals lead to results not enough accurate. So, they have been replaced for most accurate functionals including corrections that impose nonlocality.

The generalized gradient approximation (GGA)

The electron density in atoms, molecules and solids varies significantly from one place to another, thus they are systems which cannot be correctly described as a locally homogenous electron gas (as in LDA and LSDA). Indeed, they can be largely replaced by an approach including information about not only the electron density in a specific point, but also in the immediate neighborhood of that point. More specifically, this approach uses both the electron density and its gradient, the slope which is the first derivative with respect to the position. This is the reason why this approximation is called generalized gradient approximation and makes use of *gradient-corrected* functionals, also better known as *semi-local* functionals [21].

$$\varepsilon_x^{GGA}[\rho(r)] = \varepsilon_x^{LDA}[\rho(r)] - \sum_\sigma F \left(\frac{\nabla \rho_\sigma}{\rho_\sigma^{4/3}(r)} \right) \rho_\sigma^{4/3}(r) dr \quad (2.3.24)$$

These functionals are typically constructed by adding gradient corrections to the LDA functionals, in a way like Taylor series expansion framework.

Some of these GGA functionals are semi-empirical functionals, namely they use adjusted parameters by fitting experimental data, such as the atomic energies. But other parameter-free GGA functionals exist, which are known for their general applicability giving rather accurate results for a wide range of systems, as the PBE functional. A further improvement over LDA functionals is represented by the inclusion of the dependence on the second order derivative of the density, which basically corresponds to the Laplacian. Such functionals are called *meta*-GGA functionals. Nevertheless, due to numerical issues with the calculation of the second derivative of the electron density, a generally used formalism includes the dependence on the kinetic energy density τ , which practically corresponds to the Laplacian of the KS orbitals χ_i determined by the SCF procedure:

$$\tau(r) = \sum_i^{\text{occupied}} \frac{1}{2} |\nabla \chi_i(r)|^2 \quad (2.3.25)$$

The Adiabatic connection method

Within the KS approximation one usually assumes a fictitious non-interacting reference system of particles and calculates the total energy of the real system as a perturbation of the reference one. The adiabatic connection rather relates the physical and KS systems in a continuous fashion but following the electron-electron interaction with an external parameter λ . This latter establishes somehow the relation between the real and non-interacting system varying from 0 to 1. At $\lambda = 0$ the electrons do not interact, the wavefunction corresponds to the KS wavefunction and the external potential can be calculated as KS potential. On the other hand, at $\lambda = 1$ the system returns to be fully interacting correlated. Using the Hellmann-Feynman theorem, one can express the exchange and correlation potential as a function of λ , which controls the amount of the DFT exchange and correlation functional and the exact HF exchange. Particularly, the potential can be written as a polynomial function of degree $n-1$, where n controls the velocity according to which the correction brought to the DFT is canceled for λ that tends to 1:

$$v_{xc}^\lambda[\rho] = E_{xc,\lambda}^{DFT}[\rho] + (E_x^{HF} - E_{xc}^{DFT}[\rho]) + (1 - \lambda)^{n-1} \quad (2.3.26)$$

Trough the integration of (2.3.26) over the interval $\lambda \in [0,1]$ one can obtain:

$$E_{xc}[\rho] = \int_0^1 v_{xc}^\lambda[\rho] d\lambda = E_{xc}^{DFT}[\rho] + \frac{1}{n} (E_x^{HF} + E_{xc}^{DFT}[\rho]) \quad (2.3.27)$$

One can derive that the exchange-correlation energy can be computed as follows [18]:

$$E_{xc}[\rho] = \int_0^1 \langle \Psi(\lambda) | v_{xc}(\lambda) | \Psi(\lambda) \rangle \quad (2.3.28)$$

For simplicity, it is useful to refer to the geometrical representation of this integral. The overall electron-electron interaction can be portioned in two parts, represented by the rectangle A and part of rectangle B. The bottom rectangle A exemplifies the exact exchange for the non-interacting system, which is the expectation value computed by HF method using KS orbitals. The remaining area below the red curve is represented by a fraction z of the upper rectangle B and depicts the contribution of the electronic interaction due to the exchange-correlation energy. As both z parameter and the expectation value of the fully interacting exchange - correlation potential are not known, one can consider z as an empirical constant to be optimized, and thus weight the selected DFT functional (GGA, *meta*-GGA functionals for example) by z in order to approximate the fully interacting system.

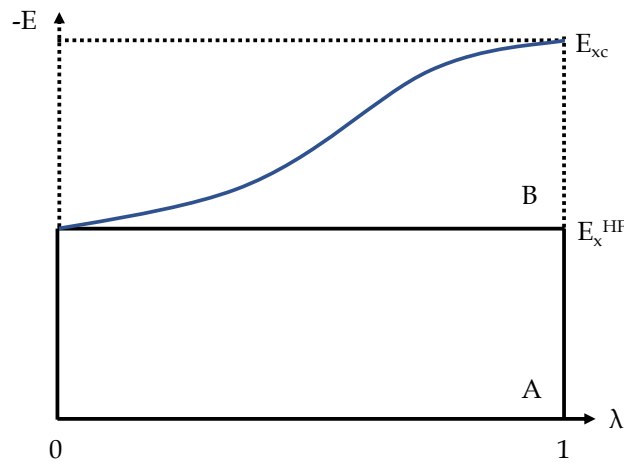


Figure 2 Schematic representation of the adiabatic connection method. Rectangle A represents the fully non-interacting system contributing only for the exchange interaction. The sum of the area of rectangle A plus that under the blue curve in rectangle B (a x fraction of rectangle B) represents the full exchange-correlation energy.

Particularly, the total area under the expectation value curve can be estimated as:

$$E_{xc} = E_x^{HF} + z(E_{xc}^{DFT} - E_x^{HF}) \quad (2.3.29)$$

Or more commonly, by substitution of $a = 1 - z$

$$E_{xc} = (1 - a) E_{xc}^{DFT} + a E_x^{HF} \quad (2.3.30)$$

Therefore, the mixing of a fraction of the exact exchange calculated by HF method with DFT functionals (standard LDA or GGA) stems the basis of the adiabatic connection method (ACM), such defined since its formulation allows the connection between the non-interacting and the fully interacting states. Functionals such defined are called *hybrid functionals*. An example is the B3LYP functional [22], which contains additional empirical parameters to improve the computation of the total exchange correlation energy defined as:

$$E_{xc}^{B3LYP} = (1 - a) E_x^{LSDA} + aE_x^{HF} + b\Delta E_x^B + (1 - c)E_c^{LSDA} + cE_c^{LYP} \quad (2.3.31)$$

Where $a = 0.20$, $b = 0.72$, $c = 0.81$, E_x^B is the GGA exchange functional developed by Becke and E_c^{LYP} is the correlated functional developed by Lyp. Another hybrid functional widely used is the PBE0 defined as [23]:

$$E_{xc} = E_c^{PBE} + E_x^{PBE} + \frac{1}{4}(E_x^{HF} - E_x^{PBE}) \quad (2.3.32)$$

In this case the DFT functional used to approximate the fully interacting system is the PBE - Perdew, Burke and Ernzerhoff [21]. From its definition, it is possible to see that the exchange and correlation contribution are separated, and the ACM has been applied only on the exchange part. The HF part represents the 25%, so $a = 0.25$. Since the a parameter derives from perturbation theory arguments and the PBE does not contain empirical parameters, thus the PBE0 functional is considered as a parameter-free global hybrid functional.

2.3.4 Self-interaction energy and different types of hybrid functionals

Despite the developments during the last years, the DFT remains a theory which cannot be used to properly describe intermolecular interactions, such as van der Waals forces (dispersions), charge transfer (CT) complexes, transition states energies (thus reaction barriers), IP from Koopmans, calculations of the band gap in semiconductors, bond length alternation, magnetic properties. All these failures stem on the inability of the DFT to deal with the self-interaction error (SIE) by the xc-functional. In the Hartree energy, the self-interaction is included by construction and then cancelled by the exact exchange correlation energy, giving reasonable results at dissociation limit. On the contrary, as concern the DFT method, the self-interaction contribution in the Coulomb term of the xc-functional is not canceled by the self-interaction in the exchange term. This error gives rise to spurious and unphysical orbital energies and moreover, does not permit an exact reproduction of the potential energy surface (PES) to describe several physical processes.

In general, this self-interaction error should be connected somehow to the properties of the xc-potential. One can imagine removing an electron from a neutral system to the infinity. Such electron will interact with the hole created by the electron removing process, thus implying that the potential felt by the isolated electron should exhibit the $-\frac{1}{r}$ asymptotic behavior:

$$\lim_{|r| \rightarrow \infty} v_{xc}(r) = -\frac{1}{|r|} \quad (2.3.33)$$

The average potential calculated from the HF method is able to correctly describe this behavior, while the LDA potential decays much faster at long-range distance. Hence, the correct asymptotic decay of the xc-potential is an important condition for the improvement of the theory.

Range-separated hybrid functionals

The aforementioned global hybrid functionals incorporate a fraction of the HF exact exchange, thus correcting many failures of local or semi-local functionals and giving rather accurate results for a wide range of properties. Nevertheless, none of them is actually self-interaction free and the asymptotic decay of the potential from them is $-a/r$, proportional to the fraction of the exact exchange a . In order to correct describe the long-range behavior, an improvement of the hybrid functionals has been proposed, *i.e.* the class of *range-separated hybrids (RSH)* functionals. They have been developed by partitioning the electron-electron interaction in two terms, namely the short-range (SR) interaction described by local DFT exchange functionals, and the long-range (LR) interaction described by exact HF exchange:

$$\frac{1}{r} = \underbrace{\frac{\xi_{sr}^{\omega}(r)}{r}}_{DFT} + \underbrace{\frac{1 - \xi_{sr}^{\omega}(r)}{r}}_{HF} \quad (2.3.34)$$

$\xi_{sr}^{\omega}(r)$ is a smooth range separation function usually defined by a complementary error function $\xi_{sr}^{\omega}(r) = 1 - \text{erf}(\omega r)$. The exact long-range HF exchange mimics the correct asymptotic decay and simultaneously at short-range the theory gains still benefit from the mutual error cancellation of the DFT exchange and correlation functionals:

$$E_{xc}^{RSH} = aE_x^{SR-HF}(\omega) + (1 - a)E_x^{SR-DFA}(\omega) + bE_x^{LR-HF}(\omega) + (1 - b)E_x^{LR-DFA}(\omega) + E_c^{DFA} \quad (2.3.35)$$

where DFA stands for density functional approximation. These functionals are also called *long-range corrected* (LC) functionals or as *Coulomb-attenuating method* (CAM) functionals. One can generalize (2.3.34) using extra parameters a, b and ω :

$$\frac{1}{r} = \frac{1 - [\alpha + \beta \text{erf}(\omega r)]}{r} + \frac{\alpha + \beta \text{erf}(\omega r)}{r} \quad (2.3.36)$$

The parameter a, b, μ and ω are basically determined empirically and as in the case of global hybrids, the usual procedure is fitting a standard benchmark set of molecules to experimental thermochemical data, and the obtained values are then used for all systems.

The range-separated functionals have been shown to correctly describe response properties, photoemission spectra, bond length alternation in conjugated polymers and charge transfer (CT) excitation. An example of these functionals is represented by the LC-PBE functional [24]. It combines a GGA functional, namely the PBE [21], using the range separation parameter $\omega = 0.33 \text{ Bohr}^{-1}$ and $\alpha = 0$ and $\beta = 1$. Another is the CAM-B3LYP, which combines the hybrid qualities of B3LYP [22] and the long-range correction [25]. At SR it comprises $\alpha = 0.19$ (HF) and $\beta = 0.81$ (Becke exchange

interaction), while at LR $\alpha = 0.65$ and $\beta = 0.35$. The intermediate region is smoothly described through the standard error function with $\mu = 0.33$.

Double hybrid functionals

A complex evolution of hybrid functionals is represented by the *double hybrid* (DH) functionals [26]. The implementation of these functionals is triggered by the idea that not only the exchange, but also the correlation part in KS-DFT has a non-local orbital dependency. Therefore, the innovative idea is adding a certain amount of exact HF exchange and a correction in the correlation energy from the perturbation theory. Therefore, normally a standard hybrid functional containing the common semi-local GGA for the exchange and correlation is used, and a classical self-consistent KS calculation is carried out to obtain the KS orbitals. *A posteriori*, the calculated KS orbitals are used as input for a standard second-order Møller-Plesset (MP2) type perturbation theory correction. In this way, part of the semi-local GGA correlation can be corrected. The general expression of the DH exchange and correlation functional is:

$$E_{xc}^{DH} = a_x E_x^{HF} + (1 - a_x) E_x^{DFA} + (1 - a_c) E_c^{DFA} + a_c E_c^{MP2} \quad (2.3.37)$$

It is shown that these functionals are very accurate in reproducing the thermodynamic data, and moreover they return rather precise barrier heights, isomerization energies and well reproduce transition metal reactions.

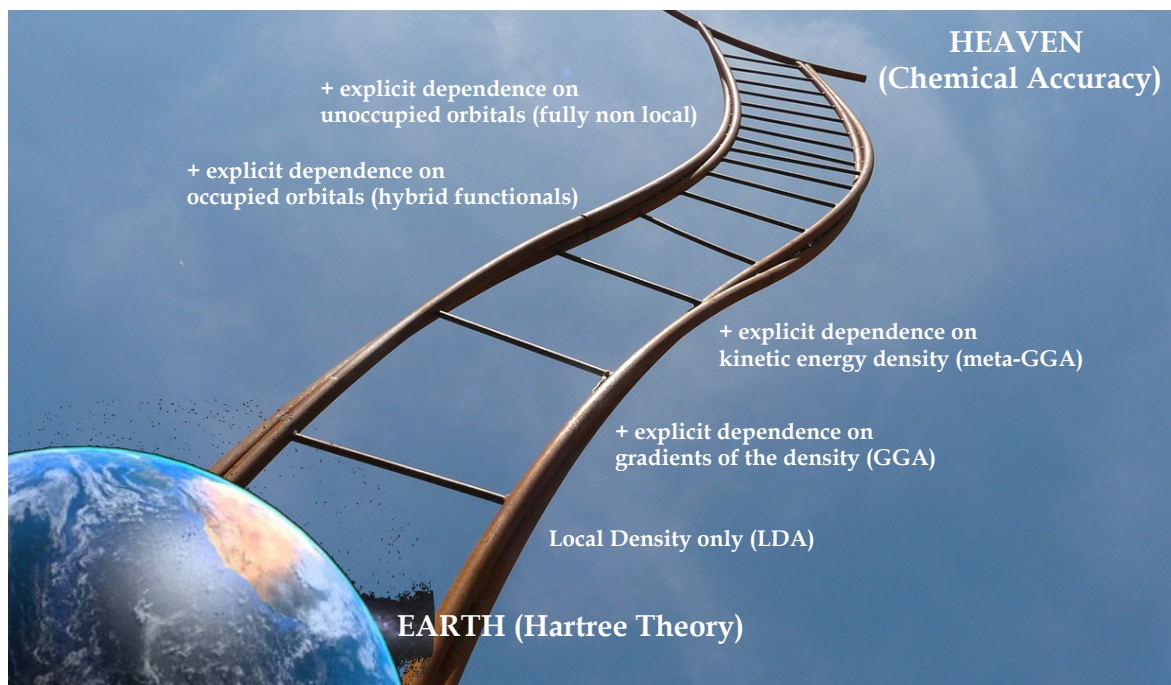


Figure 3 Schematic representation of the John Perdew Jacob Ladder.

2.4 Time-Dependent Density Functional Theory (TD-DFT)

A system undergoing a time-dependent perturbation, such as a light irradiation, can be described using the Time-dependent density functional theory (TD-DFT). Compared to the other quantum chemical methods, the main advantage of TD-DFT relies on its low computational cost to accuracy ratio, well-suit to study in particular large systems. Starting from the time-dependent SE we can write

$$\widehat{H}_{el}(r, t)\Psi_{el}(r, t) = i \frac{\partial}{\partial t} \Psi_{el}(r, t) \quad (2.4.1)$$

where the electronic Hamiltonian can be written as follows:

$$\widehat{H}_{el}(r, t) = \widehat{T}_e(r) + \widehat{V}_{ee}(r, t) + v(r, t) \quad (2.4.2)$$

As in the time-independent framework, the Hamiltonian is composed by the electronic kinetic term (\widehat{T}_e) and the electron-electron repulsion \widehat{V}_{ee} . The final term is the external potential that in this case time-dependent and can be expressed as

$$v(r, t) = v_0(r) + \theta(t - t_0)v_1(r, t) \quad (2.4.3)$$

θ is the Heaviside function. Essentially, for $t \leq t_0$ the external potential is time independent, and thus the system can be described solving the time-independent SE. For $t > t_0$, the system interacts with the same field, that in turn is time dependent.

2.4.1. Fundamental theorems in TD-DFT

Runge and Gross formalized this theory in 1984, enunciating the analog of the existence theorem of Hohenberg and Kohn for the time dependent frame [27]:

Theorem 1: *“If two time-dependent external potentials differ by more than a purely time dependent (r -independent) function, there is a one-to-one correspondence between the electronic density and these potentials, which implies that the external potential is a functional of the density”.*

This theorem demonstrated the existence of a time-dependent density $\rho(r, t)$, which is a variable enabling to determine the time-evolution of the system as the wave function does. Therefore, according to this theorem two densities $\rho(r, t)$ and $\rho'(r, t)$ evolving from the same initial state defined by Ψ_0 , subject to two different time dependent external potential $v(r, t)$ and $v'(r, t)$, become different for $t > t_0$.

Whether the Gross-Runge theorem establish the existence of this unique functional, on the other hand it does not provide a practical scheme to calculate the time dependent density in an effortless way. Instead, the KS formalism used in DFT offers a manner to

calculate the ground state energy replacing the fully interacting system with a fictitious non-interacting system having the same density. Hence, Van-Leeuwen in 1999 proposed a rigorous approximation to construct such a scheme enunciating that:

Theorem 2: *“If we consider a system described by the wave function Ψ_0 and subject to an external potential $v(r, t)$, there is another system described by another wave function Ψ'_0 subject to an external potential differing from the first by a time dependent function, such that the electron density $\rho(r, t)$ of the two systems is identical”.*

This means that if the interaction of the real and fictitious systems is identical and choosing $\Psi_0 = \Psi'_0$, there is a unique external potential $v(r, t)$ that produces the density $\rho(r, t)$ of the interacting system. So, the Gross-Runge theorem can be considered as a special case of the Van-Leeuwen theorem.

2.4.2. Linear Response approach

The direct consequence of the above-mentioned theorems is that one can utilize a KS approach to solve the SE in the TD-DFT framework. Such theory has been developed to describe the dynamical process of an excitation. Normally, during an electronic transition from the initial ground state to the final excited state, periodic charge/density fluctuations, together with dynamical many-body effect are induced. All these effects provoke the mixing of KS eigenstates and leads to a correction to the raw calculated KS eigenvalues. Therefore, the dynamical many-body effect should be somehow included. Thus, the introduction of the *exchange-correlation kernel* (f_{xc}), which can be considered as the analog in TD-DFT of the exchange-correlation functional in KS-DFT. It is worth noticing that even if the resolution of the time-dependent SE theoretically permits to access to the molecular properties at excited states, practically, its fully resolution is rather unpractical. Indeed, since the variation of the external potential can be seen as weak deviations, an alternative method is directly calculating these differences through a response approach. This means that in order to calculate the electronic excitation energy is enough considering the first order response to the perturbation [28].

In the paramount of optical spectroscopy techniques, a weak perturbation can be seen as a probing of ground state by an electric field and the corresponding linear response of the system to this stimulus contains all information about its optical spectrum. As claimed by Gross-Runge and Van-Leeuwen theorems, the time-dependent density $\rho(r, t)$ of the fully interacting system can be approximated as the density of the non-interacting time dependent Kohn Sham system subjected to the external time-dependent potential:

$$v_{ks}[\rho](r, t) = V(r, t) + \int \frac{\rho(r', t)}{|r - r'|} dr' + v_{xc}[\rho](r, t) \quad (2.4.4)$$

The perturbation acts at each t giving rise to a retarded density response at all r . It is possible to invert this relationship, writing the time-dependent density as function of the external KS potential:

$$\rho(r, t) = \rho[v_{xc}](r, t) \quad (2.4.5)$$

If the perturbation is weak enough, the density can be expanded in Taylors series and the first order term will dominate over the higher order terms. Hence, the rest can be neglected, and the first order term can be written as follows (linear response equation):

$$\rho_1(r, t) = \iint \chi_{ks}(r, t, r', t') v_{ks1}(r', t') dr' dt' \quad (2.4.6)$$

where χ_{ks} is the density-density response function for the non-interacting particle system:

$$\chi_{ks} = \left. \frac{\delta \rho[v_{xc}](r, t)}{\delta v_{ks}(r', t')} \right|_{v_{ks}[\rho_0](r)} \quad (2.4.7)$$

It yields the same response of the fully interacting many body response equation, and the corresponding linearized effective potential is:

$$v_{ks}[\rho](r, t) = V_1(r, t) + \int \frac{\rho_1(r', t)}{|r - r'|} dr' + v_{xc1}[\rho](r, t) \quad (2.4.8)$$

The first two terms, namely the external perturbation and the linearized time-dependent Hartree potential can be explicitly stated, the last term, *i.e.* the linearized exchange correlation potential can be only written via a functional Taylor expansion:

$$v_{xc1} = \iint \left. \frac{\delta v_{xc}[\rho](r, t)}{\rho(r', t')} \right|_{\rho_0(r)} \rho(r', t') \quad (2.4.9)$$

This expansion reveals the so-called time-dependent exchange correlation kernel, which is a functional of the ground state density:

$$f_{xc} = \left. \frac{\delta v_{xc}[\rho](r, t)}{\rho(r', t')} \right|_{\rho_0(r)} \quad (2.4.10)$$

This term corresponds to the crucial quantity of the TD-DFT in the linear response formalism. Once obtained the linearized potential v_{xc1} , one can substitute it in the linear response equation (2.4.6) to obtain:

(2.4.11)

$$\rho_1(r, t) = \int \int \chi_{ks}(r, t, r', t') dr' dt' \left[V_1(r, t) + \int \int \left\{ \frac{\delta(t' - \tau)}{|r' - x|} + f_{xc}(r', t', x, \tau) \right\} dx d\tau \rho_1(x, \tau) \right]$$

Here two dummy variables are introduced, namely x and τ in order to highlights the double integrals. This equation emphasizes how the linearized potential depends on the time dependent density, and thus the necessity to solve self-consistently the overall linear density response.

2.4.3. Excitation energy calculation

The linear response approach can be considered as an efficient approximation in case of slight changes of electronic structure of excited states with respect to the ground state. This is perfectly what happens during electronic transitions of the UV-visible absorption spectra. The inner electronic structure of the ground and excited states is similar, and the excited state can be treated as a slight perturbation of the ground state. The main advantage of this approach is that it is possible to compute vertical excitation energies knowing the electronic structure of the reference ground state, which in turn is easily computed by a SCF iterative minimization procedure of a DFT calculation. In order to calculate excitation energies, for practical issues, a Fourier transformation is usually performed on (2.4.11) to pass from the time domain t to the frequency domain ω :

(2.4.12)

$$\rho_1(r, \omega) = \int \chi_{ks}(r, r', \omega) dr' \left[V_1(r, \omega) + \int \left\{ \frac{1}{|r' - x|} + f_{xc}(r', x, \omega) \right\} dx \rho_1(x, \omega) \right]$$

and thus, the non-interacting Khon-Sham response function depending on frequency becomes:

(2.4.13)

$$\chi_{ks}(r, r', \omega) = \sum_{i=1}^{\infty} \sum_{j=1}^{\infty} (f_i - f_j) \frac{\phi_i^0(r) \phi_j^{0*}(r) \phi_i^{0*}(r') \phi_j^0(r')}{\omega - \omega_{ij}}$$

f_i and f_j corresponds to the occupation numbers of the KS ground state, while ω_{ij} is the difference between the KS eigenvalues (energies) for pairs of given molecular orbitals i and j ($\omega_{ij} = \varepsilon_i - \varepsilon_j$), namely the excitation energies. The double summation is necessary to include only the contributions coming from one occupied ($f = 1$) and one unoccupied ($f = 0$) molecular orbitals, while all other terms cancel out. It is worth to pinpoint that the denominator is such that the non-interacting response function presents poles at the excitation energies values of the KS system. But such KS excitation

energies are different compared to the excitation energies of the real system. Thus, during the self-consistent solution of the density response all wrong poles are canceled, while just the one that gives the exact excitation energies are conserved.

To recapitulate, the exact excitation energies are provided by the poles of the density-density response function, which diverges if the system is exposed to a perturbation at such a frequency, and the excitation energies correspond to a characteristic eigenmode of the interacting system [28]. To calculate such eigenmodes – and the eigenfrequencies – the external perturbation $V_1(r, \omega)$ is not compulsory, therefore one can rewrite (2.4.12):

$$\rho_1(r, \omega) = \int \chi_{ks}(r, r', \omega) dr' \left[\int \left\{ \frac{1}{|r' - x|} + f_{xc}(r', x, \omega) \right\} dx \rho_1(x, \omega) \right] \quad (2.4.14)$$

In this formalism the spin is not explicitly included. In any case, when spin-orbit coupling terms are absent, excitations are only allowed between orbitals with the same spin. Thus, orbital pairs of opposite spin have no distinction in space for a closed shell case. By multiplying the terms in square brackets and finally integrating over r one can obtain:

$$F_{Hxc}(x, \omega) = \sum_{i=1}^{\infty} \sum_{j=1}^{\infty} \frac{(f_i - f_j)}{\omega - \omega_{ij}} \int dr \left\{ \frac{1}{|x - r|} + f_{xc}(x, r, \omega) \right\} \phi_i^0(r) \phi_j^{0*}(r) \\ \times \int dr' \phi_i^{0*}(r') \phi_j^0(r') F_{Hxc}(r', \omega) \quad (2.4.15)$$

And

$$F_{Hxc}(r, \omega) = \int dr' \left\{ \frac{1}{|r - r'|} + f_{xc}(r', x, \omega) \right\} \rho_1(r', \omega) \quad (2.4.16)$$

By multiplying $\phi_i^{0*}(r') \phi_j^0(r')$ and integrating again over r , (2.4.15) becomes:

$$\int dr \phi_i^{0*}(r) \phi_j^0(r) F_{Hxc}(r, \omega) \\ = \sum_{i=1}^{\infty} \sum_{j=1}^{\infty} \frac{(f_i - f_j)}{\omega - \omega_{ij}} K_{ij,i',j'}(\omega) \int dr' \phi_i^{0*}(r') \phi_j^0(r') F_{Hxc}(r', \omega) \quad (2.4.17)$$

K is the matrix containing the coupling elements:

$$K_{ij,i',j'}(\omega) = \int dr \int dr' \phi_i^{0*}(r) \phi_j^0(r) \left\{ \frac{1}{|r - r'|} + f_{xc}(r, r', \omega) \right\} \phi_{i'}^{0*}(r') \phi_{j'}^0(r') \quad (2.4.18)$$

By introducing an auxiliary variable β_{ij} defined as follow:

(2.4.19)

$$\beta_{ij}(\omega) = \frac{1}{\omega - \omega_{ij}} \int dr \phi_i^{0*}(r) \phi_j^0(r) F_{Hxc}(r, \omega)$$

one can obtain the final expression, which is an eigenvalue equation giving as eigenvalues the exact excitation energies:

(2.4.20)

$$\sum_{i=1}^{\infty} \sum_{j=1}^{\infty} [\delta_{ii'} \delta_{jj'} \omega_{ij} + (f_i - f_j) K_{ij,i',j'}(\omega)] \beta_{i'j'}(\omega) = \omega \beta_{ij}(\omega)$$

The equation present finite dimension since the sums run over all bound states in KS regime and it is only defined for $f_i - f_j \neq 0$. This means that one can only consider transitions from occupied to unoccupied KS state (or viceversa). If one defines p and p' as occupied states and q and q' as unoccupied states, and introducing the occupation numbers, one may rewrite (2.4.20) as the coupled equations:

(2.4.21)

$$\sum_{i=1}^{\infty} \sum_{j=1}^{\infty} \{ [\delta_{pp'} \delta_{qq'} \omega_{pq} - K_{pq,p',q'}(\omega)] \beta_{p'q'}(\omega) + K_{pq,q',p'}(\omega) \beta_{q'p'}(\omega) \} = \omega \beta_{pq}(\omega)$$

(2.4.22)

$$\sum_{i=1}^{\infty} \sum_{j=1}^{\infty} \{ -K_{qp,p',q'}(\omega) \beta_{p'q'}(\omega) + [\delta_{qq'} \delta_{pp'} \omega_{qp} + K_{pq,p',q'}(\omega)] \beta_{q'p'}(\omega) \} = \omega \beta_{qp}(\omega)$$

Defining

$$X_{pq} = -\beta_{pq} \quad \text{and} \quad Y_{pq} = \beta_{qp} \quad (2.4.23)$$

It is possible to obtain the final eigenvalues equation to compute the exact excitation energies of a given non-interacting KS system, where the frequencies ω correspond to the desired excitation energies:

(2.4.24)

$$\sum_{i=1}^{\infty} \sum_{j=1}^{\infty} \{ [\delta_{pp'} \delta_{qq'} \omega_{pq} + K_{pq,p',q'}] X_{p'q'} + K_{pq,q',p'} Y_{p'q'} \} = \omega X_{pq}$$

(2.4.25)

$$\sum_{i=1}^{\infty} \sum_{j=1}^{\infty} \{ K_{qp,p',q'} X_{p'q'} + [\delta_{qq'} \delta_{pp'} \omega_{qp} + K_{pq,p',q'}] Y_{p'q'} \} = \omega Y_{pq}$$

Generally, these two equations are written in a compact way in matrix notation and is well known as the pseudo-eigenvalue *Casida equation* [29]:

(2.4.26)

$$\begin{pmatrix} A & B \\ B & A \end{pmatrix} \begin{pmatrix} X \\ Y \end{pmatrix} = \omega \begin{pmatrix} -1 & 0 \\ 0 & 1 \end{pmatrix} \begin{pmatrix} X \\ Y \end{pmatrix}$$

where A and B are:

$$A_{pq,p'q'} = \delta_{pp'} \delta_{qq'} \omega_{pq} + K_{pq,p',q'} \quad (2.4.27)$$

$$B_{pq,p'q'} = K_{pq,p',q'} \quad (2.4.28)$$

Of course, even in this notation the equation has finite dimension, since it is solved for a number of eigenvalues pre-defined by the user. It is worth to notice that higher is the number of computed energy eigenvalues and less is the error in computing the eigenvalue associated with a given excitation energy.

The Casida equation is able to calculate exact excitation energies of any many-body system. Nevertheless, some conditions are compulsory. Firstly, it requires the exact KS ground state of the system obtained from an exact KS density functional. Secondly an exact frequency-dependent exchange correlation kernel f_{xc} is required. That means since A and B matrix elements depend on the frequency through the exchange correlation kernel, a self-consistence procedure is used to solve the Casida equation. Moreover, the K coupling matrix elements settled equal to zero yields the KS excitation energies ω as eigenvalues, but of single excitations. Namely, TD-DFT is able only to account for single excitations and not double or multiple excitations. If we knew the exact frequency-dependent kernel, we would obtain pole of the many body response function ω with multiple-excitation character, but it is not the case. Therefore, the electronic structure of all computed excited states is built from the ground state KS wave function as a linear combination of monoelectronic excitations from the occupied to the virtual orbitals.

2.4.4. The adiabatic approximation

As for the ground state DFT the exchange-correlational functional represents the term that has to be approximated, in the same way for the TD-DFT the frequency dependent exchange correlational kernel has to be approximated somehow. The simplest approach is transferring the above mentioned DFT exchange correlation functional, such as LDA, GGA, hybrid functionals etc., to the TD-DFT, and substituting the ground state density with the frequency dependent density at each point in time (or frequency):

$$v_{xc}^A(r, \omega) = v_{xc}^{GS}[\rho(r, \omega)](r) \quad (2.4.29)$$

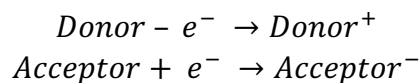
The employment of ground state functional at each point in time results in exchange correlation kernel, which depends only locally on time. This approximation is well known as the *adiabatic approximation* and it is strictly valid when the density of the system undergoes changes in time not so large [28]. Clearly, this condition is rarely verified but, despite this, the adiabatic approximation is widely utilized in TD-DFT. It

means that, since the exchange correlation kernel lacks the frequency dependence, the TD-DFT is able to correctly describe solely single-excited state.

2.4.5 Charge transfer excitations

The TD-DFT has become the most used quantum chemical approach for describing processes occurring at the excited state and, as seen before, it can be applied to calculate electronic excitation spectra of various molecular systems. Nevertheless, although it is a formally exact method, the exchange correlation kernel used to evaluate the exchange and correlation contribution suffers of different drawbacks. A well-known weakness is the description of excitations of long-range space extent, such as in the case of Rydberg states, large π -systems and charge-transfer (CT) excited states [30].

As a CT excitation occurs, one electron displaces from a donor (D) to an acceptor (A) moiety separated by a distance R . The minimum energy necessary to remove an electron from the D corresponds to the ionization potential IP_d , while the amount of energy when an electron is added to the A is the electronic affinity EA_a . This displacement can be depicted as two reactions:



Once the displacement has occurred, the two subunits feel the electrostatic interaction energy $\frac{1}{R}$ resulting from the generation of the hole-electron pair. The original formula proposed by Mulliken to compute the transition energy for CT excitation is [31]:

$$\omega_{CT} = IP_d - EA_a - \frac{1}{R} \quad (2.4.30)$$

In other words, the excitation energy corresponds to the ionization potential of the Donor partially recovered by the electron affinity of the Acceptor and the electrostatic interaction of the exciton pair. This value can be considered as a *lowest energy boundary* of a CT state in the limit that Donor and Acceptor are located at a long distance R . That is to say in the limit of one electron transfer from the HOMO to the LUMO, the poles ω_{ij} of the linear response function are sufficiently spaces, namely HOMO and LUMO are well separated in energy from the neighboring orbitals.

The corresponding excitation energy computed in TD-DFT is:

$$\begin{aligned} \omega_{CT}^{TD-DFT} &= \varepsilon_a^{DFT} - \varepsilon_d^{DFT} \\ &+ 2 \int \int \phi_a(r) \phi_a(r) \left\{ \frac{1}{|r' - x|} + f_{xc}(r, r', \omega) \right\} \phi_a(r') \phi_a(r') dr dr' \end{aligned} \quad (2.4.31)$$

The orbitals considered are the highest occupied $\phi_a(r)$ (HOMO) and the lowest unoccupied $\phi_a(r)$ (LUMO) of the donor and acceptor moieties. Since the two orbitals have an exponentially vanishing overlap, at $R \rightarrow \infty$ the final term tends to zero and consequently the excitation energies computed at TD-DFT level becomes equal the difference in the KS orbital eigenvalues:

$$\omega_{CT}^{TD-DFT} = \varepsilon_a^{DFT} - \varepsilon_d^{DFT} \quad (2.4.32)$$

The resulting excitation energy is not correctly computed since it lacks the coulombic interaction of the exciton pair, and moreover it misses of the derivative discontinuity. This latter is due to the fact that the exact exchange-correlational functional is not known. Indeed, the standard DFT functionals (LDA, GGA) provides excitation energies meaningfully underestimated because the LUMO does not account for the missing derivative discontinuity and, consequently, TD-DFT fails in the description of CT excitations.

On the other hand, the corresponding excitation energy computed in time-dependent Hartree-Fock (TD-HF) approach is:

$$\omega_{CT}^{TD-HF} = \varepsilon_a^{HF} - \varepsilon_d^{HF} - \iint \frac{\phi_a(r)\phi_a(r)\phi_a(r')\phi_a(r')}{|r-r'|} dr dr' \quad (2.4.33)$$

that in the limit of large separation becomes:

$$\omega_{CT}^{TD-HF} = \varepsilon_a^{HF} - \varepsilon_d^{HF} - \frac{1}{R} \quad (2.4.34)$$

One can notice that the exact exchange integral is responsible for the $\frac{-1}{R}$ behavior. Moreover, applying the Koopman's theorem the difference between the orbital eigenvalues can be computed as the difference between the ionization potential of the donor and the electron affinity of the acceptor [32]. In DFT, the application of Koopman's theorem leads errors coming from the approximation employed for the exchange correlational functional. Contrarily, it is exact in the context of HF. As a result, TD-HF is able to provide more accurate excitation energies than the TD-DFT. Nevertheless, it is possible to improve the results employing some approximations. As mentioned before, due to the presence of a fraction of HF exchange, hybrid exchange correlational functionals compute larger band gaps, providing an improvement over standard TD-DFT approximation for the description of CT excitation. A further approximation comes from the above-mentioned range-separated hybrid functionals. Separating the Coulomb interaction into short-range and long-range parts, they address the trade-off problem about the amount of HF exchange according to the distance R [26].

2.5 Modeling Solvent Effect

The presence of the solvent can usually influence the electronic structure of the system and its reactivity. Especially analyzing the absorption spectra and excited states of a molecular system an accurate modelling of the solvation environment is essential [33]. In order to describe the interaction between solvent and solute, two main approaches exist: the *explicit solvation* and the *implicit solvation* models [33]. The first accounts for solvent molecules physically present in a simulation box. This nomenclature is opposite to the implicit solvation, where solvent molecules are described as a continuum medium. This continuum, represented by a dielectric constant, allows to evaluate the manner in which the solvent is polarized due to the solute presence, that in turn, sees its electronic cloud polarized through the solvent response. The corresponding response of solvent and solute are accounted for in a self-consistent calculation (so that self-consistent reaction field). This approach is the so-called *polarized continuum model* (PCM) [34].

Nonetheless, certain specific interactions as hydrogen interaction or π stacking can somehow dominate the solvatochromic phenomena, especially in case of polar protic or aromatic molecules. Hence the need to explicitly include the solvent effect. Such interactions are neglected for simplicity in the PCM model, but on the other hand, they can be taken into account through an explicit modeling of the molecular neighborhood. Therefore, it is important to choose the best solvation approach according to the possible effect of solvation environment. In this thesis, the implicit PCM model is used for all calculations of optical properties in solution, utilizing when necessary its different implementations.

2.5.1 The polarizable continuum model (PCM)

The PCM is by far the most commonly employed approach for modeling the solute-solvent interaction, both in terms of computational efficiency and generality. The solute molecules are placed into a void cavity within a continuous dielectric medium mimicking the solvent. The shape of the cavity has to reproduce as well as possible the solvent molecular shape, and it is constructed by placing interlocked spheres centered on each heavy (non-hydrogen) atom of the molecule, with application of smoothing functions to prevent discontinuities in the resulting surface (or iso-density surface) of the molecule. Such sphere defines a solvent accessible surface (SAS) and a solvent excluded surface (SES). The cavity surface is split into small elements called *tesserae*, at the center of which there are point charges representing the electrostatic polarization of the solute electron density. The contribution of the reaction field to the solute free energy (G) can be expressed as:

$$G = \frac{1}{2} Vq \quad (2.5.1)$$

where V corresponds to the solute electrostatic potential and q are the apparent surface charges centered at each *tessera*. Such charges are the solution of the PCM linear system of equations, and several models are developed to determine them. A general relationship establishes the dependence on the solvent electrostatic potential V :

$$q = -DV \quad (2.5.2)$$

where D is a square matrix corresponding to the inverse of the matrix defining the PCM linear system of equations and related to geometrical parameters of the cavity and the dielectric constant ϵ of the solvent. The relative polarity of a given solvent is introduced by the dielectric constant, whose value is $\epsilon = 1$ (vacuum) in the cavity, and $\epsilon = \epsilon_{solvent}$ elsewhere.

For the treatment of solvent response at the excited states, different approaches have been developed in order to describe the electrostatic solute-solvent interaction, such as the linear response (LR) [35] and the state-specific (SS) formalism [36]. The first treats such interaction as a perturbation of the solute Hamiltonian. Within the TD-DFT, the solute-solvent interaction energy, indeed, is taken into account introducing a response operator Q , acting as a dielectric-dependent perturbative term added to the coupling matrix element K :

$$K_{pq,p',q'} = K_{pq,p',q'}^{\circ} + \sum_{IJ}^{tesserae} \phi_{pq}(r) Q_{IJ}(\epsilon) \phi_{p'q'}(r) \quad (2.5.3)$$

$K_{pq,p',q'}^{\circ}$ is the coupling matrix element for an isolated system, while the second term corresponds to the solute-solvent interaction free energy. In this case the solvent electronic degrees of freedom remain in equilibrium with the ground state. Of course, this is an approximation that is valid when ground state and excited state have similar densities.

This approximation obviously breaks down in case of electronic excitations with a significant CT character. The electrostatic potential produced by the solvent charges can be brought into equilibrium with the density of the excited state of interest in an approach known as corrected Linear Response (cLR-PCM). Indeed, during excitation phenomena, solvent molecules may respond to changes in the state of solute in different ways:

- They may polarize the electron distribution (a rapid process);
- They may reorient themselves (a slower process).

Vertical electronic excitations correspond to non-equilibrium process, since solute density change is too rapid for the solvent to have time to fully reorient towards the solute. Therefore, it is necessary a further non-equilibrium external SCF iteration as happen in a state specific (SS) procedure. This formalism treats differently the non-equilibrium solvation and the equilibrium solvation. Within this approximation, the

excited state equilibrium free energy explicitly depends on the electron density of the excited state, while the excited state non-equilibrium free energy depends on the density of the ground state. One can perform a TD-DFT calculation *in vacuo* using the electron density of the excited state of interest. Later, a further TD-DFT calculation is performed in presence of a set of polarization charges, thus obtaining a revised excited state density and update polarization charges, and this iterative procedure is performed until achieving the convergence. Eventually, the final equilibrium and non-equilibrium solvation energies can be computed, subtracting the solvation energy coming from the ground state density, which has been used as starting point for the TD calculation.

As concern the solute degrees of freedom in equilibrium (or not) with the solvent, one can divide them into two broad terms: electronic and inertial. In physical terms, the former corresponds to the degrees of freedom available to the solvent electronic density, whereas the latter corresponds to the implicit nuclear degrees of freedom of the solvent. Figure 4 depicts a representation of ground and excited-state potential energy surfaces, where one can see the ideal equilibrium state of the solute with respect to the solvent for a given property (absorption or emission).

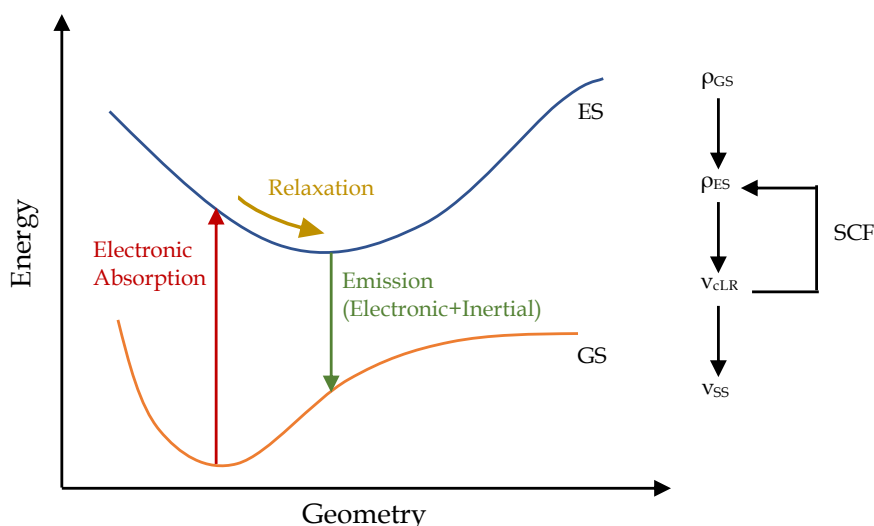


Figure 4 Left side: Arbitrary ground state (GS) and excited state (ES) potential energy surfaces. Absorption (red arrow) and emission (green arrow) electronic transitions are depicted, as well as the solvent ideal equilibrium state respect to the solute. Right: schematic representation of the procedure to obtain the corrected linear response (cLR) and state specific solutions for the excited state equilibrium of the solvent.

Chapter 3

How can we explore excited states?

An excited state has a finite lifetime, which is very short, and this consequently restricts the range of experimental techniques that can be employed to study photochemical and photophysical process occurring at excited state. However, in order to achieve a deep understanding of these processes, an accurate characterization of the electronic excited states of the system is needed and this can lead to the prediction of the photophysical behavior of new molecular systems. From this standpoint, computer simulations are playing an increasingly important role in giving valuable insights regarding these phenomena. More generally, the capacity to simulate photoinduced events often allows exploring areas of chemistry, like photochemistry, that experiments could investigate only indirectly. For instance, it is possible to compute excitation energies and estimate either the charge-transfer or valence character of corresponding excited states by looking at how the electron density reorganizes. Determining the excitation character ($n\pi^*$, $\pi\pi^*$ and charge-transfer) of electronic transition is remarkably interesting, since it is straightforwardly linked to the excited state properties and may allow predicting de-excitation processes, reaction pathways and possible interactions with environment. While the calculation of excitation energies of organic molecules nowadays is often rather reliable employing suitable quantum chemical methods, such post-HF methods or time-dependent density functional theory (TD-DFT), qualitative insights into wavefunction character are still challenging to obtain. Typically, the assignment of states nature relies on the application of some specific protocols or visualization of the canonical orbitals. Nonetheless, these methodologies may be not straightforward for delocalized orbitals or when a partial double excitation character is present, when many configurations are involved, or simply when the aforementioned character does not clearly appear.

In the last year several theoretical tools have been implemented to quantify the redistribution of charge density involved in the excitation and to offer a concise description of the electronic transition. In this way we are now capable of determining routinely the character of an electronic transition. In paragraph 3.1 of this Chapter, indeed, we summarize the state of art of such indexes, thereby providing the theoretical framework which paves the way for our research work.

While these descriptors are suitable to estimate the charge-transfer (CT) extension, on the other side the estimation of the energy of CT excited state by TD-DFT may lead an

outcome that can be affected by the approximations used in the underpinning xc functionals. In paragraph 3.2 we will explain where this error comes from and we will discuss about a methodology that has been developed to spot spurious unphysical states (often called *ghost-states*), whose energy is usually underestimated respect to the real states.

Furthermore, the comprehension of the mechanism of a photophysical process requires a full description of the excited state, not only in the Franck-Condon region where the BO approximation is fulfilled. Indeed, after the absorption that can be studied as a vertical transition, charge may reorganize leading to the population of emissive excited states. So, the exploration of the evolution of an excited state is of paramount importance to understand how relaxation phenomena occur. But following an excited state, it may happen that we can encounter regions of potential energy surfaces (PES) where an excited state can cross or interconvert. These regions are well known as *conical intersection*, but a complete comprehension of such areas is particularly challenging in the field of TD-DFT.

So, in paragraph 3.2 we will try to understand the origin of the drawback of TD-DFT in describing crossing and interconvert regions, which then led to the development of a computational inexpensive density-based index to qualitatively recognize critical regions of PES.

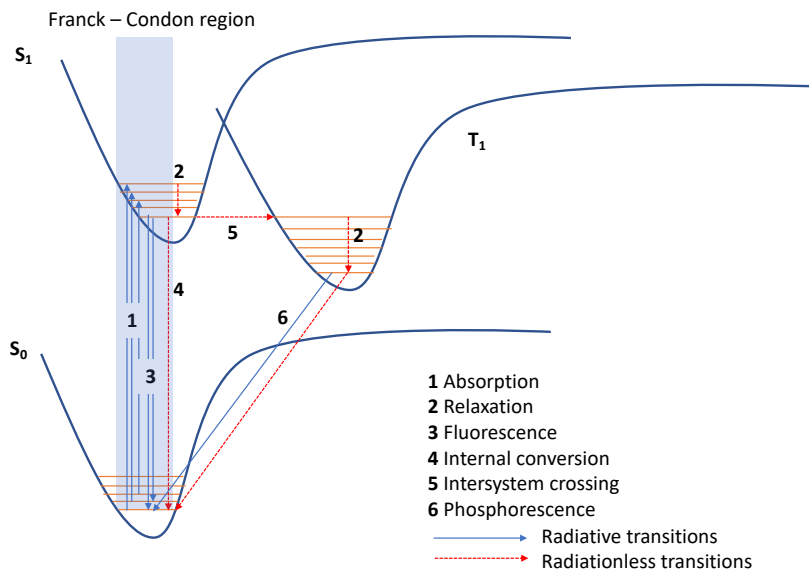


Figure 1 Jablonski diagram illustrating possible photophysical phenomena upon light absorption.

3.1 Interpreting electronic transitions through descriptors: excited states indexes

For a complete description of an excited state, an analysis of the charge flux coming along an electronic excitation is of crucial importance to gain insight into the topology of a transition. The purpose of this paragraph is to give a general overview of huge efforts spent during the last decades in order to implement methods enabling to treat and translate the outcome of an excited state calculation, thus visualizing the reorganization of the electronic structure upon excitation. The general approach consists in the development of intuitive indexes that are able to represent in a compact and local way an electronic transition. Moreover, some of these descriptors also pinpoint potential shortcomings of chosen computational protocols in describing charge transfer (CT) phenomena. Therefore, the investigation in this context continues to attract huge interest. Indeed, our developments and several applications will demonstrate how the quantification of the locality of an excited state constitutes not only an interesting achievement from a theoretical point of view, but their implementation represents an undisputed tool for the description of systems chemically relevant. A temporal excursus of the main developments in this context is presented below to help the reader have a global picture about *excited state descriptors* and contextualize this research work.

3.1.1 Luzanov (1975)

The pioneer in the development of explicit and definite criteria for interpreting the nature of an electronic transition, localized or not, was Luzanov. He, for the first time, suggested to consider non-invariant entities coming from the **transition density matrix** [37-39]. More precisely, he studied deeply the nature of the transition density matrix providing a multiconfigurational analysis of excited states in terms of elements of such matrix:

$$D_{rs}^{0\alpha} = \langle 0|E_{rs}|\alpha \rangle \quad (3.1.1)$$

where 0 is the ground state and α is the excited state, while r and s are the indices of two orbitals. So, the transition density matrix basically corresponds to the single excitation operator applied to construct the excited state. The diagonal elements of such matrix represent the locally excited states, while the off-diagonal elements correspond to the charge-transfer states. In other words, if r and s orbitals are situated on the same fragment A of the molecule, the element of D matrix corresponds to a local excitation and a charge excitation if r and s are on different fragments. Consequently, a charge transfer metric can be defined as the sum over all contributions of respective fragments A and B :

$$\Omega_{AB}^{\alpha} = \frac{1}{2} \sum_{\substack{r \in A \\ s \in B}} (D_{rs}^{0\alpha})^2 \quad (3.1.2)$$

If $A \neq B$, such metric measures the probability that an electron jumps from an atomic spin-orbital to another, while if $A = B$ it weights the local character of the excitation on the A fragment.

3.1.2 Head Gordon (1995)

An interesting framework comes from the contribution of Head Gordon and collaborators, who, for first, tried to interpret calculations of vertical electronic transitions considering the one-electron **difference density matrix** between two states [40]. This method is based on the simple idea to decompose such matrix into the negative of a “detachment density” matrix, describing a charge removal from the initial state (hole density), and an “attachment” density matrix describing its new arrangement in the excited state (particle density). Such approach originates from the intuitive hypothesis to consider an excited state as single electron promotion from occupied to unoccupied orbitals. Obviously, the attachment and detachment matrices have no physical significance, but the main advantage stands on the fact that they are always positive, contrarily to the difference density matrix. Moreover, the integration of both matrices over all space yields a *promotion number*. In other words, the trace of attachment and detachment densities corresponds to the number of electrons promoted upon an electronic transition. In this way, it is possible to obtain a clear orbital depiction even for complex excited state wave functions. The distribution of detachment density and attachment density reveals finally the character of the electronic transition.

3.1.3 Tozer (2008)

Another interesting approach is to calculate the **spatial overlap** associated to a given excitation. The idea is of Peach and Tozer [41,42], who calculated by TD-DFT the degree of overlap of canonical orbital couples, virtual (φ_a) and occupied (φ_i) involved in the characteristic expansion of an excited state. To each excitation they thus associated a Λ parameter defined as:

$$\Lambda = \frac{\sum_{ia} K_{ia}^2 \langle |\varphi_i| | \varphi_a \rangle}{\sum_{ia} K_{ia}^2} = \frac{\sum_{ia} K_{ia}^2 \int |\varphi_i(r)| |\varphi_a(r)| dr}{\sum_{ia} K_{ia}^2} \quad (3.1.3)$$

where K_{ia} is the function that weights the inner product containing both excitation (X_{ia}) and de-excitation (Y_{ia}) coefficients:

$$K_{ia} = X_{ia} + Y_{ia} \quad (3.1.4)$$

This parameter may assume values in the range of $0 < \Lambda \leq 1$. A value near zero means a long-range excitation, while a Λ value near unity stands for short-range excitation. Such Λ parameter also qualifies as a diagnostic tool of the TD-DFT exchange-correlational functional, since it simultaneously correlates the error in the computed transition energy and the locality of the charge transfer. Indeed, below a Λ threshold the exchange correlational functional without long-range correction computes transition energy values with higher error than the corresponding long-range. Therefore, its application not only includes the analysis of CT transitions, but also paved the way in developing extensive strategies to test the performance of exchange-correlation functionals for the calculation of local, Rydberg, and intramolecular CT excitation energies in TD-DFT framework.

3.1.4 Tarantelli (2010)

Tarantelli and collaborators developed an innovative theoretical framework, which is able to describe partial transfer of electronic charge, especially in case of weak intermolecular interactions. Such approach discards any charge decomposition scheme, in favor of a **charge-displacement (CD) function** [43,44]. In other words, one can profile a charge-displacement function integrating the change in electron density along an Euclidian coordinate, corresponding basically to the main interaction coordinate:

$$\Delta q(z) = \int_{-\infty}^z dz' \int_{-\infty}^{+\infty} \int_{-\infty}^{+\infty} \Delta \rho(x, y, z') dx, dy \quad (3.1.5)$$

$\Delta \rho$ practically corresponds to the electron density difference between excited and ground states. The obtained profile provides a summary and insightful picture of the whole electron cloud rearrangement arising from all the interaction components. $\Delta q(z)$ measures, indeed, the transferred electron charge upon electron excitation and gives information about direction and extent of the CT. More precisely, there is a charge transfer if the CD curve is different from zero and keeps the same sign in the region where the CT phenomena occurs, while the CT may be indeterminate if the CD curve crosses zero. The value of the CT extension can be extracted at the so-called isodensity boundary, namely the point along the chosen coordinate (z), where the electron densities of the noninteracting fragments are the same.

3.1.5 Plasser (2012)

Plasser and collaborators introduced a strategy to translate the information coming from quantum chemical excited-state calculation and then interpret excitonic exchanges produced among monomers of a dimer within a Frenkel exciton configuration (locally excited state), and within a charge-separated configuration (charge transfer states) [46]. Inspired by Luzanov [37-39], indeed, they proposed an analysis of couples of atoms (μ and ν) considering not only the one-electron **transition density matrix** (D) in the atomic orbital basis (AO), but also the **overlap matrix** (S):

$$\Omega_{AB}^{\alpha} = \frac{1}{2} \sum_{\substack{r \in A \\ s \in B}} (D^{0\alpha, [AO]} S^{[AO]})_{rs} (S^{[AO]} D^{0\alpha, [AO]})_{rs} \quad (3.1.6)$$

In this context the original idea of Plasser is to introduce compact descriptors, which have a real physical interest, such as *charge separation*, *exciton delocalization*, and *coherence*. The first descriptor enables to quantify the CT amount, especially suitable for extended systems, as polymers. It is obtained summing all off-diagonal elements:

$$CT = \frac{1}{\Omega} \sum_{\substack{A \\ B \neq A}} \Omega_{AB}^{\alpha} \quad (3.1.7)$$

where $1/\Omega$ is the normalization factor, obtained summing all Ω_{AB}^{α} , and deviates slightly from the unity. Obviously, the summation is applied only on the configurations where the initial and final orbitals are situated on different fragments ($B \neq A$). If $CT = 1$, the excited state is of charge-transfer character, whereas the descriptor assumes value of zero for locally excited or Frenkel excitonic states. From the *participation ratio* (PR) of fragments, it is instead possible to gain insight about the extent of the delocalization, which can be obtained basically computing the fragments participation in the excitation. We can compute clearly two PRs, namely PR_I referred to the initial orbital (the hole) and PR_F for the final orbital (the particle):

$$PR_I = \frac{\Omega^2}{\sum_A (\sum_B \Omega_{AB})^2} \quad (3.1.8)$$

$$PR_F = \frac{\Omega^2}{\sum_B (\sum_A \Omega_{AB})^2} \quad (3.1.9)$$

The sum in parenthesis takes into account such configurations where the initial (final) orbital is placed on a particular fragment $A(B)$ and goes over final (initial) any possible fragment. To take into account the total amount of fragments involved in the excitation one can compute the average of the two ratios:

$$PR = \frac{(PR_I + PR_F)}{2} \quad (3.1.10)$$

Finally, to have an idea of the average electron-hole separation, one can compute the *coherence length* (COH) expressed as:

$$COH = \frac{1}{PR} \frac{\Omega^2}{\sum_A (\sum_B \Omega_{AB})^2} \quad (3.1.11)$$

3.1.6 Adamo (2013)

Another alternative descriptor, the Δr , has been proposed by Guido and Adamo which makes use of **charge centroids**, thus providing a hole-electron distance upon electronic transition, particularly with natural transitional orbitals (NTOs) [46,47]. NTOs are single value decomposition of the one-electron transition density matrix associated to the excited state. Inspired by Tozer, they basically proposed a charge displacement analysis computing the average of hole-electron distance over the excitation, weighted according to the excitation coefficients:

$$\Delta r = \frac{\sum_{ia} K_{ia}^2 |\langle \varphi_a | r | \varphi_a \rangle - \langle \varphi_i | r | \varphi_i \rangle|}{\sum_{ia} K_{ia}^2} \quad (3.1.12)$$

where $|\langle \varphi_a | r | \varphi_a \rangle|$ and $|\langle \varphi_i | r | \varphi_i \rangle|$ are the norms of the initial (occupied φ_i) and final (virtual φ_a) orbital centroids. Such parameter allows one not only to differentiate valence and charge transfer states, but like Tozer's descriptor [41,42], it can be also included among the diagnostic tools to differentiate long and short-range excitations. More precisely, it works even in those cases where Λ fails, namely in charge-transfer like situation. However, it gives an effective electron displacement during the electronic transitions, but it has the main weakness to vanish for centrosymmetric molecules, by construction. Furthermore, a charge is not actually localized in the charge centroid but spreads around it. Such particle delocalization (σ_p) can be measured as:

$$\sigma_p = \sqrt{\langle \varphi_p | r^2 | \varphi_p \rangle - \langle \varphi_p | r | \varphi_p \rangle^2} \quad (3.1.13)$$

both for the electron (σ_a) and for the hole (σ_i) and consequently the average of hole and electron delocalization over the excitation can be measured:

$$\Delta \sigma = \frac{\sum_{ia} K_{ia}^2 |\sigma_a - \sigma_i|}{\sum_{ia} K_{ia}^2} \quad (3.1.14)$$

Summing Δr and $\Delta \sigma$, Adamo et al obtained a new descriptor Γ :

$$\Gamma = \Delta r + \Delta \sigma = \frac{\sum_{ia} K_{ia}^2 |\langle \varphi_a | r | \varphi_a \rangle - \langle \varphi_i | r | \varphi_i \rangle|}{\sum_{ia} K_{ia}^2} + \frac{\sum_{ia} K_{ia}^2 |\sigma_a - \sigma_i|}{\sum_{ia} K_{ia}^2} \quad (3.1.15)$$

which does not vanish for symmetric molecules ($\Gamma = \Delta\sigma$). Moreover, the presence of $\Delta\sigma$ makes Γ more suitable to describe Rydberg states, since $\Delta\sigma$ better describes diffused orbitals than Δr .

3.1.7 Etienne (2014)

The approach of Etienne and collaborators provided further contributions in the development of topological descriptors with the twofold use to study the excited state topology and simultaneously perform diagnostic tests for exchange-correlational functionals. In particular, he derived an index, ϕ_s , which stems from the **overlap between detachment and attachment densities**, also within the NTOs formalism [48,49]. Following the original approach introduced by Head-Gordon [40], the derivation starts from difference density matrix Δ . Separating the positive and the negative Δ elements, two new matrices can be defined, Γ and Λ , which represent the detachment and attachment densities matrices, respectively. Such matrices basically represent the spatial distribution of the electronic density removed (detachment) from the ground state and then reorganized (attachment) in the excited state upon absorption. Integrating the relative detachment/attachment densities (ρ_Γ/ρ_Λ) through the space, one can obtain the function ϑ_τ

$$\vartheta_\tau = \int_{R^3} d^3\xi \rho_\tau(\xi) \quad \tau \equiv \Gamma, \Lambda \quad (3.1.16)$$

By computing the overlap between these two matrices one can then derivate a dimensionless parameter ϕ_s :

$$\phi_s = \vartheta^{-1} \int_{R^3} d^3\xi \sqrt{\rho_\Gamma(\xi) \rho_\Lambda(\xi)} \quad (3.1.17)$$

$$\vartheta^{-1} = \frac{1}{2} \left[\int_{R^3} d^3\xi \sum_{\tau \equiv \Gamma, \Lambda} \rho_\tau(\xi) \right] \quad (3.1.18)$$

It may assume values between 0 and 1. Intuitively, a bound value equal to 0 denotes a situation with no overlap between detachment and attachment matrices, and thus a huge fluctuation of electron density between ground and excited states due to the charge-transfer character of the transition. On the other hand, ϕ_s is equal to 1 for localized transition. Interestingly, to establish the efficacy of the charge-separation it is possible to compute a CT distance calculating the distance between the detachment/attachment density centroids. One can clearly evidence some similarities with the former Adamo approach [46,47], also based on charge centroids. Δr is indeed a descriptor deriving from the same type of split on the Δ matrix made by Etienne. Nevertheless, Adamo worked in the real space (direct space) and on the charge density difference function. On the other hand, Etienne's derivation is performed in the Hilbert space on the Γ and Λ matrices. But, unlike Δr , as instead Γ , ϕ_s does not present any limitations in its application for symmetric systems.

3.1.8 Plasser (2014)

In 2014 Plasser and Dreuw introduced a general theory and a new comprehensive formalism for the evaluation of exciton properties [50-54]. More specifically, they introduced two CT indexes, initially between couple of atoms or molecular fragments, and later extended to solid-state physics problems. In order to conciliate, on one side, the description of the excited state for small molecules in terms of occupied (hole) and virtual (particle) orbitals, and on the other side, the solid-state view as exciton, Plasser et al proposed an unique formalism based on the *two-body wave function of the exciton*. The exciton analysis, which was initially based on the population analysis and later generalized, is aimed to quantify the linear correlation between the pair of particle (e^-) and hole (h^+) proposing two descriptors: the *covariance* (COV) and the *correlation* (COR):

$$COV(r_h r_p) = \langle r_h \cdot r_p \rangle_{exc} - \langle r_h \rangle_{exc} - \langle r_p \rangle_{exc} \quad COR = \frac{COV(r_h r_p)}{\sigma_h \sigma_p} \quad (3.1.19)$$

The COV represents the measure of the joint variability hole and particle and its sign shows the tendency in the linear relationship between hole and particle. This means that the covariance is positive when a modification in the position of the hole induces a change in the same direction in the particle. On the contrary, the covariance is negative when the hole and the particle move in opposite direction. Therefore, in the first case (positive sign) particle/hole motion is correlated, while if the COR sign is negative there is an anti-correlated behavior. Finally, a zero correlation represents a situation in which particle and hole moves independently. Such approach has been also reformulated within the NTO formalism [53]. The hallmark of this strategy resides in the independence of atom-centered basis functions and there is no need to partition the wave function into atom or fragment centered contributions.

3.1.9 D_{CT} Index (2011)

Along this timeline no reference has been made, until now, about the most applied approach utilized to analyze the character of the excited states, namely the D_{CT} [55,56]. The choice is conscious, since such descriptor represents the starting point of this research work, and for this reason it has cited as last in order to underline similarities and differences with the other abovementioned localization indexes. If one would like to group somehow all these tools, an interesting distinction could be done dividing them in two distinct families, one based on electron density and another on molecular orbitals. Approaches based on detachment/attachment densities, as the ones proposed by Head-Gordon [40] and Etienne [48,49], or Tarantelli's density partition [43,44], for example, can be ascribed to first family. On the other hand, the Tozer Λ parameter [41,42] or Adamo's descriptors [46,47] are based on a molecular orbital

derivation. Considering this intuitive distinction, one can categorize the D_{CT} index, developed in our group in 2011, in the first family, due to the fact that it relies only on the computed electronic densities for ground ($\rho^{GS}(\mathbf{r})$) and excited state ($\rho^{ES}(\mathbf{r})$). The change in density associated to the electronic transition can be calculated as:

$$\Delta\rho(\mathbf{r}) = \rho^{ES}(\mathbf{r}) - \rho^{GS}(\mathbf{r}) \quad (3.1.20)$$

From such function, one can define two functions $\rho^+(\mathbf{r})$ and $\rho^-(\mathbf{r})$, which respectively collect all the points in space where an increment and a depletion of electron density occurred upon absorption:

$$\rho^+(\mathbf{r}) = \begin{cases} \Delta\rho(\mathbf{r}) & \text{if } \Delta\rho(\mathbf{r}) > 0 \\ 0 & \text{if } \Delta\rho(\mathbf{r}) \leq 0 \end{cases} \quad (3.1.21)$$

$$\rho^-(\mathbf{r}) = \begin{cases} \Delta\rho(\mathbf{r}) & \text{if } \Delta\rho(\mathbf{r}) < 0 \\ 0 & \text{if } \Delta\rho(\mathbf{r}) \geq 0 \end{cases} \quad (3.1.22)$$

Discretizing $\rho^+(\mathbf{r})$ and $\rho^-(\mathbf{r})$ on a three-dimensional grid around the molecule, one can identify the barycenters of charges relative to these two distributions:

$$\mathbf{R}^+ = \frac{\int \rho^+(\mathbf{r})\mathbf{r}d\mathbf{r}}{\int \rho^+(\mathbf{r})d\mathbf{r}} = (x_+, y_+, z_+) \quad (3.1.23)$$

$$\mathbf{R}^- = \frac{\int \rho^-(\mathbf{r})\mathbf{r}d\mathbf{r}}{\int \rho^-(\mathbf{r})d\mathbf{r}} = (x_-, y_-, z_-) \quad (3.1.24)$$

The D_{CT} can be finally expressed as the spatial distance between the two barycenters of the positive and negative charge distributions as follows.

$$D_{CT} = \mathbf{R}^+ - \mathbf{R}^- \quad (3.1.24)$$

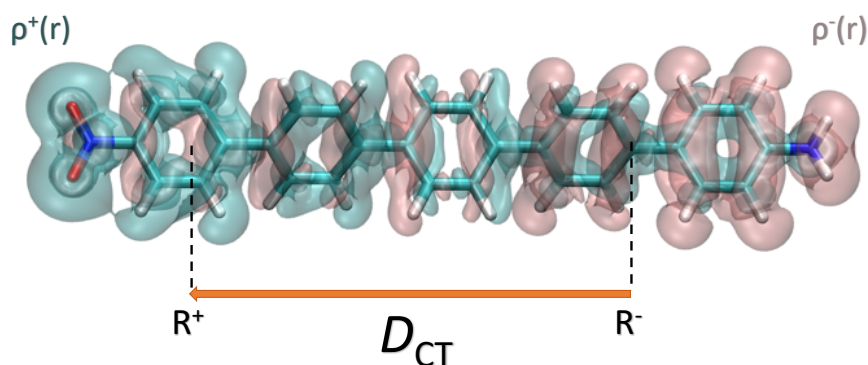


Figure 2 D_{CT} Schematic Representation. The accumulation (cyan isosurface) and depletion (pink isosurface) of electronic charge is shown together with the corresponding barycenters of the two electron densities.

It presents a vectorial character since corresponds to the difference between two spatial points (*i.e.* the positions of the two barycenters) and basically measures the effective distance of the electron and hole upon excitation. Indeed, contrary to the charge displacement analysis for excited states proposed by Tarantelli [43,44], it condenses the information on charge reorganization upon electronic excitation to a CT distance. The entire derivation of such index can be also performed within the atomic charge formalism, using some partitioning scheme of the density (like for example Mulliken's or Hirshfeld's procedure) [57]:

$$\Delta Q_i = Q_i^{ES} - Q_i^{GS} \quad (3.1.25)$$

$$Q_i^+ = \begin{cases} = \Delta Q_i & \text{if } \Delta Q_i > 0 \\ = 0 & \text{if } \Delta Q_i \leq 0 \end{cases} \quad (3.1.26)$$

$$Q_i^- = \begin{cases} = \Delta Q_i & \text{if } \Delta Q_i < 0 \\ = 0 & \text{if } \Delta Q_i \geq 0 \end{cases} \quad (3.1.27)$$

$$\mathbf{R}^+ = \frac{\sum_i Q_i^+ \mathbf{r}}{\sum_i Q_i} \quad (3.1.28)$$

$$\mathbf{R}^- = \frac{\sum_i Q_i^- \mathbf{r}}{\sum_i Q_i}. \quad (3.1.29)$$

Atomic charge schemes, indeed, have been proven to be able to reproduce the dipole moments variation between the ground and excited states, whose norm is basically demonstrated to be equal to the product between the D_{CT} and the amount of transferred charge.

It is worth to notice that the preliminary step to calculate the difference in electron density between the ground and the excited state is in common with the Etienne approach [48,49]. The difference lies in the fact that our approach performs it in the direct space, while to determine the ϕ_s parameter one should calculate such difference in the Hilbert space. Moreover, being ϕ_s the overlap of detachment/attachment density it is dimensionless, unlike the D_{CT} , which is conversely estimated in Å (or in Bohr), and it is able to gain insight into the directionality of the transition due to its vectorial character. Moreover, contrary to the other indexes, the D_{CT} is fully computed from the density associated with the ground and the excited state, and for this reason is directly extendable to any quantum chemical method, DFT or post-HF based, thus enabling a direct comparison of the outcomes obtained with different approaches [58-60]. Furthermore, the D_{CT} computed by relaxed and unrelaxed excited state density has been proven to provide the same description regardless of the transition nature (CT or localized) and of the exchange correlational functional [61]. Hence the possibility to characterize the nature of electronic transition by use of D_{CT} computed on-the-fly by unrelaxed density without computational cost. Another interesting aspect is that from a theoretical point of view, the index formulation has the clear advantage of making no arbitrary choice in the localization scheme adopted. Nevertheless, such feature makes the D_{CT} null by construction for symmetric systems, since the barycenters of density depleted and incremented zones coincide. Accordingly, as in the Adamo derivation [46,47], in order to achieve information regarding the nature of an electronic

transition even for symmetric molecules, the spreading of the positive and negative density regions has been considered calculating the root main square deviation of the density along the tree axis $\sigma_{a,j}$, where $j = x, y, z$ and $a = + or -$

$$\sigma_{a,j} = \sqrt{\frac{\sum_i \rho_a(r_i)(j_i - j_a)}{\sum_i \rho_a(r_i)}} \quad (3.1.30)$$

From that two additional descriptors have been introduced:

- H that measures the spread of the positive and negative density regions along a selected axis (H)

$$H = \frac{\sigma_{+x} + \sigma_{-x}}{2} \quad (3.1.31)$$

- t defined as the difference between the CT distance and the spread:

$$t = D_{CT} - H \quad (3.1.32)$$

If H parameter is larger than D_{CT} this means that charges distributions are more diffused, thus resulting a larger overlap between centroids of depletion/increment electron density regions along with a specific axis. t can thus be used also as a *diagnostic index* to identify possible pathologic through space transitions, which are actually not well described at the Time Dependent Density Functional Theory (TD-DFT) level using standard exchange–correlation functionals. So, H does not necessarily vanish in centrosymmetric configurations, although on turn it does not present any physical relationship with CT extension as the D_{CT} .

This is the main reason why beside this important weakness, the D_{CT} index has been widely applied until now, not only to characterize molecular systems but also to follow excited state reactions implying a structural reorganization and inter or intra-molecular CT, as Excited State Proton Transfer class of reactions (ESPT). To this aim, a modified version of D_{CT} has been proposed, $D_{CTreact}$ in order to gain insight into reaction path (thus stationary points) and describe structural and electronic reorganization at the same time [62, 63]. It has been defined, as the parental one, as a distance between barycenters of two difference density distributions $\rho_{react}^+(\mathbf{r})$ and $\rho_{react}^-(\mathbf{r})$, but in this case calculated differently. Indeed, the difference in electron density $\Delta\rho(\mathbf{r})$ is defined as the difference of electron density calculated in the ground state at the geometry corresponding to the minimum of the excited state of interest ρ_{minES}^{GS} and the one calculated in the excited state at a given point i along the excited state potential energy surface (PES) ρ_i^{ES}

$$\Delta\rho(\mathbf{r})_{react} = \rho_i^{ES}(\mathbf{r}) - \rho_{minES}^{GS}(\mathbf{r}) \quad (3.1.33)$$

The $D_{CTreact}$ calculated in such way is able to define how much the density changes from the most stable excited state conformation for the reactants along the excited state

PES. In this manner one can implicitly consider the electronic reorganization upon absorption, and simultaneously have an idea about the structural reorganization for each point of the PES, which actually do not necessarily affect the same part of the molecule, where the electron density redistribution occurs.

Following the same trend of modifying and improving such intuitive and simple descriptor, in order to exploit to the full all its potentials, a part of this research work is aimed to solve the unique major drawback of the D_{CT} , namely the quantification of CT extension for centrosymmetric system. Indeed, the computational low cost, the wide application in any quantum chemical method and the interesting chemical applicability, not only to characterize the transition nature but also to follow a reaction mechanism at the excited state, make the D_{CT} the most applied localization index. Hence the need to overcome its weakness and to boost the range of applicability, extending the analysis even in case of symmetric configurations, as shown in Chapters 4 and 5.

3.2 The problematic description of excited states by (TD)-DFT

3.2.1 The problem of Charge-Transfer in TD-DFT

In the last decades the TD-DFT has become the most popular quantum chemical approach in order to treat electronically excited state [14]. The reason lies in the fact that it can be basically considered as an extension of the fundamental ideas of the ground state DFT, thus preserving all its bright features. Indeed, TD-DFT equations are simple to manage numerically, and they can be routinely solved even for systems with a large number of electrons. Hence, the continuous developments in this context have made possible now to calculate excited state properties for a large variety of molecules in gas-phase, in solution and even in more complex environment conserving the outstanding accuracy without prejudging the computational cost. Nevertheless, several limitations can be encountered solving the Schrödinger equation (SE) by means of such *ab-initio* approach. As a matter of fact, since in principle TD-DFT is an exact theory (as the DFT counterpart), such drawbacks are related only to the approximations that are made, thus introducing systematic errors in the calculated results. Particularly, TD-DFT is quite ineffective in computing (long-range) charge-transfer (CT) excitations, which are actually a class of electronic transitions of biological and technological interest. As underlined in Chapter 2 the issue comes from the exchange–correlation (xc) potential, which lacks the correct $1/r$ asymptotic behavior (r is the nucleus-electron distance), and the derivative discontinuity. On one hand this shortcoming can be mitigated by the use of global and range-separated hybrid functionals, introducing a Hartree-Fock like exchange, on the other hand

excitation energies computed such way still remain by error in the estimation of CT transition, hence not suitable for precise comparisons with experimental spectra. In Section 3.1 we introduced some dedicated localization indexes, which are not only charge transfer metrics for the excited state analysis, but they are also able to monitor the erroneous evaluation of electronic energy for CT transition, such as the Tozer's Λ , the Adamo's Δr , the Etienne's ϕ_s and finally the D_{CT} . However, a major drawback of TD-DFT is the energy underestimation of CT virtual orbitals producing the appearance of low-lying CT *ghost-state*, which have an energy well below the bright states of a given system for both intermolecular and intramolecular excitations [10,11]. Such spurious effect may lead an incorrect interpretation of the photophysical behavior, since it would suggest a non-radiatively decay of an energetically higher state (bright) into an energetically lower CT state (ghost), thus quenching the fluorescence of the bright excited state due to the electron transfer. In order to avoid the incorrect interpretation and prediction of spectroscopic properties of a given molecular system, a simple and robust reliable tool has been implemented, the M_{AC} index, which will be well deeply described in the next paragraph.

M_{AC} index

The M_{AC} index is an ingenious and useful theoretical tool purposely developed to detect, on-the-fly, *ghost charge-transfer* states, which represents one of the major drawbacks of TD-DFT, as seen in the previous introduction. It is due to the incorrect calculation of charge transfer (CT) excitations, ascribed to the self-interaction error in the orbital energies from the ground-state DFT calculation, which leads to an underestimation of the HOMO-LUMO gap.

Drew and Head-Gordon were the first to discuss about the existence of such ghost low-lying CT states, who analyzed the case of a push-pull system containing a donor (D) and an acceptor (A) group [64,65]. These authors showed that the transition energy calculated by the TD-DFT approach does not satisfy the formula originally proposed by Mulliken [31]:

$$\omega_{CT} = IP_D - EA_A - \frac{1}{R} \quad (3.2.1)$$

where ω_{CT} corresponds to the excitation energy necessary for a net single electron transfer from the donor to the acceptor placed at a distance R . IP_D is the ionization potential of the Donor, EA_A the electron affinity of the acceptor, while $1/R$ the Coulombic interaction between the D and A expressed in atomic units. The equation (3.2.1) is an easy and intuitive expression, which can be considered as the lower energetic value for a bright CT transition, compared with the nature of the TD-DFT excitations has to be verified. It is worth nothing that R parameter basically correspond to the physical distance between acceptor and donor, that may not correspond correctly to the real hole-electron distance. For this reason, in our group it has derived from the originally Mulliken formula (3.2.1) a descriptor, which has been called M_{AC} , acronym of *Mulliken averaged configuration*, substituting R with the D_{CT} index, which

on the contrary computes a more realist CT extent. As seen in Paragraph 3.1.9, indeed, this last is computed as the distance between two barycenters of the spatial regions corresponding to an increase (particle) and decrease (hole) of the electron density upon excitation. Moreover, since a given electron transition basically corresponds to the combination of different single electronic excitations, applying the Koopmans' theorem [32] IP_D and EA_A can be approximated as a weighted average of the starting (ε_i) and final (ε_a) Kohn-Sham orbital energies. So, computationally inexpensive this index is derived as a modification of the Mulliken estimation of transition energy for CT excitations, relying on two basic ingredients: an effective CT distance (D_{CT}) and an orbital weighted estimation of the Ionization Potential and Electron Affinity [66]:

$$M_{AC} = \frac{\sum_{ia} C_{ia}(-\varepsilon_i - \varepsilon_a)}{\sum_{ia} C_{ia}^2} - \frac{1}{D_{CT}} \quad (3.2.2)$$

Finally, from the calculation of the M_{AC} index for all transitions of interest and its comparison with the corresponding TD-DFT computed excitation energies, it is possible to detect proper or ghost CT transition as follows:

If $E_{TD-DFT} > M_{AC} \rightarrow$ real CT state

If $E_{TD-DFT} < M_{AC} \rightarrow$ ghost state

3.2.2 The problem of conical intersections in TD-DFT

The problematic description of excited states by TD-DFT does not only concern the mere error in the electronic energy calculation, but it regards even the full description of excited states, within and far from the vertical excitation in the Franck-Condon region. As a matter of fact, the regions of the potential energy surfaces (PES) outside the Franck-Condon area are the ones involved in excited state decay phenomena. Hence, in order to rationalize and understand radiative and non-radiative phenomena, it is crucial to locate and search such regions, which represent actually the conditions for which the Born-Oppenheimer approximation breaks down. Therefore, the complete study of excited state evolution within and outside the vertical excitation region is yet a considerable challenge for any theoretical methods. In particular, it is well known that the TD-DFT is not able to well describe *conical intersections* (CI), which are crossing regions between potential energy surfaces of different states and play important roles in many photochemical mechanisms. CI are perhaps the most significant mechanistic features of chemical reactions occurring at excited states. In particular, they are efficient "funnel" region where the higher state efficiently and non-radiatively decays to the lower state. Hence, they govern the branching ratio of products of excited state reactions, similar to what the transition states do for ground-state reactivity. In this context, the correct description of potential energy surfaces, especially in proximity of CI, is crucial for understanding the mechanism and

dynamics of excited-state reactions. Unfortunately, such conical intersections cannot be treated within the TD-DFT formalism. Actually, the incorrect description is attributed to three distinct types of failures in linear response adiabatic TDDFT:

- 1) *dimensionality of the intersection space*: the wavefunction used to express the density is not able to describe both interacting states in the vicinity of the intersection, since the interaction matrix elements connecting the initial state (ground state) and response states (excited state) are excluded from the formulation;
- 2) *rapid variation of the energy of response states* near intersections with the ground state;
- 3) *lack of double excitations*.

For such reasons, indeed, normally in order to efficiently map the excited-state deactivation path of the system, one should prefer *ab-initio* multiconfigurational quantum chemical methods, like complete active-space self-Consistent Field (CASSCF) or second-order perturbation method (CASPT2) version. Nevertheless, if the main purpose is the qualitative localization of the conical intersection regions, rather than the mere calculation of the correct adiabatic coupling, it is strongly recommended the use of an electron density-based descriptor, the χ index. It is basically an inexpensive tool, which can be successfully used to get qualitative yet instructive insights about more probably decay channel along potential energy surfaces. More details about its implementation and practical use will be highlighted in the next paragraph.

χ Index

Despite the drawbacks highlighted in the previous sections, TD-DFT still remains the most utilized quantum chemical approach in order to study excited states due to the low computational cost to accuracy ratio. With the aim to use such powerful theoretical method to fully characterize potential energy surfaces, thus understanding the mechanism of photochemical and photophysical phenomena, a new inexpensive descriptor tool, the χ index was developed in the group [67]. Such descriptor is able to qualitatively map potential energy regions of excited states where the non-radiative decay probability is high. Actually, these are the areas of potential energy surfaces where TD-DFT fails, as seen in the previous introduction, and basically corresponds to crossing regions. Intuitively, the probability that two (or more) potential energy surfaces cross is high when

- 1) their energy difference (ΔE) is the smallest
- 2) where the electron density is the most similar.

The Π index has been developed starting from these two simple intuitions, with the aim to restrict the PES region of interest for non-radiative process:

$$\Pi = \frac{1}{\Delta E \times D_{CT} \times q_{CT}} \quad (3.2.3)$$

The first criterion is translated in the Π expression as the inverse of the energy difference (ΔE) between the states involved in the transition. Indeed, the probability of non-radiative decay is maximal if the two states are degenerate. The second condition derives from the chemical intuition that a non-radiative decay more easily occurs from states where the electronic density redistribution associated to the transition is the smallest. Such criterion is translated as the inverse of the product between the transferred charge (q_{CT}) and charge transfer displacement (D_{CT}). As highlighted in 3.1.9 Paragraph, the D_{CT} is able, indeed, to define how much the electronic density changes between the states for which it is calculated.

Consequently, high values of Π will thus define the regions corresponding to the higher decay probability. In other words, efficient non-radiative decay pathways are likely to occur or if two states are degenerate (first condition), or where the density rearrangement occurring upon excitation is the least (second condition), or where both conditions are fulfilled. Due to its simplicity and the fact that it contains the D_{CT} index, the Π index can be calculated by any quantum chemical method, from density functional to wavefunction methods.

As a matter of fact, the Π formulation can be also discussed on the basis of classical electromagnetism formalism. Indeed, the electrostatic work to interconvert two states can be calculated in terms of work to rearrange a collection of charges in an electromagnetic field. In this last case, such work corresponds to the integral over the space of the product between the moving charge (q), the electromagnetic field (E_0) and the infinitesimal displacement (dS):

$$W_{CT} = \int_V q E_0 dS \quad (3.2.4)$$

Comparing (3.2.3) and (3.2.4) we can assume that

$$\Pi \propto \frac{1}{W_{CT}} \quad (3.2.5)$$

since the moving charge q corresponds to the electronic charge rearranged when going from one electronic state to another q_{CT} , the transition energy ΔE is proportional to the field (E_0) in which such rearrangement takes place and finally the D_{CT} index represents the charge separation length.

Until now, the Π index has been used to qualitatively identify regions at excited-state PESs that are possibly involved into non-radiative decay pathway in very simple reaction. In particular, Savarese et al. applied the Π index to analyze a photoinduced

ring-opening reaction of a spiropyran leading to the formation of the corresponding merocyanine [67]. Upon the absorption, a very efficient internal conversion path involving the first excited state (S_1) and the ground state (S_0), far from the Franck-Condon region, permits the ring-opening reaction.

Maschietto et al. [68], as well, applied the Π index to disclose decay channels to gain insight about the mechanism of a simple excited state intramolecular Proton Transfer reaction (ESIPT), and to explain the dual-emissive behavior of the dimethylaminobenzonitrile (DMABN), by a photoisomerization process. In both cases, the highest excited state computed to carry out the analysis of the Π index is the second excited state (S_2).

Therefore, the doubt that has arisen is whether the density-based descriptor Π is such satisfying even in case of conical intersections between higher excited states, and not exclusively with the ground state. Indeed, in Chapter 6, the Π index has applied to a more complex photochemical reaction extending the analysis up to the sixth excited state (S_6), thus validating the efficiency of the theoretical approach in disclosing efficient decay pathways even for complicated photoinduced phenomena.

Developments

General Introduction

In the Chapters that will follow, we will present in detail the developments that have been realised throughout this thesis in the field of topological analysis of the electronic transitions and the strategy that has been adopted in order to study the full evolution of excited state potential energy surfaces (PES), allowing to interpret the absorption and emission properties.

In particular, Chapter 4 and Chapter 5 report our contribution in revising an existing descriptor, namely the D_{CT} index, in order to quantify the particle-hole distance at the excited state. This is actually a simple and intuitive theoretical tool widely used to estimate the charge-transfer extent [55]. Nevertheless, by definition it cannot be used to study charge-transfer (CT) excitation in symmetric systems. Hence, we proposed initially a partial D_{CT} index (Chapter 4) to compute the CT associated to the contribution of a selected subset of atoms in a molecule, thus overcoming its limitation. Later on, we developed a general average index ($^A D_{CT}$) (Chapter 5), which can be used indistinctly to estimate the CT extent both in symmetric and non-symmetric compounds.

Chapter 6 and Chapter 7 will focus on another density-based index, namely the Π index, that has been used in order to follow excited states evolution and individuate regions of the potential energy surface where the decay probability is the highest. In this way, we were able to gain insight into the origin of the dual emission behaviour of a phenanthroline derivative (Chapter 6) and into the mechanism of the deoxygenation reaction of heteroaromatic N-oxides using organosilane as the terminal reductant, which occurs at excited state (Chapter 7).

Finally, in Chapter 8 we will show a multiscale approach that we adopted in order to study the effect of the environment on the optical properties of a new cool coating pigment, which is known form stable aggregates.

Finally, in Chapter 9 some Conclusions and Perspectives of this research work will be outlined and discussed.

Chapter 4

A new metric to study charge-transfer excitations in symmetric systems

4.1 Context

Several indexes outlined in Chapter 3 have been developed during the last decades with the aim to analyze the nature of excited states from a theoretical standpoint. In particular, these methods quantify somehow the redistribution of electron density involved in the excitation, thus offering a concise description of the electronic transition nature. Among them, a simple model was proposed a measure of the charge-transfer (CT) extent based on the computation of the electron density in a real-space representation for the ground state and the excited state: the so called D_{CT} index [55]. As demonstrated by the various contributions in the literature concerning its application, it is a really simple and intuitive descriptor enabling the physical estimation of the particle-hole distance by spotting the barycenters of negative and positive charges. Nevertheless, by definition the D_{CT} can be only applied on non-symmetric molecules, otherwise for symmetric molecules it gives, by construction, a particle-hole distance equal to zero, even in case of charge-transfer transition. Such drawback encouraged us to focus our efforts in revising its definition to broaden its field of application. Indeed, in a recent publication of ours [69] entitled “Quantifying partial hole-particle distance at the excited state: A revised version of the D_{CT} index”, by myself, Marco Campetella and Ilaria Ciofini, published in Chemical Physics Letters, we proposed a new density-based index enabling to study charge-transfer excitation in symmetric molecules. Starting from the general definition of the D_{CT} index, we adapted its formulation just considering a subset of atoms composing the molecule of interest, which constitutes the smallest asymmetric fragment where one can calculate the CT extent. More details are reported in this Chapter, which can be considered as an adaptation of the abovementioned publication.

4.2 Introduction

Excited states with substantial charge transfer (CT) character are increasingly synthetically targeted in molecule-based devices for very diverse applications ranging from photocatalysis to photovoltaics. In this context, theoretical approaches able to both qualitatively rationalize and quantitatively predict the nature and energy of excited states could provide invaluable help in the rational design of new devices. To this end, both accurate ab-initio, non parameterized approaches for the prediction of excited states energies and tools of analysis able to quantify their CT character are needed.

Time-dependent density functional theory (TD-DFT) [70,71] has become one of the most popular quantum chemical approaches for calculating electronic spectra of medium to large molecular systems. The main advantage of this method is its low computational cost to accuracy ratio. Nevertheless, it is well documented in literature that TD-DFT has a number of shortcomings [72–74] that may affect the reliability of predicted spectra. Among them, the drawback which most strongly prevents its use for the prediction of functional dye properties is likely related to the correct description of excitation energies of charge transfer (CT) states. Several works have pointed out that this incorrect behavior is related to the asymptotic behavior of the underlying exchange-correlation functional [75,76]. This error can stem from an erroneous prediction of excitation energies to, in the most severe situations, the prediction of unphysical low-lying excited states, often referred as ‘ghost states’ [65–66, 77]. Since charge transfer excited states are a target in many fields of application such as photosynthesis, [78] photovoltaic devices, [79] molecular switches, [80] and are relevant for many phenomena such as nanoscale conductance or reactions which occur at interfaces, [81] much attention has been given from the theoretical community to both quantify CT in molecules and to design indexes to detect erroneous behavior of TD-DFT approaches when describing CT states. For the latter, pioneering works have been published by Gritsenko and Baerends [73] and by Tozer and collaborators [41,42]. The Λ parameter, for instance, has been extensively used to detect transitions that can be problematic at TD-DFT level [42]. Starting from these seminal works, a number of new descriptors have been devised during last years to diagnose problematic cases for TD-DFT, [37–55] with the more general aim of simply quantifying the particle-hole distance at the excited state.

These indexes can be categorized in two main groups: (i) methods based on the use of molecular orbitals and, (ii) methods based on the electron density. As representative examples for the first class we can cite the already mentioned Λ index, indexes based on charge centroids of Natural Transition Orbitals (NTOs) [47] or those based on density matrix analysis [50–53]. Instead, the second family concerns indexes based on total densities [55] detachment/attachment densities [48,49]. In recent work, [82] it has been shown how two of these approaches, which belong to different families can

provide very similar descriptions both in term of quantitative and qualitative results, as should be expected due to the intrinsic relation between their underpinning variables: the electronic density and molecular orbitals. Among density-based indexes, some very simple ones recently proposed and based on total densities (*i.e.* the D_{CT} and the related M_{AC} indexes [55,66]) suffer from a severe limitation related to the fact that the computed particle-hole distance is evaluated as the distance between the barycenters of hole and electron charge distributions. Therefore, in the case of symmetric systems this quantity – which is a global property of the entire molecule – is zero by definition. Let us consider the **DA₂-R** family of molecules depicted in Figure 1. In this case, a CT transition from the donor to the acceptor units is expected but, for symmetry reasons, the barycenters of the electron and the hole will coincide, providing a globally null CT distance when computed using the D_{CT} index. Nevertheless, for practical applications, it would be interesting to give a measure of the partial CT occurring from the central donor group to each of the acceptor units, both in terms of distance and direction (*i.e.* to access to a partial CT vector, hereafter named as D_{CT}^P). Having access to D_{CT}^P index would enable their use in characterizing and designing new systems for potential applications, in analogy with what has already been done using the D_{CT} index independently of the topology of the donor-acceptor connection and, in particular, also in the case of symmetric systems [56, 61,68]. In this context, with the aim of providing a tool to compute the partial particle-hole distance, we propose here a revised version of the D_{CT} index, [55] which is able to compute the CT associated to the contribution of a selected subset of atoms in a molecule. This index can be used in the case of symmetric molecules as a suitable alternative to the standard D_{CT} index, but also in the case of non-symmetric systems in order to analyze the effect of specific substituents of the molecule on its global behavior. For this purpose, we have implemented two different approaches: the first one based on the calculation of the electron density of the ground and excited states stemming only from the contribution of selected atoms and a second one making use of different partial atomic charges (PAC) models, namely those of Mulliken and Hirshfeld [57].

To test these approaches, we have considered three families of symmetric push pull molecules functionalized with different acceptor groups ($R = CN, F, NO_2$) schematically depicted in Figure 1. The first two families (**DA₂-R** and **DA₃-R**, Figure 1) are actually experimentally studied since they display thermally activated delayed fluorescence (TADF) [83,84] and can be used to fabricate highly efficient organic light-emitted diodes (OLEDs), while the last group of molecules (**DA₄-R**, Figure 1) has been chosen since it contains a structural motif often found in hole transport materials, which are used for a wide variety of applications ranging from photocopiers to electroluminescent display devices [85].

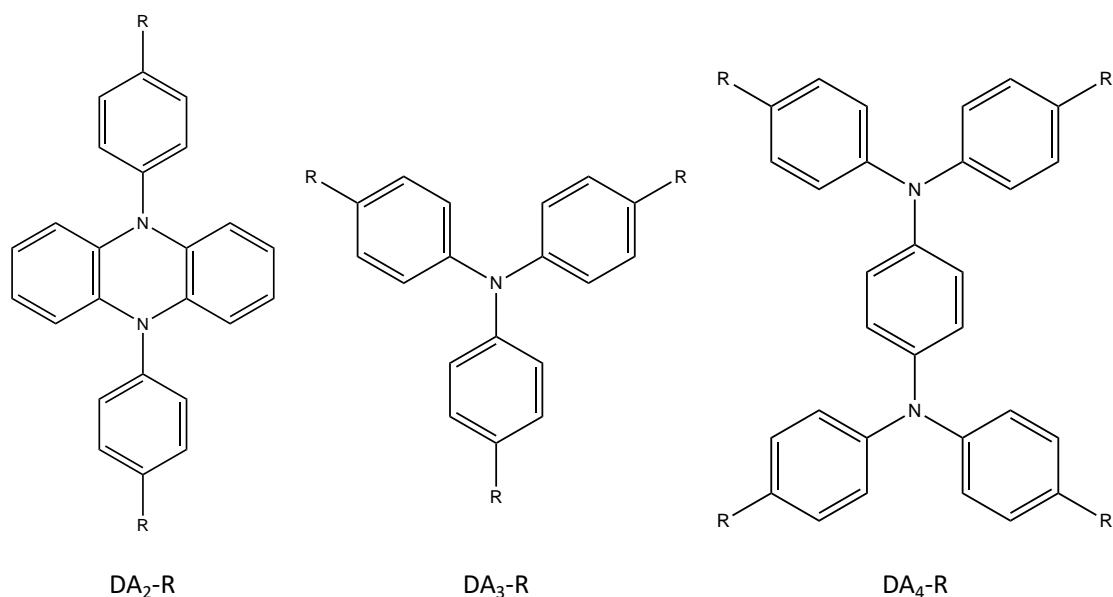


Figure 1 Schematic representation of the $\text{DA}_2\text{-R}$, $\text{DA}_3\text{-R}$ and $\text{DA}_4\text{-R}$ families of molecules ($\text{R} = \text{NO}_2, \text{CN}$ and F) considered in this Chapter.

4.3 Computational Methods and Details

To estimate the partial hole-electron distance R , we have used a revised version of the D_{CT} . As mentioned before, it is possible to obtain this index from two different procedures: the first directly making use of the electron density, and the second employing PAC models. We will start by describing briefly the first approach. To construct this index, in analogy with the parent global D_{CT} approach, we shall define two electronic density distributions $\rho_{\text{GS}}^P(\mathbf{r})$ and $\rho_{\text{ES}}^P(\mathbf{r})$ corresponding to the electron densities of the molecule at the ground and excited states, respectively, obtained from a given subset of atoms. These quantities can be expressed in terms of the atomic basis functions (χ) as:

$$\rho_{\text{GS}}^P(\mathbf{r}) = \sum_{\mu, \nu \in \text{SA}} S_{\mu\nu} \chi_{\mu}(\mathbf{r}) \chi_{\nu}(\mathbf{r}) \quad \rho_{\text{ES}}^P(\mathbf{r}) = \sum_{\mu, \nu \in \text{SA}} T_{\mu\nu} \chi_{\mu}(\mathbf{r}) \chi_{\nu}(\mathbf{r}) \quad (4.3.1)$$

where χ_{ν} are the atomic basis function, $S_{\mu\nu}$ and $T_{\mu\nu}$ are the ground state (GS) and the excited state (ES) density matrices, respectively, written in the atomic orbital (AO) basis. The summation runs only over the AO basis centered on the subset of atoms of interest (SA). The resulting partial electron density variation is therefore expressed as:

$$\Delta\rho^P(\mathbf{r}) = \rho_{\text{ES}}^P - \rho_{\text{GS}}^P \quad (4.3.2)$$

Analogously to the original D_{CT} formulation, the regions in space that experience an increase (decrease) in electron density can be represented by the function $\rho_+^P(\mathbf{r})$ ($\rho_-^P(\mathbf{r})$). These quantities correspond to the positive (negative) values of $\Delta\rho(\mathbf{r})^P$, respectively. The partial transferred charge during the transition is therefore defined as:

$$Q_{CT}^P = \int \rho_+^P(\mathbf{r}) d\mathbf{r} = - \int \rho_-^P(\mathbf{r}) d\mathbf{r} \quad (4.3.3)$$

Defining the barycenters of the above defined partial charge distributions as R_+^P and R_-^P respectively, the partial D_{CT} can be simply defined as:

$$D_{CT}^P = |R_+^P - R_-^P| \quad (4.3.4)$$

Starting from these definitions, it is straightforward to formulate the partial D_{CT} in terms of partial atomic charges, rather than densities, computed for the ground and excited states.

First of all, for each selected atom i belonging to the subset of atoms (SA) of interest, located in the position $\mathbf{r}_i = (x_i, y_i, z_i)$, we define the difference of PAC between the excited and the ground state:

$$\delta q_i = q_{GS,i} - q_{ES,i} \quad (4.3.5)$$

If we compare Equation (4.3.2) and Equation (4.3.5), we can see that in this formulation the δq_i function between the ground and the excited state electron distribution has an opposite sign to keep consistency in sign since an increment in electronic density corresponds to a decrease in PAC. Subsequently, one gathers the atoms in two groups: $q_{i,+}$ if $\delta q_i > 0$ or $q_{i,-}$ if $\delta q_i < 0$. The associated partial transferred charge can be written as :

$$q_{CT}^P = \sum_i^{SA} q_{i,+} = - \sum_i^{SA} q_{i,-} \quad (4.3.6)$$

Analogously, defining r_+^P and r_-^P the barycenters of the $q_{i,+}$ and $q_{i,-}$ charge distributions, the partial D_{CT} value (d_{CT}^P) can be defined as:

$$d_{CT}^P = |r_+^P - r_-^P| \quad (4.3.7)$$

The descriptors based on both total density and PAC have been computed using a freely available code [86].

DFT and TD-DFT were used to compute the ground and the excited state of each molecule. All calculations were performed in the gas phase. The ground state structures were obtained at B3LYP [22] level with the 6-311g(d,p) [87] basis, while ground and vertical excited state densities were computed at the PBE0 [23] level with the 6-311 g(d,p) basis. In order to guarantee a direct comparison between the density

and PAC-based models, the latter were computed at the same level of theory. All calculations were performed by means of the Gaussian 09 suite of programs [88]. To carry the density analysis, we have focused exclusively on the lowest lying excited state possessing a net donor-to-acceptor charge transfer character (see below for further explanation). In all considered cases, the subset of atoms of interest will consist of a donor and an acceptor unit. Their complete definition is detailed for each class of compounds later on.

4.4 Results and Discussion

In order to exemplify how the partial charge analysis works, we will firstly consider the **DA₂-R** family of molecules, which are experimentally characterized, [83] and next move to the model **DA₃-R** and **DA₄-R** families. Our aim is not to identify the electronic structure approach that best reproduces the experimental transition energies of a given molecule, but, using an arbitrary electronic structure method, to provide an index able to quantify the hole-particle distance within a user defined subset of atoms composing such molecule.

The **DA₂-R** molecules are characterized by the presence of a substituted diphenyl hydrophenazine moiety, whose peripheral phenyl rings are para substituted by an electron acceptor group (*R*, Figure 1). At the ground state two distinct stable minima exist for all molecules, hereafter defined as *R_twist* and *R_boat* (*R* = *F*, *NO₂*, *CN*). Their schematic representation is provided in Figure 2. *R_twist* conformers are the more stable independently of the substituents and characterized by the phenyl rings roughly orthogonal to the hydrophenazine core. *R_boat* conformers are characterized, on the other hand, by a boat shape structure of the di-phenyl hydrophenazine core. The energy difference between the two conformers ranges from roughly 4.0 kcal/mol (for *R* = *CN*) to 9.7 kcal/mol (for *R* = *F*).

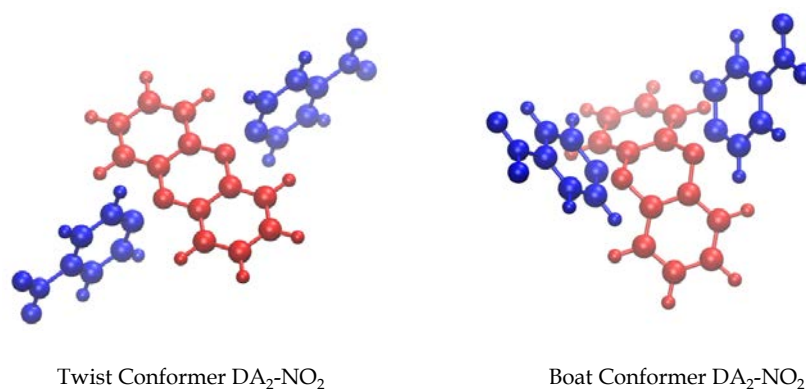


Figure 2 Schematic representations of the twist conformer **DA₂-NO₂** (on the left) and the boat conformer **DA₂-NO₂** (on the right). The donor moiety is represented in red, while the acceptors ones are depicted in blue.

Independently of the substituents, for all twist conformers the first electronic transition consists essentially of a HOMO-LUMO excitation with partial CT character (Figure 3 and Table 1). The HOMO is mainly localized on the hydrophenazine moiety (acting as an electron donor), while the LUMO shows contributions from the peripheral rings (phenyl substituted groups). The same holds for the corresponding boat conformers in the case of the nitro substituted molecules, as depicted in Figure 3. A stronger localization of the donor and acceptor units is observed for the twisted conformers with respect to the analogous boat ones due to the larger structural decoupling between units. For completeness, it should also be noted that in the case of boat conformers, the CT transition does not correspond to the lowest in energy for the cyano and fluorine substituted molecules (Table 1).

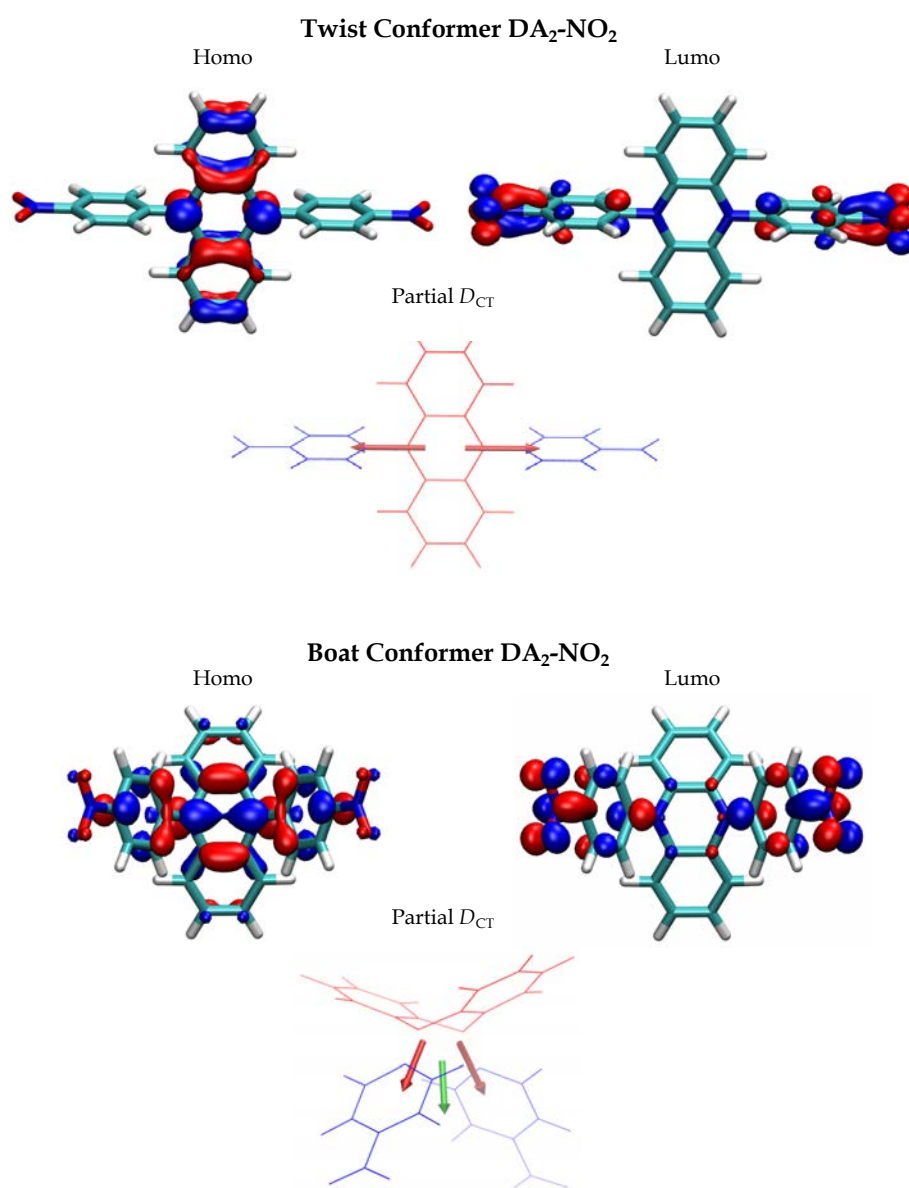
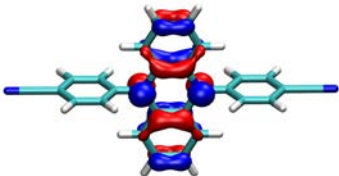
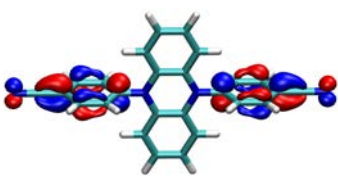
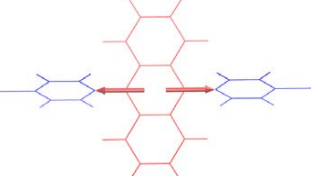
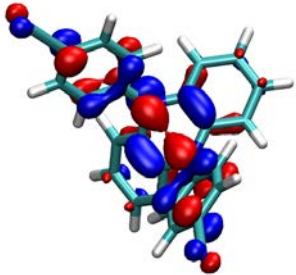
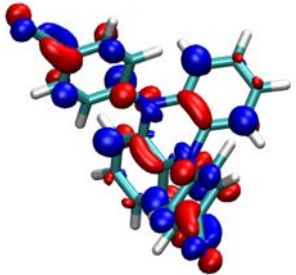
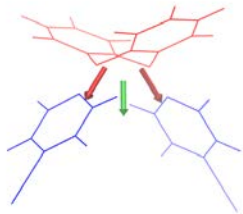
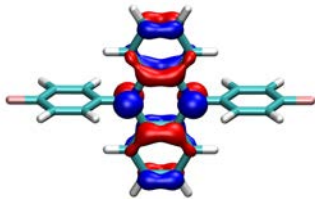
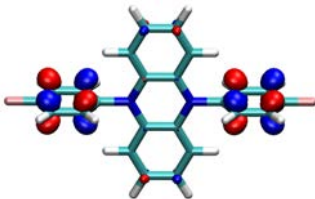
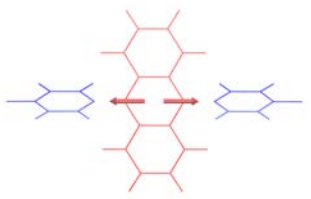
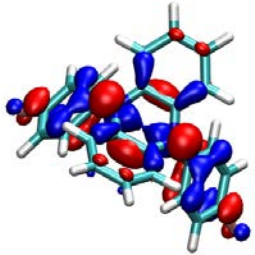
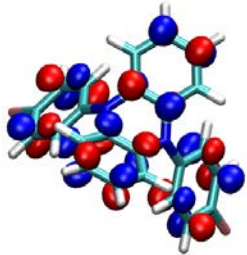
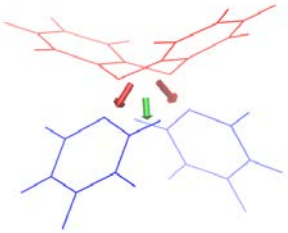


Figure 3 HOMO and LUMO orbitals together with partial (red) and total (green) D_{CT} vectors computed for twisted (upper panel) and boat (lower panel) conformers of **DA₂-R** ($R = NO_2$) molecule. The donor moiety is represented in red, while the acceptor ones in blue.

Table 1 Representation of orbital involved in the CT transition computed for twisted and boat conformers of the DA_2-R family ($R= CN, F$) together with the computed partial and total D_{CT} represented as red and green arrows, respectively.

DA_2-CN twist	Homo	Lumo	Partial D_{CT}
			
DA_2-CN boat	Homo	Lumo+3	Partial D_{CT}
			
DA_2-F twist	Homo	Lumo	Partial D_{CT}
			
DA_2-F boat	Homo	Lumo+4	Partial D_{CT}
			

When computing a partial charge transfer index, it appears quite straightforward to define the group of atoms belonging to the Donor as those present in the hydrophenazine core (in red in Figure 3 and in Table 1) and the two Acceptor as the substituted phenyl groups (in blue in Figure 3 and in Table 1). Using such a definition, for each molecule two partial D_{CT} values have been computed, namely those corresponding to two partitions each one consisting of one acceptor group and the same donor moiety. The corresponding computed values are reported in Table 2.

Even if both the twist and the boat conformers are characterized by a symmetric A-D-A structure, only the twisted molecules (presenting an overall D_2 symmetry) have net null D_{CT} . For the boat conformers (possessing a C_{2v} symmetry) a non-vanishing D_{CT} is indeed expected and obtained. A schematic representation of the CT vectors associated to the partial (red arrows) and total (in the case of boat compounds only, green arrow) hole to electron distance is also reported in Figure 3 in the case of nitro substituted compounds. Corresponding data for all other R groups (cyano and fluorine) are reported in Table 1.

Thanks to the partial D_{CT} analysis it is possible to quantify the effect of the strength on the electron acceptor also in the case of an overall zero D_{CT} value (namely for the twist compounds). As expected, the compound substituted with the nitro group, which is the most electrophilic one, exhibits the largest partial hole to electron distances and transferred charges independently of the method chosen to evaluate them. Such values decrease going to the cyano and fluorine substituents.

A qualitatively consistent trend is obtained independently of the method used to compute the charge transfer indexes (*i.e.* densities or PAC). PAC computed values are all significantly higher than those derived from density-based calculations (Table 2). These results are consistent with a previous investigation performed on non-symmetric push-pull organic compounds using the global D_{CT} analysis [55] that showed that PAC models may lead to quantitatively different results in terms of distance and amount of charge transferred. Regarding our systems, it is likely owed to excessive estimation of charge localization on the electrophilic groups that are at the extremities of the molecules when using the PAC models.

For instance, considering Mulliken PAC in the case of the nitro substituted molecule, a net transfer of $0.16 |e^-|$ electronic charge is computed on each nitro group, which is mostly localized on the peripheral oxygen atoms ($0.16 |e^-|$).

In the case of the boat conformers, due to their molecular symmetry, a net CT value is indeed computed (as graphically represented by the green arrow in Figure 3 and in Table 1) since the vector, sum of the two partial D_{CT} , does not cancel out although the two charge transfer vectors are of the same magnitude, as expected for symmetry.

As already pointed out for the twist isomers, the partial CT values follow also in this case the acceptor groups' relative strength, namely the largest values have been computed for the nitro derivative, followed by cyano and fluorine. With respect to the analogous twist conformers, a smaller partial CT is indeed computed due to the largest delocalization of the HOMO on the phenyl groups displacing the hole from the dihydrophenazine core towards the peripheral acceptor moieties. Again, the PAC and density-based models show similar trends but qualitatively different partial CT values, with larger absolute values computed for the latter.

Table 2 Computed total and partial D_{CT} values (in Å, upper table) together with the corresponding transferred charges (in |e-| lower table). Analysis based on total density (D_{CTn}^P and ΔQ_n^P ; $n=1,2$) different PAC models (d_{CTn}^x and Δq_n^x ; $n=1,2$ and $x=Mulliken$ or $Hirshfeld$) are reported.

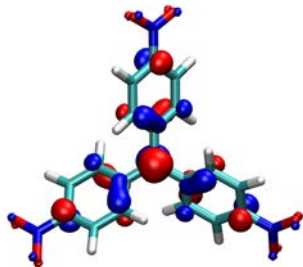
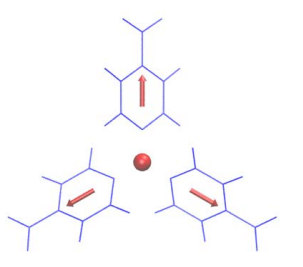
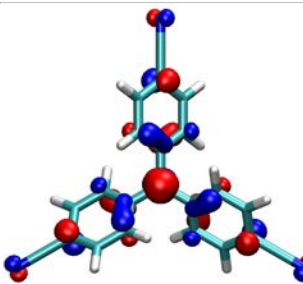
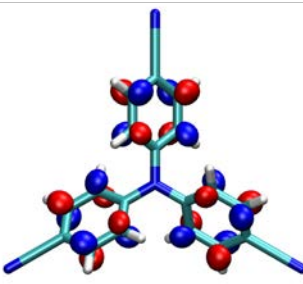
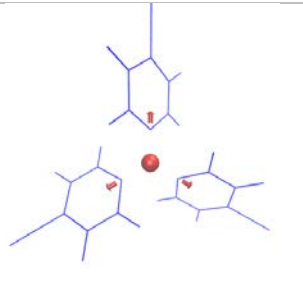
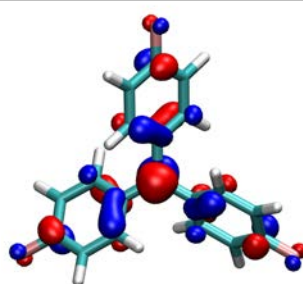
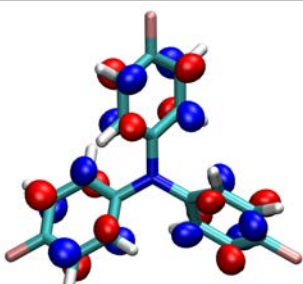
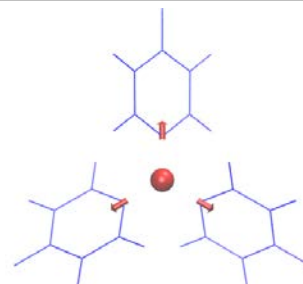
Molecule	D_{CT}	$D_{CT1}^P = D_{CT2}^P$	d_{CT}^{Mul}	$d_{CT1}^{Mul} = d_{CT2}^{Mul}$	d_{CT}^{Hir}	$d_{CT1}^{Hir} = d_{CT2}^{Hir}$
NO ₂ -Twist	0.00	2.73	0.00	5.44	0.00	5.65
CN - Twist	0.00	2.31	0.00	4.68	0.00	4.83
F - Twist	0.00	1.67	0.00	3.18	0.00	4.12
NO ₂ -Boat	1.66	2.10	2.92	4.56	3.80	5.84
CN - Boat ^a	1.31	1.60	2.43	3.74	3.36	5.01
F - Boat ^b	0.67	1.03	1.54	2.68	1.79	3.40

Molecule	ΔQ	$\Delta Q_1^P = \Delta Q_2^P$	Δq^{Mul}	$\Delta q_1^{Mul} = \Delta q_2^{Mul}$	Δq^{Hir}	$\Delta q_1^{Hir} = \Delta q_2^{Hir}$
NO ₂ -Twist	0.00	0.88	0.00	0.51	0.00	0.49
CN - Twist	0.00	0.83	0.00	0.47	0.00	0.47
F - Twist	0.00	0.64	0.00	0.38	0.00	0.31
NO ₂ -Boat	0.64	0.45	0.36	0.24	0.28	0.19
CN - Boat ^a	0.46	0.32	0.24	0.17	0.18	0.13
F - Boat ^b	0.53	0.40	0.25	0.18	0.21	0.15

^a Root 8; ^b Root 5

In order to further exemplify the information that the partial D_{CT} index can provide in the analysis of polynuclear push-pull systems, we considered two families of molecules constructed using the same acceptor groups considered in the previous section (that is phenyl substituted moieties) and two acceptors units, both based on an amino motif, namely a nitrogen atom center and the diamino phenyl group giving rise, respectively, to the **DA₃-R** and **DA₄-R** families depicted in Figure 1. As in the previous case, a partial conjugation of the defined donor and acceptor moieties is expected as a consequence of the structural coupling of these units due to the absence of a strict orthogonality between the donor and acceptor units. Indeed, the orbitals most involved in the CT excitations are somehow delocalized over both the donor and acceptor units, as reported in Table 3-4 for the nitro-substituted compounds. Notably, for such systems, the CT transition does not always correspond to a HOMO-LUMO excitation and it is not always the lowest in energy (refer to Table 3-4). Due to their molecular symmetry (C_3 for **DA₃-R** and D_2 for **DA₄-R**, respectively) the total D_{CT} value is expected - and computed - to be zero. For the sake of clarity in Table 5 only one partial D_{CT} value has been reported, the others being strictly identical for symmetry reasons. The partial D_{CT} values computed for a given system (Table 5) are actually smaller than the corresponding ones computed for the **DA₂-R** family, thus suggesting a smaller donating character of the amino with respect to the hydrophenazine and, more generally, a larger delocalization of the hole in these systems. Contrary to the previous example, both in the case of **DA₃-R** and **DA₄-R**, when using a density-based approach fluorine substituted molecules are predicted to display a slightly larger CT (roughly of 0.2 Å) with respect to cyano substituted ones.

Table 3 Representation of orbital involved in the CT transition computed for the **DA₃-R** family ($R = \text{NO}_2, \text{CN}, \text{F}$) together with the computed partial D_{CT} represented as red arrows.

DA ₃ -NO ₂	Homo	Lumo+2	Partial D_{CT}
			
DA ₃ -CN	Homo	Lumo+2	Partial D_{CT}
			
DA ₃ -F	Homo	Lumo	Partial D_{CT}
			

This trend is also predicted using PAC models in the case of the **DA₃-R** systems but not in the case of the **DA₄-R** systems for which the trend on partial D_{CT} computed using a density based or a PAC models are not the same. A possible explanation, stemming from the analysis of the main molecular orbital involved in the transition (reported in Table 3-4), is an incorrect description (overestimation) of the charge distribution on the terminal substituents (*i.e.* N atom the CN group). In general, it should be noted that the partial computed value will strongly depend on partition considered: this latter should be chosen consistently across different systems when aiming for a meaningful comparison.

Table 4 Representation of orbital involved in the CT transition computed for the **DA₄-R** family ($R = \text{NO}_2, \text{CN}, \text{F}$) together with the computed partial D_{CT} represented as red arrows.

DA₄-NO₂	Homo	Lumo+2	Partial D_{CT}
DA₄-CN	Homo	Lumo+2	Partial D_{CT}
DA₄-F	Homo	Lumo +2	Partial D_{CT}

Table 5 Computed partial D_{CT} (in Å, upper table) together with the corresponding transferred charges (in $|e^-|$ lower table), for the **DA₃-R** compounds (left) and **DA₄-R** compounds (right). Analysis based on total density and different PAC (Mulliken or Hirshfeld) models are reported.

DA₃-R	$D_{\text{CT}1}^P$	$d_{\text{CT}1}^{\text{Mul}}$	$d_{\text{CT}1}^{\text{Hir}}$	DA₃-R	$D_{\text{CT}1}^P$	$d_{\text{CT}1}^{\text{Mul}}$	$d_{\text{CT}1}^{\text{Hir}}$
NO ₂ ^a	1.40	2.98	3.96	NO ₂ ^b	1.77	5.52	6.23
CN ^c	0.45	1.50	1.40	CN ^d	1.20	4.76	5.19
F ^b	0.60	1.92	2.03	F ^c	1.44	4.37	4.48

DA₃-R	ΔQ_1^P	Δq_1^{Mul}	Δq_1^{Hir}	DA₃-R	ΔQ_1^P	Δq_1^{Mul}	Δq_1^{Hir}
NO ₂ ^a	0.27	0.15	0.11	NO ₂ ^b	0.34	0.18	0.16
CN ^c	0.26	0.12	0.10	CN ^d	0.32	0.14	0.13
F ^b	0.26	0.11	0.09	F ^c	0.24	0.19	0.18

^a Root 6; ^b Root 1; ^c Root 3; ^d Root 2.

4.5 Conclusions

In this Chapter we have presented a new tool that is able to quantify the partial particle-hole distance in charge transfer excitations by means of a revised version of the D_{CT} index, rooted only in ground and excited state density analysis. Indeed, it is now possible to overcome two - intrinsically linked - major limitations of the global D_{CT} :

- (i) difficulty to dissect the total particle-hole distance along certain directions, overcome by considering only the contribution of a given subset of atoms;
- (ii) inability to provide information on charge transfer excitations within symmetric molecules for which the global CT is null.

This analysis was exemplified in the case of three families of push-pull systems, characterized by an increasing number of acceptor units and either by vanishing or by a non-vanishing global D_{CT} value.

Chapter 5

A new general index for the analysis of charge-transfer in symmetric and non-symmetric compounds

5.1 Context

If one is interested in measuring the spatial extent of a photoinduced charge-transfer (CT) to interpret photochemical reactions, and more generally whatever CT process, a valid theoretical approach might be the use of the electron density-based index D_{CT} [55]. In particular, it defines the charge transfer extent as the distance between the two barycenters of the hole and electron distributions. However, special attention should be paid in its application for symmetric molecules, since in that case it gives wrong outcomes, which is to say it returns a zero CT extent even in case of CT transition. For such reason, we have proposed a revised version of the D_{CT} index, namely the partial D_{CT} ($^P D_{CT}$), widely presented in Chapter 4. Briefly, it estimates the CT extent in the exact same way of the parental one, but on the smallest asymmetric fragments of the symmetric molecule of interest. This, however, implies an *a priori* definition of the subset of atoms constituting the asymmetric fragment, which could add possible artifacts, including the double counting coming from specific molecular fragments. With the idea to provide a unique descriptor to compute the CT extent for whatever molecular structure, symmetric or not, and avoid any user manipulation, we have developed a new density-based index, the average D_{CT} index ($^A D_{CT}$). Instead of defining the CT extent as the distance between two average points of charge distributions as in the D_{CT} (and $^P D_{CT}$), the $^A D_{CT}$ weights the average of the distances between hole and electron distributions (Figure 1). In the present Chapter we will discuss the implementation of this novel descriptor, highlighting its positive features and comparing its outcomes with the ones obtained by the previous indexes (D_{CT} and $^P D_{CT}$). In particular, such Chapter can be considered as an adaptation of a recent publication of ours entitled “A general density-based index to analyse charge transfer phenomena: from models to butterfly molecules”, by myself, Léon Huet, Francesco

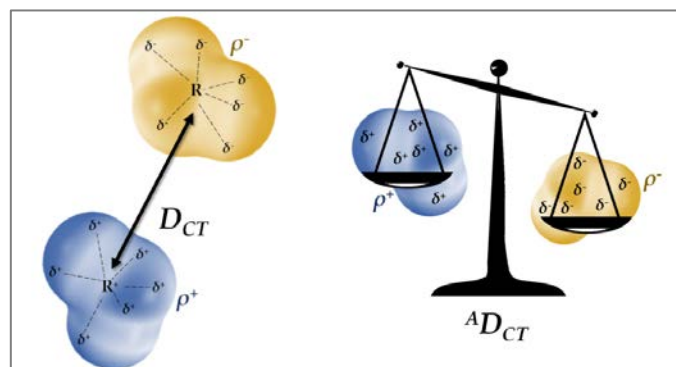


Figure 1 Schematic representation of the D_{CT} and $A_{D_{CT}}$ theoretical approach.

5.2 Introduction

Photoinduced charge-transfer (CT) and charge-separation are nowadays phenomena of paramount importance in many and diverse domains of application ranging from energy production through light-harvesting, [90] efficient chemoreceptive sensors, [91] to organic field-effect transistors (OFETs) [92]. However, a complete experimental characterization of the electronic absorption processes could be complex, since the nature of the observed excitations is not always plainly evident. Time-resolved [93] as well as two-colors UV-Vis experiments [94] can yield additional information on the interplay between the various excited states and on their lifetimes, yet they require complex instrumentation and still cannot provide an orbital picture of excitation and de-excitation phenomena.

In this field, theoretical studies of photochemical and photophysical processes can give valuable and complementary insights on the inner processes of photon molecular absorption and emission. To achieve a deeper understanding of photophysical processes, an accurate characterization of the energetics and of the chemical nature of the electronic excited states is needed. Indeed, great efforts have been spent to develop quantum chemical approaches to this end [95, 96]. At the same time, this task could be made easier by the development of simple, and possibly computationally inexpensive, descriptors quantifying in a condensed way information about the nature of the electronic transitions involved.

The characterization of excited states often and routinely relies on the visualization and analysis of the (canonical) orbitals involved in the transitions [40, 50, 97]. However, this approach may be not straightforwardly employed especially when many configurations are contributing to the excited states or the character of the

orbitals involved in the transition is difficult to interpret and define. Furthermore, orbital analysis may be difficult to be directly connected to simple chemical parameters and concepts such as, for instance, charge transfer extent.

For these reasons, in the last decade several approaches have been derived to analyze the character of the excited states, and specifically to quantify the degree of locality of an excitation, meaning by this quantifying the hole-electron distance produced upon irradiation.

Among others, one of the most applied is the so-called D_{CT} index, which is a simple and intuitive measure of the CT distance [55]. This index achieved great popularity and it has been adopted to investigate a wide range of very different molecular systems. Just to name a few, it has been used to characterize the optical response of BODIPY dyes, [98] ruthenium and copper complexes, [99-102] fluoride sensors, [103] colorants for dye-sensitized solar cells, [104-105] materials with enhanced delayed fluorescence, [106] and the formation of radical pairs for biological applications [107]. The wide application of the D_{CT} index is due to its simplicity, effectiveness, and straightforward interpretation that allows it to be easily implemented into popular quantum chemical codes, such as Gaussian [88] or MultiWFN [108].

The D_{CT} index is evaluated from the knowledge of the density difference between the two electronic states of interest. This descriptor is based on the analysis of the total electronic density in a real-space representation, [55] computed for the ground and excited states and it allows to monitor the nature of the excited states. The D_{CT} is indeed calculated as the module of the distance between the barycenters (R^+ and R^-) of the charge density distribution corresponding to the hole and particle:

$$D_{CT} = |\vec{R}_+ - \vec{R}_-| \quad (5.2.1)$$

Positive (R^+) and negative (R^-) barycenters are obtained by integration of the associated electron densities, ρ^+ and ρ^- . These latter are derived from the difference in total density of the two states S_i, S_j involved in the electronic transition - where $i=0, j > i$, with both i and $j \in \mathcal{N}$.

A drawback of the D_{CT} , already pointed out in the original paper, [55] is that for symmetric system the barycenters of the hole and of the electron density distributions may coincide due to symmetry constraints, and thus the D_{CT} will vanish even if a net charge-transfer occurs. As demonstrated by a recent paper, [69] and in Chapter 4 in such cases, the index may still be evaluated by identifying the corresponding symmetric irreducible subunits and limiting the density calculations on these latter. Conversely, a great advantage of the D_{CT} is that, since it relies only on the computed electronic densities for ground and excited state, it can be computed at any level of theory, such as density-functional and wave-function based methods, delivering the same qualitative description and quantitatively analysis of excited state evolution [60]. Since then, many other descriptors have been developed in literature. For instance, Etienne et al., [48,49] following the original approach introduced by Head-Gordon et al. [40] have derived several descriptors to study the excited state topology by means

of centroids of charges obtained from attachment/detachment density matrices. Another alternative descriptor was proposed by Adamo et al., [46,47] Δr , which relies on the calculation of the charge centroids of natural transition orbitals pairs. Peach, instead, proposed an indicator that computes the spatial overlap in a given excitation [41,42]. It can also be considered as a diagnostic tool for failures of time-dependent density functional theory (TD-DFT), establishing the reliability of a general electronic transition. Because the effects due to excitons formation may be crucial for a correct interpretation of the electronic excitations in solid-state physics, as well as for large molecular systems, Plasser et al. [50-54] have provided a general theory and comprehensive formalism for the correct evaluation of excitons properties. Through the definition of the exciton wave function, and its corresponding electron-hole correlation function, also Sharifzadeh made contributions in the quantification of the extent and directionality of the solid-state exciton, and the associated degree of CT character [109]. If on the one hand large real-space supercells are necessary for good convergence of the exciton wave functions, on the other side his analysis is general and can be applied to quantify CT in complex molecular systems, symmetric or not. In order to further expand the domain of applicability of D_{CT} , which still remains the most used descriptor to estimate the CT length, the present Chapter is proposing a new formulation for the D_{CT} index enabling the treatment of all systems independently of their symmetry. To this end, instead of defining the charge transfer extent as the distance between two average points of the hole and electron distribution (*i.e.* the two barycenters of charge distributions as in the D_{CT}), a novel density-based descriptor, the so called "Average Distance of Charge Transfer" ${}^A D_{CT}$ index, was designed as a weighted average of the distances between hole and electron distributions. As for the original D_{CT} , the ${}^A D_{CT}$ is general and can be used in combination with any quantum-chemical method yielding electronic densities for the ground and excited states. The main advantage of ${}^A D_{CT}$ is its general applicability to both symmetric and non-symmetric systems, without requiring an *ad hoc* definition of fragments [69]. Anyway, contrary to the D_{CT} , being an average of distances, the index has no vectorial character (*i.e.* it is a scalar quantity).

This Chapter has been organized as follows. After the description of the new index and an explanation of technical points, the results obtained are reported in the Results and Discussion paragraph first for some model compounds, namely a family of push-pull system that have been spectroscopically analyzed, and then for a set of large molecules, particularly interesting for their practical application in many different technologies like organic light-emitting diodes (OLEDs).

5.3 Computational Methods and Details

As we deeply illustrated in Chapter 3, the original formulation of the D_{CT} index is extremely simple, since it requires only the calculation of the electronic density of the

ground (ρ^{GS}) and excited state (ρ^{GS}) of interest. The density change associated to the electronic transition $\Delta\rho(\mathbf{r})$ is given by their difference, through which one can define two functions ρ^+ and ρ^- , which collect the points in the space, where an increment and a depletion of electron density occurs upon excitation. Associated to each distribution, one can define respectively two barycenters of charges R^+ and R^- , whose distance corresponds to the CT extent that D_{CT} measures. D_{CT} itself has, therefore, a vectorial character, being the difference between the position of the two barycenters. Nevertheless, this index vanishes for symmetric molecules by construction. To overcome this limitation, we implemented a revised version of the D_{CT} index, namely the ${}^P D_{CT}$, which has been developed in the same way of the parental one but considering only the subset of atoms that constitutes the smallest asymmetric fragment (for more details refer to Chapter 4). Nevertheless, this approach requires a previous knowledge about the nature of the charge-transfer transition since the user has to define the subset of atoms that makes up the smallest asymmetric fragment, thereby adding possible artifacts to the final result, including double counting coming from specific molecular fragments.

Here we propose a more general way to compute the particle-hole distance to consider the average of all possible distances between $\rho^+(\mathbf{r})$ and $\rho^-(\mathbf{r})$ density distributions, that is:

$${}^A D_{CT} = \frac{\int \int \mathbb{C}(\mathbf{r}, \mathbf{r}') |\mathbf{r} - \mathbf{r}'| d\mathbf{r} d\mathbf{r}'}{\int \int \mathbb{C}(\mathbf{r}, \mathbf{r}') d\mathbf{r} d\mathbf{r}'} \quad (5.3.1)$$

Here \mathbb{C} designates a weight, which has been defined based on the following considerations:

- it has to contain the information related to both $\rho^+(\mathbf{r})$ and $\rho^-(\mathbf{r})$;
- the distances between maxima of $\rho^+(\mathbf{r})$ and $\rho^-(\mathbf{r})$ should be the dominant terms;
- the distance between two points of describing the same density distribution (that is the hole or the electron) should have no weight.

In order to satisfy these constraints, the \mathbb{C} coefficient is defined as follows:

$$\mathbb{C}(\mathbf{r}, \mathbf{r}') = \rho^+(\mathbf{r}) \rho^-(\mathbf{r}') \quad (5.3.2)$$

Substituting Equation (5.3.2) into Equation (5.3.1) we get:

$${}^A D_{CT} = \frac{\int \int \rho^+(\mathbf{r}) \rho^-(\mathbf{r}') |\mathbf{r} - \mathbf{r}'| d\mathbf{r} d\mathbf{r}'}{\int \int \rho^+(\mathbf{r}) \rho^-(\mathbf{r}') d\mathbf{r} d\mathbf{r}'} \quad (5.3.3)$$

We stress here that while D_{CT} (and ${}^P D_{CT}$ as well) have a vectorial character, being the difference between to positions R^+ and R^- , the ${}^A D_{CT}$ is a scalar.

One can show that ${}^A D_{CT}$ may be considered as an upper bound of the module of D_{CT} . In fact, starting from Equation (5.2.1) and substituting Equations (3.1.23) and (3.1.24) in it, we obtain:

$$\begin{aligned}
|D_{CT}| &= |\mathbf{R}^+ - \mathbf{R}^-| = \left| \frac{\int \rho^+(\mathbf{r}) \mathbf{r} d\mathbf{r}}{\int \rho^+(\mathbf{r}) d\mathbf{r}} - \frac{\int \rho^-(\mathbf{r}) \mathbf{r} d\mathbf{r}}{\int \rho^-(\mathbf{r}) d\mathbf{r}} \right| \\
&= \left| \frac{\int \rho_-(\mathbf{r}') d\mathbf{r}' \int \rho_+(\mathbf{r}) \mathbf{r} d\mathbf{r} - \int \rho_+(\mathbf{r}) d\mathbf{r} \int \rho_-(\mathbf{r}') \mathbf{r}' d\mathbf{r}'}{\int \rho_-(\mathbf{r}') d\mathbf{r}' \int \rho_+(\mathbf{r}) d\mathbf{r}} \right| \\
&= \left| \frac{\int \rho_+(\mathbf{r}) \rho_-(\mathbf{r}') \mathbf{r} d\mathbf{r} d\mathbf{r}' - \int \rho_+(\mathbf{r}) \rho_-(\mathbf{r}') \mathbf{r}' d\mathbf{r} d\mathbf{r}'}{\int \rho_+(\mathbf{r}) \rho_-(\mathbf{r}') d\mathbf{r}' d\mathbf{r}} \right| = \left| \frac{\int \rho_+(\mathbf{r}) \rho_-(\mathbf{r}') (\mathbf{r} - \mathbf{r}') d\mathbf{r} d\mathbf{r}'}{\int \rho_+(\mathbf{r}) \rho_-(\mathbf{r}') d\mathbf{r}' d\mathbf{r}} \right|
\end{aligned} \tag{5.3.4}$$

Comparing Equation (5.3.4) with Equation (5.3.3), it is worth to notice that

$$|D_{CT}| \leq {}^A D_{CT} \tag{5.3.5}$$

since the ${}^A D_{CT}$ computes an average of all possible distances, unlike the D_{CT} index, which on the contrary estimates the distance between two averaged points.

In practice, the integration is performed as a sum on a large but finite number of grid points on which difference densities are computed. Nonetheless, in the case of ${}^A D_{CT}$, this direct procedure may be impractical due to their large amount and it is therefore possible to compute the ${}^A D_{CT}$ using a discrete number of condensed charges that in our case will be the atomic charges obtained according to some partitioning scheme (like for example Mulliken's or Hirshfeld's procedures), in analogy to Equations (3.1.25) - (3.1.29). This type of procedure has already been applied to the D_{CT} and ${}^P D_{CT}$ (see Chapters 3 and 4), and the corresponding Equations for the ${}^A D_{CT}$ are:

$$\Delta Q_i = Q_i^{ES} - Q_i^{GS} \tag{5.3.6}$$

$$Q_i^+ = \begin{cases} = \Delta Q_i & \text{if } \Delta Q_i > 0 \\ = 0 & \text{if } \Delta Q_i \leq 0 \end{cases} \tag{5.3.7}$$

$$Q_i^- = \begin{cases} = \Delta Q_i & \text{if } \Delta Q_i < 0 \\ = 0 & \text{if } \Delta Q_i \geq 0 \end{cases} \tag{5.3.8}$$

$${}^A D_{CT} = \frac{\sum_i \sum_j Q_i^+ Q_j^- |\mathbf{r}_i - \mathbf{r}_j|}{\sum_i \sum_j Q_i^+ Q_j^-} \tag{5.3.9}$$

Ground state structures and vertical excitation energies were computed, respectively, at the density functional theory (DFT) and at the time-dependent DFT (TD-DFT) levels, [110, 111] using the PBE0 functional [23] and the 6-31G(d) basis set [112]. All calculations have been performed using the Gaussian16 software, [88] while the D_{CT} , the ${}^P D_{CT}$ and the ${}^A D_{CT}$ have been evaluated using an in-house developed and freely available code [86]. Ground and excited state densities were generated using the *cubegen* and *cubeman* utilities of the Gaussian16 Package applying default options for grids. The electronic densities considered here are all relaxed densities [88].

In this Chapter we considered in particular the properties of those excited S_n states ($n=1, \dots$) that have a non-negligible oscillator strength, and that, as a consequence, have an appreciable probability to be populated upon light irradiation.

5.4 Results and Discussion

In order to validate and compare ${}^A D_{CT}$ with previously developed descriptors, we firstly considered a set of test case molecules, prototypes of systems containing donor and/or acceptor groups, and spectroscopically well characterized [113] (**1a** to **3** in Figure 2). For a subset of these model compounds the index was computed both using electron densities distributions and Mulliken atomic charges. Then, we have analyzed a set of symmetric push-pull molecules (**4-11** in Figure 2).

We recall here that the aim of the present Chapter is to compare different descriptors and not to investigate the ability of the underlying computational approach (*i.e.* here of the selected exchange and correlation functional) to capture the photophysics of the systems under analysis.

We have first considered three of the systems depicted in Figure 2, namely, those possessing a single phenyl ring acting as a bridge, with in para positions either two electron donors (**3**), or two electron acceptors (**2**), or one electron donor and one electron acceptor groups (**1a**).

For these systems we computed the D_{CT} , ${}^P D_{CT}$ and ${}^A D_{CT}$ indexes using both densities and Mulliken charges, as reported in Figure 3 and Table 1. Independently of the model used to quantify the CT, charge transfer distances computed using Mulliken charges are all consistently higher than those derived from density-based calculations: these results are in agreement with a previous investigation performed on symmetric push-pull organic compounds using the global and partial D_{CT} analysis [69].

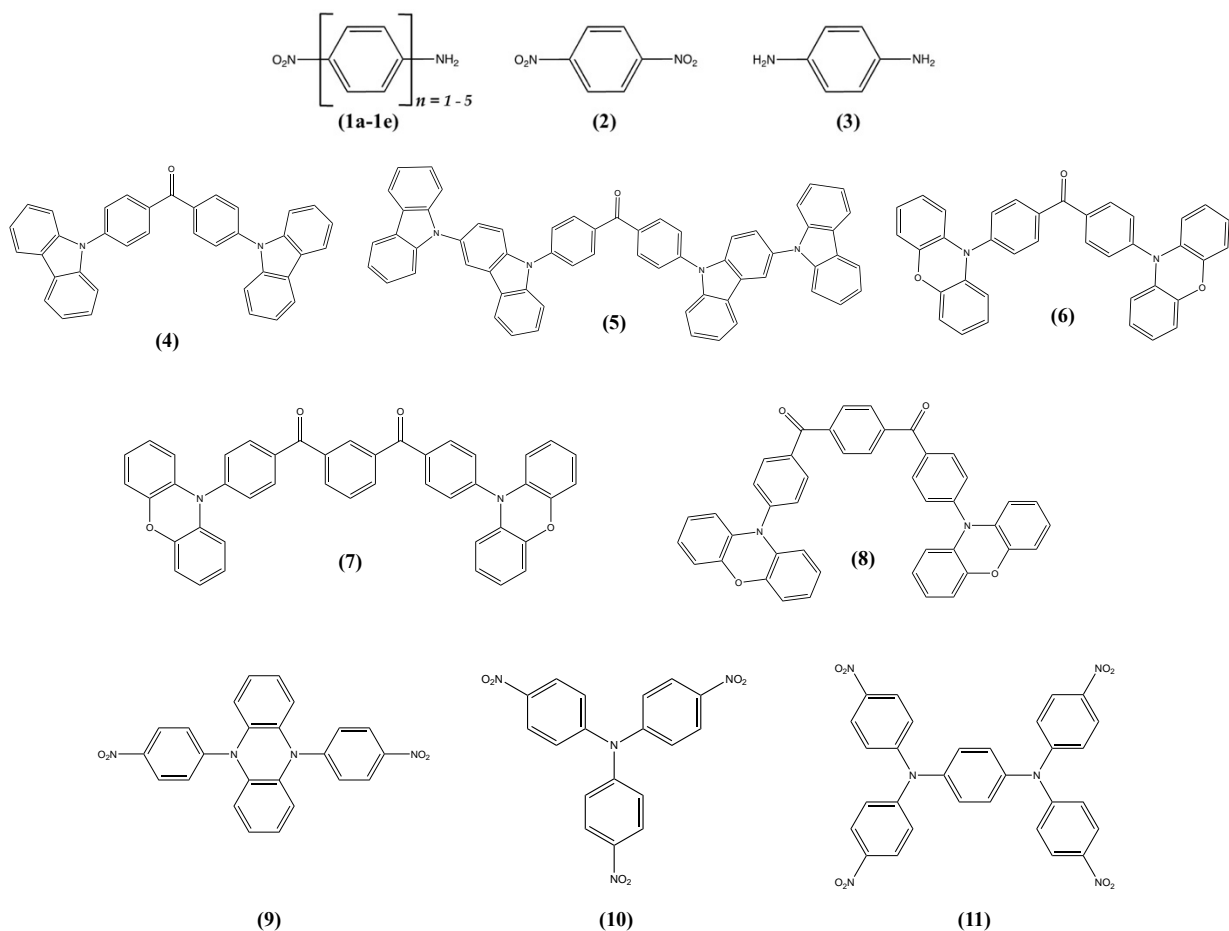


Figure 2 Schematic representation of the model compounds used as donor-acceptor (D-A, **1a-1e** for $n=1,5$), acceptor-acceptor (A-A, **2**), and donor-donor (D-D, **3**) together with structural formulae of the butterfly-shaped benzophenone derivatives (**4-8**) and of DA₂-NO₂, DA₃-NO₂ and DA₄-NO₂ molecules (**9-11**).

Table 1 Computed Excitation energies (in eV) and associated oscillator strength (f , in a.u.) together with D_{CT} , ${}^A D_{CT}$ and ${}^P D_{CT}$ values (in Å) computed by means of an analysis based on electronic density and Mulliken charges. The A-D length (in Å) is the geometrical distance between the N atoms of NH₂ or NO₂ groups with respect to the center of the Ph ring for molecule **2-3**, while it is the distance between the two N atoms for molecule **1a**, and it serves as a rough estimate of the Acceptor-Donor distance.

Molecules	S_n	E (eV)	f (a.u.)	A-D distance	Indexes computed via electronic Density			Indexes computed via Mulliken Charges		
					D_{CT} (Å)	${}^A D_{CT}$ (Å)	${}^P D_{CT}$ (Å)	D_{CT} (Å)	${}^A D_{CT}$ (Å)	${}^P D_{CT}$ (Å)
1a	$n=2$	4.30	0.3455	5.76	2.05	3.45	1.11 (NO ₂) 0.84 (NH ₂)	3.49	4.05	2.29 (NO ₂) 0.77 (NH ₂)
2	$n=5$	4.43	0.0194	2.83	0.00	3.46	1.45	0.00	3.87	3.26
3	$n=1$	4.45	0.0522	2.81	0.00	3.28	1.11	0.00	3.40	2.79

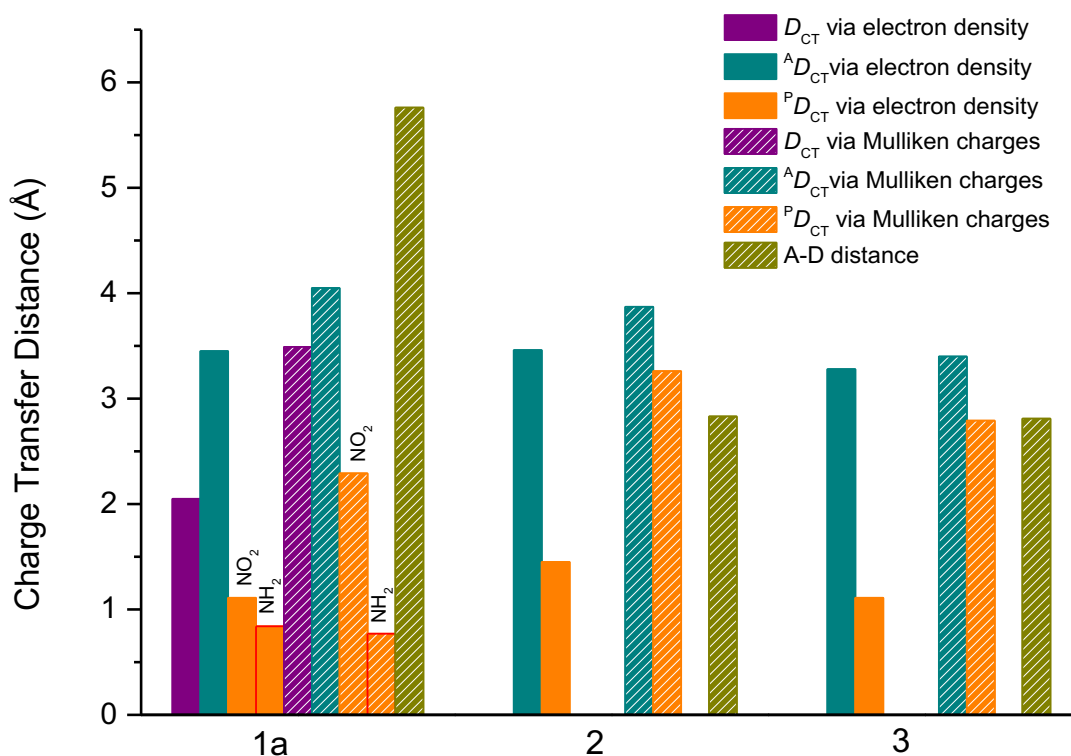


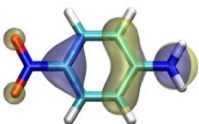
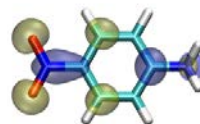
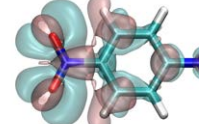
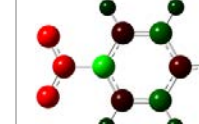
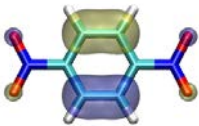
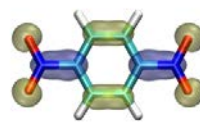
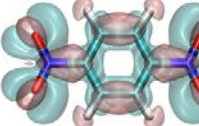
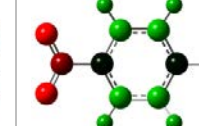
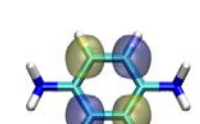
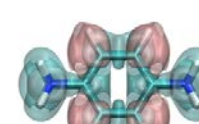
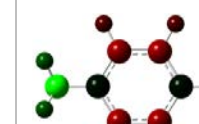
Figure 3 Computed D_{CT} (violet), ${}^A D_{CT}$ (green) and ${}^P D_{CT}$ (orange) values (in Å), using total electronic density (full bar) or Mulliken charges (dashed). Actual numerical data are reported in Table 1.

Indeed, the partial charges lead to quantitatively higher results in terms of CT distance due to an excessive estimation of charge localization on the electrophilic and nucleophilic groups. This effect is larger when considering the D_{CT} and ${}^P D_{CT}$ descriptors with respect to the ${}^A D_{CT}$: the reason is that the $\rho^+(\mathbf{r})$ and $\rho^-(\mathbf{r}')$ weighting factor in the ${}^A D_{CT}$ (see Equation (5.3.3)) magnifies the contribution of the terminal groups. Therefore, the ${}^A D_{CT}$ index appears as less sensitive to the use of either density or Mulliken charges for its evaluation.

Therefore, as the relationship between CT indexes computed from densities and partial charges is well established [57,69], hereafter we present only the analysis carried out with the latter method, as it is easier to implement and perform. The analysis of ${}^P D_{CT}$ has been performed considering the Ph-NO₂ and Ph-NH₂ moieties as acceptor and donor fragments, respectively.

We considered only the lowest, bright (*i.e.* with a sizable oscillator strength) charge transfer excitations in all cases. These excitations correspond to the first electronic transition ($S_1 \leftarrow S_0$) for p-phenylenediamine (**3**), and to the second ($S_2 \leftarrow S_0$) and to the fifth ($S_5 \leftarrow S_0$) transitions for p-nitroaniline (**1a**) and p-dinitrobenzene (**2**), respectively. All these lowest lying CT states correspond mainly to a one-electron excitation from HOMO to the LUMO as reported in Table 2.

Table 2 Isosurface representation of the HOMO and LUMO (contour value 0.04 a.u., positive and negative values represented in yellow and blue respectively) and $\Delta\rho$ (contour value 0.0004 for a.u., positive and negative values represented in cyan and pink respectively), computed for model systems **1a**, **2** and **3**. The representation with charges is reported in the rightmost column ($\Delta q < 0$ in red, $\Delta q > 0$ in green).

	HOMO	LUMO	$\Delta\rho$	Δq	Δq
1a					
2					
3					

The values computed with $^A D_{CT}$ are close for the three molecules because in all these cases the hole (the HOMO in a single-excitation picture) is mainly localized on the phenyl ring. Molecules containing the nitro group (*i.e.* molecules **1a** and **2**) display the highest values because their LUMOs are mainly localized on their NO₂ moieties, whereas (even when it is present) the contribution of amino groups seems negligible. Regarding molecule **1a**, D_{CT} achieves a value of 3.49 Å, lower than the physical distance between the donor and/or acceptor group evaluated here as the distance between their nitrogen atoms (5.76 Å). This finding is reasonable due to the electron delocalization of both the HOMO and the LUMO on the phenyl bridge (Table 2), which reduces the CT distance of the transition. As expected, we calculated a null D_{CT} for molecule **2** and **3** because of their symmetric structure. Because of that, an analysis of the $^P D_{CT}$ has been performed to estimate the CT in these two cases. Such values (Figure 3 and Table 1) decrease as expected in going from nitro to amino substituted. Referring to the $^P D_{CT}$ values, it is possible to observe a qualitatively consistent trend with molecules **1a-3**. Thanks to an averaged approach, it is possible to quantify the CT entity even in the case of an overall zero D_{CT} . The $^A D_{CT}$ yields results higher than D_{CT} and $^P D_{CT}$, as expected (see Equation (5.3.5)).

To further compare the different descriptors and their ability to describe CT transitions, we considered the push-pull dyad **1a** (Figure 2) and enlarged the spacer length by increasing the number of phenyl rings from 1 (**1a**) to 5 (**1e**). In all cases the lowest and bright CT transition corresponds to a HOMO→LUMO excitation calculated as the first excited state for every system, except for **1a**. The computed HOMO and LUMO together with corresponding difference in density and in charges are reported in Table 3. We notice that the oscillator strengths tend to decrease upon addition of a phenyl ring, ranging from 0.42 to 0.22 (see Table 4). We actually focused on bright excited states (*i.e.* excited states that have a significant oscillator strength and as a consequence a high probability to be populated upon irradiation), which correspond to S_1 states for all the molecules but for molecule **1a** (in this latter case we considered state S_2 instead because the S_1 state is dark). The dihedral angle (N-C)---(C-N) ranges between values of 180° for the relaxed structure of **1a** to the minimum value of 160° for **1e**. So, the increase of non-planarity decreases the transition probability for these HOMO (mostly localized on the donor moiety) → LUMO (mostly localized on the acceptor group) excitations. Already from a simple visual inspection of the MOs involved in the CT transition it is clear that, due to the orbital delocalization of the donor moiety (see HOMO orbitals in Table 3), the effective CT distance must be smaller than the physical distance between the donor (-NH₂) and the acceptor (-NO₂). The latter is very localized independently from the number of the phenyl spacers (Table 3, LUMO orbitals).

The D_{CT} and ${}^A D_{CT}$ values (Figure 4 and Table 4) consistently quantify this observation; whatever the method used to calculate the CT distance the values increase adding a phenyl group in the range from 3.50 Å (for molecule **1a**) to 16.00 Å (for molecule **1e**). Furthermore, both indexes (D_{CT} and ${}^A D_{CT}$) provide values that are quantitatively equivalent (Figure 4) and their (small) difference decrease upon elongation of the phenyl chain (see Table 4).

The differences Δ reported in Table 4 decrease upon elongation of the phenyl chain because as the ${}^A D_{CT}$ represents the upper limit of the D_{CT} , the two indexes converge as the charge separation distance increases. Upon addition of each phenyl unit the physical distance between A and D increases of ca. 4.33 Å, yet the corresponding increment in the CT distance is about 3.00 Å independently on the D_{CT} type considered (as graphically represented by the normalized D_{CT} plot reported in Figure 5, whose values are collected in Table 5). Indeed, upon addition of the phenyl rings both the hole and the electron become more delocalized along the aromatic chain. Reassuringly, both indexes are able to capture this feature both qualitatively and quantitatively.

Table 3 Isosurface representation of the HOMO and LUMO (contour value 0.04 a.u., positive and negative values represented in red and green) and $\Delta\rho$ (contour value 0.0004 for a.u.), computed for model systems **1a-e**. The representation with charges is reported in the lower-right column ($\Delta q < 0$ in red, $\Delta q > 0$ in green).

	HOMOs	LUMOs
1a		
1b		
1c		
1d		
1e		
	$\Delta\rho$	Δq
1a		
1b		
1c		
1d		
1e		

Table 4 Computed Excitation energies (in eV) and oscillator strength (in a.u.) together with D_{CT} , ${}^A D_{CT}$ values (in Å) and difference ($\Delta = {}^A D_{CT} - D_{CT}$ in Å) for molecules **1a-e**.

Molecules	S_n	E (eV)	f (a.u.)	D_{CT} (Å)	${}^A D_{CT}$ (Å)	Δ
1a	n=2	4.30	0.3455	3.49	4.05	0.56
1b	n=1	3.43	0.4228	6.49	6.90	0.41
1c	n=1	3.12	0.3792	9.76	10.1	0.34
1d	n=1	3.02	0.3013	12.3	12.6	0.30
1e	n=1	2.30	0.2198	15.8	16.0	0.20

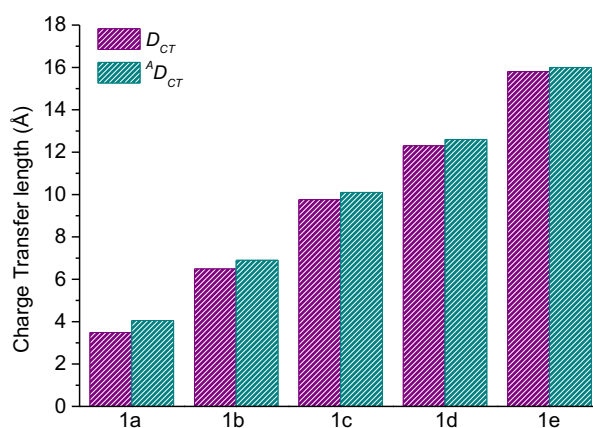


Figure 4 Bar diagram of D_{CT} and ${}^A D_{CT}$ values (in Å) calculated from atomic Mulliken charges.

Table 5 The total D_{CT} and ${}^A D_{CT}$ values (in Å) calculated by means of Mulliken charges and normalized by the average phenyl length set to 4.33 Å.

Molecules	Normalized D_{CT} (Å)	Normalized ${}^A D_{CT}$ (Å)
1a	0.81	0.94
1b	1.50	1.59
1c	2.25	2.33
1d	2.84	2.91
1e	3.65	3.70

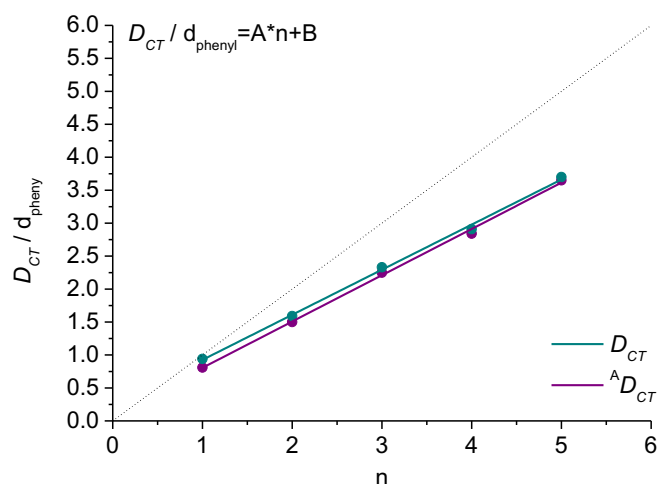


Figure 5 Normalized D_{CT} (D_{CT}/d_{phenyl} , where d_{phenyl} is the average phenyl length set to 4.33 Å) as a function of the number of phenyl spacer (n): for molecule **1a** $n=1$, for molecule **1b** $n=2$, ..., for molecule **1e** $n=5$.

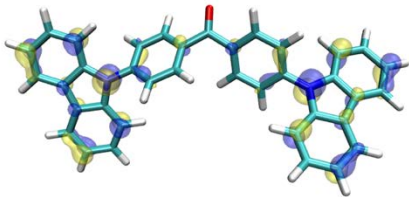
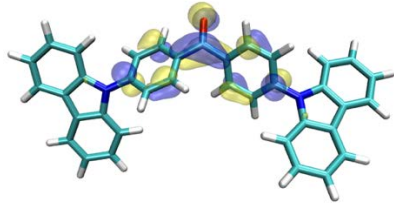
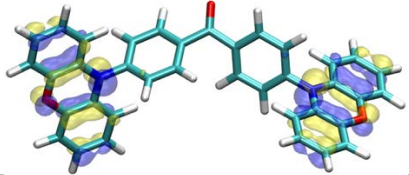
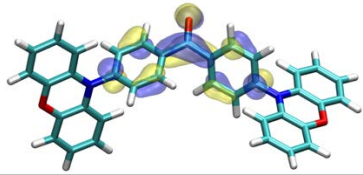
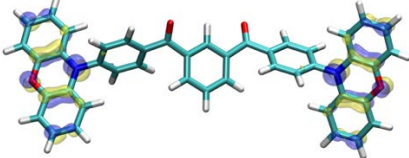
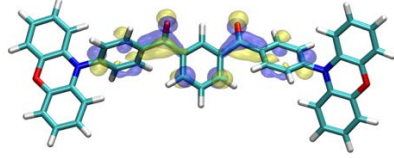
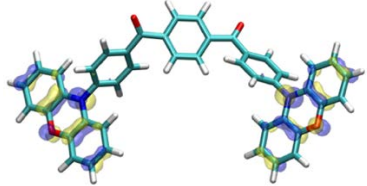
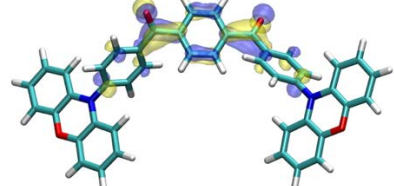
Next, as real DA symmetric molecules we have selected the push-pull systems molecules **4-11** represented in Figure 2. Experimentally, these “butterfly-shaped” molecules (**4-8** in Figure 2) are interesting since an efficient thermal activated delayed fluorescence (TADF) [114,115] can be achieved, making them promise for application as organic light-emitting diodes (OLEDs). Moreover, computational and experimental studies have demonstrated that the careful molecular design of benzophenone derivatives based on Donor-Acceptor-Donor (D-A-D) structure is useful to produce organic luminophores with efficient full-color TADF emission [116]. Previous quantum chemical calculations performed on these compounds suggested that the modulation of the intramolecular charge-transfer (ICT) character of the transitions correlates with a change in the emission wavelength [116]. Therefore, the quantification of CT is of the utmost importance for the design of new compounds. Systems **9-10** (Figure 2) are also promising for OLEDs applications [83,84], while the DA₄-NO₂ (Molecule **11** in Figure 2) has been chosen since it contains a structural motif often found in hole transport materials applied for a wide range of technologies, from photocopiers to electroluminescent display devices [85].

The lowest energy $S_1 \leftarrow S_0$ excitations correspond essentially to a one-electron HOMO \rightarrow LUMO transition for all the butterfly molecules investigated here (**4-8**, Figure 6). These transitions correspond to an intermolecular charge transfer (ICT) as the nature of the HOMO and LUMO distributions shows (see Table 6). Indeed, for all the compounds the LUMO is predominantly located on the central electron-accepting benzophenone core, whereas the HOMO is mainly localized on the electron-donating peripheral carbazole or phenoxazine substituents due to the highly twisted geometry of the molecules which renders coupling of the donor and of acceptor constituents negligible. Indeed, for compounds **4** and **5** the dihedral angles between the phenyl rings of the benzophenone unit and adjacent carbazoles are calculated to be around 50° and for **6**, **7** and **8** with phenoxazines to be around 70°. Consistently, by analysis of oscillator strengths (Table 7) it may be noted that the S_1 states for **4** and **5** have

relatively large oscillator strength ($f = 0.43$ and 0.25 , respectively), which tends to decrease upon substitution with more sterically-hindered phenoxazine donor units ($f = 0.04$ – 0.10 for compounds **6**–**8**).

As expected from the symmetry of these molecules (space group C_{2v}), the D_{CT} values do not reflect the evident CT nature of the lowest-energy transitions. Indeed, D_{CT} is null for **5** or achieves values which do not exceed 2.00 \AA for the other molecules, but **8** ($D_{CT} = 3.57 \text{ \AA}$).

Table 6 Representation of HOMO and LUMO orbitals involved in the CT transition for butterfly-shaped molecules (**4**–**8**).

	Transition	Excited State 1	
4	Homo→Lumo		
5	Homo→Lumo		
6	Homo→Lumo		
7	Homo→Lumo		
8	Homo→Lumo		

On the other hand, as expected, the ${}^P D_{CT}$ index is able to quantify the CT entity for all the benzophenone derivatives, as it is straightforward to define the two asymmetric D-A fragments, each of them consisting of one donor moiety and the same acceptor group, which corresponds for all molecules to the benzophenone core (Figure 6). Using this latter definition, we computed the ${}^P D_{CT}$ values for all butterfly molecules, collected in Figure 7 and reported in Table 7.

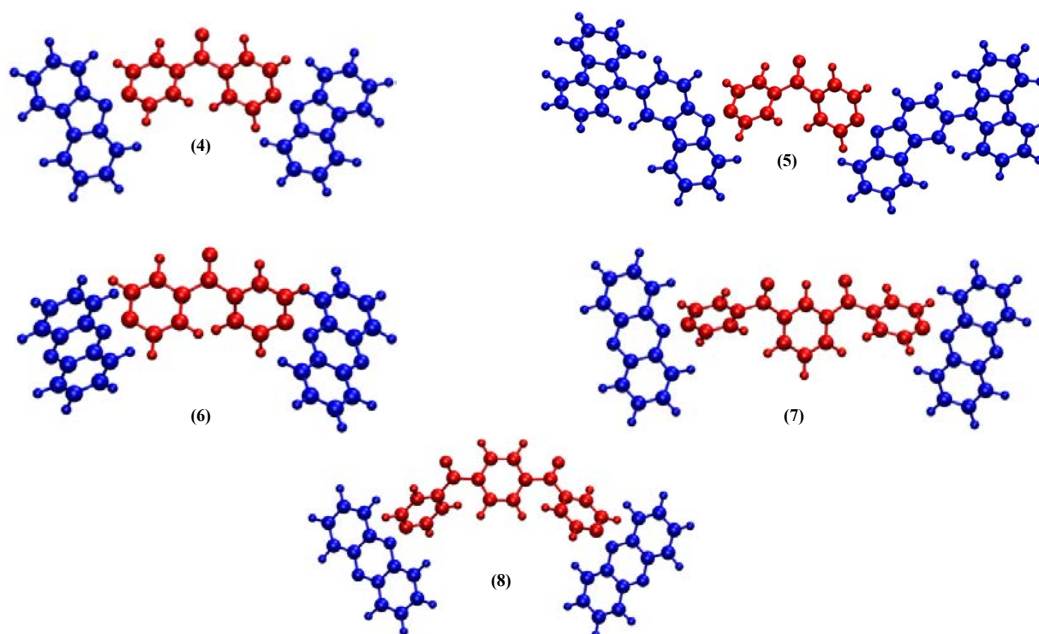


Figure 6 Schematic representations of the Butterfly-shaped benzophenone derivatives (4-8). The acceptor moieties are represented in red, while the donor ones are depicted in blue.

Table 7 Computed Excitation energies (in eV) and oscillator strength (in a.u.). The D_{CT} , ${}^A D_{CT}$ and ${}^P D_{CT}$ values (in Å) have been calculated by means of Mulliken charges for the five butterfly-shaped molecules (4-8).

Molecules	Sym	E (eV)	f (a.u.)	D_{CT} (Å)	${}^A D_{CT}$ (Å)	${}^P D_{CT}$ (Å)
4	C_2	3.26	0.4324	1.99	7.13	5.76
5	C_2	2.96	0.2475	0.00	10.28	8.56
6	C_2	2.35	0.0790	1.86	6.97	5.77
7	C_2	2.37	0.0962	1.03	9.35	8.17
8	C_2	2.16	0.0414	3.57	9.06	7.61

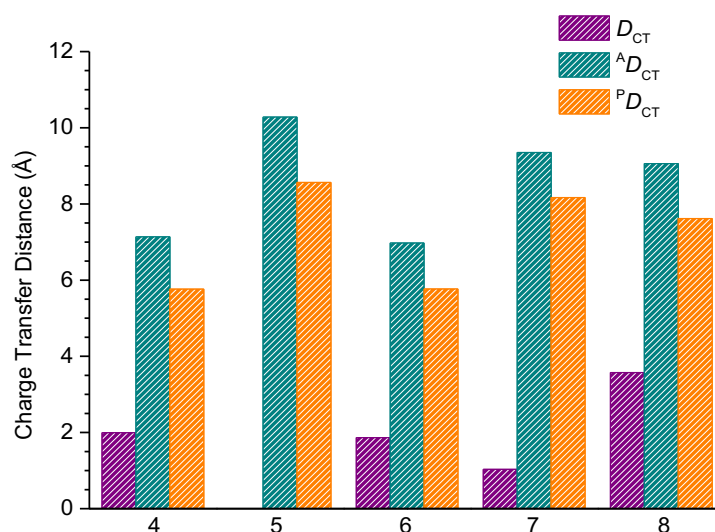


Figure 7 Computed D_{CT} , ${}^A D_{CT}$ and ${}^P D_{CT}$ values (in Å) for molecules 4-8.

Reasonably, having a similar structure, molecules **4** and **6** present the same ${}^P D_{CT}$ value (5.76 Å): the carbazole (for **4**) or phenoxazine (for **6**) lateral groups act as donors towards the acceptor benzophenone core (see Figure 6). Molecules **5** and **7**, which are characterized by large sterically-hindered peripheral moieties, show the highest ${}^P D_{CT}$, ranging from 8.00 Å to 8.50 Å. As a matter of fact, the strong conjugated residues present in these systems allow an efficient intermolecular charge transfer, notwithstanding a clear physical distance between D and A. The same applies to the molecule **8**, whose ${}^P D_{CT}$ achieves a value of 7.61 Å.

Firstly, it is worth to notice that we obtained generally higher ${}^A D_{CT}$ values (≥ 7 Å, see Figure 7 and Table 7), in accordance with the qualitative analysis of HOMO and LUMO orbitals, which are localized on distinct and far apart atoms of the molecule. Moreover, we obtained the same consistent trend individuated by the ${}^P D_{CT}$ analysis. The highest ${}^A D_{CT}$ values are found for molecules **5**, **7** and **8** (9.0-10.0 Å), while for molecules **4** and **6** the ${}^A D_{CT}$ values decrease to about 7.0 Å. By the analysis of the bar diagram in Figure 7, it could be also pinpointed that the ${}^A D_{CT}$ values are higher than ${}^P D_{CT}$ ones for all considered molecules. As mentioned, the explanation stems from the mathematical definition of the averaged descriptor, which takes into account all possible physical distances between opposite charges and does not estimate a unique distance between two averaged barycenters of charges.

Contrary to the symmetric systems **4-8** characterized by a D-A-D structure, in **9-11** the peripheral nitro-substituted phenyl rings act as electron-accepting moieties while the electron-donating core is represented by a substituted di-phenyl hydrophenazine moiety, a nitrogen atom and a di-amino phenyl group for DA₂-NO₂ (**9**), DA₃-NO₂ (**10**) and DA₄-NO₂ (**11**) respectively (Figure 8).

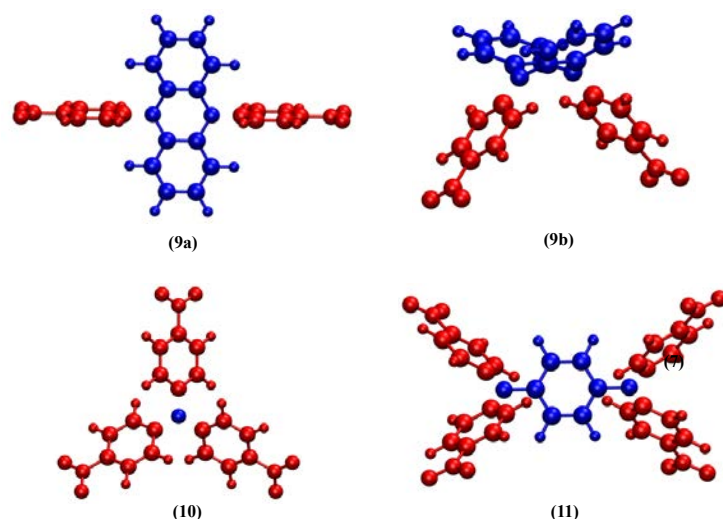
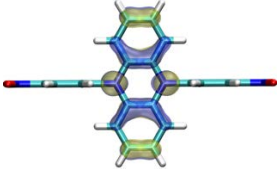
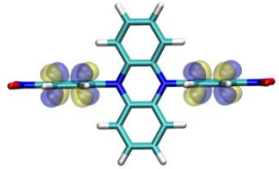
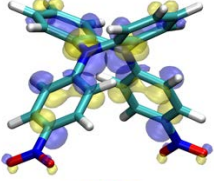
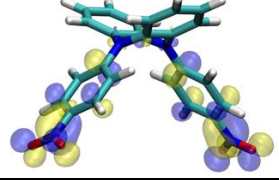
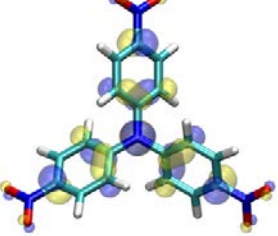
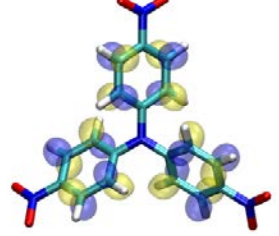
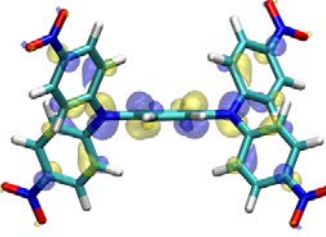
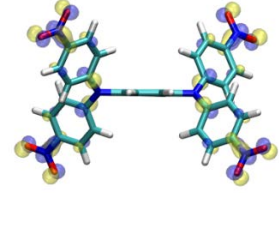


Figure 8 Schematic representations of DA₂-NO₂ (**9a-b**), DA₃-NO₂ (**10**) and DA₄-NO₂ (**11**) molecules. The acceptor moieties are represented in red, while the donor ones are depicted in blue.

It is important to point out here that, at the ground state, two distinct stable conformers exist for the DA₂-NO₂ molecule, *i.e.* a twist (**9a**) and a boat (**9b**) conformation. The latter is characterized by a boat shape disposition of diphenyl hydrophenazine core and it is more stable of 1.40 kcal/mol than the twist conformer, with the nitro substituted phenyl rings roughly orthogonal to the hydrophenazine core. Notably, the lowest-energy bright symmetric CT transitions are not of the HOMO→LUMO type for all these systems and do not always correspond to the S₁←S₀ excitations. Specifically, we studied the fourth ES (*i.e.* S₄←S₀) and the seventh ES (*i.e.* S₇←S₀) for **9a** and **10**, respectively, and in both cases these transitions correspond to a HOMO→LUMO +3 excitation, as reported in Table 8.

Table 8 Representation of HOMO and LUMO orbitals involved in the CT transition for DA₂-NO₂ (**9a-b**), DA₃-NO₂ (**10**) and DA₄-NO₂ (**11**) molecules.

Molecules	Transition		
9a	Homo→Lumo+3		
9b	Homo→Lumo		
10	Homo→Lumo+3		
11	Homo→Lumo		

From the molecular orbitals analysis (Table 8), we can notice that the HOMO is mainly localized in the core of the system, while the LUMO for **9b** and **11** and the LUMO+3 for **9a** and **10** are predominantly located on the peripheral nitrophenyl groups, acting as acceptors due to the presence of the strong electron withdrawing groups.

Despite the fact that the two conformers of molecule **9** have the same symmetric A-D-A framework, only the twisted one with D₂ symmetry has a D_{CT} almost equal to zero.

On the contrary, for the boat-like conformer (**9b**) we expected a non-vanishing D_{CT} , due to a C_{2V} symmetric arrangement (3.26 Å). For molecules **10** and **11** we obtained null D_{CT} values as expected due to their C_3 and D_2 symmetries, respectively. Compared to these values indeed, the $^P D_{CT}$ reveals a more delocalized topology of the excited states. Considering only the smallest D-A asymmetric fragment, the partial CT length is somewhat increased achieving values from 1.66 Å (for molecule **10**) to 5.50 Å (for molecule **11**).

Interestingly, the $^A D_{CT}$ values present the same qualitative trend of the $^P D_{CT}$: we find the smallest value for molecule **10** (4.72 Å), while we obtained the highest for molecule **11** (7.03 Å), see Table 9 and Figure 9.

Table 9 Computed Excitation energies (in eV) and oscillator strength (in a.u.). The D_{CT} , $^A D_{CT}$ and $^P D_{CT}$ values (in Å) have been calculated by means of Mulliken charges for DA₂-NO₂ (**9a-b**), DA₃-NO₂ (**10**) and DA₄-NO₂ molecules.

Molecules	Sym	S _n	E (ev)	f (a.u.)	D_{CT}	$^A D_{CT}$	$^P D_{CT}$
9a	D ₂	n=4	3.07	0.001	0.11	5.44	4.08
9b	C _{2V}	n=1	3.47	0.400	3.26	6.39	5.08
10	C ₃	n=7	4.20	0.004	0.00	4.72	1.66
11	D ₂	n=1	3.12	0.296	0.00	7.04	5.57

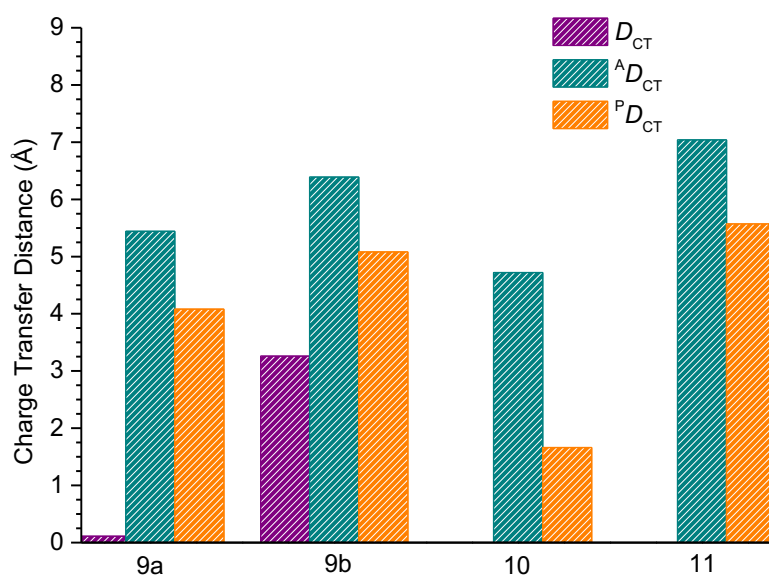


Figure 9 Computed D_{CT} , $^A D_{CT}$ and $^P D_{CT}$ values (in Å) for molecules **9a-11**.

We deem worth pinpointing again that, as in the previous cases and how demonstrated by the mathematical definition, the average values are always higher than the ones calculated by the definition of the barycenters of charges.

From all these data we can conclude that the ${}^A D_{CT}$ descriptor allows to describe systems rather unfeasible with standard density-based index (e.g. molecules with Donors or Acceptors connected by a symmetry operation). Nonetheless for the sake of completeness, we will illustrate here the singular case of a symmetric donor-acceptor (DA) molecule, which well displays the averaged character of the ${}^A D_{CT}$ formulation. This hypothetical model system (Figure 10), hereafter referred to as AD-Ph₄-AD, shows a peculiar topology possessing an overall C_{2V} symmetry with two symmetry related NH_2 residues acting as donors, and two symmetry related acceptor groups (NO_2). Overall the systems present therefore two symmetry equivalent D-A pair. In this case, two $NO_2 \leftarrow NH_2$ charge transfers can be considered: one at a short distance, represented by the DA pair of the same phenyl (5 Å), and another at longer distance represented by the pair of D and A placed on the opposite sides of the molecule (~16 Å), as schematically depicted in Figure 10.

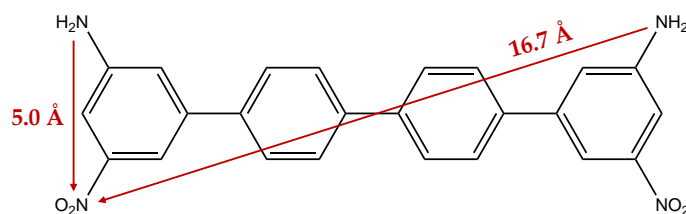


Figure 10 Representation of the AD-Ph₄-AD systems (C_{2V} symmetry) with two possible CT distances here measured as the distance between the N atoms of $-NH_2$ groups and $-NO_2$ groups.

In this C_{2V} conformation, the two possible $A \leftarrow D$ (*i.e.* $NO_2 \leftarrow NH_2$) charge transfers are energetically degenerate. For symmetry reasons, the long-range CT contributions cancel out in a D_{CT} formalism leading to a very small global value independently of the fact that charges or density are used to evaluate it (Table 10). On the contrary, the ${}^A D_{CT}$ formalism yields a value (~10 Å), which is close to the average of the two possible $NH_2 \rightarrow NO_2$ distances (~5.0 Å and ~16.7 Å, respectively).

This example clearly shows that the ${}^A D_{CT}$ corresponds to the global average distance of two energetically degenerate CTs and it cannot give insights on the CT distances associated to the different phenomena. If the user aims quantifying separately the two A-D distances, in this case we suggest using the ${}^P D_{CT}$ method, since in that way one can select the corresponding fragments contributing to the desired transition.

Table 10 Computed D_{CT} and ${}^A D_{CT}$ (Å) for the AD-Ph₄-AD molecule along with the isosurfaces of the orbitals involved in the transition and difference in ground and excited state densities ($\Delta\rho = \rho_{ES} - \rho_{GS}$)

			Indexes computed via electronic Density		Indexes computed via Mulliken Charges	
S_n	E / eV	Symmetry	D_{CT}	${}^A D_{CT}$	D_{CT}	${}^A D_{CT}$
n=6	4.29	C_{2v}	1.51	9.70	3.52	9.86

5.5 Conclusions

Here we have presented and discussed a density-based index (called ${}^A D_{CT}$) enabling to quantify the charge transfer length associated to an electronic transition. With respect to previously developed density-based indexes like D_{CT} and ${}^P D_{CT}$, the ${}^A D_{CT}$ allows to achieve a description that is independent of the system topology. Indeed, from a theoretical standpoint, this index yields reasonable amounts and distance of charge-transfer even for most symmetric molecules, which are the systems usually not correctly described by density-based descriptors. This descriptor retains the positive aspects of the previous density-based descriptors:

- it has a particularly low computational burden if used in conjunction with atomic charges (for instance Mulliken's ones).
- it can be applied independently on the level of theory adopted (as long as it allows to investigate electronic excited states), thus can be applied "out-of-the-box" both with calculations based on density functional theory as well as on wave-function theory.

For sake of completeness, we also have to pinpoint that the ${}^A D_{CT}$, as the name implies, yields an average value, so it is inherently a scalar (and not a vectorial) quantity. Indeed, contrary to the original D_{CT} it does not provide a physically correlated origin of the displacement of the electron and the hole. As long as donor and acceptor groups

are easily identified this does not represent a significant drawback. Since the ${}^A D_{CT}$ is an average, when applied on systems with two (or more) symmetry equivalent donor-acceptor pairs, it will not provide a value of the intra and inter-pair charge transfer distances individually, but instead their average and thus it requires care in its use and interpretation.

Chapter 6

Investigating excited states via the analysis of electron density rearrangement

6.1 Context

Up to now we have extensively discussed about quantifying charge-transfer, what are the theoretical approaches enabling to measure the spatial extent of an electronic transition, and the challenges associated with it and how to handle them. Moreover, until now we have applied all these concepts in the framework of vertical transitions, leaving out the problems related to the modelling of the excited state potential energy surfaces (PES) outside the Franck Condon region. Nevertheless, when interested in knowing how the system evolves upon light absorption, and thus understanding the mechanism of possible emission phenomena, it is rather necessary to investigate the subsequent charge reorganization leading to the population of the emissive states. Therefore, to gain insight into emission phenomena, and furthermore to comprehend the mechanism of reactions occurring at excited states a full characterization of the excited state potential energy surfaces is required. As highlighted in Chapter 3, even though TD-DFT is the most popular theoretical approach to obtain excited electronic states of molecules, it is not recommended to fully describe the evolution of excited state potential energy surfaces, since it yields incorrect results in close proximity of conical intersection regions. The cause is to be sought in the absence of coupling between the ground state (the reference state) and the excited states (the response states) within the Linear Response formalism within these limits. In this regard, in this Chapter we outline the application of a cost-effective approach, the Δ index, that has been developed to qualitatively recognize regions of crossing between potential energy surfaces. This permits to exploit the efficiency of TD-DFT not only in the mere calculations of excited states, but even in the computational inexpensive characterization -on the fly- of the evolution of them. In particular, in Chapter 3 we emphasized that such density-based descriptor can be used to obtain a qualitative measure of the work necessary to redistribute the electron density going from one excited state to another at a given electronic configuration. Indeed, it basically

combines the information about electron density distribution coming from the D_{CT} index, together with energy criteria (ΔE) in order to detect possible non-radiative decay regions [67,68]. Intuitively, two electronic states may interconvert either if they are degenerate and/or if the electron density rearrangement is small. Besides, since the D_{CT} can be calculated by quantum methods based on both electron density and wave function, the Δ index can be coupled with any quantum approach able to provide a description of electronic excited states. Previously, it has been applied to disclose non-radiative decay channels from the ground state to the first excited states, while in this Chapter we boosted its potential in revealing crossing regions involving higher excited states with the aim to interpret the origin of the dual emission behavior of a phenanthroline derivative. This Chapter basically constitutes an adaptation of a previous article published in the Journal of Photochemistry and Photobiology A by me, Federica Maschietto and Ilaria Ciofini entitled "Following excited states in molecular systems using density-based indexes: A dual emissive system as a test case" [117].

6.2 Introduction

Dual emission in molecular systems is a phenomenon increasingly reported in the literature and attracting ever-growing interest [118–123]. Depending on the mechanism at the origin of dual emission, various classes of compounds may be identified. Indeed, widely documented is dual fluorescence occurring in small organic dyes undergoing excited state intramolecular proton transfer (ESIPT) reactions [124–126] or excited state intramolecular charge transfer processes [120,127–129]. Such dual emission phenomena have been exploited in the synthesis of various novel chemosensors with different target applications. [124,125] Dual emission through Thermally Activated Delayed Fluorescence (TADF) deserves of being explicitly mentioned. [118,119,122,123] These systems are indeed regarded as promising next-generation organic electro-luminescent materials due to their potentially high internal quantum efficiency.

Beside their relevance for applications, molecules displaying dual emission provide a perfect playground to test and validate theoretical approaches aiming to investigate the structural and electronic features of excited states yielding both to radiative [60, 130] and non-radiative [127] decay pathways. Indeed, besides molecular systems where dual emission is associated to a change in the chemical nature of the emitting specie (ex. protonation state), [124–126] native dual emission is usually associated to the presence of two emissive -bright- excited states of different character that can be both populated and that are stabilized by a differential structural reorganization.

In this respect, theoretical approaches aiming at describing this kind of phenomena are of great interest. There are at least two criteria that a method shall fulfill in order

to deliver a good understanding of photochemical processes. Firstly, it should reproduce correctly the potential energy surfaces (PES) of the excited states of interest, within and far from the Franck Condon (vertical excitation) region. Next, it should deliver a coherent picture of the photochemical process from the absorption to the emission.

Ab-initio excited state dynamic approaches can provide this type of information but are often expensive for a routine analysis. By contrast, a static investigation of the PES as the one proposed in the present Chapter may provide a simplified picture of the possible decay channels in play, delivering a realistic, yet qualitative understanding of the whole process at an affordable computational cost.

In this study we use density-based descriptors to follow the evolution of excited states along a given reaction coordinate, with the aim of proposing a strategy to rationalize the mechanism of the dual emission phenomena in Phen-PENMe₂ (Phen-PENMe₂ = 5-(4-dimethylamino-phenylene)ethynyl)-1,10-phenanthroline).

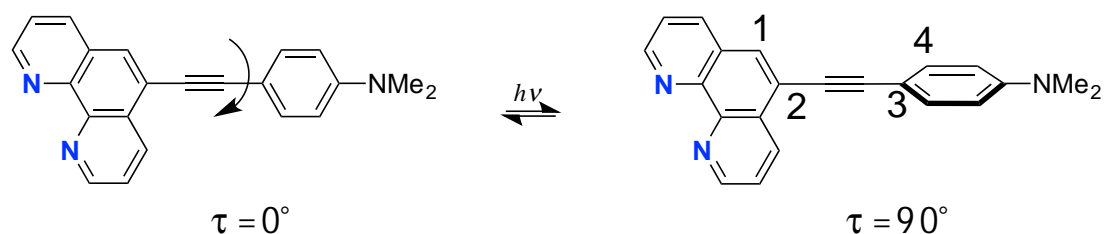
Indeed, from a theoretical point of view, a large number of studies, including our previous ones has focused on the description of the excited states using density-based descriptors to analyze the nature of the excited states responsible for the observed absorption and emission, both from a structural and energetic point of view. For a recent and complete review see for instance reference [131]. To this end, in the last years, we introduced some strategies for the description of excited states, coupling Time-Dependent density functional theory (TD-DFT) with descriptors based on electron density [55,60,61,69]. This type of indexes was primarily aiming at the diagnostic and description of excited states with a charge-transfer character, with the use of the so-called D_{CT} , [55] acronym of Distance of charge transfer and M_{AC} , acronym of Mulliken averaged configuration [66]. Recently a new index - so called Π - was also developed enabling to qualitatively identify excited-state potential energy regions where decay channels (both radiative and non-radiative) are highly expected [67,68]. Unlike previous density descriptors, the Π index provides an estimate of the probability of different electronic states to interconvert, thus allowing to map the evolution of an excited state along a reaction coordinate. Up to now, this approach has been tested to explore simple photochemical processes, such as ESIPT or to analyze the excited states PES of prototype dual emissive systems such as the 4-*N,N*-dimethylaminobenzonitrile molecule (DMABN) [68].

In the present Chapter, we apply this strategy to study the photophysical behavior of Phen-PENMe₂ here considered as a complex but experimentally well-characterized example of a single dual-emissive molecule [127,128]. To this end, we explored by the mean of the Π index, all its possible decay pathways thereby providing a deeper understanding of the electronic origins of the observed dual emissive behavior.

The Phen-PENMe₂ can be considered as a typical push-pull system thus similar to many dual emissive molecules relying on a Donor- π bridge-Acceptor structure (D- π -A), starting from the pioneering DMABN [132] system. The Phen-PENMe₂ molecule is composed of a 1,10-phenanthroline core (Scheme 1) functionalized with a dimethylaminophenyl group acting as an electron donor. Recent combined

experimental and theoretical studies performed by some of us [127,128] clarified that the observed dual emission is associated with the existence of two different emissive states: a planar Intra- Molecular Charge Transfer (ICT) state corresponding to an electronic transition from the donor moiety to the phenanthroline core, and a Locally Excited (LE) - state centered on the 1,10-phenanthroline, in which the donor and acceptor are orthogonally oriented. These earlier experimental and theoretical studies also investigated the solvent dependence of the dual emission phenomenon and highlighted the importance of the use of polar-aprotic solution to allow for the formation of both conformations, thus yielding the dual emission. If the nature of the emissive states has been disclosed, [127,128] the pathways connecting the excited states initially populated in absorption to the ones that actually emit has not yet been thoroughly analyzed. This is the question we aim to answer in this Chapter, using density-based descriptors.

The Chapter is organized as it follows. We briefly introduce the density descriptors and quantum methods applied in the Computational Methods and Details section. Later on, in the Result and Discussion section we provide the reader a general description of the excited states responsible for the peculiar photochemical behavior of Phen-PENMe₂, through a simple analysis of the energetics, and of the nature of the vertical electronic transitions. These two simple elements are very informative and deliver an approximate -yet coherent- picture of the process, though missing some crucial features. Further on, we investigate the same process using the Π index. This descriptor combines the information delivered by the energy and the D_{CT} into a more elaborate function, giving access to additional knowledge on the excited state decay pathway. As a result, we identify a number of decay channels, and rationalize, the photochemical behavior of Phen-PENMe₂ from the vertical absorption to the emission. Finally, we draw some general conclusions.



Scheme 1 Schematic structure of the Phen-PENMe₂ molecule in its planar ($\tau = 0^\circ$) and twisted conformations ($\tau = 90^\circ$).

6.3 Computational Methods and Details

In previous experimental and theoretical works [127,128] it has been showed that two structurally distinct forms, differing by the orientation of the phenyl and phenanthroline rings are responsible for the observed dual emission. The reaction coordinate connecting these two forms is the dihedral angle $C_1C_2C_3C_4$ (see Scheme 1), which we refer to as τ in the following. We performed a relaxed scan starting from the ground state - planar - optimized structure by varying τ from 0° to 90° in increments of 10° . The resulting ten geometries encompass the full transformation from the planar to the twisted (perpendicular) structure. Excited states were computed vertically on top of each structure. In line with previous works on the same system, all computations were performed at density functional theory (DFT) and TD-DFT [112] level, respectively for the ground (GS) and excited states (ES), and applying the CAM-B3LYP range-separated hybrid exchange-correlation functional, [25] in combination with the 6-311+G (d,p) basis set [87]. Of note, the CAM-B3LYP functional have proven to provide reliable ES-PES and have been specifically validated in the case of push-pull system giving rise to twisted conformations at the excited state (which is also the present case), see for instance the work of Tozer et al. [133] and Adamo et al [134]. Solvent effects (here acetonitrile) were taken into account employing the polarizable continuum model (PCM), in its conductor-like version (CPCM) [34] using a linear response (LR) scheme. An extensive literature is available on the comparison between State Specific (SS) and LR schemes for the evaluation of solvent effect on both CT and LE states see for instance ref. [135] Nonetheless the computationally less expensive LR scheme has been here applied on the basis of the results obtained in a previous benchmark, showing that the present computational protocol is able to correctly reproduce the experimental absorption and emission profiles - recorded in polar aprotic solvents for the present molecule [127,128]. All calculations were performed with the Gaussian16 software [88]. To characterize the nature and the evolution of the excited states, we computed both the D_{CT} and the Π indexes all along the reaction coordinate. A detailed description of the indexes mentioned above is provided in Chapter 3. For ease of reading, here, we briefly recall some of their features:

- the D_{CT} quantifies the length of the hole-electron separation associated with a given electronic transition and therefore provides an estimate of the spatial extent of a given electronic transition, allowing to monitor the changes in the character of the excited states, for instance Locally Excited (LE) versus Charge Transfer (CT). This index is calculated as the module of the distance between the barycenters (R^+ and R^-) of the charge density corresponding to the hole and particle distributions (Equation (3.1.24)).
- The Π index broadens the information provided by the D_{CT} , by coupling this last both with a charge displacement and an energetic term. (Equation (3.2.3)). It is correlated to the inverse of the work needed to accomplish the charge

rearrangement associated to an electronic transition from one electronic state to another. Therefore, it can be used to identify, in a qualitative manner, regions of the excited state potential energy surfaces where decay pathways are more likely to occur.

D_{CT} and Π index values have been evaluated using an in-house developed and freely available code [86]. Absorption spectra are simulated by Gaussian convolution of the computed vertical transition energies using a full width at half maximum (fwhm) value of 0.2 eV.

6.4 Results and Discussion

To investigate the photophysical behavior of the Phen-PENMe₂ molecule we have analyzed the evolution of the ground state and of the first six excited states, along the coordinate of interest (in Scheme 1). This last involves the formation of a planar and an orthogonal conformer, which differ in the orientation of phenyl and phenanthroline rings.

6.4.1 An excursion through the excited states

Ground state DFT calculations computed at each reaction step revealed a rather flat ground state potential curve. The planar structure ($\tau = 0^\circ$) is the minimum, though only by 0.04 eV (1.45 kcal/mol) lower in energy compared to the orthogonal conformation ($\tau = 90^\circ$), the maximum of the ground state curve. Excitation in the 3.5 – 4.0 eV (354 - 310 nm) energy regime, populates the first excited state (S_1). All along the reaction coordinate, the potential energy curve of S_1 (in yellow in the upper panels of Figure 1) increases monotonically, without any crossing over other excited states curves. The absorption is most efficient in the Franck-Condon region - where the oscillator strength is maximal (1.60 a.u.) - and decreases ceaselessly, down to a value of 0.0 a.u. for the twisted conformation ($\tau = 90^\circ$). Figure 2, showing the normalized Boltzmann distributions of each state, points out to similar conclusions. Indeed, the ground state appears to be equally populated at all reaction steps, while the first excited state S_1 is only accessible in the $0^\circ < \tau < 20^\circ$ region. As a remark, conventional DFT functionals tend to overestimate the strength of π - conjugation, with a consequential flattening of the ground state profile, [136] and deprecation of the GS Boltzmann population, though by using a range separated hybrid we mitigate this effect.

To identify the local or non-local character of each state, we rely on the computed D_{CT} values. [55] S_1 possesses a charge-transfer character, as indicated by the large D_{CT} values all along the reaction coordinate - ranging from 4.096 Å ($\tau = 0^\circ$) to 4.699 Å ($\tau =$

90°). Accordingly, the two main-contributing natural transition orbitals (NTO) (in Figure 1 of the Appendix) occupy two spatially different regions: the hole-orbital localizes on the dimethylaminophenyl donor fragment, while the particle sits on the phenanthroline as expected for a donor to acceptor transition. The marked CT character may also be inferred by the significant dipole moment variation computed for the S_1 - S_0 transition (≈ 12 Debye at $\tau = 0^\circ$). Consistently, the D_{CT} is indeed related to the norm of the difference in dipole moment $\Delta\mu_{ES-GS}$. [42] Irradiation at 4.0–4.2 eV (309–293 nm) allows the second excited state to be accessed (orange curve in upper-left image in Figure 1). The energy profile of S_2 increases in energy until it reaches its maximum and approaches the third excited state at about $\tau = 80^\circ$. At this point, we have the choice to analyze the energy profiles either according to their placement relative to the ground state curve or according to the nature of each excited state.

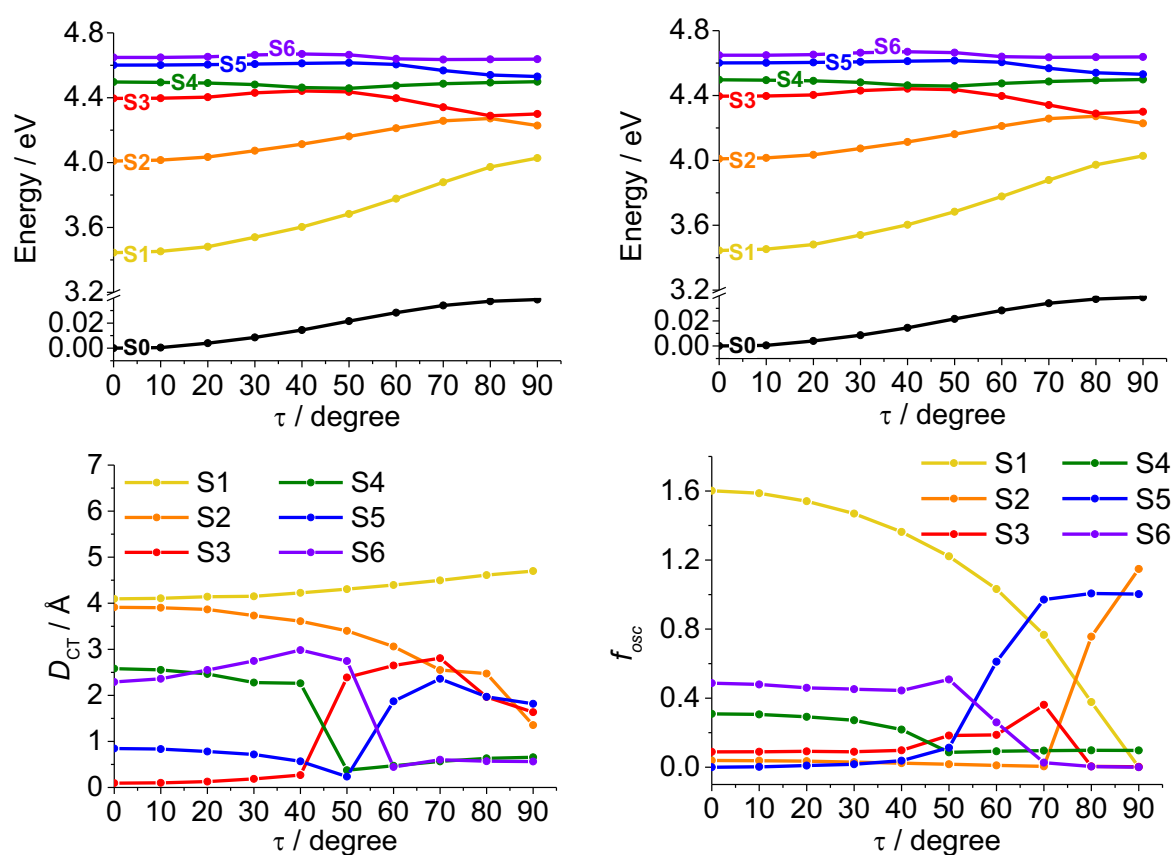


Figure 1 Upper panels: Ground (S_0) and first excited states (S_1 - S_6) computed energy profiles (in eV) along the τ torsional degree of freedom. Upper-left panel: the excited state labels follow the energy indexing at $\tau = 0^\circ$; upper-right panel: the excited state labels are assigned according to their nature at $\tau = 0^\circ$. Lower panels: computed D_{CT} (in Å) and oscillator strength (f_{osc} in a.u.) associated to each excited state, labelled according to the energy.

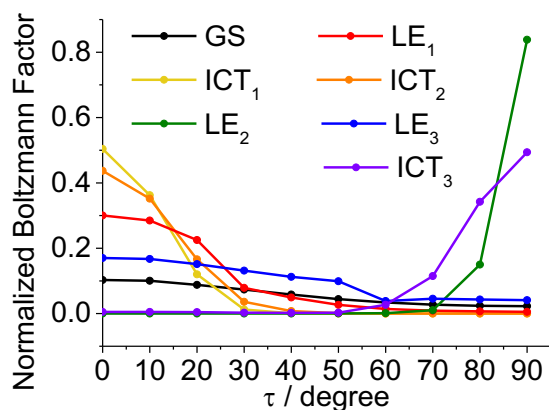


Figure 2 Computed normalized Boltzmann factors for the ground state and first six excited states (labelled as a function of their nature, Figure 1 upper-right panel) as a function of τ dihedral angle. Each curve is normalized w.r.t. its maximum value.

This duple representation (shown in the upper left and right panels of Figure 1), turns out to be a handful approach, precisely to follow the evolution of the excited states, condensing the information provided by different observables - energy D_{CT} , and oscillator strength (f_{osc}) - in a unique picture. The Boltzmann population curves (Figure 2) are also labeled according to the nature of the states. The D_{CT} profile computed for S_2 ranges from 3.913 Å at $\tau = 0^\circ$ to 1.355 at $\tau = 90^\circ$, denoting a change in nature from a charge-transfer state to a locally excited one. Accordingly, the $\Delta\mu_{ES-GS}$ decreases by one order of magnitude, converging towards the ground state value (10 Debye at $\tau = 90^\circ$). Besides, S_2 changes from a dark state at $\tau = 0^\circ$ ($f_{osc} = 0.039$) to a bright state at $\tau = 90^\circ$ ($f_{osc} = 1.148$). S_3 (red curve in the upper-right panel of Figure 1) is only accessed irradiating at energies higher than 4.4 eV (289 nm). Also, this excited state approaches both S_4 and S_2 at $\tau \approx 30^\circ$ and $\tau \approx 80^\circ$ respectively. According to Figure 2, the population of S_3 (LE_1), decreases considerably, going from 0° to 90° , while the opposite occurs for S_4 . As a result, one may infer that a crossing involving S_4 and S_3 occurs around $\tau = 30^\circ$ - 40° . This inversion also appears in the D_{CT} profiles, where the S_4 and S_3 curves cross, pointing out a change in nature of the two states. In the $\tau=0^\circ$ to $\tau=40^\circ$ window, S_4 has a marked CT character, which translates in D_{CT} values ranging from 2.581 to 2.262 Å. S_3 , on the other hand, exhibits small D_{CT} values, synonymous of a localized transition (0.1-0.2 Å). At $\tau \approx 50^\circ$, the picture is inverted. Here, the fourth excited state localizes on the dimethylaminophenyl fragment - the D_{CT} value drops to 0.374 Å, while S_3 takes over the CT character (2.388 Å). At this stage, S_4 remains unvaried till the completion of the twist, while S_3 approaches S_2 close to $\tau \approx 80^\circ$. The CT length decreases for both S_2 and S_3 states to ≈ 1.5 Å for the fully twisted conformation. As we will discuss later on, the S_4 - S_3 inversion is the critical step to access the dual emission.

The photochemical pathway outlined results in the population of the S_4 state. In summary, S_3 acts as a bridge between S_4 - a bright CT state in the FC region - and S_2 , a LE state - initially dark, and turning into a bright state around 80° . The NTOs, available in Figure 1 of the Appendix, render an orbital picture of the changes in nature of the corresponding electronic transitions.

Finally, the higher excited states, S_5 and S_6 , require respectively excitation energies of 4.60 eV (269 nm) and 4.65 eV (267 nm) to be populated. The corresponding D_{CT} curves cross around $\tau = 55^\circ$, suggesting an inversion in their character. S_5 approaches then the trajectory of S_4 at $\tau \approx 90^\circ$. The latter, though, lies ≈ 0.2 eV above S_3 , limiting the mixing with the lower lying states. S_6 (ICT_4), however, appears to be populated between 50° and 90° , suggesting that it may contribute to feeding a non-radiative channel transferring its population to the lower states. It is worth recalling that, due to the very low energetic barrier, at the GS the molecule is able to freely rotate, hence all conformations are accessed. Irradiating the molecule at low energies limits the access to the excited state levels to the sole S_1 . This, in turn, prevents the twisting and with it the formation of the LE state, thereby leading to a single emission from the planar ICT_1 (S_1). By contrast, exciting with sufficient energy, all excited states may be reached, leading to a multitude of decay pathways.

6.4.2 Simulation of the observed absorption spectrum

Before analyzing in detail the decay pathways, it is useful to comment on the absorption properties of Phen-PENMe₂, as such analysis will later be helpful to disclose the mechanism leading to the dual emission.

The simulated absorption spectrum at each internal conversion coordinate (in Figure 3) reflects the vanishing of the ICT_1 state and rising of the LE state as the molecule twists. In the planar conformation ($\tau = 0^\circ$), the absorption is dominated by a single transition at 355 nm (3.49 eV). The resulting broad absorption band is ascribed to the lowest excited state, S_1 (ICT_1), of CT character. The band at 270 nm (4.59 eV) arises from two higher ICT states - S_4 and S_6 - and, to a smaller extent, from an LE state of $n-\pi^*$ character (S_3). Despite the low oscillator strength of the states involved - they are not exceeding 0.5 a.u. at 0° - the band appears intense, as the three states involved (S_3 , S_4 , and S_6) are relatively close in energy. At $\tau = 90^\circ$, the absorption spectrum consists of a single band at 296 nm (4.19 eV) - with a shoulder at higher energy (276 nm / 4.49 eV). This band is ascribed to transitions involving two states: a LE state (S_2) of $\pi-\pi^*$ character centered on the 1,10-phenathroline fragment and an ICT state (S_5).

The absorption spectra computed at intermediate values of τ smoothly connect these two limiting pictures. The lowest energy band blue-shifts as the molecule twists and disappears entirely at $\tau \sim 90^\circ$. At the same time, the highest energy band rises, while increasingly red shifting. Considering the ground state PES of Phen-PENMe₂ computed in acetonitrile we can estimate that the molecule freely twists so that each conformation can contribute to the absorption.

Therefore, it is convenient to estimate an average absorption by pondering each of the spectra - calculated at different values of τ - using their corresponding GS Boltzmann weights. The outcome is shown in Figure 4. The band around 350 nm (3.54 eV) is the result of the ICT_1 (S_0 to S_1) transition. The highest energy band at 265–295 nm (4.68–4.20 eV) arises from the convolution of mainly two different states, whose contribution is highlighted with a blue background in the simplified Jablonski diagram reported

on the right hand of Figure 4. The transitions lying between 280 and 295 nm (4.43 and 4.20 eV) correspond to the evolution of the ICT₃ state, stemming from the S₀-S₄ transition in the 0° < τ < 40° window. The same state is then populated by S₀-S₃ transition at dihedral values between 40° and 70°, and by S₀-S₂ transition at 70° < τ < 90°. Slightly higher in energy, at 280–270 nm (4.43–4.59 eV) the S₀-S₄ (0° < τ < 60°) and S₀-S₅ transition (60° < τ < 90°) sum up with the other closely lying transitions to contribute to the second band.

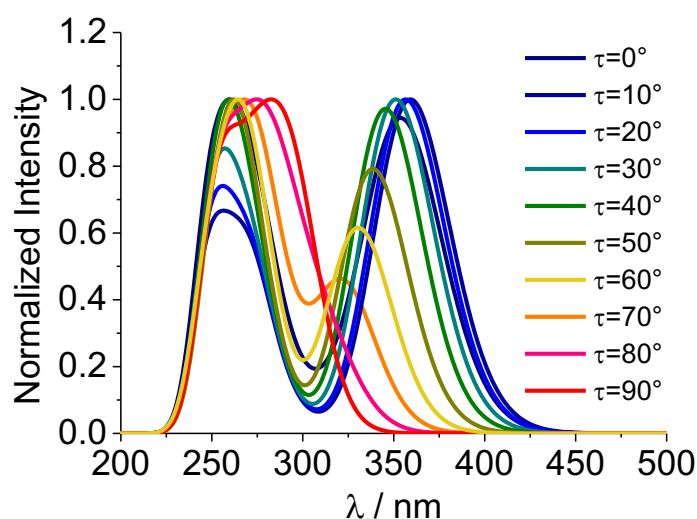


Figure 3 Absorption spectrum of Phen-PENMe₂ at fixed dihedral angles, ranging from 0° to 90° simulated by Gaussian convolution of the computed vertical transition energies using a fwhm value of 0.2 eV. The color-coding highlights the raising and vanishing of the LE and ICT₁, respectively.

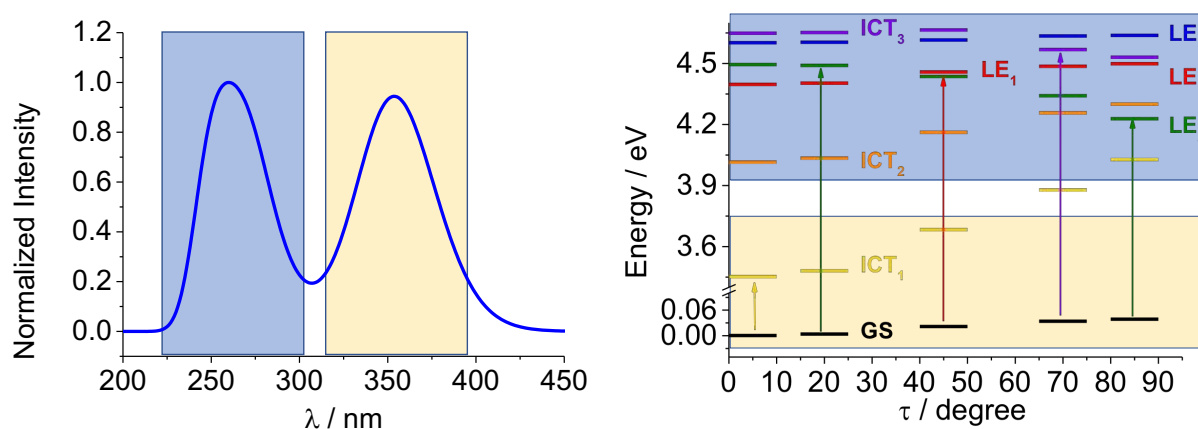


Figure 4 Left: Boltzmann weighted simulated absorption spectra of Phen-PENMe₂ Right: Jablonski diagram describing the absorption phenomena occurring in the Phen-PENMe₂ molecule.

6.4.3 Interpretation of the dual emission through the Π index

Up to now, we have used a combination of several observables, each bearing a different physical meaning, to sketch a map of the excited state pathways from the absorption region to the emitting one. Also, we have postulated the existence of several decay channels. However, to reach the correct interpretation, it is essential to assess the relative importance of each. To answer this question, the Π index is here used. It is important to mention though that the methodology we are about to discuss is based on static considerations. Therefore, it does not give any indication on the timescale of the photochemical process. As a result, any consideration on the kinetics of the electronic process remains out of our scope.

As previously mentioned, the Π index combines energetic arguments - ΔE - and a measure for charge rearrangement - $D_{CT} \cdot q_{CT}$ - and can be used as criteria to detect the presence of non-radiative decay channels. It is useful to compare the relative value of the Π index between electronic transitions that involve a common electronic state. This approach provides a reasonable estimate of the relative likelihood of the existence of a decay channel, connecting more efficiently an electronic state with one or another state, lower in energy. Intuitively, this information shall be coupled with the vertical absorption, in order to map the excited states all through the pathway that brings to the emission. As for this aspect, a radiative relaxation yielding an emission from any excited state S_n necessarily implies that this particular state of interest is populated either directly, by irradiation, or by decay from an energetically higher excited state. The Π index, combined with the absorption data, provides precisely this information, thereby allowing to estimate the relative efficiency of the relaxation pathways connecting any two states all along a reaction coordinate. The result is a qualitative strategy, which delivers a consonant interpretation of a photochemical process, in an uncomplicated manner. Besides, the Π index is also computationally inexpensive, which is often not the case when one uses alternative approaches to deal with such questions. Undoubtedly, the global understanding of the physical phenomena will strongly depend on the quality of the ground, and excited states computed PES and thus will be affected by the level of theory (method and basis set) used to calculate densities and energies. This said, the level of theory which we have used to perform our calculations was chosen based on the result of a previous benchmark, which proved to give a good agreement with experimental data, both for absorption and emission. More details are provided in Computational Methods and Details paragraph. The Π index curves - in logarithmic scale - are reported in Figure 5 (left panel). We recall that high values of the Π index correlate with a high probability of interconversion from a state to another. Two regions of decay result unequivocally. The first is the S_4 to S_3 decay, appearing around $\tau=40^\circ$ in the solid olive-green curve. The second connects S_3 and S_2 and is indicated by the marked increment of the Π index associated with the S_3 - S_2 transition between $\tau = 60^\circ$ and $\tau=90^\circ$. These two curves allow identifying a leading non-radiative decay channel connecting S_4 to S_2 via S_3 . This decay pathway is essentially energy-driven, *i.e.* it is promoted by the energy nearness of the

three states, at specific reaction coordinates. This channel corresponds to the S_4 -to- S_2 decay pathway that we had anticipated earlier through the energetic analysis (refer to Figure 2 and related discussion).

The case of those decay channels that are governed by the product $D_{CT} \cdot q_{CT}$ is subtler. The analysis of Figure 5 suggests the existence of two further decay and emission channels at $\tau = 0^\circ$ and $\tau = 90^\circ$.

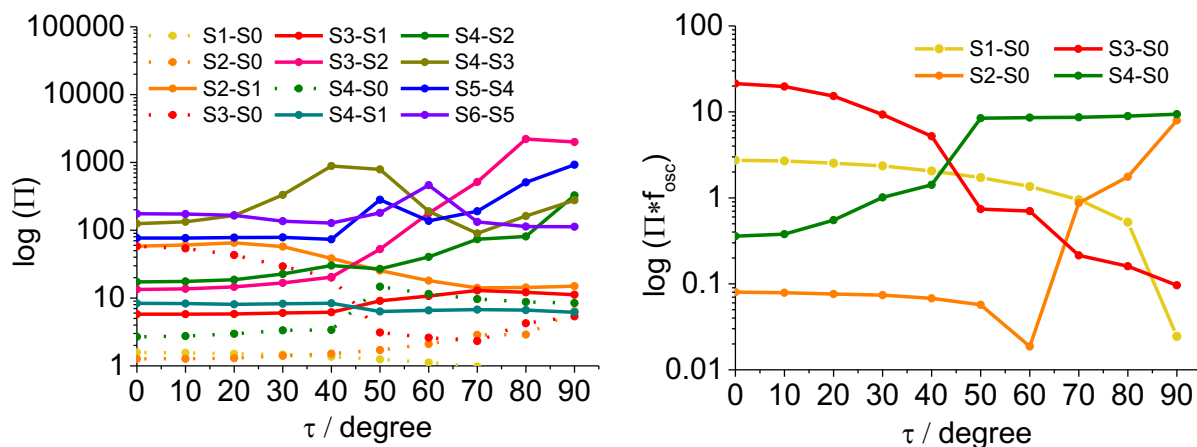


Figure 5 Left: Evolution of Π index (in logarithm scale) along the reaction coordinated (the dihedral angle τ). (Right) The evolution of Π weighted by the oscillator strength (in logarithm scale).

In the right panel of Figure 5, we collected the Π curves relative to the S_n - S_0 transitions, weighted by their corresponding oscillator strength. As the oscillator strength is directly proportional to the transition probability, weighted- Π values provide a better estimate of the existing emission channels.

The largest weighted- Π value appears at $\tau = 0^\circ$ and is associated with the S_3 - S_0 transition (see right side of Figure 5), followed, in the same region by the S_1 - S_0 transition. The observed shapes of the S_3 - S_0 and S_1 - S_0 curves suggest that the LE (π - π^*) state, corresponding to S_3 , together with the ICT₁ state (S_1) are likely to be primarily responsible for the emission in the Franck-Condon region. Additionally, the computed Π profiles point out an efficient interconversion between S_2 - S_1 (solid orange curve) and a non-negligible interconversion between S_3 - S_2 (solid red curve) that transfer the electronic population to the lowest excited state. We conclude that the ICT₁ emission is compliant with Kasha's rule. Although both S_3 and S_1 may be populated upon absorption, only the S_1 emits, and the S_3 - S_2 and S_2 - S_1 non-radiative decays enhance this emission channel. These outcomes agree with the experimental data substantiating the existence of an efficient ICT₁ radiative channel [127,128]. The vertical deactivation pathway transferring the electronic population from S_4 to S_1 (through the S_3 - S_2 - S_1 decay channels) and leading to the ICT₁ emission, is poorly efficient compared to the relaxation pathway activated by the torsion. As anticipated earlier in the discussion, if the molecule is irradiated with sufficiently high energy one

activates the structural relaxation, which in turn results in populating (LE) S_2 state at 90° . The pathway involves the conversion between state S_4 to state S_3 (at around 50°) followed by the conversion of S_3 to S_2 at $t \sim 80^\circ$. Furthermore, as the twist approaches 90° , two channels establish, which transfer the electronic population from S_4 to S_2 . By contrast, the oscillator strength of S_4 (0.09 a.u. in the twisted region) is connotative of a poor absorption, suggesting that the existence of an emissive path from S_4 is conditioned to the presence of a higher excited state, transferring its population to S_4 through a non-radiative channel. The steep increase of the Π index associated with the S_5 to S_4 decay at $\tau = 90^\circ$ validates this hypothesis. Similar reasoning holds for S_5 , whose population is maintained by S_6 , which absorbs at 0° and approaches S_5 at 60° .

Close to $\tau = 90^\circ$, all Π curves, except that computed for the S_3 - S_1 , S_2 - S_1 and the S_1 - S_0 interconversion visibly rise. This increase again points out the formation of several interconnected decay sub-channels (S_4 - S_3 , S_4 - S_2 , S_3 - S_2 ,) enhancing the transfer of population from S_4 to S_2 . Once more, these sub-channels are not necessarily driven by the energy gap, which ranges between 0.01 a.u. for S_4 - S_2 and 0.003 a.u. (0.08 eV), for S_3 - S_2 . As such, the formation of these channels is supported by the similar distributions of the electronic densities of the states involved, as witnessed by the small $D_{CT} \cdot q_{CT}$ values - computed Π values are reported in Table 3 of the Appendix. Remarkably, the drop in the S_1 - S_0 weighted- Π curve suggests the absence of the emission from S_1 (ICT_1) at 90° . Indeed, the orthogonality of the donor (dimethylaminophenyl) and acceptor (1,10-Phenanthroline) moieties hinders the formation of the ICT_1 state. As a consequence, the lowest emitting state at $\tau = 90^\circ$ is S_2 (LE).

In light of the discussion above, the dual emission mechanism observed in Phen-PENMe₂ can be summarized by the Jablonski diagram shown in Figure 6.

The population of the S_1 - ICT_1 planar state in the FC region - leads to the ICT_1 emission experimentally observed at 560 nm [127]. Moreover, irradiation at a higher excitation wavelength allows reaching S_4 . From S_4 a decay channel can open, leading to the population of S_2 , a π - π^* state of local character (LE). The relaxation through the vibrational sublevels of S_2 causes the observed fluorescence band observed at 421 nm in the experimental spectrum [127].

The S_4 - S_0 curve suggests the existence of a further radiative decay at $\tau = 90^\circ$. This channel is connected to S_6 - in the planar conformation. However, further internal deactivation channels between S_4 - S_3 and S_3 - S_2 can intervene, reducing the decay from S_4 and resulting in an enhanced S_2 - S_0 emission. Similarly, S_3 - S_1 and S_3 - S_2 curves hint to the existence of two non-radiative channels which, in the planar conformation, contribute to impoverish the S_3 - S_0 channel. All of the observable evidence leads to the conclusion that the emission from LE violates Kasha's rule. To explain this unusual behavior, it is instructive to examine the energy, and $D_{CT} \cdot q_{CT}$ values of the S_2 - S_1 transition, at $\tau=0^\circ$ and $\tau=90^\circ$. At $\tau=0^\circ$ ΔE equals 0.021 a.u. (0.57 eV). The $D_{CT} \cdot q_{CT}$ product is small (0.83 a.u.), which reflects a high similarity in the character of the two states. On the other hand, at 90° , while the energy gap shrinks to 0.007 a.u., $D_{CT} \cdot q_{CT}$ increases by one order of magnitude (9.07 a.u.). Although S_1 and S_2 are closer in energy at 90° than at 0° , the computed Π index is higher at 0° , reinforcing the hypothesis that

a decay channel transfers the population from S_2 to S_1 at 0° , but not at 90° , allowing S_2 to emit radiatively.

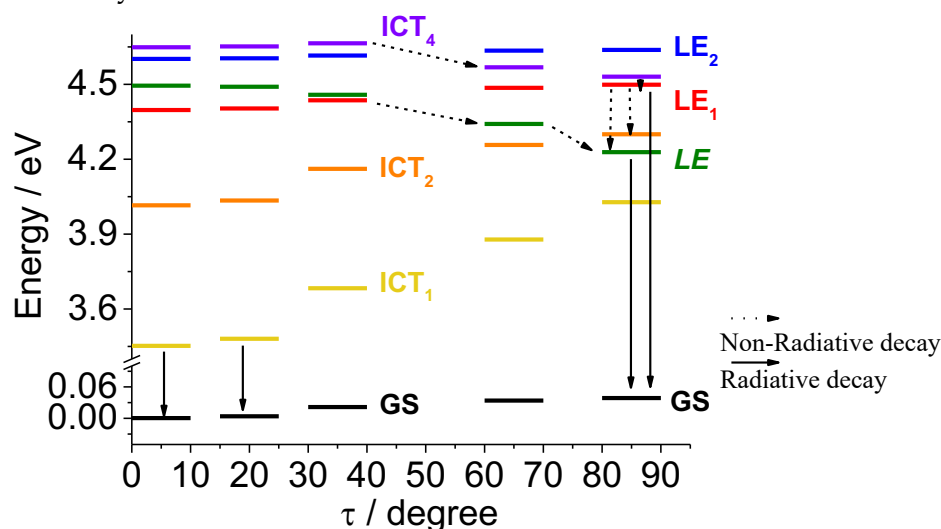


Figure 6 Jablonski Diagram describing the anti-Kasha dual emission of Phen-PENMe₂ molecule.

6.5 Conclusions

In summary, we have applied the index Π to unravel the excited state decay pathway of the Phen-PENMe₂ molecule. We have postulated the existence of different radiative and non-radiative decay pathways, related to structural reorganization occurring at the excited state, which bring to the formation of the observed dual emission.

Two factors are crucial when the interconversion between states is concerned. The closer in energy are the two states, the higher the likelihood that the interconversion occurs. On the other hand, the more similar the electronic densities of the two states, the higher the possibility of decay. The Π index includes both criteria in a single definition. The energy proximity of the two states is evaluated as the energy difference between two states, while the similarity between their electron densities is recovered through the product $q_{CT} \cdot D_{CT}$ - equivalent to the norm of the difference between their dipole moments.

Using the index Π , we could estimate the relative probabilities of different radiative and non-radiative channels and infer a coherent picture of the decay pathways of the states involved in this photochemical process.

In particular, we have individuated:

- two main radiative channels, which lead to the formation of two structurally different emissive species, a planar and a 90° twisted one. These findings also agree with the outcomes of previous works [127,128].
- the anti-Kasha mechanism of the LE emission.

- several sub-channels that play an essential role, enhancing either of the two emissions.

To conclude, the analysis that we have carried out shows the capability of the Π index to draw a qualitative map of a photochemical reaction. Although we have focused on one particular system, such analysis could be performed in a similar fashion to unveil the mechanism of other photochemical reactions of interest. Finally, in a more general perspective the present computational strategy may be particularly interesting for the rational design of substituted Phen-PENMe₂ derivatives with a targeted dual emission.

Chapter 7

Understanding the mechanism of a reaction by the use of density-based indexes

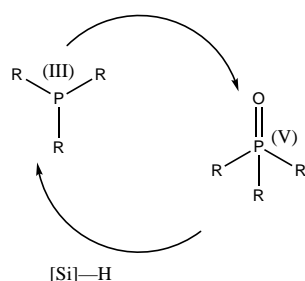
7.1 Context

In the previous Chapters we have widely discussed about density-based indexes, which have been developed, on one side, with the aim to treat the density functionals drawbacks, and on the other side to fully exploring excited states potential energy surfaces, thus giving a better description of photoinduced phenomena. Such theoretical descriptors actually provide information about important physical properties by translating computational results into simple chemical and physical concepts. As a matter of fact, up to now they have been applied to measure the charge-transfer extent upon light absorption and to effectively define the most important photophysical pathways occurring simultaneously at excited state, such as electronic reorganization, radiative and non-radiative decay. A logical step forward is the integration of these tools into a unique protocol with the aim to deal with a computationally inexpensive study of photoinduced phenomena involving more than a single molecule. In this Chapter we will present a synthetic and mechanistic study of a metal-free reaction occurring at excited state, particularly developed for the selective photodeoxygenation of amine *N*-oxides. In the following, a complete and exhaustive computational analysis based on DFT and TD-DFT, together with density-based descriptors has been combined with an experimental study in order to gain insight into the reaction mechanism. This represents actually a clear example of how inexpensive density-based descriptors, in particular the D_{CT} , [55] the $\Delta\epsilon$ [67,68] and the M_{AC} [66] introduced in Chapter 3, can easily and efficiently applied, for example, to support and guide experimentalists in their research about the conception of innovative and more sustainable metal-free reactions. The combined theoretical and experimental study that will follow is an adaptation of a publication by me, Sami Lakhdar, William Lecroq, Jules Schleinitz, Mallaury Billoue, Jacques Lalevée, Annie-Claude Gaumont, Ilaria Ciofini and Laurence Grimaud submitted to *Angewandte Chemie Journal* entitled "Photo-organocatalytic Deoxygenation of Heteroaromatic

N-Oxides: Synthetic and Mechanistic Studies”, and of another publication which is still in preparation [137].

7.2 Introduction

Trivalent organophosphorus compounds such as phosphanes find widespread use throughout numerous fields of synthetic chemistry. Indeed, apart from their use as ligands in transition metal catalysis or as organocatalysts, they have been widely employed as stoichiometric reagents in various synthetic transformations such as Wittig, Appel, Staudinger or Mitsunobu reactions, to name a few [138]. The driving force for all these transformations is the formation of high molecular weight phosphine oxide as a byproduct, which poses separation and waste disposal problem. Thus, the development of catalytic variants of these reactions in organophosphorus reagent and utilizing alternative feedstocks is highly important [139]. In this context, the use of silanes as reducing agents of phosphine oxides (Scheme 1) has appeared as an efficient solution enabling the development of numerous interesting phosphane-catalyzed processes [140]. Remarkably, in these polar reactions, the silane reacts selectively with phosphine oxide and not with other reagents present in the media [141].

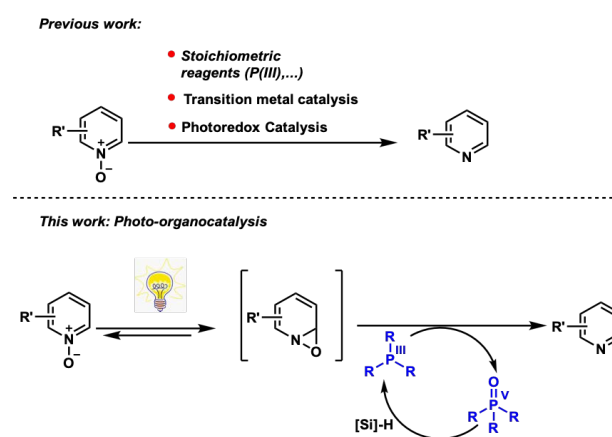


Scheme 1 Redox cycle P(III) \leftrightarrow P(V) in presence of silane as reducing agent.

While the P(III) \leftrightarrow P(V) redox cycling approach has been frequently used in polar organic reactions, it has, to the best of our knowledge, never been applied to photoinduced processes, where phosphanes are still used in stoichiometric amounts [142]. This could be explained by the fact that radicals generated under photoinduced conditions can react with silanes through hydrogen atom transfer of Si-H bonds, thus preventing the reduction of phosphine oxide to regenerate the phosphane. However, as many photochemical processes are known to involve electronically neutral transient intermediates, we reasoned that P(III) \leftrightarrow P(V) redox cycling might be applicable for those reactions.

In this context, the deoxygenation of heteroaromatic *N*-oxides [143] (Scheme 2) has captured our attention because of:

- i) its great importance in various area going from synthesis to catalysis [144] and biology; [145]
- ii) the non-catalyzed version requires a large amount of phosphane and proceeds at high temperature; [146]
- iii) previous physical organic studies postulated the formation of oxaziridine intermediate upon excitation of heteroaromatic *N*-oxides with light [147].



Scheme 2 Deoxygenation of heteroaromatic *N*-oxides.

The highly reactive oxaziridine intermediate should react fast with phosphane to give the heteroaromatic compound along with phosphine oxide. Based on this assumption and considering that phosphanes are more nucleophilic than silanes, [148,149] we supposed the silane would reduce the *in situ* generated phosphine oxide rather than reacting with the oxaziridine (Scheme 2). To test this hypothesis and thus gain insight into the reaction mechanism we conducted a combined experimental and computational study. The Chapter is organized as it follows. We briefly introduce the quantum methods and the density descriptors applied in the Computational Methods and Details section. Later on, in the Result and Discussion section we will present before some interesting experimental results starting from which we later conducted the computational study. In particular, through TD-DFT calculations and a simple analysis of the density-based indexes, we compared the experimental data and validated outcomes concerning the hypothesized reaction mechanism. Finally, we draw some general results.

7.3 Computational Methods and Details

Combined experimental and computational studies enabled a deep understanding of factors controlling the deoxygenation reaction of heteroaromatic and aliphatic *N*-oxides. In order to calculate ground state (GS) and excited states (ES) we performed calculations at Density Functional Theory (DFT) and Time dependent - DFT (TD-DFT) level [95,112]. Structural optimizations at GS and ES were performed using a 6-31+G(d) all electron basis set for all atoms [87]. Solvent effects (here acetonitrile) have been included using an implicit solvent model, the polarizable continuum model (PCM) in its conductor-like version (CPCM) [34]. All calculations were performed with the Gaussian16 software [88].

As concern the modeling to explain aliphatic *N*-oxides, we optimized the interested structures and by means of harmonic vibrational frequencies analysis we confirmed the nature of all stationary points (minima and first order transition states). The free energies along the reaction coordinate of Figure 11 in the Results and Discussion section have been computed referring to a zero-energy value assigned to the sum of the isolated species energies, *i.e.* pyridine *N*-oxide (**1a**), phenyl silane and *N,N* dimethylaniline *N*-oxide (**4a**).

Regarding the modeling of the photodeoxygenation of heteroaromatic *N*-oxides, we at first simulated absorption spectra by Gaussian convolution of the computed vertical transition energies using a full width at half maximum (fwhm) value of 0.2 eV. To be sure that we did not take into account unphysical low-lying excited state we computed the M_{AC} index [66] for all analyzed excited state. On the other hand, to characterize the nature and the evolution of the excited states, we computed both the D_{CT} [55] and the Π indexes [67,68] all along the reaction coordinate. A detailed description of the indexes mentioned above is provided in Chapter 3. For ease of reading, here, we briefly recall some of their features:

- The M_{AC} index is able to harvest unphysical low-lying excited states of charge transfer (CT) character, known as “ghost-states”. Computationally inexpensive this index is derived as a modification of the Mulliken estimation of transition energy for CT excitations (Equation 3.2.2) and comparing it with the corresponding TD-DFT computed excitation energies, it is possible to detect proper or ghost transitions.
- the D_{CT} quantifies the length of the hole-electron separation associated with a given electronic transition and therefore provides an estimate of the spatial extent of a given electronic transition, allowing to monitor the changes in the character of the excited states, for instance Locally Excited (LE) versus Charge Transfer (CT). This index is calculated as the module of the distance between

the barycenters (R^+ and R^-) of the charge density corresponding to the hole and particle distributions (Equation 3.1.24).

- The Π index broadens the information provided by the D_{CT} , by coupling this last both with a charge displacement and an energetic term. (Equation 3.2.3). It is correlated to the inverse of the work needed to accomplish the charge rearrangement associated to an electronic transition from one electronic state to another. Therefore, it can be used to identify, in a qualitative manner, regions of the excited state potential energy surfaces where decay pathways are more likely to occur.

M_{AC} , D_{CT} and Π index values have been evaluated using an in-house developed and freely available code [86].

Marcus theory and used notation

The estimation of the single electron transfer (SET) activation energy was performed following a simplified version of Marcus theory [150]. Assuming that the diffusion step of reactants, before and after the reaction, can be neglected, and moreover, the energy surfaces of reactants and products can be represented as parabolas with the same curvature, we obtain the following formula:

$$\Delta E^\ddagger = \frac{1}{4\lambda}(\lambda + \Delta E^\circ)^2 \quad (7.3.1)$$

Here, ΔE° corresponds to the reaction energy, while λ parameter quantifies the reorganization energy of molecules and solvent due to the charge transfer. The λ parameter can be defined as the average of the intrinsic reorganization energies of the two molecules involved in the reaction:

$$\lambda = \frac{1}{2}(\lambda_a + \lambda_b) \quad (7.3.2)$$

The intrinsic reorganization energies can be expressed as follows:

$$\lambda_i = [E_c(R_n) - E_n(R_n)] + [E_n(R_c) - E_c(R_c)] \quad (7.3.3)$$

$E_n(R_n)$ and $E_c(R_c)$ were obtained from the geometry optimizations performed on the neutral and charged species respectively, using the above mentioned PCM method to take into account the solvent effect implicitly. Meanwhile, $E_c(R_n)$ and $E_n(R_c)$ correspond to the energies of the charged and neutral species at the minimum energy geometries of the neutral and charged species respectively. In Figure 1 a schematic representation of this approach is depicted. These energies were calculated using the State Specific Approach available in the Gaussian software [88].

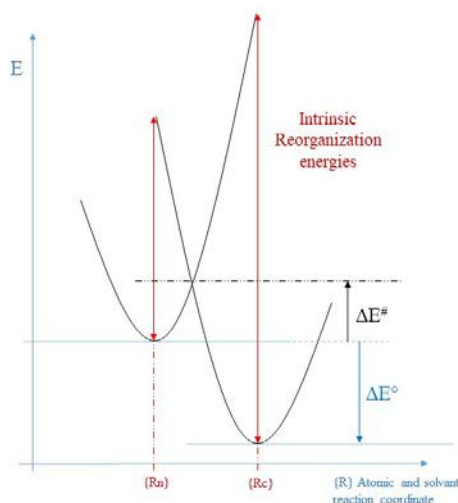


Figure 1 Classical Marcus model of the energy surfaces of the reactants (left parabola) and the products (right parabola) along a reaction coordinate. The activation and reaction energies (respectively ΔE^\ddagger and ΔE°) along with the intrinsic reorganization energies are evidenced on the figure. The intrinsic reorganization parameter λ_i corresponds to the sum of the two red arrows.

Normally, during excited state calculations, the solvent may respond in different ways to changes in the state of solute:

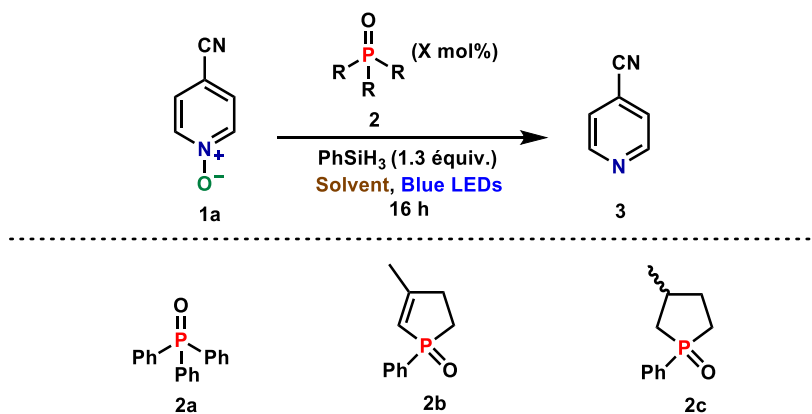
- ◆ It polarizes its electron distribution (a rapid process);
- ◆ The solvent molecules reorient themselves (a slower process).

Vertical electronic excitations are non-equilibrium calculations, too rapid for the solvent to have time to fully reorient towards the solute. Therefore, in our case it is necessary a further non-equilibrium external iteration calculation to store the information about non-equilibrium solvation at ground state and use it to calculate the energy of the charged (reduced or oxidized) products at the minimum energy geometries of the neutral and charged species, *i.e.* $E_c(R_n)$ and $E_n(R_c)$.

7.4 Results and Discussion

7.4.1 Experimental results

To test the hypothesis that $P(\text{III}) \leftrightarrow P(\text{V})$ redox cycling is compatible with light in order to drive efficient and practically simple deoxygenation of a variety of heteroatomic *N*-oxides, we investigated the deoxygenation of 4-cyano pyridine *N*-oxide (**1a** in Scheme 3), in the presence of a catalytic amount of different phosphine oxides (**2a**, **2b**, **2c** in Scheme 3) and phenylsilane (PhSiH_3) as a reducing agent.



Scheme 3 Deoxygenation of 4-cyano pyridine *N*-oxide (**1a**) in presence of different phosphine oxides (**2a**, **2b**, **2c**) and phenylsilane leading to 4-cyano pyridine (**3a**).

In order to find the best reaction condition, several solvents have been employed as acetonitrile, toluene and DMF under blue light irradiation. After the screening, interestingly the commercially available 3-methyl-1-phenyl-phospholane oxide **2b** in acetonitrile, in presence of phenylsilane and Blue LED resulted to be essential for the deoxygenation reaction as no conversion has been observed in their absence. Once optimized the reaction conditions (solvent, catalyst amount, wavelength irradiation etc.), the reaction has been performed with different *N*-oxide derivatives (**1** in Figure 2).

As shown in Figure 2, the reaction proceeds well with pyridine *N*-oxides *para*-substituted with either electron-withdrawing (**3a-d**) or electron-donating (**3e-h**) groups in good to excellent yields. Pyridine *N*-oxides bearing substituents in *meta* position (**3i-k**) or *ortho*- (**3l-p**) positions can be smoothly deoxygenated under the optimized conditions. Notably, different functional groups CF₃ (**3c**, 93%), CO₂Et (**3d**, 82%), CH₂OH (**3h**, 57%), CN (**3j**, 94%) and chloride (**3l**, 71%) on the aromatic rings were well tolerated. Similarly, a large variety of quinoline oxides, bearing different electronic substituents on the aromatic and/or heteroaromatic rings (**3q-3z**), performed well under the optimized reaction conditions, affording the corresponding reduced heterocycles in good to excellent yields (69–91%). 5,6,7,8-tetrahydroquinoline *N*-oxide can also be deoxygenated and the corresponding heteroaromatic **3za** was obtained in modest yield (54%). By contrast, acridine *N*-oxides (**3zb-3zc**) were unreactive under the optimized conditions. More importantly, when starting with a bis-*N*-oxide, bearing both a quinoline and pyridine *N*-oxides, only the former is deoxygenated under our photochemical conditions affording **3zd** in 64% yield. It should be noted that a similar chemoselective approach has recently been reported by Kim and Lee, where [Ru(bpy)₃]-Cl₂·6H₂O was used as a photocatalyst in the presence of excess of hydrazine hydrate, which acts as reductive quencher and hydrogen source (**6g**).

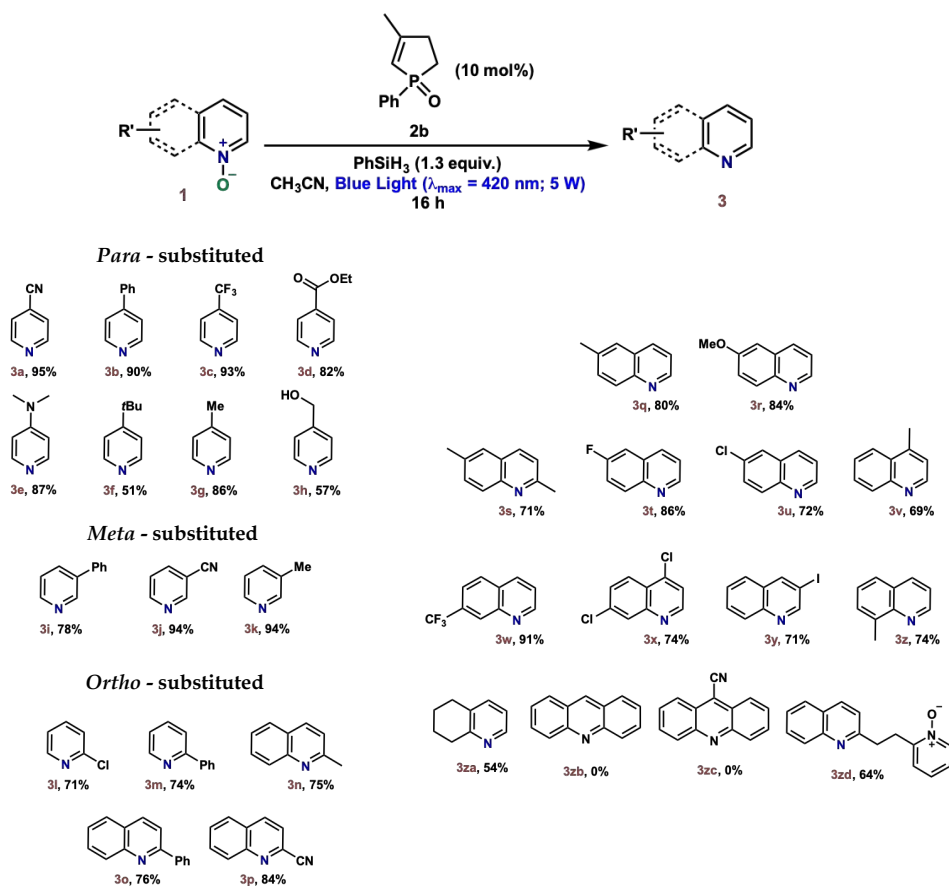


Figure 2 Scope of the photochemical deoxygenation of heteroaromatic N-oxides. Reaction conditions: **1** (0.5 mmol, 1 equiv.), phenylsilane (0.65 mmol, 1.3 equiv.), **2b** (10 mol %), acetonitrile (5 mL), Blue LEDs (5 W), 16h.

Moreover, to evaluate the general applicability of our photorganocatalytic approach, we investigated the deoxygenation of aliphatic amine N-oxides, like dialkylarylamine N-oxides depicted in Figure 3. Since these derivatives do not exhibit absorbance in the visible range, we hypothesized that the use of white light irradiation might be suitable for the deoxygenation reaction.

When optimizing the deoxygenation of *N,N*-dimethylaniline N-oxide (**4a**), we were surprised to find that the reaction takes place smoothly in the absence of both light and organocatalyst (**2b**). By combining various aniline N-oxides and phenylsilane (1.3 equiv.) in acetonitrile the corresponding anilines (**5a-5g**) can be obtained within 10 min in very good yields (82–92%). Equally important, the deoxygenation of a series of *N*-benzylpyrrolidine N-oxides, bearing electron-rich and withdrawing substituents on the aromatic rings, works smoothly, delivering the amines (**5h-5l**) in yields ranging from 59 to 87%. The deoxygenation of Rhodamine B N-oxide can easily be performed under the optimized conditions to yield the fluorescent dye **5m** in good yield (83%). It is noteworthy mentioning that this cleaving bond reaction is now used for sensing metal and non-metal species found in biological assays.

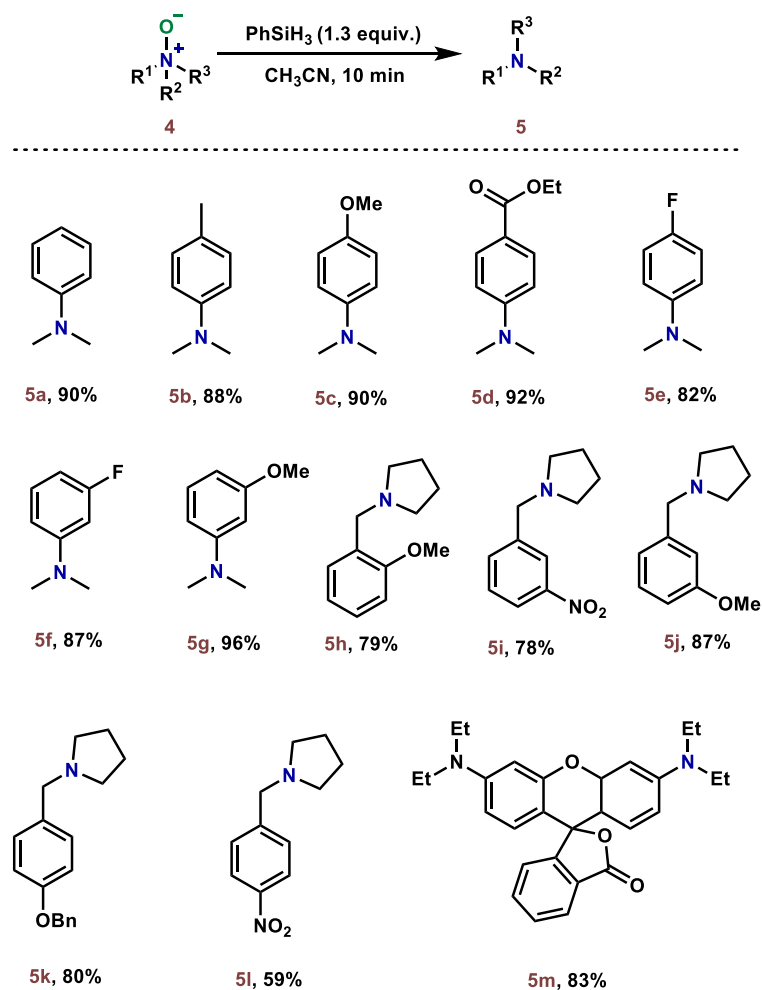


Figure 3 Scope of the photochemical deoxygenation of aliphatic amine *N*-oxides. Reaction conditions: **4** (0.5 mmol, 1 eq.), phenylsilane (0.65 mmol, 1.3 eq.), acetonitrile (5 mL), 10 min.

In order to gain insights into the reaction mechanism of the photodeoxygenation of heteroaromatic-*N*-oxides (Figure 2) and deoxygenation of aliphatic amine *N*-oxides at room temperature (Figure 3), a parallel computational study has been performed, whose results are deeply illustrated in the next paragraph.

7.4.2 Computational results

As concern the photodeoxygenation of heteroaromatic substrates (Figure 2), to understand the reaction mechanism we considered the 4-cyanopyridine *N*-oxide (**1a**) as model system. Since in this case the reaction takes place only under illumination, we firstly experimentally ascertain the nature of the photoactive species. To this end, we optimized the ground state geometry for **1a**, **2ba** and the π -complex between **1a** and **2ba** (**a**) and performed TD-DFT calculations to calculate the first excited states

energies. Moreover, in order to analyze the character of the excited states, specifically to quantify the degree of locality of each excitation, we utilized the D_{CT} descriptor, which, as we saw in Chapter 3, estimates the charge-transfer extent [55]. In order to be sure that all excited states calculated by TD-DFT are not unphysical ghost states, we computed the M_{AC} index [66] for all analyzed excited states. All corresponding data are collected in Table 1.

Once performed the detection of ghost excited states, on-the-fly, we simulated the absorption spectra by Gaussian convolution of the computed vertical transition energies. In Figure 4, we depicted the computed absorption spectra of the three potential absorbing systems, *i.e.* the phosphine (**2ba**), the *p*-cyanopyridine *N*-oxide (**1a**) and the corresponding possible π -complex ground state (**a**). As we can see, the phosphine (red line) cannot absorb alone the blue light used to perform the reaction, while the *p*-cyano pyridine *N*-oxide (magenta line) absorbs slightly around 400 nm.

Table 1 Excitation energies (E , in eV), Mulliken averaged configurations index (M_{AC} in eV), Ionization Potential of Donor (IP in eV), Electron Affinity of Acceptor (EA in eV), charge transfer distance index (D_{CT} in Å), Oscillator Strength (f in a.u.) and the assignment for the first four electronic transitions of the π -complex between the phosphine and the *p*-cyano pyridine *N*-oxide (**a**), and for the first three electronic transitions for the *p*-cyano pyridine *N*-oxide (**1a**) and the phosphine (**2ba**).

a.

Transition $S_0 \rightarrow S_n$	E (eV)	M_{AC} (eV)	D_{CT} (Å)	f (a.u.)	Character
1	3.08	5.61	4.98	0.00	Ghost state
2	4.08	5.16	2.70	0.00	Possible ghost state
3	4.12	4.39	4.78	0.01	Possible ghost state
4	4.19	3.00	2.23	0.58	LE

1a.

Transition $S_0 \rightarrow S_n$	E (eV)	M_{AC} (eV)	D_{CT} (Å)	f (a.u.)	Character
1	4.07	5.16	2.70	0.00	Possible ghost state
2	4.20	2.93	2.21	0.73	LE
3	4.53	-0.52	1.53	0.01	LE

2ba.

Transition $S_0 \rightarrow S_n$	E (eV)	M_{AC} (eV)	D_{CT} (Å)	f (a.u.)	Character
1	4.34	2.64	3.39	0.04	LE
2	4.76	2.23	3.31	0.12	LE
3	5.17	-16.23	0.64	0.39	LE

Furthermore, experimentally it has been seen that the addition of **2ab** does not induce any bathochromic shift to the spectra of **1a**, ruling out the formation of an intermolecular adduct between these species. Indeed, if we look at the calculated absorption spectra of the π -complex between the pyridine *N*-oxide and the phosphine (black line), it is visible just a slight broad absorption peak around 400 nm, which actually comes from the first excited state that has been harvested as “ghost state” from the M_{AC} analysis. But, with the aim to excluding any hypothesis that may exist a charge transfer upon the photon absorption, it was then necessary a further orbitals investigation to visualize the nature of calculated electronic transitions for the π complex (**a**), whose data referring to the four simulated absorption transitions are collected in Table 1. The oscillator strength values show that for the π -complex the effectively absorbing transition is the fourth one ($f = 0.58$). A more detailed analysis of such transition is provided in Table 2 and Figure 5, which shows that the bright electronic excitation is mostly localized on the *p*-cyano pyridine *N*-oxide fragment. Furthermore, the corresponding computed D_{CT} index (see Table 1) confirms the localized character (2.23 Å), thus excluding a direct photoinduced charge transfer.

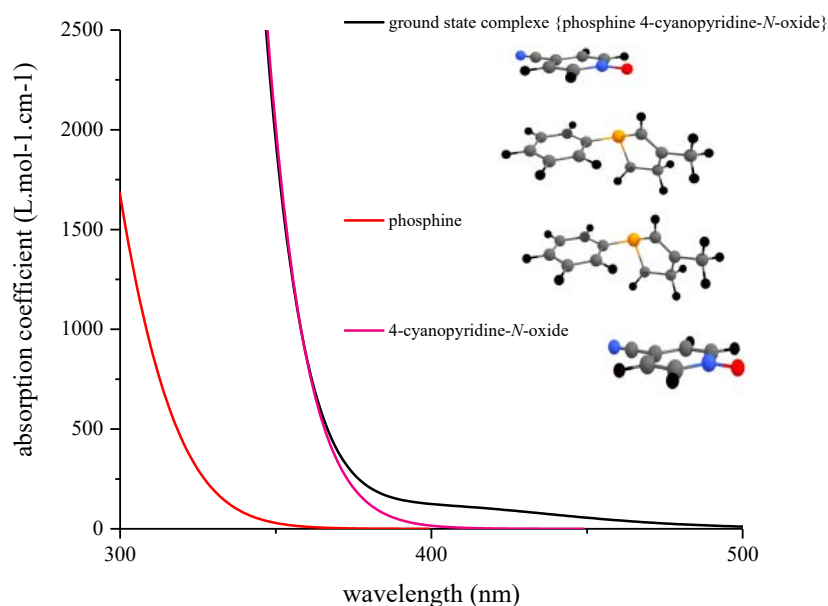


Figure 4 Absorption spectra of phosphine, *p*-cyanopyridine *N*-oxide and the corresponding possible π -complex ground state simulated by Gaussian convolution of the computed vertical transition energies using a fwhm value of 0.2 eV. Their corresponding structures are depicted on the right.

Table 2 TD-DFT vertical transitions from ground state (S_0) to the 4th excited state (S_4), corresponding oscillator strength (f in a.u.) values, molecular orbitals (MOs) involved in the transition and the corresponding weight of single determinant.

Transition $S_0 \rightarrow S_n$	f (a.u.)	MOs	Single determinant weight
1	0.00	HOMO \rightarrow LUMO	0.7066
2	0.00	HOMO-5 \rightarrow LUMO	0.6882
3	0.01	HOMO \rightarrow LUMO+1	0.6990
4	0.58	HOMO-1 \rightarrow LUMO	0.6732
4	0.58	HOMO-3 \rightarrow LUMO	0.1630

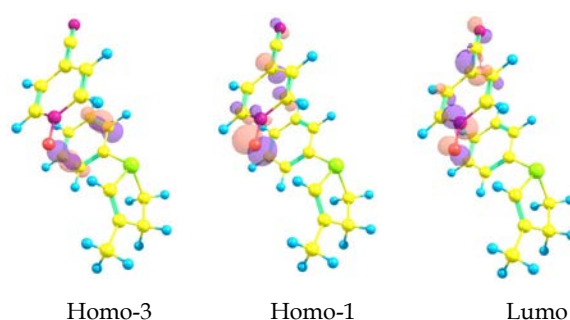
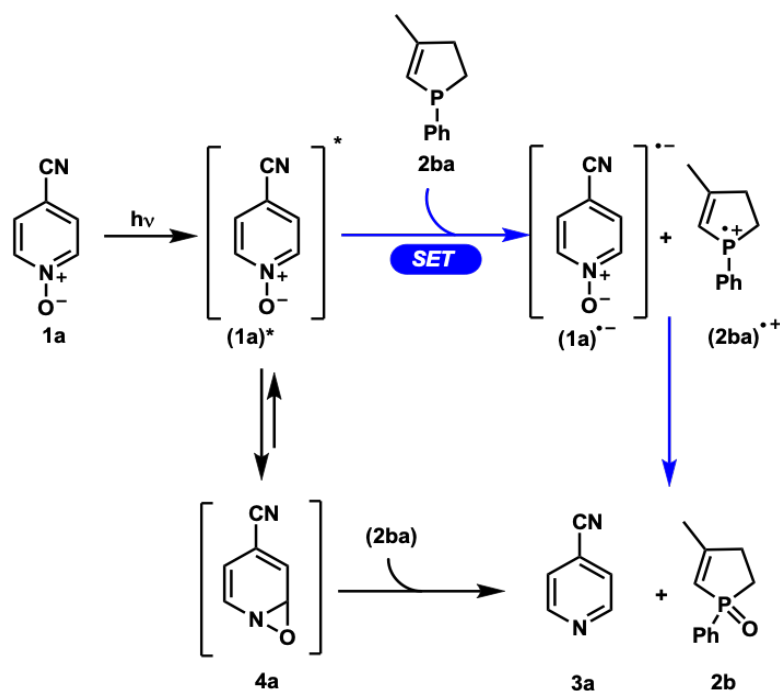


Figure 5 Molecular orbitals involved in the fourth vertical transition of the π complex between phosphine and 4-cyanopyridine N -oxide. From the left to the right: Homo -3, Homo-1 and Lumo.

Once neglected the possibility that **1a** and **2ba** may form an intermolecular adduct, we assume a photoactivation of the pyridine N -oxide (**1a**) leading to the formation of the excited (**1a**)^{*} specie. At this point, two scenarios can next be envisaged in an aprotic solvent, schematically depicted in Scheme 3:

- i) a photoisomerization leading to the formation of an unstable fused oxaziridine **4a**, which can further react with **2ba** to yield the pyridine **3a**;
- ii) a single electron transfer (SET) from the phosphane (**2ba**) to (**1a**)^{*} to generate the phosphoniumyl radical (**2ba**)^{•+} along with the reduced pyridine N -oxide species (**1a**)^{•-} (Scheme 3, blue arrows).

Even if both reaction mechanisms have been previously postulated in literature, [151] experimental evidence of the formation of oxaziridine intermediates could be given only for few cases since many heteroaromatic N -oxides do not show transient absorption by laser flash photolysis. As suggested by Albini back in the '80, theoretical approaches may therefore provide valuable insights, but, to the best of our knowledge, were not applied so far [151].



Scheme 3 Two postulated mechanisms for the deoxygenation of 4-cyanopyridine *N*-oxide (**1a**).

Therefore, to investigate what might be the most feasible reaction mechanism, we resorted on Density Functional Theory (DFT) and Time Dependent DFT to model ground and excited state reactivity.

First, to assess the photoisomerization hypothesis, we computed the ground and excited state potential energy surfaces (PES) describing the formation of the oxaziridine intermediate (**4a**) from **1a**, as this is supposed to be the key step of the process. As relevant structural parameters, two angles (α and β in Figure 6) were considered. These two angles describe respectively, the closure of the CNO ring and the out of plane position of the O atom with respect to the heteroaromatic ring (Figure 6). To obtain the full PES for the ground state and the first excited state, we performed a relaxed scan starting from the ground state planar *N*-oxide optimized structure by varying α from 120° to 50° in increment of 6° and β from -180° to -96° in increment of 7° . The resulting 124 geometries encompass the full photoisomerization from the *p*-cyano pyridine *N*-oxide to the oxaziridine (Figure 6).

As shown in Figure 6, the minima corresponding to **1a** and **4a** can be located on the ground state (S_0), the latter corresponding to an $\alpha=56.8^\circ$ and $\beta=-107.7^\circ$, characteristic of the oxaziridine geometry. Analysis of the ground and excited state PES reveals the presence of a region, close to the transition state of the ground state, with a small difference in energy (~ 5 kcal/mol) between S_1 and S_0 . In this region, relaxation from the excited to the ground state is likely to occur. On this basis, we can reasonably assume that the photoisomerization reaction occurs following a four-step mechanism (Figure 6):

Step 1: vertical absorption leading to the population of the S_1 excited state (dashed blue arrow);

Step 2: vibrational relaxation leads to the S_1 energy minimum (red arrow);

Step 3: $S_1 \rightarrow S_0$ vertical decay if sufficient energy is provided yielding the oxaziridine isomer (dashed black arrow);

Step 4: vibrationally relaxation of the oxaziridine isomer toward its corresponding minimum at the ground state (blue arrow).

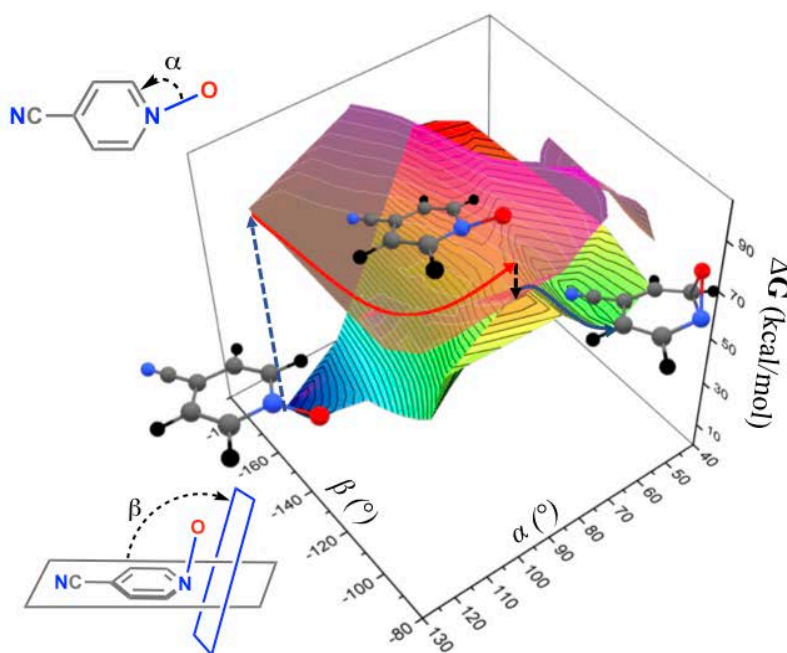


Figure 6 S_0 and S_1 free energy surfaces for the 4-cyano pyridine *N*-oxide (**1a**).

Analyzing the evolution of S_0 and S_1 PESs along the two coordinates of interest, it is worth to notice that the radiationless decay may happen around $\alpha = 90^\circ$ and $\beta = -100^\circ$, where the crossing between S_0 and S_1 points out an avoided intersystem crossing (Figure 6). To correctly estimate the free activation energy of the photoisomerization process, it is necessary to properly localize the $S_1 \rightarrow S_0$ transition. As we largely explained in Chapter 3, one can utilize the Π index to identify regions of GS and ES PES, where decay pathways are more likely to occur. In particular, high values of Π will define the regions corresponding to the higher decay probability.

So, for each optimized/extrapolated geometry we collected the energy difference between S_0 and S_1 , the transferred charge and the D_{CT} , which corresponds to the distance between the barycenters of charges after and before the transition. Coupling these variables, we computed the Π function, which represents a magnitude

proportional to the work necessary to rearrange two charges distributions, depicted in Figure 7 as a function of the angles of interest.

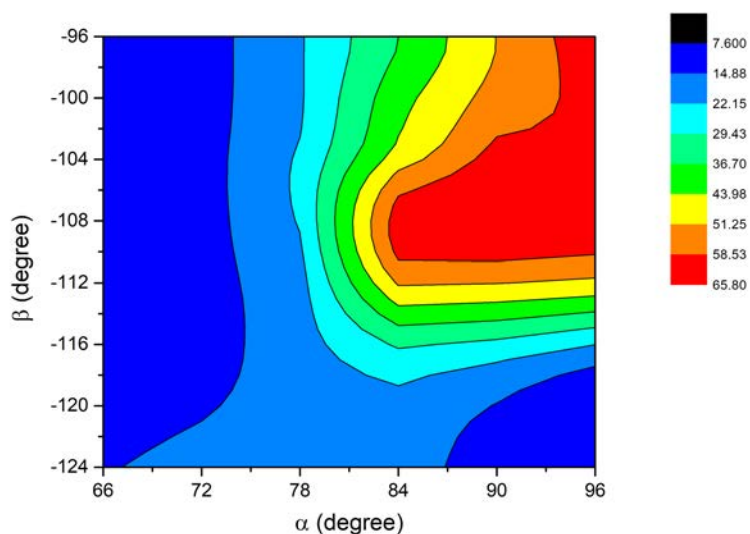


Figure 7 2D map of the $[I]$ index calculated along the two reaction coordinates (α valence angle and the β dihedral angle).

The $[I]$ index map yields a clear picture of the crossing topology. At $84^\circ < \alpha < 96^\circ$ and $-112^\circ < \beta < -96^\circ$ the non-radiative $S_1 \rightarrow S_0$ transition is very likely to occur. It corroborates the previous assumption about the avoided intersystem crossing around $\alpha = 90^\circ$ and $\beta = -100^\circ$.

The estimation of the free activation energy of the photoisomerization process has been calculated at two meaningful reaction coordinates:

- 1) at $\alpha = 84^\circ$ and $\beta = -96^\circ$, corresponding to the reaction coordinate where $[I]$ index analysis yielded the maximum transition probability;
- 2) at $\alpha = 85^\circ$ and $\beta = -105^\circ$, corresponding to the reaction coordinate where we calculated the lowest activation energy on the GS PES, having a 50% probability of yielding the oxaziridine.

The Figure 8 evidences that in a classical description, once the S_0 surface is reached, the system with zero kinetic energy has an equal probability to go towards the oxaziridine and the *N*-oxide, if and only if it corresponds to a saddle point. For both above-mentioned points we can consider the corresponding free energy on the S_1 PES, and thus estimating an activation energy by simple difference between S_1 free energies calculated in point 1 and point 2 and the free energy minimum of S_1 . Particularly, the first point gives an activation energy of 5.3 kcal/mol, while the second one an activation energy of 8 kcal/mol.

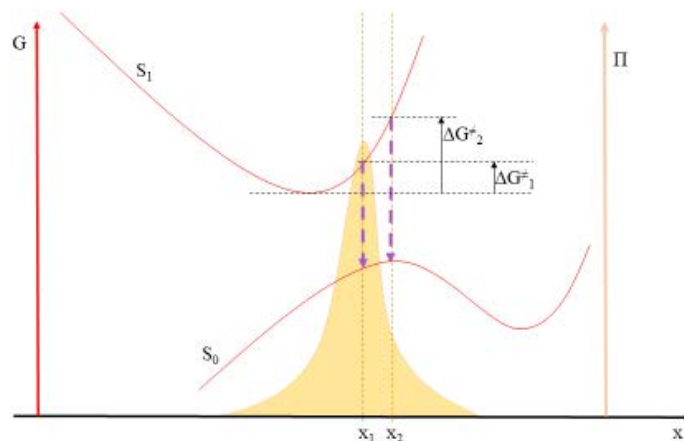


Figure 8 Schematic description of the free energy surfaces involved in the photoisomerization step. The potential energy surfaces along the x reaction coordinated are depicted in red. Free activation energies for the $S_1 \rightarrow S_0$ radiationless transitions are depicted as purple arrows. In beige, the Π index map along x . x_1 corresponds to the Π maximum and x_2 to the saddle point of S_0 . The corresponding free activation energies calculated by difference with the S_1 minimum are shown on the left of the figure.

Applying the mechanistic modeling described above for the 4-cyanopyridine N -oxide (**1a**), we were able to quantify the free energy difference ($\Delta G_{\text{gs-oxa}}$) between the N -oxide first excited state minimum and the oxaziridine intermediate on the ground state PES, and the activation energy ($\Delta G_{\text{oxa}}^\ddagger$) related to the rate determining step of the photocyclization, *i.e.* the isomerization process from the first excited state minimum of the N -oxide to the oxaziridine (step 2 to step 3). From data collected in Table 3, one can assume that the reaction of **1a** is thermodynamically favored ($\Delta G_{\text{gs-oxa}} = -43.6$ kcal/mol) and kinetically feasible at room temperature ($\Delta G_{\text{oxa}}^\ddagger = 5$ to 8 kcal/mol). As regard, however, the out of sphere single electron transfer mechanism displayed in Scheme 3, with the aim to verify if it could also play a role in the deoxygenation reaction, we applied the Marcus Theory well described in the Computational Methods and Details section. In particular, we investigate the feasibility of SET mechanism computing both activation and reaction energies collected in Table 3. This pathway was found to be kinetically ($\Delta E_{\text{SET}}^\ddagger = 2.24$ kcal/mol) and thermodynamically favored ($\Delta E_{\text{SET}} = -29.2$ kcal/mol). However, a direct comparison between both mechanisms was not possible because of the difficult evaluation of the entropic contribution [152]. To overcome this issue we applied the same methodology to three additional substrates, namely the electron-rich N',N' -dimethylaminopyridine N -oxide (**1e**) giving **3e** in high yield, and two acridine N -oxides **1zb** and **1zc**, which failed to react under these conditions. The results presented in Table 3 show that, if SET is computed to be feasible in all cases, it is found to be more favorable with acridine N -oxides **1zb,c** than with the pyridine N -oxide **1e**, which is in disagreement with experimental results. The formation of the oxaziridine intermediate is favored in the case of **1a,e**

showing the smallest activation energies, while deoxygenation of **1zb,c** is expected to be unlikely to occur and indeed did not proceed under our optimized conditions. On this basis the computed photoisomerization mechanism involving the formation of the oxaziridine **6** as a key intermediate is consistent with the observed yields, hence it can be considered as the most realistic reaction mechanism of photodeoxygenation of heteroaromatic *N*-oxides.

Table 3 Computed Free energies (ΔG_{gs-oxa} and ΔE_{SET}) activation energies ($\Delta G^{\ddagger}_{oxa}$ and $\Delta E^{\ddagger}_{SET}$) associated to the photoisomerization yielding to the oxaziridine formation (oxa) and the single electron transfer mechanism (SET). Refer to Scheme 3 for detail.

Substrate	$\Delta G_{gs-oxa}^{[a]}$ (kcal/mol)	$\Delta G^{\ddagger}_{oxa}^{[b]}$ (kcal/mol)	$\Delta E_{SET}^{[c]}$ (kcal/mol)	$\Delta E^{\ddagger}_{SET}^{[d]}$ (kcal/mol)
1a	-43.61	5 to 8	-29.20	2.24
1e	-39.94	2 to 6	5.95	10.54
1acr-a	-15.26	18 to 22	-4.69	9.97
1acr-b	-11.29	20 to 24	-15.67	2.58

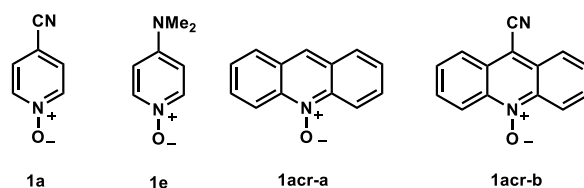


Figure 9 Schematic representation of 4-cyanopyridine *N*-oxide (**1a**), *N,N'*-dimethylaminopyridine *N*-oxide (**1e**) and two acridine *N*-oxides **1zb** and **1zc**.

Finally, the mechanism of deoxygenation of aliphatic amine *N*-oxides at room temperature remains to be elucidated. To this end, we considered the reaction of phenylsilane with *N,N*-dimethylaniline *N*-oxide (**4a**). Moreover, to explain the reason why the deoxygenation reaction in presence of phenyl silane does not take place for heteroaromatic amine *N*-oxides at room temperature, we extended the same study also to the 4-cyanopyridine *N*-oxide **1a**.

Hereby we propose a single step pathway to explain the deoxygenation reaction. The proposed concerted mechanism involves two molecular orbitals: the antibonding N-O orbital and the bonding Si-H, which can almost be considered as a silane hydride (Figure 10).

In order to gain insight into the mechanism and determine the origin of the chemoselectivity, we performed a computational study at DFT level. The optimized structures for all stationary points along the potential energy surfaces (PES) are

depicted in Figure 11. The zero-energy value corresponds to the sum of the isolated species energies, *i.e.* the pyridine *N*-oxide, phenyl silane and *N,N* dimethylaniline *N*-oxide. The path **a**, concerning the deoxygenation of **4a** is represented in black, while the one of **1a** (path **b**) is in red. The path **a** leads to the formation of silanol and *N,N* dimethylaniline aniline (**5a**), while via path **b** phenyl silanol and pyridine (**3a**) are produced.

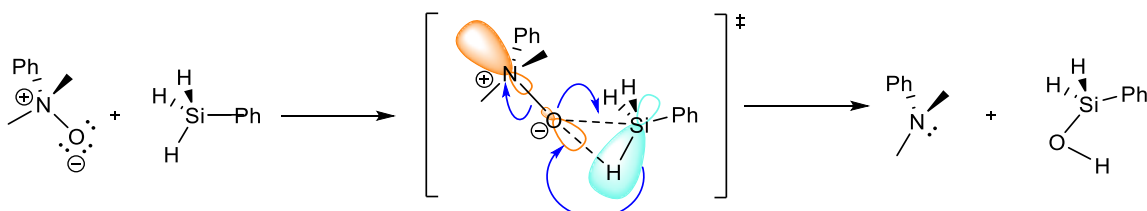


Figure 10 Suggested concerted mechanism leading to the reduction of the *N,N* dimethylaniline *N*-oxide (**4a**).

In both cases, the first step corresponds to the approaching of the two reagents (**1a**, **4a**), namely the formation of the precomplex. As concerns path **a**, in **4a** the oxygen atom is bonded to nitrogen (O-N 1.36 Å) and is oriented perfectly toward the silicon atom at a distance of 2.91 Å. The energetic barrier to overcome for the formation of the final product is found to be 18.6 kcal/mol. In **TSa** the oxygen atom is bridging the nitrogen, the silicon and the hydrogen atoms (O-N 1.73 Å, O-Si 1.76 Å, O-H 1.66 Å), in a quasi linear arrangement (N-O-H valence angle of 178.4°). Finally, the **5a** shows the oxygen bonded to the silicon atom (O-Si 1.68 Å) and consequently the hydrogen bonded to the oxygen atom (0.97 Å), while N-O bond is stretched up to breaking (N-O 4.13 Å).

On the other hand, as concern the path **b**, **1a** shows the pyridine *N*-oxide approached to phenyl silane (O-Si 2.93 Å). This step leads to the formation of the final products via **TSb**. The higher free energy barrier (34.9 kcal/mol) computed for this path confirms the experimental evidence. In the involved transition state, once more, the oxygen bridges the nitrogen and silicon atoms at an average distance of 1.70-1.75 Å. Simultaneously, the hydrogen atom approaches the oxygen at a distance of 1.61 Å, rearranging quasi linearly (N-O-H valence angle of 178.4°). The process terminates with the formation of the pyridine and the phenyl silanol. In the transition state, the interaction of the hydride with the antibonding N-O orbital and the bonding Si-H, weakens the strong N-O bond, until it breaks allowing the formation of O-Si bond. Therefore, we postulate that the limiting factor may be the N-O bond breaking. Indeed, the N-O bond of the pyridine *N*-oxide (1.29 Å) is much stronger than the *N,N* dimethyl aniline *N*-oxide (1.36 Å). Rather, the silicon is electron rich and the hydride transfer to the oxygen is thereby facilitated by the oxygen coordination to the silicon (Figure 9). As a consequence, although the reaction of the pyridine *N*-oxide **1a** proceed via a similar transition state (**TSb**), the required activation energy is around 20 kcal/mol higher than that for the reaction of **4a** with phenyl silane, in agreement with

the experimental observation of the failure of **1a** to react with phenylsilane at room temperature. The difference of reactivity between **1a** and **4a** stems indeed to the high nucleophilicity of the oxygen center of the latter compared to the former, where the negative charge is conjugated with the heterocycle. In summury, the reaction is chemoselective towards the *N,N* dimethyl aniline *N*-oxide derivatives.

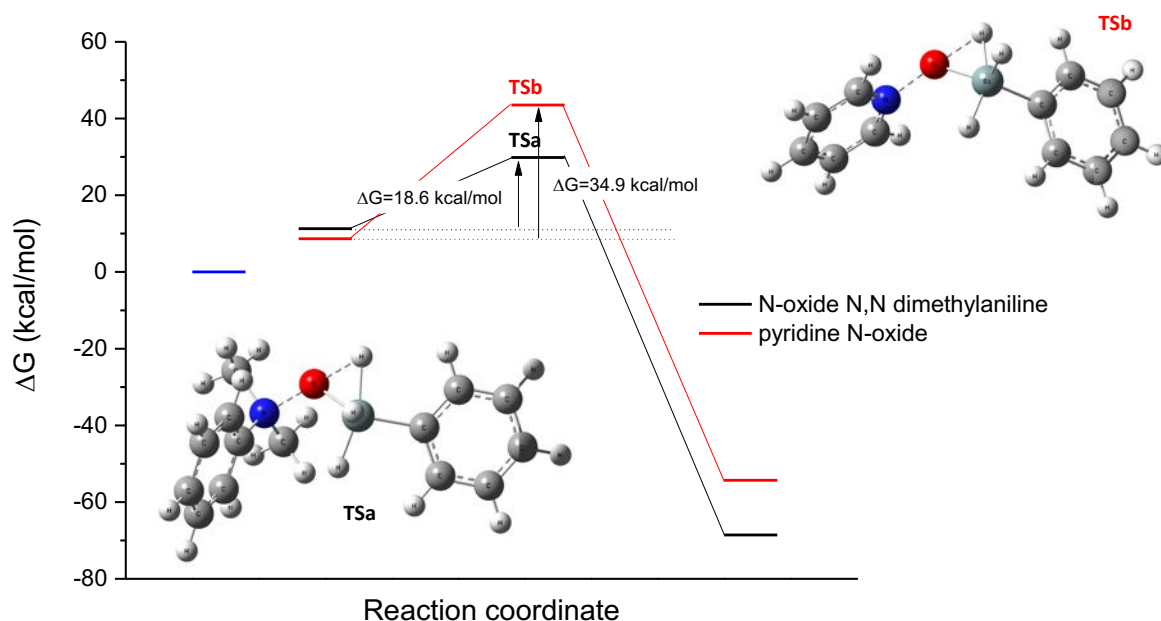


Figure 11 DFT calculated Gibbs energy profiles for the reactions of phenylsilane with **1a** and **4a**, respectively.

7.5 Conclusions

In conclusion, in this Chapter we demonstrated the compatibility of P(III) \leftrightarrow P(V) redox cycling with light to drive efficient and practically simple deoxygenation of a large variety of bis *N*-oxides. In order to understand the factors controlling the deoxygenation reaction, a combined experimental and theoretical study based on DFT and TD-DFT calculations, together with density-based descriptors has been performed.

- It was shown that the photochemical deoxygenation of heteroaromatic amine *N*-oxides proceeds most likely through the formation of a transient fused oxaziridine as a key intermediate reacting with phosphane to yield the heteroarene. By using the \square index we localized the boundaries of the crossing region between the first excited and the ground state, leading to the formation

of the oxaziridine intermediate, and we calculated reaction energies in agreement with the experimental observation.

- It was demonstrated that the deoxygenation reaction takes place at room temperature through a concerted pathway. But the activation energy computed for the deoxygenation of dialkylarylamine *N*-oxide (aliphatic amine *N*-oxide) is lower than the one calculated for the pyridine *N*-oxide (heteroaromatic amine *N*-oxide) with the reductant (phenylsilane).
- Therefore, the deoxygenation of aliphatic amine *N*-oxides proceeds even at room temperature, while heteroaromatic amine *N*-oxides react with phenylsilane via a photochemical deoxygenation.

Considering the importance of selective bis *N*-oxides deoxygenation in different domains going from catalysis to biology, these two metal-free simple approaches should find wide applications.

Chapter 8

How can the environment affect optical properties?

8.1 Context

In the context of modeling photoactive materials an important aspect to take into account is how the excited-state properties are modified by the condensed-phase environment, which has to be properly accounted for. The condensed-phase effects are those induced by, for example, surrounding solvent molecules in the case of solution, or other photoactive molecules in the case of crystalline or amorphous-phase materials. Therefore, in-depth theoretical investigations including the explicit treatment of the surrounding are highly required to gain accurate insight into different excited state processes, which can give rise to potentially useful photophysical properties exploited in smart photoactive materials. In particular, the solid phase modeling is of paramount importance, especially when dealing with aggregation process. In this case theoretical models capable of modeling electrostatic interactions with the solid-state environment are strongly required to properly include short - and long-range electrostatic effects and possible intermolecular interactions. The modeling of this type of effects is the core of this Chapter, where calculations including a proper treatment of the condensed phases have been performed in order to support and clarify experimental outcomes concerning a new chromogenic dye, a perylene bis-imide derivative (PBI), also interesting for the Near-Infrared (NIR) transparency and mechanochromism. Such properties are attributed to the high-symmetry of the PBI molecule that favors the formation of crystalline supramolecular assemblies promoted by the intermolecular π - π interactions between the perylene cores. The combined theoretical and experimental study that will follow is an adaptation of a publication by me, Cosimo Micheletti, Pierpaolo Minei, Marco Carlotti, Virgilio Mattoli, Francesco Muniz-Miranda, Ilaria Ciofini, Carlo Adamo, Giacomo Ruggeri, Andrea Pucci submitted to the *Macromolecular Rapid Communications Journal* [153].

8.2 Introduction

Nowadays, smart materials with chromogenic features are widely employed in the detection of external stimuli such as deformation, temperature alterations, and light exposure [154]. Such optical sensors are founded on the predictable relationship between the presence of the relevant stimulus and changes in the wavelength of light absorbed and/or emitted by the sensing system. The introduction of chromogenic species into polymers in the form of dispersed or covalently bonded chromophores have been reported as the most exciting and versatile procedure for conferring color features that are strongly depending on the environment variations [155,156]. Moreover, the possible formation of dye aggregates opens a wealth of exciting opportunities for the development of polymers with targeted chromogenic features. Notably, molecular aggregates can display entirely new features with respect to the isolated dye molecules and result extremely sensitive to medium variations thus supporting smart materials as sensitive optical sensors [157]. Polymers that respond to mechanical stimuli through variations of their optical features are called mechanochromic. Mechanochromism in polymers was reported for the first time by Weder in 2002 [158] and it has been supported by using diverse polymeric materials and different classes of aggregachromic dyes and fluorophores [159-163]. Notably, the optical responses towards mechanical solicitations are consistent with variations in the absorption and/or emission of these dye/polymer assemblies due to modifications of their interphase interactions and chromophore orientation towards the stress direction [155, 156, 160, 165]. Many practical applications can be predicted, *i.e.* mechano- and pressure sensors, [166, 167] indicators of mechano-history, security plastics and papers and data storage devices, [168-172] and new solutions are provided everyday [173-177]. Among the different chromogenic dyes, perylene bis-imide derivatives (PBIs) are one of the most investigated since their optical features result strongly depending on molecular packing among the chromophoric units [157, 178-180]. The disaggregation phenomena of PBIs assemblies triggered by polymer deformation caused a clear modification of the their optical features with very evident changes especially in emission [160,181]. Moreover, after polymer orientation, a well-defined dichroic behavior was displayed in polarized light owing to the oriented chromophore nuclei towards the drawing direction of the film. Furthermore, very recently, there has been a growing interest in the application of PBIs as Near-Infrared (NIR) transparent and reflective organic pigments for the development of cool organic coatings for different surfaces [182-185]. One of the most effective PBIs with NIR reflective features is Paliogen® Black L0086 (P-black, Figure 1) that is distributed by BASF as pigment for solar heat management in paints [186]. Such properties are attributed to the high-symmetry PBI conformation that favors the formation of crystalline supramolecular assemblies promoted by the intermolecular π - π interactions among perylene nuclei [183,185,187-190]. Its supramolecular structure

preserved within the polymer coatings allowed NIR reflectances close to 50% and consistent cooling effects [182, 191].

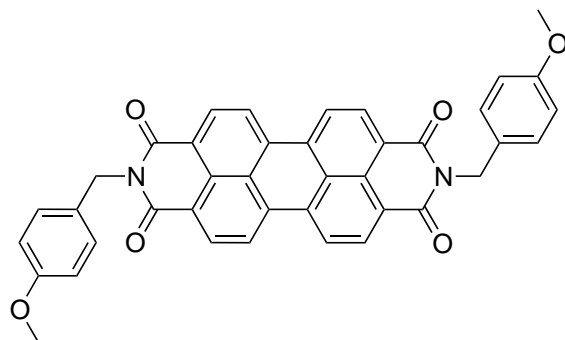


Figure 1 Chemical structure of Paliogen® Black L0086 (P-black).

Because the NIR reflective features strongly depend on the supramolecular packing, polymer drawing may promote the exfoliation of the dispersed PBIs aggregates, thus causing loss of NIR reflection that, in turn, substantially reduces the cooling effect of film surfaces.

In this Chapter, we propose a combined experimental and computational study to recommend the use of P-black pigment as an aggregachromic additive for low-density polyethylene (LLDPE) aimed to endow LLDPE films with a mechanochromic behavior both in the visible and in the NIR region of the spectrum of light. The external stress applied to the LLDPE film is thus detectable as color variations in the visible and reflectance reduction in the NIR, this last causing a prompt temperature variation of the film surface under IR irradiation.

8.3 Computational Methods and Details

P-black molecules have been computationally investigated to analyze and interpret their optical and structural features. We adopted various models to elucidate the available experimental data in both solvent/vacuum medium and inside a crystal field. To properly include short- and long-range electrostatic effects and possible intermolecular interactions we have investigated the monomer, dimer and trimer in each phase.

8.3.1 Solvent/vacuum calculations

The molecular structure of P-black molecules has been relaxed in the ground state (GS) using the Gaussian 16 program, [88] adopting the B3LYP exchange and correlation functional [22] in conjunction with 6-31+G** basis set and Grimme's D3-BJ

correction [192] : this level of theory proved to be suitable in a previous investigation of some of us on a similar system (dye Paliogen Red [188]). All relaxed structures (monomer and dimer) are potential energy minima, as all normal modes have a positive frequency.

Calculations of electronic excited states have been performed with the TD-DFT approach using the range-separated exchange and correlation functional CAM-B3LYP [25], to better describe charge-transfer transitions and the spectral shape. The solvent, here acetonitrile, is simulated using the implicit solvation model (polarizable continuum model [193]).

8.3.2 Crystal-embedded calculations

Periodic calculations have been carried out with the Crystal 17 code [194] at the B3LYP-D3 level with a modified all-electron 6-31+G(d,p) basis set to match that of in vacuo calculations. Numerical DFT integration has been performed considering 75 radial points and 974 angular points, ensuring an error on the integrated electron density to an accuracy of 10^{-5} e per unit cell. The Coulomb and exchange series were truncated with threshold values of 10^{-7} , 10^{-7} , 10^{-7} , 10^{-7} , and 10^{-21} . A tolerance of 10^{-7} a.u. has been used for the convergence of the self-consistent field procedure.

Cell parameters and atomic positions have been let free to relax during geometry optimization. Convergence was determined from the root mean square and absolute value of the largest component of the forces and displacements, considering default values (0.00045 and 0.00067 au for the forces, and 0.0018 and 0.0027 au for the displacements, respectively). The crystalline structure of P-black belongs to the triclinic P1 space group, with flat perylenetetracarboxylicdiimide portions packed in stacks through π - π interactions, with experimental lattice parameters of $a = 4.09 \text{ \AA}$, $b = 9.71 \text{ \AA}$, and $c = 17.11 \text{ \AA}$, $\alpha = 98.82^\circ$, $\beta = 91.07^\circ$, $\gamma = 101.58^\circ$ [195]. The optimized lattice parameters obtained are $a = 3.99 \text{ \AA}$, $b = 9.78 \text{ \AA}$, $c = 16.96 \text{ \AA}$, $\alpha = 96.72^\circ$, $\beta = 90.04^\circ$, and $\gamma = 101.67^\circ$. In addition, the flat portions of neighboring molecules are found at about 3.49 \AA apart, with respect to an experimental value of 3.59 \AA . To create a more cubic-like box, we adopted a $7 \times 3 \times 2$ monoclinic supercell, resulting in a simulation box of volume $\sim 28 \times 29 \times 34 \text{ \AA}^3$.

Starting from the optimized crystal structure obtained, a large supercell was built and partitioned into three zones, according to the SC-Ewald approach [196].

At the inner first zone treated at the QM level, two different clusters with either one, two, or three P-black molecules have been considered. The intermediate second zone consisted of point charges fixed at the value of the Mulliken atomic charges of the periodic calculation, while the point charge values of the outer third zone have been adjusted to impose the exact Madelung potential of the infinite periodic system on the first two zone sites. Further details can be found in ref [197].

Vertical TD-DFT calculations with the aforementioned models (embedded monomer and dimer of P-black) have been carried out with Gaussian 16, thus including the effects of the crystal environment. The embedded dimer model was also used to test

the dependence of computed spectra on the intermolecular distance and relative translation. All calculations (both embedded and nonembedded) have been carried out using the Pople's 6-31+G(d,p) basis set, and dispersion forces were modeled employing Grimme's D3-BJ correction.

8.4 Results and Discussion

P-black is an insoluble PBI pigment that was dispersed by ultrasonication into toluene solutions containing the 5 wt% of linear low-density polyethylene (LLDPE). LLDPE films containing different concentrations (2.5-10 wt%) of P-black were prepared by compression molding of the respective LLDPE mixtures. The UV-Vis spectra P-black/LLDPE films show absorption maxima centered at 430 and 680 nm (Figure 2), whose bands progressively widen with concentration until reaching almost a continuous contribution all over the visible spectrum at the highest pigment content of 10 wt%. Nevertheless, no additional absorption bands due to aggregation phenomena appeared by increasing the P-black content in LLDPE films from 2.5 to 10 wt%. Moreover, P-black/LLDPE films did not display any emission behavior, thus suggesting the de-excitation pathways was mainly governed by the typical aggregation-caused quenching phenomenon [198].

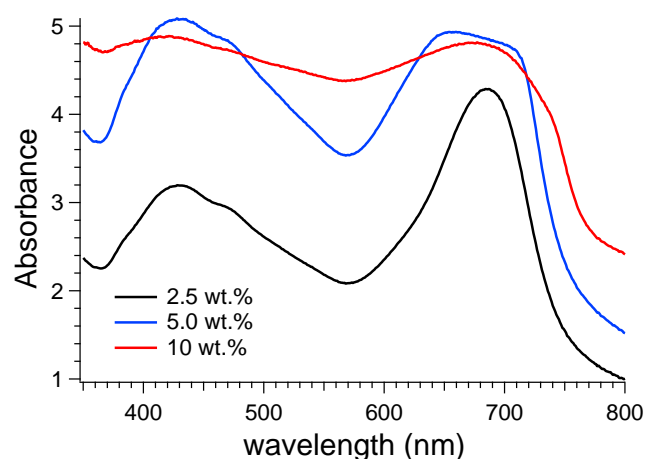


Figure 2 UV-Vis absorption spectra of the P-black/LLDPE films at different P-black content.

Calculations were employed to investigate the nature of the electronic transitions that originate the P-black color. As explained in the Computational Details, we have simulated P-black molecules in vacuo, in acetonitrile solvent, and in an electrostatic field built to mimic a crystal environment, for the monomer, dimer and trimer. As can be seen, there are at least two main peaks (peaks I and III) and a possible minor peak/

shoulder (peak II). The position of the lowest energy transition (part of peak I) is centered at ~ 474 nm in vacuo, and ~ 529 nm in acetonitrile.

We analyzed the nature of the most intense transitions responsible for the first three peaks observed in the UV of the monomer (Figure 3) by the molecular orbital representation (Figure 4). As can be seen all transitions are mainly localized on the perylene core, without appreciable charge transfer to the peripheral groups, as also confirmed by calculated D_{CT} index [55]. equal to zero (Table 1). Moreover, the effect of the solvent on the shape of these orbitals is negligible.

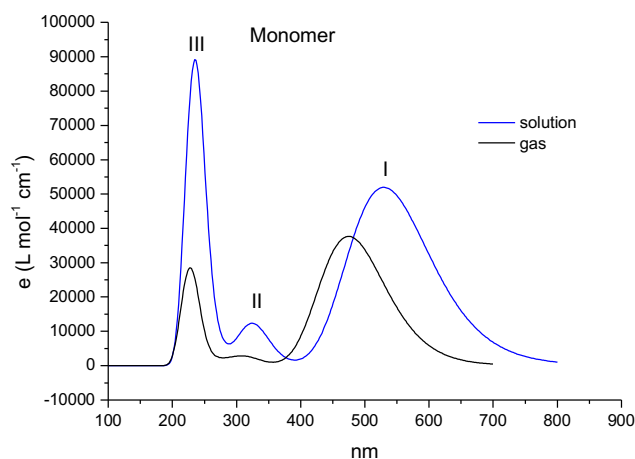


Figure 3 Computed TD-CAM-B3LYP/6-31G** spectra of a molecule of P-black in vacuum (black line) and solvent (dichlorobenzene, DCB, blue line) phase. Spectra have been smoothed with a Gaussian function with half-width at half-height of 0.333 eV.

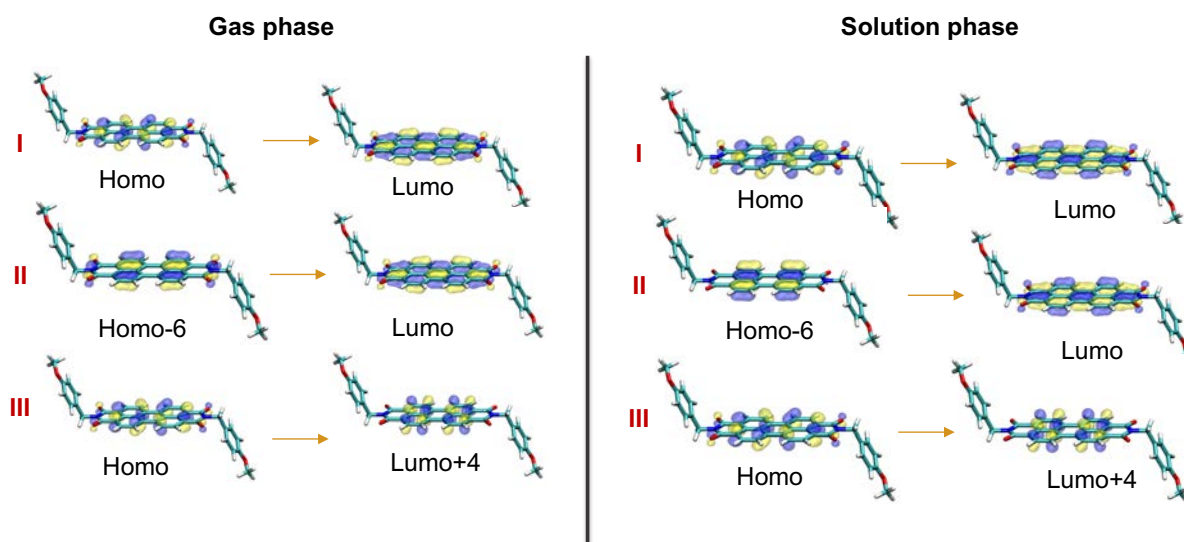


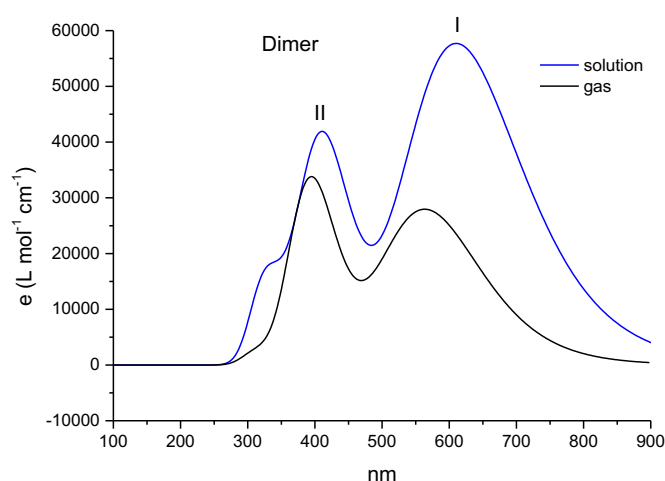
Figure 4 Isosurfaces of the orbitals (TD-CAM-B3LYP/6-31G** level of theory) of a molecule of P-black in vacuum (on the left) and in solution phase (on the right). The transitions (I, II, and III) are those shown in Figure 3.

Table 1 Computed excitation energies and associated D_{CT} values for the selected transitions.

Gas phase			Solution phase		
Transition	E (nm)	D_{CT} (Å)	Transition	E (nm)	D_{CT} (Å)
Ex. State 1	475	0.000	Ex. State 1	529	0.000
Ex. State 6	314	0.000	Ex. State 5	325	0.000
Ex. State 25	231	0.000	Ex. State 21	240	0.000

In order to gain insight into the effect of stacking P-black, and thus to take explicitly into account intermolecular interactions, we have simulated the UV-visible spectra of groups of 2 and 3 molecules extracted from the available crystal structure and depicted in Figure 5 and 7, respectively. We can see that they are rather similar in shape presenting two main bands at redshifted energies with respect to the single-molecule model.

The analysis of the nature of these transitions in terms of orbitals contribution is depicted in Figure 6 for the dimer and in Figure 8 for the trimer. Also in these two cases, one cannot see any appreciable inter nor intra molecular charge transfer character, both in gas and solution phase. Indeed, the electronic transitions involve orbitals localized on the perylene core of all molecules composing the dimer (Figure 6) and the trimer (Figure 8). The localized character is also confirmed by the D_{CT} descriptor computed for the dimer (Table 2) and the trimer (Table 3).

**Figure 5** Computed TD-CAM-B3LYP/6-31G** spectra of 2 stacked molecules of P-black in vacuum and solvent (acetonitrile) phase. Spectra have been smoothed with a Gaussian function with half-width at half-height of 0.333 eV.

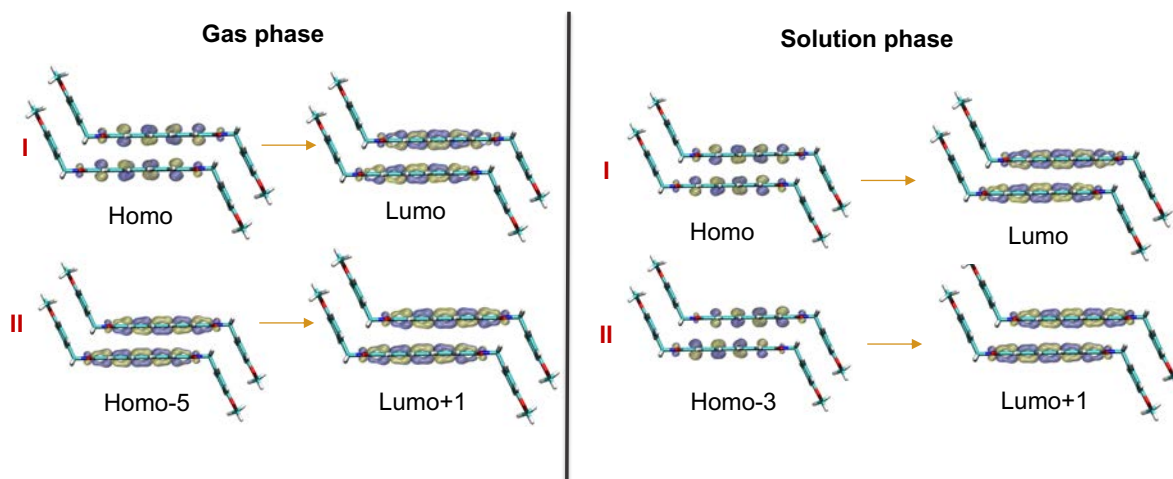


Figure 6 Isosurfaces of the orbitals (TD-CAM-B3LYP / 6-31G** level of theory) of 2 molecules of P-black in vacuum (on the left) and in solution phase (on the right). The transitions (I, II) are those shown in Figure 5.

Table 2 Computed excitation energies and associated D_{CT} values for the selected transitions.

Gas phase			Solution phase		
Transition	E (nm)	D_{CT} (Å)	Transition	E (nm)	D_{CT} (Å)
Ex. State 1	565	0.000	Ex. State 1	610	0.00
Ex. State 6	395	0.002	Ex. State 5	412	0.00

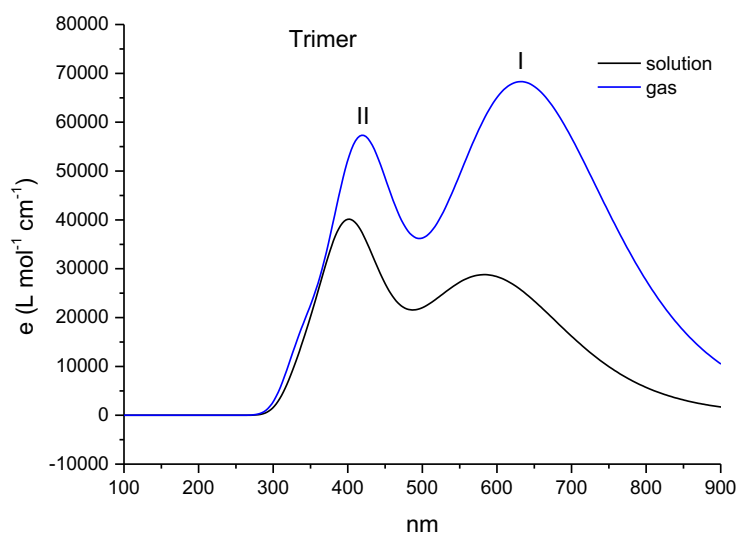


Figure 7 Computed TD-CAM-B3LYP/6-31G** spectra of 2 stacked molecules of P-black in vacuum and solvent (acetonitrile) phase. Spectra have been smoothed with a Gaussian function with half-width at half-height of 0.333 eV.

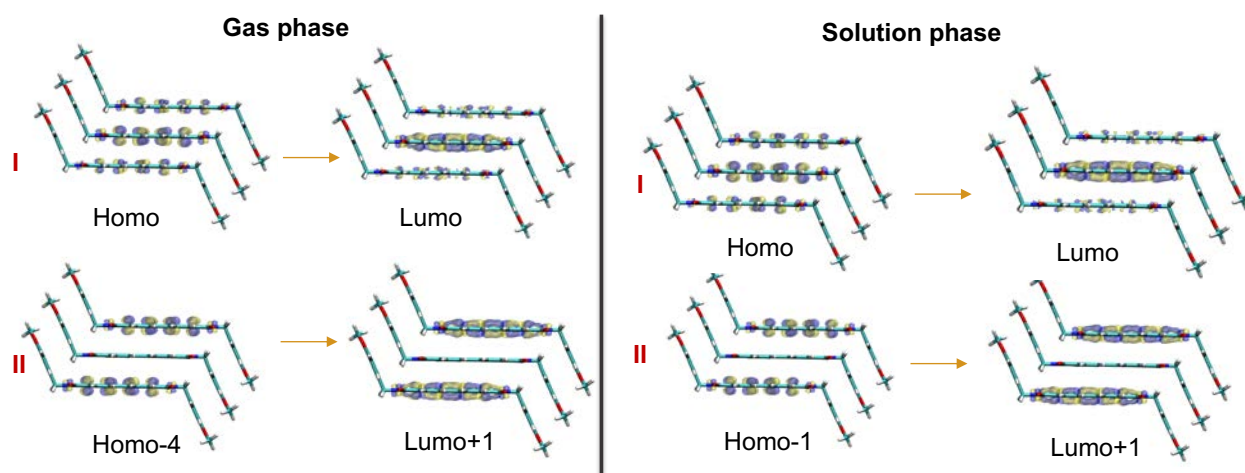


Figure 8 Isosurfaces of the orbitals (TD-CAM-B3LYP / 6-31G** level of theory) of 3 molecules of P-black in vacuum (on the left) and in solution phase (on the right). The transitions (I, II) are those shown in Figure 5.

Table 3 Computed excitation energies and associated D_{CT} values for the selected transitions.

Gas phase			Solution phase		
Transition	E (nm)	D_{CT} (Å)	Transition	E (nm)	D_{CT} (Å)
Ex. State 1	614	0.000	Ex. State 1	651	0.00
Ex. State 11	404	0.000	Ex. State 7	419	0.00

The spectra obtained with the crystal-embedded scheme (discussed in the Computational details) are reported in the left panel of Figure 9, treating explicitly at the quantum level a single molecule (black line) and a pair of adjacent molecules (blue line). As can be noticed, the spectra are significantly altered by the addition of a molecule at the quantum level of theory, both regarding the band shape and the energetics of the systems, which is redshifted. In particular, this suggests that an exciton may form which requires more than one P-black molecule to be considered explicitly in the model. To assess this hypothesis, we investigated the orbitals involved into the S_1 transitions of both models (see right Panel of Figure 9) and it is apparent that while there is no charge transfer in the single-molecule model, in the 2-molecules model an intermolecular charge transfer occurs. A more quantitative measure of this can be obtained using the aforementioned D_{CT} index, which indeed yields a non-zero distance of about 1.5 Å for the charge transfer in the 2-molecules model, as reported in Table 4.

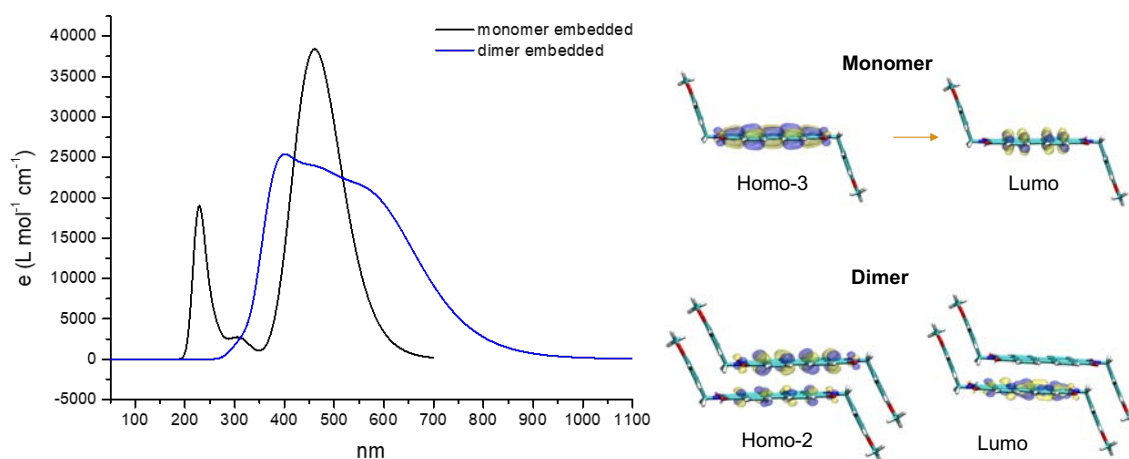


Figure 9 Left panel: Computed TD-CAM-B3LYP/ 6-31G**spectra for a single molecule (black line) and a pair of molecules (blue line) embedded into a crystal field. 30 excited states (*i.e.* S_1 - S_{30}) were considered. Right panel: Isosurfaces of the orbitals (TD-CAM-B3LYP / 6-31G** level of theory) of the orbitals involved in the S_1 transition of the single and 2-molecules models of P-black embedded into its crystal field.

Table 4 Computed excitation energies and associated D_{CT} values for the selected transitions.

	Transition	E (nm)	D_{CT} (Å)
Monomer	Ex. State 1	460	0.00
Dimer	Ex. State 1	585	3.19

Since the two-molecule model is able to reproduce excitonic effects, if present, in order to highlight differences and similarities, we compared the optical spectra obtained from calculations carried out in gas and solution phases with the one obtained from periodic calculations, only on the dimer (see left panel of Figure 10).

As can be seen, two main peaks can be located, around ~ 610 nm and ~ 410 nm for the solution phase: these values are within 0.2 eV from the observed peaks in solid phase, close to the inherent inaccuracy of the TD-DFT procedure; the CAM-B3LYP functional is also known to overestimate excitation energies [199].

Embedding two molecules in a crystal field yields instead a less structured spectrum, with significant absorption in the 300 – 700 nm range of wavelengths, thus spanning a large portion of the visible range (as expected from a black material). The nature of the first excitation (I^* in the right panel of Figure 9) is also different, with a more pronounced inter-molecular charge-transfer character, a behavior found also in the TD-DFT study of so-called Paliogen Red molecule (or Pigment Red 179 [188]) when embedded into a crystal. Indeed, the D_{CT} [55] quantum descriptor for charge transfer suggests a hole-electron distance of ~ 3.15 Å (Table 4), to be compared with an intermolecular distance between P-black molecules in the crystal of ~ 3.4 Å. On the

contrary, as seen before, models that include just a single P-black molecule or do not take into account the effect of the environment yields a vanishing value for the D_{CT} descriptor (Tables 1-3).

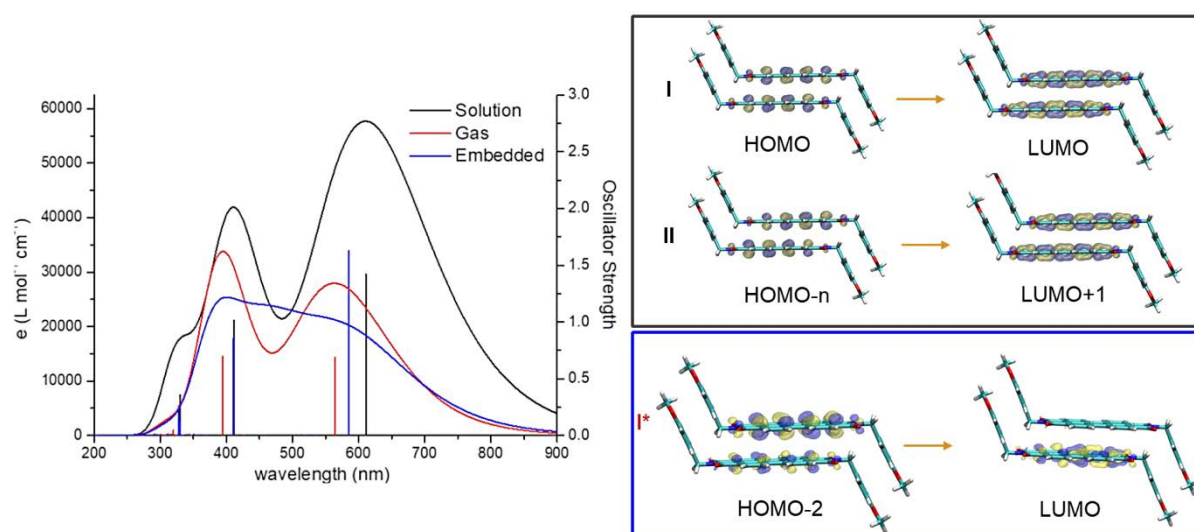


Figure 10 Left panel: Computed optical spectra at the TD-CAM-B3LYP level of theory in acetonitrile (black), vacuo (red), and embedded into the crystal field (blue); the curved are smoothed with Gaussian functions of half width at half height of 0.33 eV, while vertical lines are actual vertical $S_n \leftarrow S_0$ transitions. Right panel: main orbitals involved into the first (I) and second (II) calculated band, for the solution/gas calculations (black) and the crystal-embedded one (blue).

8.4.1 UV-Vis response to mechanical drawing

The P-black/LLDPE films were then oriented by uniaxial drawing at different draw ratios up to a maximum of 6 (elongation = 500%). The anisotropic behavior of the stretched films was evaluated by UV-Vis spectroscopy in polarized light (Figure 11), *i.e.* at different polarization angle with respect to the drawing direction of the film. The mechanical drawing of the P-black/LLDPE films conferred to the plastic materials a well-defined dichroic behavior under polarized light. It was worth noting that by varying the direction of the polarization angle with respect to the drawing direction of the films the absorption bands experienced an opposite behavior (Figure 11 a-c). Notably, the band at 430 nm increased its intensity whereas that at longer wavelengths (*i.e.*, 680 nm) decreased its contribution, flanked by the existence of a clear isosbestic point at about 570 nm, thus supporting the existence of two different populations of chromophoric assemblies. The behavior was confirmed for all the films investigated, therefore suggesting that dichroic assemblies of pigment molecules were generated also at the highest pigment content of 10 wt%, even if with a less evident intensity variations of the absorption bands (Figure 11c). We did not find such behavior in unstretched samples, indicating that the drawing can efficiently orient the P-Black aggregates. Moreover, the mechanochromic response was clearly visible simply by

observing the oriented portions of the LLDPE films under a linear polarizer (Figure 11d). The color changed accordingly to the absorption variations from yellow-green (0°) to dark-cyan (90°).

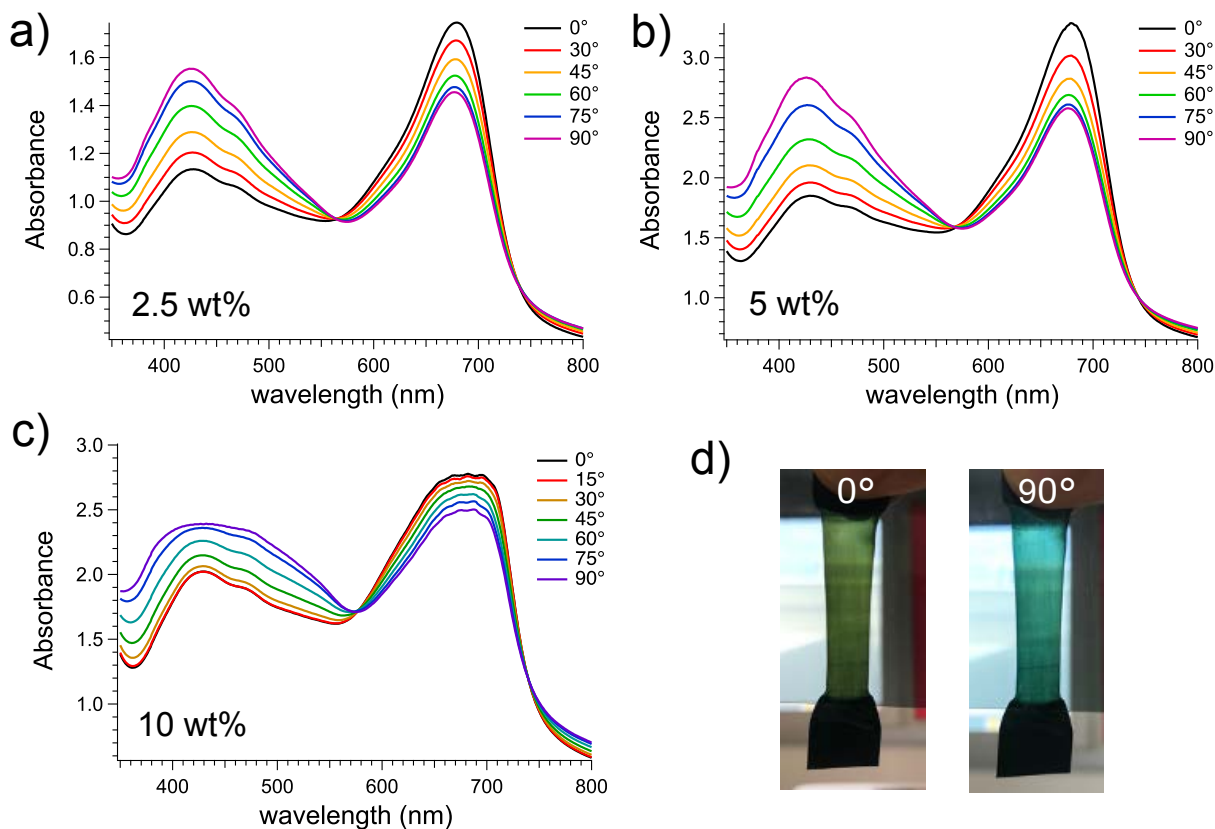


Figure 11 UV-vis absorption spectra as a function of the polarization angle for P-black/LLDPE oriented films containing a) 2.5 wt%, b) 5 wt%, c) 10 wt% of pigment; d) photos of the same 5 wt% P-black/LLDPE oriented film taken by superimposing a linear polarized oriented parallel (0°) and perpendicular (90°) with respect to the drawing direction. $Dr = 6$ in all cases.

The effect provided by the P-black content and the draw ratios on the chromogenic behavior was determined by the quantification of the absorbance variation ΔA (Table 5 and Figure 12).

The data reported in Table 5 revealed that the dichroic phenomenon was already obtained at the smallest deformation extent ($Dr = 3$) and particularly evidenced in the LLDPE films containing the lowest 2.5 wt% content, i.e. reaching absorbance variations of 0.46. P-black/LLDPE films containing the 5 wt% of the pigment revealed as the most sensitive towards mechanical drawing, with ΔA values progressively raising with draw ratio. Notably, a maximum of $\Delta A \sim 1$ was reached at the highest $Dr = 6$. Conversely, LLDPE films containing the 2.5 and 10 wt% of P-black showed lower sensitivity towards uniaxial drawing with ΔA values mostly similar for all the draw ratio investigated. This phenomenon could be possibly attributed for the former to a maximum chromophore orientation already gathered during the early stages of uniaxial deformation and for the latter to the difficulties of orienting the large content

of P-black assemblies (*i.e.*, 10 wt%) along the drawing direction and confined in the amorphous phase between polymer crystallites even at the highest $Dr = 6$.

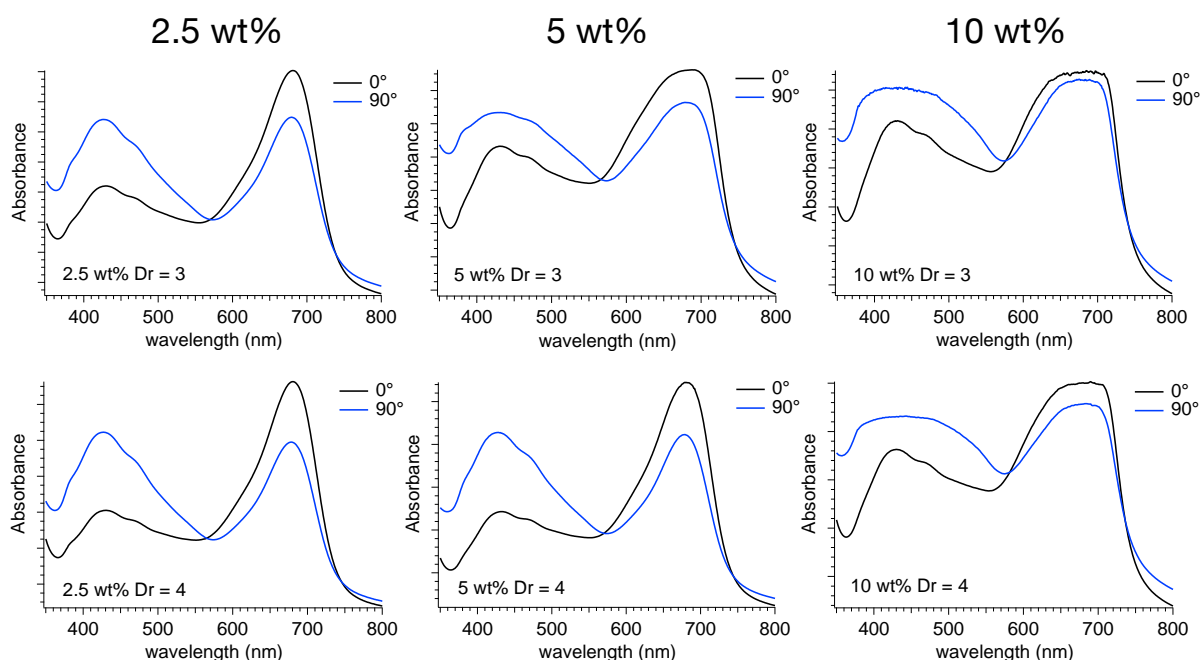


Figure 12 UV-Vis absorption spectra of oriented P-black/LLDPE films at different pigment content and draw ratio (Dr).

Table 5 Absorbance variations at 430 and 680 nm for P-black/LLDPE films at different pigment content and draw ratio (Dr). $\Delta A = A_{90^\circ} - A_{0^\circ}$

Entry	$Dr = 3$		$Dr = 4$		$Dr = 6$	
	ΔA_{430}	ΔA_{680}	ΔA_{430}	ΔA_{680}	ΔA_{430}	ΔA_{680}
2.5 wt% P-black/LLDPE	0.46	-0.30	0.45	-0.34	0.42	-0.29
5 wt% P-black/LLDPE	0.21	-0.19	0.93	-0.61	0.98	-0.71
10 wt% P-black/LLDPE	0.40	-0.11	0.40	-0.22	0.37	-0.27

In order to assess the effect of a relative translation among molecules we have carried out TD-CAM-B3LYP calculations on models, where one molecule is slightly shifted in one of the two most likely directions of shearing. The change in energy along these directions is depicted in Figure 13 for the 2-molecules model: the energy behavior has been depicted up to translations of 1 Å for sake of completeness, but we have to pinpoint that such large displacements have little physical meaning. Also, in the case of the x-axis translation the two excited states S_1 and S_2 come close (~ 0.4 Å) and switch, probably due to a conical intersection.

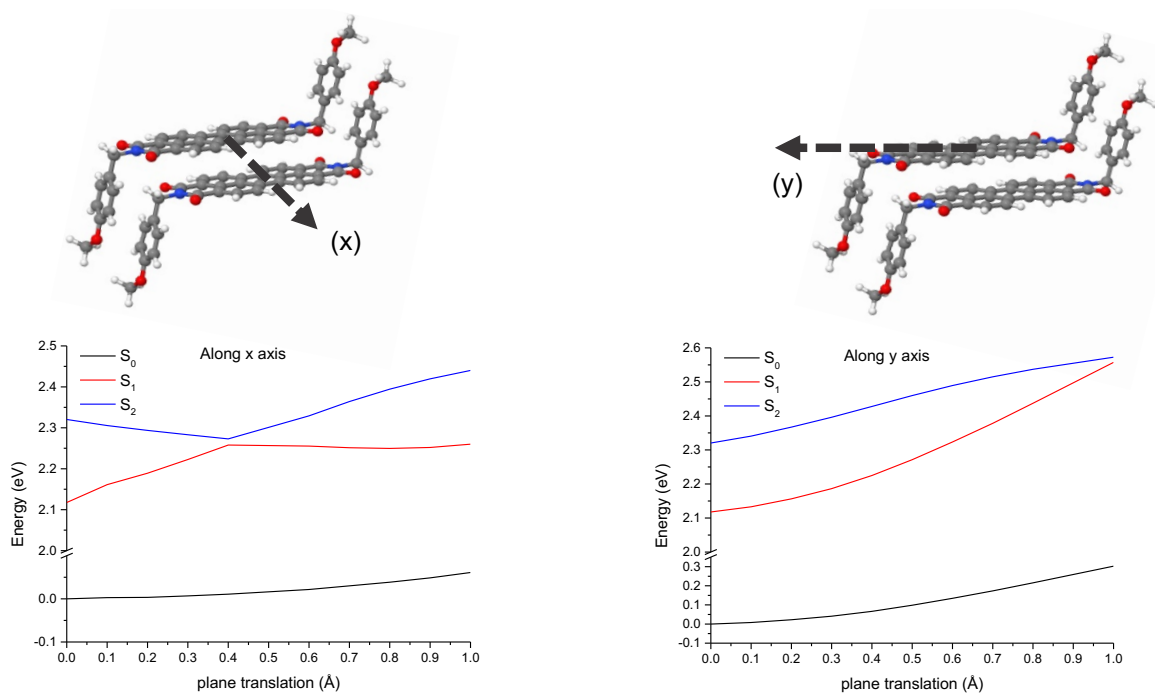


Figure 13 Effect of translations on the ground state (S_0) (black line) and the two lowest energy excited states S_1 and S_2 (in red and blue line respectively).

It was worth noting that the absorption band at about 430 nm appeared more sensitive to uniaxial deformation than that at about 680 nm for all the P-black/LLDPE films investigated (Figure 12). This behavior can be traced back to the transition dipole moments of the optical excitations. In particular, the three components of the transition dipole moments of the most intense $S_n \leftarrow S_0$ transitions show a certain extent of variability (reported in Table 6).

Table 6 Energies and associated D_{CT} values for the S_1 transition with the relative translation of the P-black in the 2-molecules model embedded into the crystal field. x and y axes are defined as in Figure 13.

x axis shift (Å)	Dipole (Debye)	Trans. Dipole (S_1) (Debye)	E (eV)	D_{CT} (Å)
0.1	8.74	7.58	2.10	1.53
0.2	8.99	7.07	2.11	1.54
0.3	9.25	6.37	2.13	1.54
0.4	9.42	5.43	2.14	1.54
0.5	9.45	4.22	2.16	1.53
0.6	9.22	2.89	2.17	1.51
0.7	8.69	1.92	2.17	1.47
0.8	8.17	0.94	2.17	1.43
0.9	7.68	0.47	2.16	1.37
1	7.32	0.22	2.15	1.32

y axis shift (Å)	Dipole (Debye)	Trans. Dipole (S ₁) (Debye)	E (eV)	D _{CT} (Å)
0.1	8.65	7.95	2.10	1.54
0.2	8.65	8.09	2.12	1.55
0.3	8.55	8.39	2.14	1.56
0.4	8.34	8.85	2.16	1.56
0.5	8.07	9.42	2.18	1.54
0.6	7.81	10.06	2.21	1.52
0.7	7.60	10.75	2.23	1.48
0.8	7.39	11.43	2.26	1.44
0.9	7.22	12.09	2.28	1.38
1	7.08	12.68	2.30	1.29

In particular, transitions #11 and #27, which occur at higher energies, show rather small values of the x component axis, as defined in Figure 13 (0.03 and 0.11 Debye, respectively) associated with significantly larger values for the y and z components (larger than 0.20 Debye for transition 11, larger than 0.35 Debye for transition 27), suggesting that these transitions could show significantly different absorptions if oriented differently in a single crystal.

Indeed, this anisotropy increases when a translation is made along the x-axis (see Table 7 in the Appendix), suggesting that the second band of the spectrum is more sensible to the orientation with respect to incoming light when subject to a lateral stress, as experimentally observed.

Optical microscopy taken on pristine and oriented P-black/LLDPE films (e.g., those containing the 5 wt% of P-black, Figure 14) revealed that the mechanical drawing was particularly effective in reducing the size of P-black aggregates from about 30-40 μm to 5-10 μm and in orienting them towards the drawing direction.

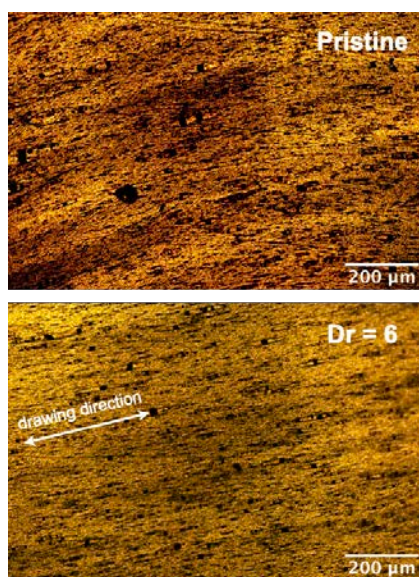


Figure 14 Optical microscopy images of pristine and oriented ($Dr = 6$) P-Black/LLDPE films containing the 5 wt% of P-black.

Notably, microscopy images taken on oriented films at $Dr = 6$ and in polarized light (Figure 15) confirmed the results gathered from UV-Vis spectroscopy (Figure 2). It was worth noting that all the oriented samples displayed color variations in absorption as a function of the polarization angle (*i.e.*, 0° and 90°) with P-black micro-sized aggregates mostly oriented towards the orientation direction of the film. The dichroic behavior appeared more evident for the oriented P-black/LLDPE film containing the 5 wt% of pigment and in agreement with the data reported in Table 5, even if the phenomenon resulted well-detectable also for the film with the lowest 2.5 wt% concentration. The highest P-black content of 10 wt% strongly affected the light transmission of the film and rendered difficult the determination of the aggregates anisotropy throughout the film sample.

Nevertheless, notwithstanding the high absorption of the films, optical microscopy was effective in revealing the dichroic behavior of P-black/LLDPE films at the early stages of mechanical deformation and containing the highest pigment content (10 wt% of P-black, Figure 16). Noteworthy, the uniaxial elongation corresponding to $Dr = 1.2$ conferred LLDPE film a chromogenic response in polarized light, thus suggesting that even at very small LLDPE deformations the supramolecular structure of P-black assemblies resulted effectively affected. This result was particularly relevant since it demonstrated the sensitivity of the designed P-black/LLDPE system in providing a prompt mechanochromic response towards uniaxial deformation.

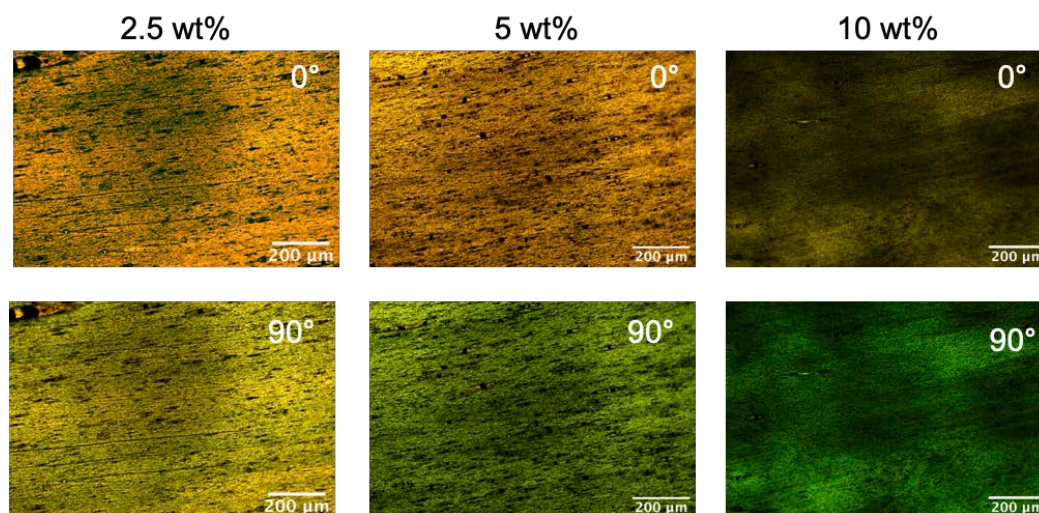


Figure 15 Optical microscopy images of oriented P-Black/LLDPE films as a function of the P-black content and polarization angle. $Dr = 6$ for all cases.

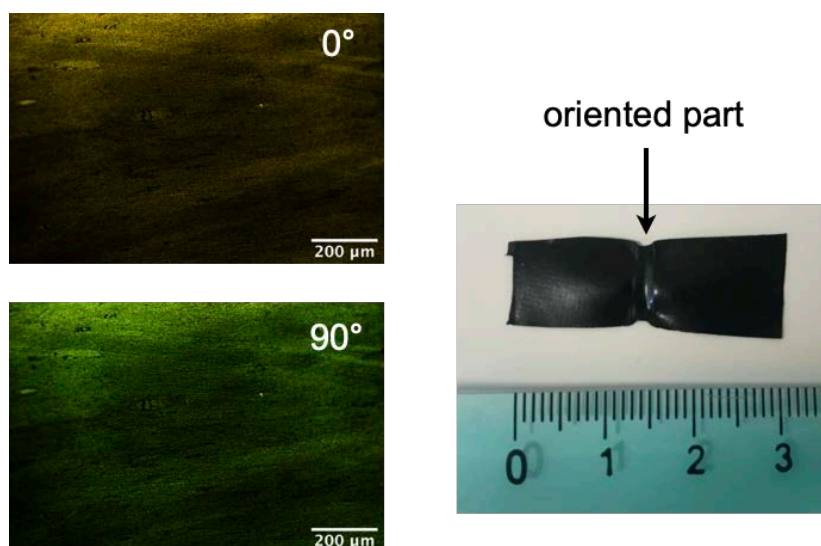


Figure 16 Optical microscopy images of the oriented portion of a 10 wt% P-Black/LLDPE film as a function of the polarization angle and photo of the film sample after orientation at $Dr = 1.2$.

8.4.2 NIR response to mechanical drawing

We then investigated the influence of the P-black content and the polymer uniaxial drawing on the film reflectivity in the visible and NIR region (Figure 17). In agreement with literature data, the reflectance spectra were depending on the optical features of the P-black chromophoric unit, *i.e.* a strong absorption in the visible region and maximum reflectivity around 800 nm flanked by a long tail throughout the NIR region [32, 38].

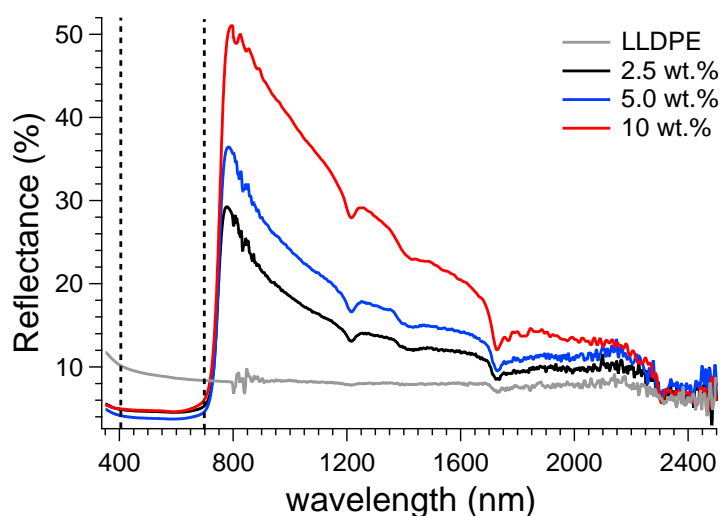


Figure 17 UV-VIS-NIR reflectance spectra of P-black/LLDPE films at different P-black content. The black dashed lines delimit the visible region (400–700 nm).

Notably, reflectance values progressively raised from 10% up to about 51% on passing from the neat LLDPE film to that doped by the 10 wt% of pigment, respectively, due to the increased number of dispersed micro-sized NIR reflective P-black aggregates. [31, 39] NIR reflectances close to 50% are particularly beneficial for the development of dark organic coatings with cooling characteristics since the affected wavelength region represents about the 25% of the total solar energy [34].

The mechanical drawing of the P-black/LLDPE films ($Dr = 6$) effectively affected the reflectance of the films with decreasing of about 30-40% of the maximum at around 800 nm. This phenomenon might be possibly addressed to a combination of effect: the first resides on the fact that uniaxial drawing caused P-black dilution throughout the oriented film portion; the second consist on the partial exfoliation of the pigment aggregates during deformation as revealed by optical microscopy (Figure 14). The reduction of the average aggregate size of P-black assemblies has been recently reported to adversely affect pigment reflectivity and, in turn, the pigment cooling characteristics [39].

The films were then placed over the black surface of a Leneta® checkerboard chart and irradiated by means of an IR lamp for 5 seconds to investigate the different cooling features of the oriented and pristine portions of the P-black doped LLDPE films. Thermal images taken during lamp irradiation revealed consistent temperature raising of the oriented LLDPE film of about 5 - 6 °C and in agreement with reflectance variations. In summary, the addition of P-black endowed LLDPE film with NIR-reflective and cooling characteristics as demonstrated by the progressive temperature reduction from 38.7 °C to 32.2 °C on passing from the neat LLDPE film (Figure 18) to that doped with the 10 wt% of pigment (Figure 19).

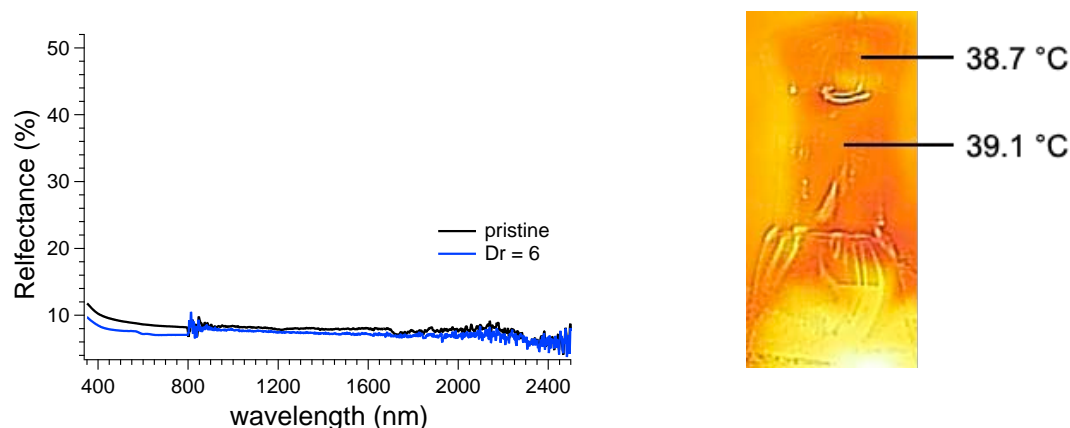


Figure 18 UV-VIS-NIR reflectance spectra of neat LLDPE film after uniaxial deformation at $Dr = 6$ (left). Thermal image of the same film with temperatures recorded for the oriented and unoriented portion (right).

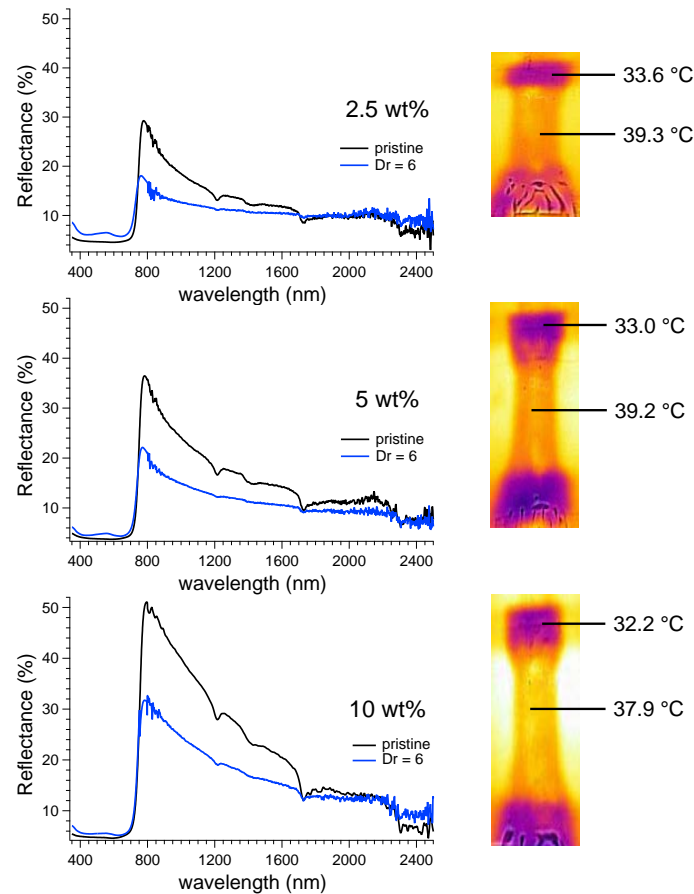


Figure 19 UV-VIS-NIR reflectance spectra of P-black/LLDPE films at different P-black content before (pristine) and after uniaxial deformation at $Dr = 6$. Thermal images of the same films with temperatures recorded for the oriented and unoriented portion of the films.

As soon as the mechanical drawing was applied to the films, reflectance reduction of about 20-30% caused a raise in temperature of about 5 - 6 °C. It is worth noting that temperature variations were also detected for the poorly oriented 10 wt% P-black/LLDPE film ($Dr = 1.2$) with the deformed film portion 4.5 °C warmer than the unoriented counterpart (Figure 20). This worthwhile characteristic flanked by the dichroic response in absorption rendered P-black pigment as a new solution to promptly detect mechanical deformations of polyethylene films through optical and temperature outputs.

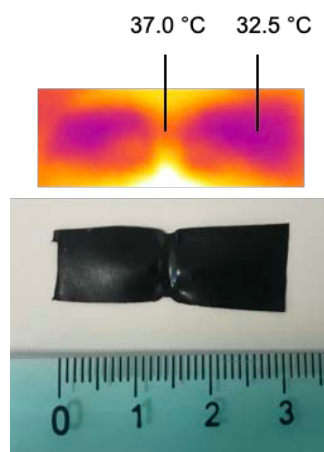


Figure 20 Photo and thermal image of a 10 wt% P-Black/LLDPE film oriented at $Dr = 1.2$ with temperatures recorded for the oriented and unoriented portion.

8.5 Conclusions

This work enabled the use of P-black as a unique pigment that once embedded into LLDPE films provided combined optical variations in the visible and reflectivity response in the NIR after mechanical uniaxial deformation. With computational methods based on the time-dependent density functional theory we have elucidated the origin of the electronic transitions accountable for the color of the dye, and the dipole anisotropy responsible for the mechanochromic properties. Notably, LLDPE films containing the 2.5-10 wt.% of P-black showed a dichroic absorption profile in linearly polarized light with clear isosbestic points and color variations from yellow-green to dark-cyan. This feature was addressed by density functional theory calculations to the different anisotropic behavior of the transition dipole moments of the P-black chromophoric assemblies within the oriented LLDPE matrix. Mechanical drawing was also responsible in reducing the average size of P-black aggregates from $\sim 30\text{-}40\ \mu\text{m}$ in the pristine film to $\sim 5\text{-}10\ \mu\text{m}$ after maximum film deformation at $Dr = 6$, thus also causing substantial reflectivity decrease of $\sim 30\text{-}40\%$ due also to the concomitant Pblack dilution all over the oriented portion of the LLDPE film. Such reflectivity loss was ingeniously exploited since the oriented film in contact with a black substrate displayed a noteworthy warming of $5\text{-}6\ ^\circ\text{C}$ maximum when illuminated with an IR lamp for 5 seconds. Both optical and thermal outputs revealed very sensitive to mechanical drawing thus opening a new avenue for the direct determination of mechanical deformations of plastic films.

Chapter 9

General conclusions and Perspectives

The aim of this research work is the development and the application of effective and inexpensive theoretical tools allowing the detailed description of potential energy surfaces of excited states, not exclusively in the Frank-Condon region. The ultimate goal is the interpretation of the photophysical behavior of systems and the rationalization of the structural and electronic characteristics of excited states giving rise to radiative and non-radiative decay pathways. This allows the *in-silico* design of new compounds to solve important problems, including the use of sustainable materials and the global energy crisis.

To this end, we have developed *ad hoc* descriptors that we applied in the context of time-dependent density functional theory (TD-DFT), but they actually can be combined with both electron density and wave function based methods. Since the information concerning the response of the system to the light induced perturbation is contained in the electron density, we based the implementation of such theoretical tools on this fundamental observable. Indeed, we tried to interpret photoinduced phenomena in light of the changing in the electron density distribution upon absorption. In particular, these theoretical descriptors are able to yield novel insights on relevant physical properties, thus translating the computational outcomes into simple chemical and physical concepts. An example is represented by the D_{CT} , which gives information about the strength and the spatial extent of the charge separation produced by an electronic excitation. Based on the simple computation of the electron density in a real-space representation for the ground state and the excited state, the D_{CT} measures the particle-hole distance by spotting the barycenters of negative and positive charges. Its simple and intuitive formulation in condensing the information on charge reorganization upon electronic excitation makes the D_{CT} one of the most commonly used descriptors to measure a CT distance. Nevertheless, in its original formulation this descriptor was unable to describe charge transfer in the case of symmetric molecules being by construction null independently of the presence of local charge transfer phenomena.

Hence the need to revise the D_{CT} to expand the area of application, thus permitting its use for whatever system, symmetric or not. For this purpose, in **Chapter 4** we have presented a new density-based index, the partial D_{CT} ($^P D_{CT}$), enabling to measure the

charge transfer extent in symmetric conformations. It has been basically implemented by adapting the classical formulation of the D_{CT} index on the subset of atoms composing the smallest asymmetric fragment of the symmetric molecule of interest. In this way, one calculates the CT extent for each asymmetric fragment avoiding the calculation of the overall D_{CT} index, which is equal to zero by definition. For this purpose, we have considered three families of push-pull systems, characterized by an increasing number of acceptor units and either by vanishing or by a non-vanishing global D_{CT} value, and we tested on them our new tool. Effectively, we showed that now it is possible to overcome the inability to provide information on charge transfer excitations within symmetric molecules for which the global CT is null. Moreover, since the D_{CT} is calculated by considering only the contribution of a given subset of atoms, it is now possible to dissect the total particle-hole distance along certain directions of interest, for which it could be interesting to have independent information. However, the use of the ${}^P D_{CT}$ implies an *a priori* definition of the subset of atoms constituting the asymmetric fragment, which could add possible artifacts, including the double (triple, etc..) counting coming from specific molecular fragments. Therefore, in **Chapter 5** we provided another density-based descriptor, the average D_{CT} index (${}^A D_{CT}$), which can be used indistinctively for whatever molecular conformation, symmetric or not, thus avoiding any user manipulation. Unlike the D_{CT} (and ${}^P D_{CT}$), which measures the CT extent as the distance between two average points of charge distributions, the ${}^A D_{CT}$ weights the average of the distances between all possible hole and electron distributions present in the system of interest, thus permitting a description that is independent of the system topology. In order to validate and compare ${}^A D_{CT}$ with previously developed descriptors (D_{CT} and ${}^P D_{CT}$) we firstly considered a set of test case molecules, prototypes of systems containing donor (D) and/or acceptor (A) groups, and spectroscopically well characterized and then real DA symmetric push-pull molecules. We saw that this index yields reasonable CT extents even for most symmetric molecules and retains the positive aspects of the previous density-based descriptors, namely it has a particularly low computational burden if used in conjunction with atomic charges (for instance Mulliken's ones) and it can be applied independently on the level of theory adopted. As the name implies, it yields an average value, so it is inherently a scalar (and not a vectorial) quantity, unlike the previous ones, and consequently it does not provide a physically correlated origin of the displacement of the electron and the hole.

In the context of modeling excited state profiles with the aim of gaining insight into complex photoinduced phenomena, in **Chapter 6** and **Chapter 7** we extended our computational framework to investigate how the system evolves upon light absorption, by viewing the consequent electron density rearrangement. In particular, we applied a previously defined density-based index, the Π , to spot internal conversion between ground and excited states in order to pinpoint possible regions where radiative and non-radiative decay are likely to occur. This allowed us to understand the origin of the dual emission behavior of a phenantroline derivative (Chapter 6), and to support experimental evidences regarding the feasibility of a

hypothesized reaction mechanism explaining a metal-free deoxygenation reaction occurring at excited state (Chapter 7).

Therefore, this allowed us the description of not only excited state properties of single molecular system, but also to understand the complex reactivity at excited state. One of the most arguable features of this approach is that the actual interpretation of the photophysical pathway depends on the accuracy of the computed density, more generally on the chosen quantum chemical level of theory. Moreover, the reader is invited to consider the overall picture obtained by such approaches more qualitative than a precise characterization of funnel regions. Indeed, the density-based indexes here proposed should be intended as a primary cheap and effective methodology to explore and have an immediate view - on the fly - about potential energy surfaces and possible reaction paths. An already solid departure point for both helping the interpretation and rationalization of experimental outcomes, and to support the classical excited state characterization by computationally expensive quantum methods.

As a matter of fact, some improvements and suggestions could be proposed to efficiently use such density-based descriptors without having problem of application on particular molecules. Effectively, if one applies the $\Delta\rho$ index *sic et simpliciter* for symmetric molecules for which the D_{CT} is null by definition, the $\Delta\rho$ index would incorrectly diverge. But we implemented the ${}^P D_{CT}$ to measure the CT extent in case of molecules with symmetric configuration (see **Chapter 4**). So, a solution would be to use the ${}^P D_{CT}$ definition in the $\Delta\rho$ index. On the contrary, the use of ${}^A D_{CT}$ descriptor (**Chapter 5**) is not recommended since being a scalar magnitude it does not contain the directional information, and therefore is not compatible with the $\Delta\rho$ index, which is based on the idea to follow the directionality of the electron density change. The ${}^A D_{CT}$ descriptor could be rather integrated in the M_{AC} descriptor (**Chapter 3**), which basically tries to replace the transition energy formulation of Mulliken through an average orbital weighted estimation of the ionization potential and electron affinity together with an effective CT distance (D_{CT}). In particular, ${}^A D_{CT}$ could be used in place of the global D_{CT} , thus avoiding the inconvenient to pay attention if the molecule is symmetric or not.

A possible repercussion of my research work could be the integration of all these theoretical tools into a unique and effective protocol specifically implemented to simulate *in-silico* UV-visible emission spectra for a wide range of molecules. The idea would be to develop an efficient, computationally inexpensive predictive protocol to design new biocompatible chromophores. Indeed, as the 2030 Agenda for Sustainable Development requires us to take the path of sustainability, industries are also called upon to take new steps to achieve the famous 17 goals, such as the use of sustainable materials. The common chemical dyes are included in the archive of materials to be replaced with eco-materials. Therefore, the idea is to use the over-mentioned protocol to predict possible chromophores suitable to create durable and natural dyes, thus avoiding industries to use the wasteful trial-and-error approach. This represents the

aim of the IRIS project which has awarded of the funding from PSL-Pepite program in the context of “AAP Preuve de concept 2020” competition.

The further logical step has been to try to reproduce the effect of the environment in the modulation of the spectra both in shape and energy. In particular, efforts have been spent in the modeling of the solid phase in order to take into account condensed-phase effects, of paramount importance especially when dealing with aggregation process. In this context, in **Chapter 8** we have studied the mechanical, optical and electronic properties of dye Paliogen Black, a perylene bis-imide derivative with high-symmetry conformation that favors the formation of crystalline supramolecular assemblies promoted by the intermolecular π - π interactions among perylene nuclei. We have investigated it by both experimental and computational means: with the former we have assessed its properties as a “cool” pigment, *i.e.* its high reflectiveness to near infrared radiation, and its mechanochromic behavior when introduced into a low-density polyethylene matrix and subject to directional stress. With computational methods based on the time-dependent density functional theory we have elucidated the origin of the electronic transitions accountable for the color of the dye, and the dipole anisotropy responsible for the mechanochromic properties.

As a matter of fact, we have utilized such accurate multiscale simulation to highlight the structural and optical features, and thus the different behavior, in three distinctive phases, namely gas phase, solution, and solid state. To properly include short- and long-range electrostatic effects and possible intermolecular interactions the investigation has been initially conducted on the monomer and then extended to the dimer and trimer in each phase. This actually could represent an efficient protocol that can be adopted to study complex mechanisms involving phenomena at different scale, where a very high accuracy is required at each size. A sort of coarse-grained approach to simulate complex phenomena like aggregation-induced emission (AIE) or aggregation caused quenching (ACQ). Indeed, a future idea could be establishing an accurate multiscale computational protocol for a deep description of the mechanism underlying the AIE phenomena. In this way, the investigation of the structure-property relationship of systems that can yield AIE phenomena could be essential to guide the rational design of novel AIEgens with improved performance and enhanced applicability.

Appendix

Appendix to Chapter 6

Table 1: Detailed vertical excitations energies (in eV), considered by energy and by character, D_{CT} (in Å) oscillator strength (in a.u.), dipole moment (in Debye) data computed for each excited state.

Angle (°)	Energy (eV) w.r.t. mings (<i>Energy based</i>)						
	GS	ES1	ES2	ES3	ES4	ES5	ES6
0	0.0000	3.4442	4.0096	4.3959	4.4968	4.6013	4.6485
10	0.0005	3.4527	4.0152	4.3972	4.4948	4.6018	4.6488
20	0.0040	3.4810	4.0345	4.4033	4.4905	4.6043	4.6519
30	0.0086	3.5395	4.0737	4.4302	4.4810	4.6079	4.6639
40	0.0145	3.6030	4.1137	4.4423	4.4629	4.6120	4.6696
50	0.0216	3.6834	4.1617	4.4362	4.4582	4.6152	4.6643
60	0.0283	3.7776	4.2121	4.3973	4.4743	4.6051	4.6396
70	0.0340	3.8785	4.2574	4.3412	4.4863	4.5681	4.6353
80	0.0374	3.9728	4.2724	4.2886	4.4935	4.5400	4.6366
90	0.0388	4.0278	4.2282	4.2999	4.4988	4.5306	4.6379
Angle (°)	Energy (eV) w.r.t. mings (<i>Character based</i>)						
	GS	ES1	ES2	ES3	ES4	ES5	ES6
0	0.0000	3.4442	4.0096	4.3959	4.4968	4.6013	4.6485
10	0.0005	3.4527	4.0152	4.3972	4.4948	4.6018	4.6488
20	0.0040	3.4810	4.0345	4.4033	4.4905	4.6043	4.6519
30	0.0086	3.5395	4.0737	4.4302	4.4810	4.6079	4.6639
40	0.0145	3.6030	4.1137	4.4423	4.4629	4.6120	4.6696
50	0.0216	3.6834	4.1617	4.4582	4.4362	4.6152	4.6643
60	0.0283	3.7776	4.2121	4.4743	4.3973	4.6396	4.6051
70	0.0340	3.8785	4.2574	4.4863	4.3412	4.6353	4.5681
80	0.0374	3.9728	4.2886	4.4935	4.2724	4.6366	4.5400
90	0.0388	4.0278	4.2999	4.4988	4.2282	4.6379	4.5306
Angle (°)	D_{CT} (Å)						
	GS	ES1	ES2	ES3	ES4	ES5	ES6
0		4.096	3.913	0.094	2.581	0.846	2.290
10		4.108	3.903	0.101	2.553	0.833	2.360
20		4.142	3.865	0.126	2.465	0.780	2.551
30		4.151	3.732	0.187	2.278	0.716	2.748
40		4.226	3.609	0.268	2.262	0.568	2.983
50		4.307	3.400	2.388	0.374	0.235	2.745
60		4.396	3.060	2.648	0.471	1.871	0.444
70		4.496	2.551	2.806	0.565	2.360	0.602
80		4.611	2.473	1.964	0.632	1.969	0.569
90		4.699	1.355	1.635	0.656	1.817	0.564
Angle (°)	Oscillator strength (a.u.)						
	GS	ES1	ES2	ES3	ES4	ES5	ES6
0		1.6017	0.0391	0.0893	0.3092	0.0000	0.4874
10		1.5870	0.0381	0.0898	0.3058	0.0024	0.4796
20		1.5409	0.0352	0.0917	0.2918	0.0098	0.4599
30		1.4693	0.0293	0.0896	0.2720	0.0172	0.4519
40		1.3628	0.0237	0.0979	0.2183	0.0381	0.4444
50		1.2218	0.0172	0.1835	0.0862	0.1132	0.5081
60		1.0322	0.0107	0.1873	0.0926	0.6111	0.2598
70		0.7666	0.0052	0.3615	0.0962	0.9711	0.0267
80		0.3779	0.7561	0.0051	0.0980	1.0067	0.0039
90		0.0006	1.1481	0.0022	0.0973	1.0028	0.0002
Angle (°)	Dipole moment (Debye)						
	GS	ES1	ES2	ES3	ES4	ES5	ES6
0	9.9385	22.5202	23.5272	10.1365	15.6349	7.1779	15.561
10	9.9299	22.6172	23.4199	10.1686	15.4865	7.2279	15.720
20	9.8875	22.8891	23.0307	10.2364	15.0659	7.3940	16.157
30	9.6883	22.8481	21.7690	10.2175	14.3255	7.4070	16.506
40	9.6106	23.5273	20.7365	10.3791	14.1615	7.8565	17.259
50	9.5023	24.3885	19.2220	14.4397	10.5660	9.0604	16.872
60	9.3901	25.5857	17.2321	15.3068	10.7129	14.5213	10.210

70	9.3021	27.4669	14.9946	16.0584	10.8732	15.2363	7.5213
80	9.2566	30.7316	14.8227	13.0864	11.0070	13.8257	7.5517
90	9.2426	34.5470	11.8128	12.2619	11.0653	13.2866	7.5287

Scan 001 dihedral =0°				Scan 002 dihedral =10°			
Ex.St.	Hole	Particle	Character	Ex.St.	Hole	Particle	Character
1			CT	1			CT
2			CT	2			CT
3			$\pi\pi^*$	3			$\pi\pi^*$
4			CT	4			CT
5			$n\pi^*$	5			$n\pi^*$
6			CT	6			CT
Scan 003 dihedral =20°				Scan 004 dihedral =30°			
Ex.St.	Hole	Particle	Character	Ex.St.	Hole	Particle	Character
1			CT	1			CT
2			CT	2			CT
3			$\pi\pi^*$	3			$\pi\pi^*$
4			CT	4			CT
5			$n\pi^*$	5			$n\pi^*$
6			CT	6			CT

Figure 1: Selected NTO orbitals relative to the relaxed scan over the dihedral angle for the six excited states of the PhenPENNMe₂ molecule. Orbitals are computed at the CAM-B3LYP/6-311G(d,p) level of theory using isodensity value of 0.04/ $e^- \cdot \text{Å}^3$.

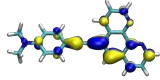
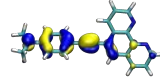
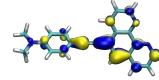
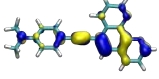
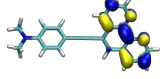
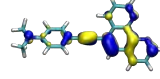
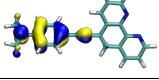
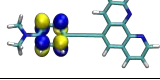
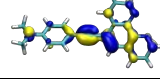
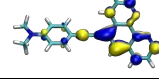
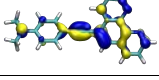
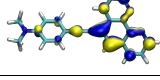
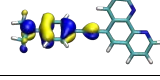
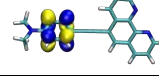
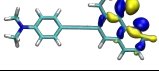
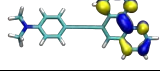
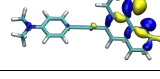
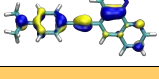
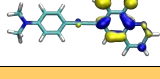
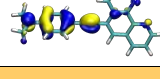
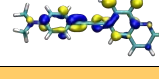
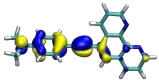
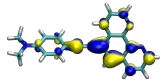
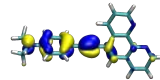
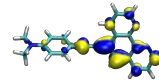
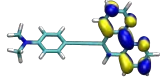
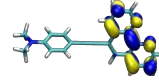
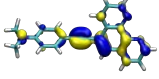
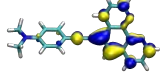
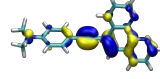
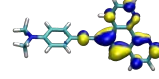
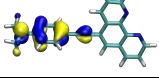
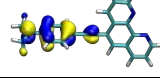
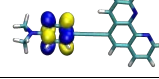
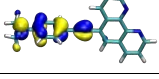
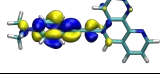
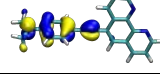
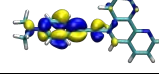
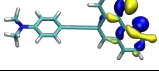
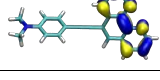
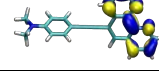
Scan 005 dihedral =40°				Scan 006 dihedral =50°			
Ex.St.	Hole	Particle	Character	Ex.St.	Hole	Particle	Character
1			CT	1			CT
2			CT	2			CT
3			$\pi\pi^*$	3			CT
4			CT	4			$\pi\pi^*$
5			$n\pi^*$	5			$n\pi^*$
6			CT	6			CT
Scan 007 dihedral =60°				Scan 008 dihedral =70°			
Ex.St.	Hole	Particle	Character	Ex.St.	Hole	Particle	Character
1			CT	1			CT
2			CT	2			CT
3			CT	3			CT
4			$\pi\pi^*$	4			$\pi\pi^*$
5			CT	5			CT
6			$n\pi^*$	6			$n\pi^*$

Figure 1: Selected NTO orbitals relative to the relaxed scan over the dihedral angle for the six excited states of the PhenPENNMe₂ molecule. Orbitals are computed at the CAM-B3LYP/6-311G(d,p) level of theory using isodensity value of 0.04/ e⁻ · Å³.

Scan 009 dihedral =80°				Scan 010 dihedral =90°			
Ex.St.	Hole	Particle	Character	Ex.St.	Hole	Particle	Character
1			CT	1			CT
2			CT	2			LE
3			LE	3			LE
4			$\pi\pi^*$	4			$\pi\pi^*$
5			LE	5			LE
6			$n\pi^*$	6			$n\pi^*$

Figure 1: Selected NTO orbitals relative to the relaxed scan over the dihedral angle for the six excited states of the PhenPENNMe₂ molecule. Orbitals are computed at the CAM-B3LYP/6-311G(d,p) level of theory using isodensity value of 0.04/ e⁻ · Å³.

Table 2: Detailed absorption energies (in nm) and oscillator strength (in a.u) data used to calculate the UV-visible absorption spectrum.

Angle (°)	ES1		ES2		ES3		ES4		ES5		ES6	
	λ (nm)	fi (a.u)										
0	360	1.6017	309	0.0391	282	0.0893	276	0.3092	269	0.0000	267	0.4874
10	359	1.5870	309	0.0381	282	0.0898	276	0.3058	269	0.0024	267	0.4796
20	357	1.5409	308	0.0352	282	0.0917	276	0.2918	270	0.0098	267	0.4599
30	351	1.4693	305	0.0293	280	0.0896	277	0.2720	270	0.0172	266	0.4519
40	346	1.3628	302	0.0237	280	0.0979	279	0.2183	270	0.0381	266	0.4444
50	339	1.2218	299	0.0172	281	0.1835	279	0.0862	270	0.1132	267	0.5081
60	331	1.0322	296	0.0107	284	0.1873	279	0.0926	271	0.6111	269	0.2598
70	323	0.7666	294	0.0052	288	0.3615	278	0.0962	273	0.9711	269	0.0267
80	315	0.3779	293	0.7561	292	0.0051	278	0.0980	275	1.0067	270	0.0039
90	311	0.0006	296	1.1481	291	0.0022	278	0.0973	276	1.0028	270	0.0002

Table 3: Detailed energy difference (in au), D_{CT} (in Bohr), q_{CT} (Q), Π data computed for each excited state.

Angle (°)	Transition S6-S5				Transition S5-S4			
	ΔE (au)	q_{CT} (Q)	D_{CT} (Bohr)	Π	ΔE (au)	q_{CT} (Q)	D_{CT} (Bohr)	Π
0	0.0017	0.931	3.542	174.909	0.0038	0.997	3.408	76.619
10	0.0017	0.920	3.635	173.119	0.0039	0.990	3.346	76.798
20	0.0017	0.875	3.946	165.629	0.0041	0.961	3.190	77.978
30	0.0021	0.830	4.302	136.202	0.0047	0.946	2.889	78.495
40	0.0021	0.753	4.921	127.469	0.0055	0.914	2.724	73.278
50	0.0018	0.632	4.849	180.674	0.0058	1.156	0.532	281.580
60	0.0012	0.462	3.701	461.716	0.0048	0.821	1.845	137.276
70	0.0025	1.071	2.849	132.739	0.0030	0.659	2.649	190.743
80	0.0036	1.131	2.193	113.516	0.0017	0.625	1.843	508.479
90	0.0039	1.138	1.980	112.513	0.0012	0.614	1.511	923.294

Angle (°)	Transition S4-S3				Transition S4-S2			
	ΔE (au)	q_{CT} (Q)	D_{CT} (Bohr)	Π	ΔE (au)	q_{CT} (Q)	D_{CT} (Bohr)	Π
0	0.004	0.754	2.857	125.166	0.018	0.659	4.902	17.302
10	0.004	0.752	2.784	133.216	0.018	0.659	4.900	17.580
20	0.003	0.744	2.544	164.747	0.017	0.658	4.868	18.630
30	0.002	0.741	2.178	331.741	0.015	0.660	4.474	22.610
40	0.001	0.763	1.958	885.463	0.013	0.659	3.923	30.142
50	0.001	0.803	1.957	789.924	0.011	0.987	3.465	26.848
60	0.003	0.868	2.142	190.202	0.010	0.965	2.661	40.422
70	0.005	0.913	2.282	89.962	0.008	0.937	1.724	73.580
80	0.008	0.917	0.894	161.945	0.008	0.912	1.670	80.815
90	0.007	0.912	0.543	276.486	0.010	0.902	0.341	326.625

Angle (°)	Transition S4-S1				Transition S4-S0			
	ΔE (au)	q_{CT} (Q)	D_{CT} (Bohr)	Π	ΔE (au)	q_{CT} (Q)	D_{CT} (Bohr)	Π
0	0.039	0.511	6.053	8.360	0.165	0.463	4.866	2.683
10	0.038	0.509	6.183	8.292	0.165	0.456	4.826	2.751
20	0.037	0.505	6.602	8.085	0.165	0.437	4.671	2.972
30	0.035	0.502	6.990	8.228	0.164	0.424	4.302	3.336
40	0.032	0.520	7.259	8.376	0.163	0.422	4.279	3.384
50	0.028	0.923	6.005	6.338	0.163	0.596	0.700	14.722
60	0.026	0.958	6.208	6.566	0.163	0.596	0.894	11.492
70	0.022	1.007	6.578	6.756	0.164	0.592	1.068	9.658
80	0.019	1.097	7.163	6.650	0.164	0.592	1.179	8.743
90	0.017	1.212	7.719	6.176	0.164	0.592	1.222	8.429

Angle (°)	Transition S3-S2				Transition S3-S1			
	ΔE (au)	q_{CT} (Q)	D_{CT} (Bohr)	Π	ΔE (au)	q_{CT} (Q)	D_{CT} (Bohr)	Π
0	0.014	1.041	5.052	13.396	0.035	0.868	5.691	5.785
10	0.014	1.040	5.013	13.662	0.035	0.871	5.709	5.794
20	0.014	1.031	4.891	14.634	0.034	0.876	5.775	5.832
30	0.013	1.020	4.474	16.728	0.033	0.884	5.730	6.033
40	0.012	1.008	4.043	20.320	0.031	0.902	5.825	6.170
50	0.010	0.646	2.920	52.514	0.028	0.545	7.290	9.101
60	0.007	0.630	1.311	178.030	0.023	0.573	7.137	10.736
70	0.003	0.614	1.029	514.122	0.017	0.631	7.203	12.944
80	0.001	0.555	1.365	2213.650	0.012	1.079	6.570	12.150
90	0.003	0.438	0.432	2001.711	0.010	1.247	7.157	11.207

Angle (°)	Transition S3-S0				Transition S2-S1			
	ΔE (au)	q_{CT} (Q)	D_{CT} (Bohr)	Π	ΔE (au)	q_{CT} (Q)	D_{CT} (Bohr)	Π
0	0.162	0.606	0.176	57.944	0.021	0.731	1.131	58.237
10	0.162	0.607	0.189	53.933	0.021	0.732	1.091	60.583
20	0.162	0.603	0.238	43.112	0.020	0.734	1.028	65.137
30	0.162	0.602	0.348	29.347	0.020	0.742	1.194	57.455
40	0.163	0.601	0.510	20.058	0.019	0.761	1.822	38.411
50	0.162	0.440	4.513	3.104	0.018	0.790	2.837	25.390
60	0.161	0.478	5.002	2.606	0.016	0.844	4.102	18.093
70	0.158	0.513	5.303	2.323	0.014	0.930	5.458	14.148
80	0.156	0.408	3.705	4.238	0.011	0.804	7.893	14.316
90	0.157	0.386	3.075	5.379	0.007	1.081	8.394	14.974

Angle (°)	Transition S2-S0				Transition S1-S0			
	ΔE (au)	q_{CT} (Q)	D_{CT} (Bohr)	Π	ΔE (au)	q_{CT} (Q)	D_{CT} (Bohr)	Π
0	0.147	0.726	7.366	1.269	0.127	0.650	7.715	1.577
10	0.148	0.722	7.358	1.276	0.127	0.653	7.744	1.560
20	0.148	0.708	7.324	1.302	0.128	0.662	7.842	1.508
30	0.149	0.676	7.057	1.404	0.130	0.672	7.829	1.466
40	0.151	0.644	6.818	1.511	0.132	0.698	7.975	1.362
50	0.152	0.597	6.433	1.711	0.135	0.732	8.141	1.248
60	0.154	0.537	5.777	2.098	0.138	0.781	8.300	1.120
70	0.155	0.466	4.821	2.865	0.141	0.855	8.497	0.975
80	0.156	0.477	4.670	2.886	0.145	0.984	8.701	0.808
90	0.154	0.398	2.551	6.396	0.147	1.140	8.830	0.678

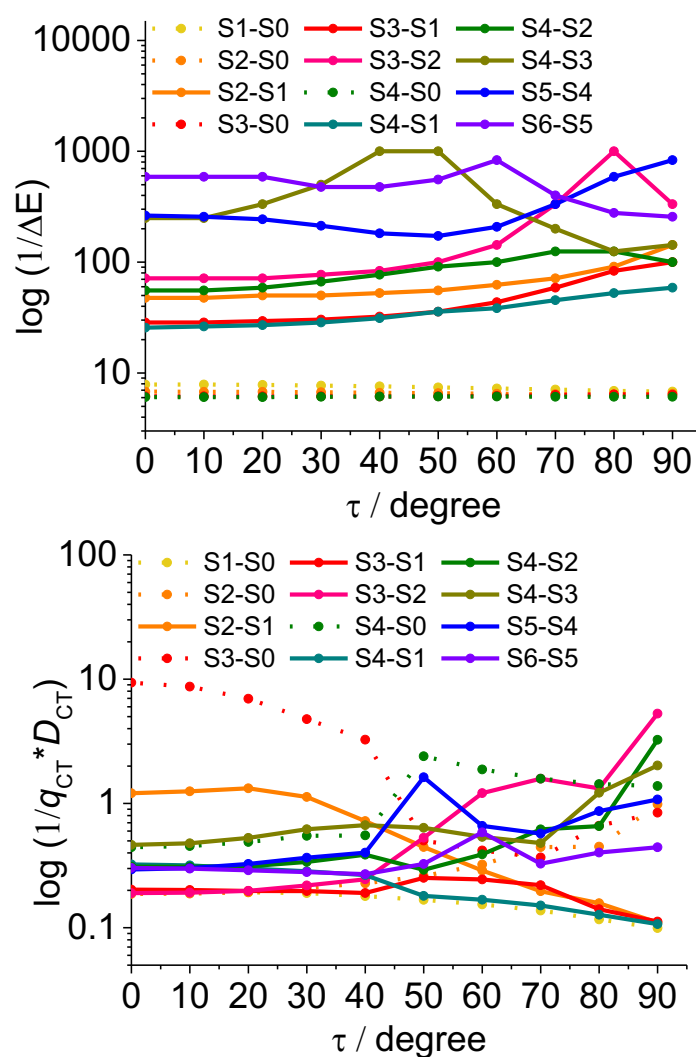


Figure 2: (Left) The Evolution of $1/\Delta E$ (in $1/\text{a.u.}$) (in logarithm scale) along the reaction coordinated (the dihedral angle τ). (Right) The evolution of $1/D_{CT} * q_{CT}$ (in $1/\text{Bohr} * \text{Q}$) (in logarithm scale).

Table 5: Detailed emission energies (in nm) and oscillator strength (in a.u) data used to calculate the UV-visible emission spectrum.

Angle (°)	ES1		ES2		ES3		ES4		ES5		ES6	
	λ (nm)	fi (a.u)										
0	447	1.7338	340	0.0631	300	0.3684	287	0.1335	284	0.2561	275	0.0044
10	446	1.7200	339	0.0618	300	0.3664	287	0.1375	285	0.2312	275	0.0214
20	444	1.6776	338	0.0584	301	0.3541	287	0.1853	286	0.1624	275	0.0628
30	440	1.6073	336	0.0527	303	0.3174	288	0.3037	287	0.0864	275	0.1353
40	434	1.5091	333	0.0449	307	0.2595	290	0.4185	286	0.0961	276	0.2828
50	427	1.3807	329	0.0333	312	0.2384	292	0.5729	286	0.0961	276	0.3520
60	419	1.2116	325	0.0089	318	0.2690	294	0.7471	285	0.0956	277	0.3023
70	409	0.9753	326	0.3046	319	0.0923	296	0.8968	285	0.0956	278	0.2357
80	400	0.6454	333	0.6097	315	0.0378	299	1.0216	284	0.0973	278	0.1529
90	390	0.0361	340	1.2438	308	0.0179	303	1.1154	285	0.1013	281	0.0196

Appendix to Chapter 8

Table 6 Energies, oscillator strength (f), and transition dipole moments (total and module of x,y,z components) for the 2-molecule model embedded in the crystal field.

transition	wavelength / nm	f	trans. dipole	components of trans. dipole (absolute value)		
				x	y	z
1	593	0.41	7.91	1.62	1.21	1.96
2	516	0.05	0.78	0.55	0.35	0.59
5	465	0.43	6.60	1.58	1.05	1.73
10	385	0.52	6.62	1.49	1.14	1.76
11	376	0.01	0.17	0.03	0.25	0.34
27	313	0.03	0.32	0.11	0.42	0.37

Table 7 Energies, oscillator strength (f), and transition dipole moments (total and absolute value of x,y,z components) for the 2-molecule model embedded in the crystal field at different values of the translation along x-axis.

X-axis

translation=0.0 Å

transition	wavelength / nm	f	trans. Dipole			
				x	y	z
1	593	0.41	7.91	1.62	1.21	1.96
2	516	0.05	0.78	0.55	0.35	0.59
5	465	0.43	6.60	1.58	1.05	1.73
10	385	0.52	6.62	1.49	1.14	1.76
11	376	0.01	0.17	0.03	0.25	0.34
27	313	0.03	0.32	0.11	0.42	0.37

translation=0.1 Å

transition	wavelength / nm	f	trans. Dipole	x	y	z
1	590	0.39	7.58	1.58	1.18	1.92
2	517	0.06	0.99	0.61	0.4	0.67
5	465	0.44	6.72	1.6	1.05	1.74
10	387	0.51	6.46	1.48	1.13	1.73
11	375	0.01	0.18	0.01	0.24	0.36
27	314	0.03	0.31	0.12	0.42	0.35

translation=0.2 Å

transition	wavelength / nm	f	trans. Dipole	x	y	z
1	587	0.37	7.07	1.52	1.14	1.86
2	518	0.08	1.35	0.71	0.47	0.79
5	464	0.45	6.87	1.61	1.08	1.76
10	389	0.49	6.22	1.46	1.11	1.69
11	372	0.02	0.19	0.01	0.24	0.36
27	315	0.01	0.07	0.02	0.21	0.16

translation=0.3 Å

transition	wavelength / nm	f	trans. Dipole	x	y	z
1	587	0.37	6.37	1.43	1.08	1.77
2	518	0.08	1.89	0.83	0.56	0.93
5	464	0.45	5.76	1.48	0.99	1.61
10	389	0.49	5.90	1.43	1.08	1.63
11	372	0.02	0.19	0.02	0.25	0.35
27	315	0.01	0.06	0.07	0.17	0.15

translation=0.4 Å

transition	wavelength / nm	f	trans. Dipole	x	y	z
1	583	0.33	6.37	1.43	1.08	1.77
2	520	0.11	1.89	0.83	0.56	0.93
5	462	0.38	5.76	1.48	0.99	1.61
10	392	0.46	5.90	1.43	1.08	1.63
11	371	0.02	0.19	0.02	0.25	0.35
27	317	0.01	0.06	0.07	0.17	0.15

translation=0.5 Å

transition	wavelength / nm	f	trans. Dipole	x	y	z
1	578	0.28	5.42	1.31	1	1.64
2	521	0.15	2.65	0.98	0.68	1.11
5	455	0.04	0.53	0.48	0.28	0.48
10	395	0.00	0.01	0.08	0.07	0.05
11	369	0.01	0.19	0.03	0.26	0.34
27	319	0.00	0.04	0.05	0.16	0.11

translation=0.6
Å

transition	wavelength / nm	f	trans. Dipole	x	y	z
1	574	0.28	4.22	1.14	0.88	1.46
2	520	0.15	3.64	1.13	0.79	1.31
5	447	0.04	0.10	0.22	0.1	0.19
10	392	0.00	0.00	0.03	0.03	0.01
11	366	0.01	0.18	0.03	0.26	0.33
27	319	0.00	0.02	0.03	0.02	0.13

Bibliography

- [1] A. Kamkaew, S.H. Lim, H.B. Lee, L.V. Kiew, L.Y. Chung and K. Burgess, "BODIPY dyes in photodynamic therapy", Chemical Society Reviews, vol. 42, no. 1, pp. 77-88, 2013.
- [2] M.E. Alberto, N. Russo and C. Adamo, "The contribution of computational studies to photodynamic therapy: Challenges and opportunities for the future of computational prediction", Photodiagnosis and Photodynamic Therapy, vol.17, p. A52, 2017.
- [3] L.Ying, C.-L. Ho, H. Wu, Y. Cao and W.-Y. Wong, "White Polymer Light-Emitting Devices for Solid State Lighting: Material, Devices, and Recent Progress", Advanced Materials, vol. 26, no. 16, pp. 2459-2473, 2014.
- [4] H. Sasabe and J. Kido, "Recent Progress in Phosphorescent Organic Light-Emitting Devices", European Journal of Organic Chemistry, vol. 2013, no. 34, pp. 7653-7663, 2013.
- [5] M. Garavelli, "Computational Organic Photochemistry: Strategy, Achievements and Perspectives", Theoretical Chemistry Accounts, vol. 116, pp. 87-105, 2006.
- [6] C. Curutchet and B. Mennucci, "Quantum Chemical Studies of Light Harvesting", Chemical Reviews, vol. 117, pp. 294-343, 2016.
- [7] A. Hagfeldt, G. Boschloo, L. Sun, L. Kloo and H. Pettersson, "Dye-Sensitized Solar Cells", Chemical Reviews, vol. 110, no. 11, pp. 6595-6663, 2010.
- [8] C. Daniel, "Photochemistry and Photophysics of transition metal complexes: Quantum Chemistry", Coordination Chemistry Reviews, vol. 282-283, pp. 19-32, 2015.
- [9] C.A. Ullrich and Z. -H. Yang, "A Brief Compendium of Time-Dependent Density Functional Theory", Brazilian Journal of Physics, vol. 44, pp. 154-188, 2014.
- [10] L. Kronik, T. Stein, S. Refaely-Ambrahamson and R. Bear, "Excitation Gaps of Finite-Sized Systems from Optimally Tuned Range Separated Hybrid Functionals", Journal of Chemical Theory and Computation, vol. 8, pp. 1515-1531, 2012.
- [11] T. Stein, L. Kronik and R. Bear, "Reliable prediction of charge transfer excitations in molecular complexes using time-dependent density functional theory", Journal of the American Chemical Society, vol. 131, pp. 2818-2820, 2009.
- [12] D.J. Tozer, "Relationship between long-range charge-transfer excitation energy error and integer discontinuity in Kohn-Sham theory", The Journal of Chemical Physics, vol. 119, pp. 12697-12699, 2003.
- [13] S. Tretiak, K. Igumenshchev and V. Chernyak, "Exciton size of conducting polymers predicted by time dependent density functional theory", Physical Review B, vol. 71, p.3171, 2005.
- [14] C.A. Ullrich, Time-Dependent Density Functional Theory: Concepts and Applications. Oxford Graduate Texts, Oxford: Oxford University Press, 2011.
- [15] M. Born and R. Oppenheimer, "Zur quantentheorie der molekeln", Annalen der Physik, vol. 389, pp. 457-484, 1927.
- [16] D. R. Hartree, "The wave mechanics of an atom with a non-coulomb central field. Part I. Theory and Methods. In Mathematical Proceedings of the Cambridge Philosophical Society", Cambridge Univ Press, vol. 24, pp. 89-110, 1928.
- [17] C. C. J. Roothaan, "New developments in molecular orbital theory", Reviews of modern physics, vol. 23, p. 69, 1951.
- [18] C. J. Cramer, "Essentials of computational chemistry: theories and models", John Wiley & Sons, 2013.

- [19] P. Hohenberg and W. Kohn, "Inhomogeneous electron gas", Physical review, vol. 136, p. B864, 1964.
- [20] S. H. Vosko, L. Wilk and M. Nusair, "Accurate spin-dependent electron liquid correlation energies for local spin density calculations: a critical analysis", Canadian Journal of physics, vol. 58, pp. 1200-1211, 1980.
- [21] J. P. Perdew, K. Burke and M. Ernzerhof, "Generalized gradient approximation made simple", Physical review letters, vol. 77, p. 3865, 1996.
- [22] A. D. Becke, "Density-functional thermochemistry. III. The role of exact exchange", The Journal of Chemical Physics, vol. 98, pp. 5648-52, 1993.
- [23] C. Adamo and V. Barone, "Toward reliable density functional methods without adjustable parameters: The PBE0 model", The Journal of Chemical Physics, vol. 110, p. 6158, 1999.
- [24] H. Iikura, T. Tsuneda, T. Yanai and K. Hirao, "A long-range correction scheme for generalized-gradient-approximation exchange functionals", The Journal of Chemical Physics, vol. 115, p. 3540, 2001.
- [25] T. Yanai, D.P. Tew and N.C. Handy, "A new hybrid exchange-correlation functional using the Coulomb-attenuating method (CAM-B3LYP)", Chemical Physics Letters, vol. 393, p. 51, 2004.
- [26] T. Schwabe, S. Grimme, "Double-hybrid density functionals with long-range dispersion corrections: higher accuracy and extended applicability", Physical Chemistry Chemical Physics, vol. 9, pp. 3397-3406, 2007.
- [27] E. Runge and E.K.U. Gross, "Density-functional theory for time-dependent systems", Physical Review Letters, vol. 52, p. 997, 1984.
- [28] C. A. Ullrich, "Time-dependent density-functional theory: concepts and applications", OUP Oxford, 2011.
- [29] M. E. Casida, "Time-dependent density functional response theory of molecular systems: theory, computational methods, and functionals" in Recent developments and applications in density functional theory, 1996.
- [30] A. Dreuw, J. L. Weisman and M. H. Gordon, "Long-range charge-transfer excited states in time-dependent density functional theory require non-local exchange", The Journal of Chemical Physics, vol. 119, pp. 2943-2946, 2003.
- [31] R.S. Mulliken, "Molecular Compounds and their Spectra. II", Journal of the American Chemical Society, vol. 74, pp. 811-824, 1952.
- [32] T. Koopmans, "über die Zuordnung von Wellenfunktionen und Eigenwerten zu den Einzelnen Elektronen Eines Atoms", Physica, vol. 1, no. 1-6, pp. 104-113, 1933.
- [33] C. J. Cramer and D. G. Truhlar, "Implicit solvation models: equilibria, structure, spectra, and dynamics", Chemical Reviews, vol. 99, pp. 2161-2200, 1999.
- [34] V. Barone and M. Cossi, "Quantum calculation of molecular energies and energy gradients in solution by a conductor solvent model", The Journal of Physical Chemistry A, vol. 102, pp. 995-2001, 1998.
- [35] R. Cammi, S. Corni, B. Mennucci and J. Tomasi, "Electronic excitation energies of molecules in solution: State specific and linear response methods for nonequilibrium continuum solvation models", The Journal of Chemical Physics, vol. 122, p. 104513, 2005.
- [36] R. Improta, V. Barone, G. Scalmani and M. J. Frisch, "A state-specific polarizable continuum model time dependent density functional theory method for excited state calculations in solution", The Journal of Chemical Physics, vol. 125, p. 054103, 2006.
- [37] A. V. Luzanov, "The excited state as the superposition of singly excited configurations in the density matrix formalism", Theoretical and Experimental Chemistry, vol. 9, pp. 567-574, 1975.
- [38] A. V. Luzanov, A. A. Sukhorukov, and V. Umanskii, "Application of transition density matrix for analysis of excited states", Theoretical and Experimental Chemistry, vol. 10, pp. 354-361, 1976.
- [39] A. V. Luzanov, "Charge Transfer and Localization during electronic excitation of molecules", Theoretical and Experimental Chemistry, vol. 13, pp. 433-440, Sept. 1978.

- [40] M. Head-Gordon, A. M. Grana, D. Maurice, and C. A. White, "Analysis of electronic transitions as the difference of electron attachment and detachment densities," The Journal of Physical Chemistry, vol. 99, pp. 14261-14270, 1995.
- [41] M. J. G. Peach, C. R. L. Sueur, K. Ruud, M. Guillaume and D. J. Tozer, "TDDFT diagnostic testing and functional assessment for triazenechromophores", Physical Chemistry Chemical Physics, vol. 11, pp. 4465-4470, 2009
- [42] M. J. G. Peach and D. J. Tozer, "Overcoming Low Orbital Overlap and Triplet Instability Problems in TDDFT", The Journal of Physical Chemistry A, vol. 116, pp. 9783-9789, 2012.
- [43] D. Cappelletti, E. Ronca, L. Belpassi, F. Tarantelli and F. Pirani, "Revealing Charge-Transfer Effects in Gas-Phase Water Chemistry", Accounts of Chemical Research, vol. 45, no. 9, pp. 1571-1580, 2012.
- [44] E. Ronca, M. Pastore, L. Belpassi, F. De Angelis, C. Angeli, R. Cimraglia and F. Tarantelli, "Charge-displacement analysis for excited states", The Journal of Chemical Physics, vol. 140, no. 5, p. 054110, 2014.
- [45] F. Plasser and H. Lischka, "Analysis of Excitonic and Charge Transfer Interactions from Quantum Chemical Calculations", Journal of Chemical Theory and Computation, vol. 8, pp. 2777-2789, 2012.
- [46] C. A. Guido, P. Cortona, B. Mennucci and C. Adamo, "On the Metric of Charge Transfer Molecular Excitations: A Simple Chemical Descriptor", Journal of Chemical Theory and Computation, vol. 9, pp. 3118-3126, 2013.
- [47] C. A. Guido, P. Cortona and C. Adamo, "Effective electron displacements: A tool for time-dependent density functional theory computational spectroscopy", The Journal of Chemical Physics, vol. 140, p. 104101, 2014.
- [48] T. Etienne, X. Assfeld and A. Monari, "Toward a Quantitative Assessment of Electronic Transitions Charge-Transfer Character", Journal of Chemical Theory and Computation, vol. 10, p. 3896-3905, 2014.
- [49] T. Etienne, X. Assfeld and A. Monari, "New Insight into the Topology of Excited states through detachment/attachment", Journal of Chemical Theory and Computation, vol. 10, p. 3906-39014, 2014.
- [50] F. Plasser, M. Wormit and A. Dreuw, "New tools for the systematic analysis and visualization of electronic excitations. I. Formalism:", The Journal of Chemical Physics, vol. 141, pp. 024106-14, 2014.
- [51] F. Plasser, S. A. B  ppler, M. Wormit and A. Dreuw, "New tools for the systematic analysis and visualization excitations. II. Applications", The Journal of Chemical Physics, vol. 141, pp. 024107-13, 2014.
- [52] S. A. B  ppler, F. Plasser, M. Wormit and A. Dreuw, "Exciton analysis of many-body wave function: bridging the gap between the quasiparticle and molecular orbital pictures", Physical Review A, vol. 90, p. 052521, 2014.
- [53] F. Plasser, B. Thomitzni, S.A. B  ppler, J. Wenzel, D.R. Rehn, M. Wormit and A. Dreuw, "Statistical analysis of electronic excitation processes: Spatial location, compactness, charge transfer and electron-hole correlation", Journal of Computational Chemistry, vol. 36, p. 1609-1620, 2015.
- [54] S. Mewes, F. Plasser, A. Krylov and A. Dreuw, "Benchmarking Excited state calculations using exciton properties", Journal of Chemical Theory and Computation, vol. 14, p. 710-725, 2018.
- [55] T. Le Bahers, C. Adamo and I. Ciofini, "A Qualitative Index of Spatial Extent in Charge-Transfer Excitations", Journal of Chemical Theory and Computation, vol. 7, pp. 2498-2506, 2011.
- [56] I. Ciofini, T. Le Bahers, C. Adamo, F. Odobel and D. Jacquemin, "Through-Space Charge Transfer in Rod-Like Molecules: Lessons from Theory", The Journal of Physical Chemistry C, vol. 116, pp. 11946-11955, 2012.
- [57] D. Jacquemin, T. Le Bahers, C. Adamo and I. Ciofini, "What is the "best" atomic charge model to describe through-space charge-transfer excitations?" Physical Chemistry Chemical Physics, vol. 14, pp. 5383-5388, 2012.
- [58] C. Adamo, T. Le Bahers, M. Savarese, L. Wilbraham, G. Garc  a, R. Fukuda, M. Ehara, N. Rega and I. Ciofini, "Exploring excited states using Time Dependent Density Functional Theory and density-based indexes", Coordination Chemistry Reviews, vol. 304-305, pp. 166-178, 2015.

- [59] M. Ehara, R. Fukuda, C. Adamo and I. Ciofini, "Chemically Intuitive Indices for Charge-Transfer Excitation Based on SAC-CI and TD-DFT Calculations", Journal of Computational Chemistry, vol. 34, pp. 2498–2501, 2013.
- [60] J. Sanz García, F. Maschietto, M. Campetella and I. Ciofini, "Using Density Based Indexes and Wave Function Methods for the Description of Excited States: Excited State Proton Transfer Reactions as a Test Case", The Journal of Physical Chemistry A, vol. 122, pp. 375–382, 2018.
- [61] F. Maschietto, M. Campetella, M. J. Frisch, G. Scalmani, C. Adamo and Ciofini, "How Are the Charge Transfer Descriptors Affected by the Quality of the Underpinning Electronic Density?", Journal of Computational Chemistry, vol. 39, pp. 735–742, 2018.
- [62] M. Savarese, P. A. Netti, C. Adamo, N. Rega and Ilaria Ciofini, "Exploring the Metric of Excited State Proton Transfer Reactions", The Journal of Physical Chemistry B, vol. 117, pp. 16165–16173, 2013.
- [63] M. Savarese, U. Raucci, P. A. Netti, C. Adamo, Ilaria Ciofini and N. Rega, "Modeling of charge transfer processes to understand photophysical signatures: The case of Rhodamine 110", Chemical Physics Letters, vol. 610–611, pp. 148–152, 2014.
- [64] A. Dreuw, J.L. Weisman and M. Head-Gordon, "Long-range charge-transfer excited states in time-dependent density functional theory require non-local exchange", Journal of Chemical Physics, vol. 119, pp. 2943–2946, 2003.
- [65] A. Dreuw and M. Head-Gordon, "Failure of Time-Dependent Density Functional Theory for Long-Range Charge-Transfer Excited States: The Zincbacteriochlorin-Bacteriochlorin and Bacteriochlorophyll-Spheroidene Complexes", Journal of the American Chemical Society, vol. 126, pp. 4007–4016, 2004.
- [66] M. Campetella, F. Maschietto, M. J. Frisch, G. Scalmani, I. Ciofini and Carlo Adamo, "Charge Transfer Excitations in TDDFT: A Ghost-Hunter Index", Journal of Computational Chemistry, 2017.
- [67] M. Savarese, U. Raucci, P.A., Netti, C. Adamo, N. Rega and I. Ciofini, "A Qualitative Model to Identify Non-Radiative Decay Channels: The spiropyran as case study", Theoretical Chemistry Accounts, vol. 135, pp. 1–7, 2016.
- [68] F. Maschietto, J. S. García, M. Campetella and I. Ciofini, "Using density-based indexes to characterize excited states evolution", Journal of Computational Chemistry, 2018.
- [69] M. Campetella, A. Perfetto and I. Ciofini, "Quantifying partial hole-particle distance at the excited state: A revised version of the D_{CT} index", Chemical Physics Letters, vol. 714, pp. 81–86, 2019.
- [70] M.E. Casida, *Recent Advances in Density Functional Methods, Part I*, World Scientific, Singapore, 1995.
- [71] E.U.K. Gross, J.F. Dobson, M. Petersilka, *Density Functional Theory II*, Springer, Heidelberg, 1996.
- [72] A. Dreuw, M. Head-Gordon, "Comment on: 'Failure of time-dependent density functional methods for excitations in spatially separated systems' by Wolfgang HIERINGER and Andreas GÖRLING", Chemical Physics Letters, vol. 426, pp. 231–233, 2006.
- [73] E. J. Baerends and O. V. Gritsenko, "A Quantum Chemical View of Density Functional Theory", The Journal of Physical Chemistry A, vol. 101, pp. 5383–5403, 1997.
- [74] M. Rudolph, T. Ziegler, J. Autschbach, "Time-dependent density functional theory applied to ligand-field excitations and their circular dichroism in some transition metal complexes", Chemical Physics, vol. 391, p. 92, 2011.
- [75] M. E. Casida, C. Jamorski, K. C. Casida, and D. R. Salahub, "Molecular excitation energies to high-lying bound states from time-dependent density-functional response theory: Characterization and correction of the time-dependent local density approximation ionization threshold", The Journal of Chemical Physics, vol. 108, p. 4439, 1998.
- [76] D. J. Tozer and N. C. Handy, "Improving virtual Kohn–Sham orbitals and eigenvalues: Application to excitation energies and static polarizabilities", The Journal of Chemical Physics, vol. 109, p. 10180, 1998.
- [77] Y. Tawada, T. Tsuneda and S. Yanagisawa, "A long-range-corrected time-dependent density functional theory", The Journal of Chemical Physics, vol. 120, p. 8425, 2004.

- [78] E. Tapavicza, A.M. Meyera, F. Furche, "Unravelling the details of vitamin D photosynthesis by non-adiabatic molecular dynamics simulations", Physical Chemistry Chemical Physics, vol. 13, p. 20986, 2011.
- [79] V. Lemaur, M. Steel, D. Beljonne, J.L. Bredas, J. Cornil, "Photoinduced Charge Generation and Recombination Dynamics in Model Donor/Acceptor Pairs for Organic Solar Cell Applications: A Full Quantum-Chemical Treatment", Journal of the American Chemical Society, vol. 127, no. 16, pp. 6077-6086, 2005.
- [80] F.M. Raymo, "Digital Processing and Communication with Molecular Switches", Advanced Materials, vol. 14, p. 401, 2002.
- [81] J.M. Smieja, E.E. Benson, B. Kumar, K.A. Grice, C.S. Seu, A.J.M. Miller, J.M. Mayer and C.P. Kubiak, "Kinetic and structural studies, origins of selectivity, and interfacial charge transfer in the artificial photosynthesis of CO", PNAS, vol. 109, p. 15646, 2012.
- [82] M. Savarese, C.A. Guido, E. Bremond, I. Ciofini and C. Adamo, "Metrics for Molecular Electronic Excitations: A Comparison between Orbital- and Density-Based Descriptors.", The Journal of Physical Chemistry. A, vol. 121, p. 7543, 2017.
- [83] M.Y. Wong and E. Zysman-Colman, "Purely Organic Thermally Activated Delayed Fluorescence Materials for Organic Light-Emitting Diodes", Advanced Materials, vol. 29, p. 1605444, 2017.
- [84] J. Lee, K. Shizu, H. Tanaka, H. Nakanotani, T. Yasuda, H. Kajic and C.J. Adachi, "Controlled emission colors and singlet-triplet energy gaps of dihydrophenazine-based thermally activated delayed fluorescence emitters", Journal of Materials Chemistry C, vol. 3, p. 2175, 2015.
- [85] J. Zhang, Z. Chen, L. Yang, F.F. Pan, G. Yu, J. Yin and S.H. Liu, "Elaborately Tuning Intramolecular Electron Transfer Through Varying Oligoacene Linkers in the Bis(diarylamino) Systems", Scientific Reports, vol. 6, p. 36310, 2016.
- [86] CTM Group, www.quanthich.fr.
- [87] M.M. Francl, W.J. Pietro, W.J. Hehre, J.S. Binkley, M.S. Gordon, D.J. Defrees and J.A. Pople, "Self-consistent molecular orbital methods. XXIII. A polarization-type basis set for second-row elements", The Journal of Chemical Physics, vol. 77, p. 3654, 1982.
- [88] M.J. Frisch, G.W. Trucks, H.B. Schlegel, G.E. Scuseria, M.A. Robb, J.R. Cheeseman, G. Scalmani, V. Barone, G.A. Petersson, H. Nakatsuji, X. Li, M. Caricato, A.V. Marenich, J. Bloino, B.G. Janesko, R. Gomperts, B. Mennucci, H.P. Hratchian, J.V. Ortiz, A.F. Izmaylov, J.L. Sonnenberg, D. Williams-Young, F. Ding, F. Lipparini, F. Egidi, J. Goings, B. Peng, A. Petrone, T. Henderson, D. Ranasinghe, V.G. Zakrzewski, J. Gao, N. Rega, G. Zheng, W. Liang, M. Hada, M. Ehara, K. Toyota, R. Fukuda, J. Hasegawa, M. Ishida, T. Nakajima, Y. Honda, O. Kitao, H. Nakai, T. Vreven, K. Throssell, J.A. Montgomery Jr., J.E. Peralta, F. Ogliaro, M.J. Bearpark, J. J. Heyd, E.N. Brothers, K.N. Kudin, V.N. Staroverov, T.A. Keith, R. Kobayashi, J. Normand, K. Raghavachari, A.P. Rendell, J.C. Burant, S.S. Iyengar, J. Tomasi, M. Cossi, J.M. Millam, M. Klene, C. Adamo, R. Cammi, J.W. Ochterski, R.L. Martin, K. Morokuma, O. Farkas, J.B. Foresman, D.J. Fox, Gaussian, Inc., Wallingford CT, 2016.
- [89] A. Perfetto, L. Huet, F. Muniz-Miranda, M. Campetella, C. Adamo and Ilaria Ciofini, "General Density-Based Index to Analyze Charge Transfer Phenomena: From Models to Butterfly Molecules", Journal of Chemical Theory and Computation, vol. 16, no.7, pp. 4543-4553, 2020.
- [90] S. Kraner, R. Scholz, C. Koerner and K. Leo, "Design Proposals for Organic Materials Exhibiting a Low Exciton Binding Energy", The Journal of Physical Chemistry C, vol. 119, pp. 22820-22825, 2015.
- [91] J. Chen, M. Yan, Y. Tang, J. Yu, W. Xu, Y. Fu, H. Cao, Q. He and J. Cheng, "Rational Construction of Highly Tunable Organic Charge-Transfer Complexes for Chemiresistive Sensor Applications", ACS Applied Bio Materials, vol. 2, pp. 3678-3685, 2019.
- [92] T. Salzillo, A. Capos and M. Mas-Torrent, "Solution-processed thin films of a charge transfer complex for ambipolar field-effect transistors", Journal of Materials Chemistry C, vol. 7, pp. 10257-10263, 2019.
- [93] A. Cannizzo, "Ultrafast UV spectroscopy: From a local to a global view of dynamical processes in macromolecules", Physical Chemistry Chemical Physics, vol. 14, pp. 11205-11223, 2012.
- [94] A. Stolow, A.E. Bragg and D. M. Neumark, "Femtosecond time-resolved photoelectron spectroscopy", Chemical Reviews, vol. 104, pp. 1719-1758, 2004.

- [95] C. Adamo and D. Jacquemin, "The calculations of excited-state properties with Time-Dependent Density Functional Theory", Chemical Society Reviews, vol. 42, pp. 845-856, 2013.
- [96] P. Elliott, F. Furche and K. Burke, "Excited States from Time-Dependent Density Functional Theory". In Reviews in Computational Chemistry. Lipkowitz, K.B.; Cundari, T.R. Eds.; Wiley: Hoboken, NJ, vol. 26; p. 91, 2008.
- [97] R. L. Martin, "Natural transition orbitals", The Journal of Chemical Physics, vol. 118, pp. 4775-4777, 2003.
- [98] S. Chibani, B. Le Guennic, A. Charaf-Eddin, A.D. Laurenta and D. Jacquemin, "Revisiting the optical signatures of BODIPY with ab initio tools", Chemical Science, vol. 4, pp. 1950-1963, 2013.
- [99] B.J. Coe, A. Avramopoulos, M.G. Papadopoulos, K. Pierloot, S. Vancoillie and H. Reis, "Theoretical Modelling of Photoswitching of Hyperpolarisabilities in Ruthenium Complexes", Chemistry – A European Journal, vol. 19, pp. 15955-15963, 2013.
- [100] S. De Sousa, L. Ducasse, B. Kauffmann, T. Toupance and C. Olivier, "Functionalization of a Ruthenium-Diacetylide Organometallic Complex as a Next-Generation Push-Pull Chromophore", Chemistry – A European Journal, vol. 20, pp. 7017-7024, 2014.
- [101] S. De Sousa, S. Lyu, L. Ducasse, T. Toupance and C. Olivier, "Tuning visible-light absorption properties of Ru-diacetylide complexes: simple access to colorful efficient dyes for DSSCs", Journal of Materials Chemistry A, vol. 3, pp. 18256-18264, 2015.
- [102] M. Oлару, E. Rychagova, S. Ketkov, Y. Shynkarenko, S. Yakunin, M.V. Kovalenko, A. Yablonskiy, B. Andreev, F. Kleemiss, J. Beckmann and M. Vogt, "A Small Cationic Organo-Copper Cluster as Thermally Robust Highly Photo- and Electroluminescent Material", Journal of the American Chemical Society, vol. 142, pp. 373-381, 2020.
- [103] A.D. Laurent and D. Jacquemin, "Analyzing excited-state processes and optical signatures of a ratiometric fluorine anion sensor: a quantum look", Science China Chemistry, vol. 5, pp. 1363-1368, 2014.
- [104] X. Lu, Y. Shao, S. Wei, Z. Zhao, K. Li, C. Guo, W. Wang, M. Zhang and W. Guo, "Effect of the functionalized π -bridge on porphyrin sensitizers for dye-sensitized solar cells: an in-depth analysis of electronic structure, spectrum, excitation, and intramolecular electron transfer", Journal of Materials Chemistry C, vol. 3, pp. 10129-10139, 2015.
- [105] V. Venkatraman, M. Foscatto, V.R. Jensen and B.K. Alsberg, "Evolutionary de novo design of phenothiazine derivatives for dye-sensitized solar cells", Journal of Materials Chemistry A, vol. 3, pp. 9851-9860, 2015.
- [106] Y. Olivier, J.-C. Sancho-Garcia, L. Muccioli, G. D'Avino and D. Beljonne, "Computational Design of Thermally Activated Delayed Fluorescence Materials: The Challenges Ahead", The Journal of Physical Chemistry Letters, vol. 9, pp. 6149-6163, 2018.
- [107] A. Al Mamun, M.J. Toda, P. Lodowski, M. Jaworska and P.M. Kozlowski, "Mechanism of Light Induced Radical Pair Formation in Coenzyme B12-Dependent Ethanolamine Ammonia- Lyase", ACS Catalysis, vol. 8, pp. 7164-7178, 2018.
- [108] T. Lu and F. Chen, "Multiwfn: A multifunctional wavefunction analyzer", Journal of Computational Chemistry, vol. 33, pp. 580-592, 2012.
- [109] S. Sharifzadeh, P. Darancet, L. Kronik and J.B. Neaton, "Low-energy charge-transfer excitons in organic solids from first-principles: The case of pentacene", Journal of Physical Chemistry Letters, vol. 4, pp. 2197-2201, 2013.
- [110] G. García, C. Adamo and I. Ciofini, "Evaluating push-pull dye efficiency using TD-DFT and charge transfer indices", Physical Chemistry Chemical Physics, vol. 15, pp. 20210-20219, 2013.
- [111] H. H. Heinze, A. Görling, N. Rösch, "Efficient method for calculating molecular excitation energies by time-dependent density-functional theory", The Journal of Chemical Physics, vol. 113, p. 2088, 2000.
- [112] F. Furche and R. Ahlrichs, "Adiabatic time-dependent density functional methods for excited state properties", The Journal of Chemical Physics, vol. 117, p. 7433, 2002.
- [113] R. W. H. Berry, P. Brocklehurst and A. Burawoy, "The effect of terminal nitro and amino groups on the electronic spectra of conjugated hydrocarbon systems", Tetrahedron, vol. 10, pp. 109-117, 1960.

- [114] X. K. Chen, D. Kim, J. L. Brédas, "Thermally Activated Delayed Fluorescence (TADF) Path toward Efficient Electroluminescence in Purely Organic Materials: Molecular Level Insight", Accounts of Chemical Research, vol. 51, pp. 2215-2224, 2018.
- [115] Z. Yang, Z. Mao, Z. Xie, Y. Zhang, S. Liu, J. Zhao, J. Xu, Z. Chi and M. P. Aldred, "Recent advances in organic thermally activated delayed fluorescence materials", Chemical Society Reviews, vol. 46, pp. 915-1016, 2017.
- [116] S. Y. Lee, T. Yasuda, Y. S. Yang, Q. Zhang and C. Adachi, "Luminous Butterflies: Efficient Exciton Harvesting by Benzophenone Derivatives for Full-Color Delayed Fluorescence OLEDs", Angewandte Chemie, vol. 53, pp. 6402-6406, 2014.
- [117] A. Perfetto, F. Maschietto and I. Ciofini, "Following excited states in molecular systems using density-based indexes: A dual emissive system as a test case", Journal of Photochemistry and Photobiology A, vol. 383, p. 111978, 2019.
- [118] J. Chen, T. Yu, E. Ubba, Z. Xie, Z. Yang, Y. Zhang, S. Liu, J. Xu, M.P. Aldred and Z. Chi, "Achieving Dual-Emissive and Time-Dependent Evolutive Organic Afterglow by Bridging Molecules with Weak Intermolecular Hydrogen Bonding", Advanced Optical Materials, vol. 115, pp. 1801593-1801597, 2019.
- [119] I. Marghad, F. Bencheikh, C. Wang, S. Manolikakes, A. Rérat, C. Gosmini, D.H. Kim, J.-C. Ribierre and C. Adachi, "Control of the dual emission from a thermally activated delayed fluorescence emitter containing phenothiazine units in organic light-emitting diodes", RSC Advances, vol. 9, pp. 4336-4343, 2019.
- [120] Q. Huang, X. Mei, Z. Xie, D. Wu, S. Yang, W. Gong, Z. Chi, Z. Lin, Q. Ling, "Photo-induced phosphorescence and mechanoluminescence switching in a simple purely organic molecule", Journal of Materials Chemistry C, vol. 7, pp. 2530-2534, 2019.
- [121] B. Huang, W.-C. Chen, Z. Li, J. Zhang, W. Zhao, Y. Feng, B.Z. Tang and C.-S. Lee, "Manipulation of Molecular Aggregation States to Realize Polymorphism, AIE, MCL, and TADF in a Single Molecule", Angewandte Chemie, vol. 57, pp. 12473-12477, 2018.
- [122] Z. He, X. Cai, Z. Wang, D. Chen, Y. Li, H. Zhao, K. Liu, Y. Cao and S.-J. Su, "Reversible switching between normal and thermally activated delayed fluorescence towards "smart" and single compound white-light luminescence via controllable conformational distribution", Science China Chemistry, vol. 61, pp. 677-686, 2018.
- [123] P.L. dos Santos, M.K. Etherington and A.P. Monkman, "Chemical and conformational control of the energy gaps involved in the thermally activated delayed fluorescence mechanism", Journal of Materials Chemistry C, vol. 6, pp. 4842-4853, 2018.
- [124] W.-H. Chen, Y. Xing and Y. Pang, "A Highly Selective Pyrophosphate Sensor Based on ESIPT Turn-On in Water", Organic Letters, vol. 13, pp. 1362-1365, 2011.
- [125] B. Liu, H. Wang, T. Wang, Y. Bao, F. Du, J. Tian, Q. Li and R. Bai, "A new ratiometric ESIPT sensor for detection of palladium species in aqueous solution", Chemical Communication, vol. 48, pp. 2867-2869, 2012.
- [126] U. Warde and S. Nagaiyan, "Comprehensive study on excited state intramolecular proton transfer in 2-(benzo[d]thiazol-2-yl)-3-methoxynaphthalen-1-ol and 2-(benzo[d]thiazol-2-yl)naphthalene-1,3-diol: Effect of solvent, aggregation, viscosity and TDDFT study", Journal of Photochemistry and Photobiology A: Chemistry, vol. 337, pp. 33-43, 2017.
- [127] S. Chevreux, C. Allain, L. Wilbraham, K. Nakatani, P. Jacques, I. Ciofini and G. Lemerrier, "Solvent tuned single molecule dual emission in protic solvents: effect of polarity and H-bonding", Faraday Discuss, vol. 185, pp. 285-297, 2015.
- [128] S. Chevreux, R. Paulino Neto, C. Allain, K. Nakatani, P. Jacques, I. Ciofini and G. Lemerrier, "Solvent-tuned dual emission: a structural and electronic interplay highlighting a novel planar ICT (OPICT)", Physical Chemistry Chemical Physics, vol. 17, pp. 7639-7642, 2015.
- [129] L. Wilbraham, M. Savarese, N. Rega, C. Adamo and I. Ciofini, "Describing Excited State Intramolecular Proton Transfer in Dual Emissive Systems: A Density Functional Theory Based Analysis", The Journal of Physical Chemistry B, vol. 119, pp. 2459-2466, 2014.

- [130] J.C. Germino, C.A. Barboza, F.J. Quites, P.A.M. Vazquez and T.D.Z. Atvars, "Dual Emissions of Salicylidene-5-chloroaminepyridine Due to Excited State Intramolecular Proton Transfer: Dynamic Photophysical and Theoretical Studies", *The Journal of Physical Chemistry C*, vol. 119, pp. 27666-27675, 2015.
- [131] S.A. Mewes and A. Dreuw, "Density-based descriptors and exciton analyses for visualizing and understanding the electronic structure of excited states", *Physical Chemistry Chemical Physics*, vol. 21, pp. 2843-2856, 2019.
- [132] E. Lippert, W. Lüder, F. Moll, W. Nägele, H. Boos, H. Prigge and I. Seibold-Blankenstein, "Umwandlung von Elektronenanregungsenergie", *Angewandte Chemie*, vol. 73, pp. 695-706, 1961.
- [133] P. Wiggins, J.A.G. Williams and D.J. Tozer, "Excited state surfaces in density functional theory: A new twist on an old problem", *The Journal of Chemical Physics*, vol. 131, p. 091101, 2009.
- [134] C.A. Guido, B. Mennucci, D. Jacquemin and C. Adamo, "Planar vs. twisted intramolecular charge transfer mechanism in Nile Red: new hints from theory", *Physical Chemistry Chemical Physics*, vol. 12, pp. 8016-8023, 2010.
- [135] C.A. Guido, D. Jacquemin, C. Adamo and B. Mennucci, "Electronic Excitations in Solution: The Interplay between State Specific Approaches and a Time-Dependent Density Functional Theory Description", *Journal of Chemical Theory and Computation*, vol.11, pp. 5782-5790, 2015.
- [136] J. C. Sancho-García and A. J. Pérez-Jiménez, "Nitrobenzene rotational energy barrier: A survey of several ab initio methods", *The Journal of Chemical Physics*, vol. 119, pp. 5121-5127, 2003.
- [137] W. Lecroq, J. Schleinitz, M. Billoue, A. Perfetto, J. Lalevée, A.-C. Gaumont, I. Ciofini, L. Grimaud and S. Lakhdar, "Photo-organocatalytic Deoxygenation of Heteroaromatic N-Oxides: Synthetic and Mechanistic Studies", submitted in *Angewandte Chemie*.
- [138] H. Guo, Y. C. Fan, Z. Sun, Y. Wu and O. Kwon, "Phosphine Organocatalysis", *Chemical Reviews*, vol. 118, pp. 10049-10293, 2018.
- [139] S. Xu and Z. He, "Recent advances in stoichiometric phosphine-mediated organic synthetic reactions", *RSC Advances*, vol. 3, pp. 16885-16904, 2013.
- [140] For selected contributions, see: a) C. J. O'Brien, J. L. Tellez, Z. S. Nixon, L. J. Kang, A. L. Carter, S. R. Kunkel, K. C. Przeworski, G. A. Chass, *Angew. Chemie - Int. Ed.* 2009, 48, 6836-6839. b) K. Fourmy, A. Voituriez, *Org. Lett.* 2015, 17, 1537-1540. c) W. Zhao, P. K. Yan, A. T. Radosevich, *J. Am. Chem. Soc.* 2015, 137, 616-619. d) M. L. Schirmer, S. Adomeit, T. Werner, *Org. Lett.* 2015, 17, 3078-3081. e) X. Han, N. Saleh, P. Retailleau, A. Voituriez, *Org. Lett.* 2018, 20, 4584-4588. f) T. V. Nykaza, J. C. Cooper, G. Li, N. Mahieu, A. Ramirez, M. R. Luzung, A. T. Radosevich, *J. Am. Chem. Soc.* 2018, 140, 15200-15205. g) T. V. Nykaza, A. Ramirez, T. S. Harrison, M. R. Luzung, A. T. Radosevich, *J. Am. Chem. Soc.* 2018, 140, 3103-3113. h) L. Longwitz, A. Spannen-berg, T. Werner, *ACS Catal.* 2019, 9, 9237-9244. i) C. Lorton, T. Castanheiro, A. Voituriez, *J. Am. Chem. Soc.* 2019, 141, 10142-10147. j) L. Longwitz, T. Werner, *Pure Appl. Chem.* 2019, 91, 95-102. k) A. Ghosh, M. Lecomte, S. H. Kim-Lee, A. T. Radosevich, *Angew. Chemie - Int. Ed.* 2019, 58, 2864-2869. l) L. Longwitz, T. Werner, *Angew. Chemie - Int. Ed.* 2020, 59, 2760-2763. m) G. Li, T. V. Nykaza, J. C. Cooper, A. Ramirez, M. R. Luzung, A. T. Radosevich, *J. Am. Chem. Soc.* 2020, DOI 10.1021/jacs.0c01666.
- [141] For a recent review, see: A. Voituriez, N. Saleh, *Tetrahedron Lett.* 2016, 57, 4443-4451.
- [142] For selected articles, see: a) E. E. Stache, A. B. Ertel, T. Rovis, A. G. Doyle, *ACS Catal.* 2018, 8, 11134-11139. b) M. Zhang, X. A. Yuan, C. Zhu, J. Xie, *Angew. Chemie - Int. Ed.* 2019, 58, 312-316. c) P. J. Xia, Z. P. Ye, Y. Z. Hu, D. Song, H. Y. Xiang, X. Q. Chen, H. Yang, *Org. Lett.* 2019, 21, 2658-2662. d) J. I. Martinez Alvarado, A. B. Ertel, A. Stegner, E. E. Stache, A. G. Doyle, *Org. Lett.* 2019, 21, 9940-9944. e) Y. Q. Guo, R. Wang, H. Song, Y. Liu, Q. Wang, *Org. Lett.* 2020, 22, 709-713.
- [143] a) J. Jeong, K. Suzuki, M. Hibino, K. Yamaguchi, N. Mizuno, *ChemistrySelect* 2016, 1, 5042-5048. b) F. Ding, Y. Jiang, S. Gan, R. L. Y. Bao, K. Lin, L. Shi, *European J. Org. Chem.* 2017, 2017, 3427-3430. c) A. Chardon, O. Maubert, J. Rouden, J. Blan-chet, *ChemCatChem* 2017, 9, 4460-4464. d) J. Jeong, K. Suzuki, K. Yamaguchi, N. Mizuno, *New J. Chem.* 2017, 41, 13226-13229. e) R. Rubio-Presa, M. A. Fernández-Rodríguez, M. R. Pedrosa, F. J. Arnáiz, R. Sanz, *Adv. Synth. Catal.* 2017, 359, 1752-1757. f) S. Gupta, P. Sureshbabu, A. K. Singh, S. Sabiah, J. Kandasamy, *Tetrahedron Lett.* 2017, 58, 909-913. g) K. D. Kim, J. H. Lee, *Org. Lett.* 2018, 20, 7712-7716. h) M. O. Konev, L. Cardinale, A. Ja-cobi Von Wangelin, *Org. Lett.* 2020, 22, 1316-1320. i) H. Tinner-mann, S. Sung, B. A. Cala, H. J. Gill, R. D. Young, *Organometal-lics* 2020, DOI 10.1021/acs.organomet.9b00778.

- [144] For selected examples on the use of heteroaromatic N-oxides in C-H activation processes, see: a) L. C. Campeau, S. Rousseaux, K. Fagnou, *J. Am. Chem. Soc.* 2005, 127, 18020–18021. b) H. P. Kokatla, P. F. Thomson, S. Bae, V. R. Doddi, M. K. Lakshman, *J. Org. Chem.* 2011, 76, 7842–7848. c) X. Zhang, Z. Qi, X. Li, *Angew. Chemie - Int. Ed.* 2014, 53, 10794–10798. d) W. Jo, J. Kim, S. Choi, S. H. Cho, *Angew. Chemie - Int. Ed.* 2016, 55, 9690–9694. e) Z. Zhang, C. Pi, H. Tong, X. Cui, Y. Wu, *Org. Lett.* 2017, 19, 440–443.
- [145] a) J. Kim, C. R. Bertozzi, *Angew. Chemie - Int. Ed.* 2015, 54, 15777–15781. b) T. Hirayama, H. Tsuboi, M. Niwa, A. Miki, S. Kadota, Y. Ikeshita, K. Okuda, H. Nagasawa, *Chem. Sci.* 2017, 8, 4858–4866.
- [146] E. Howard, W. F. Olszewski, *J. Am. Chem. Soc.* 1959, 81, 1483–1484.
- [147] K. Tokumura, H. Goto, H. Kashiwabara, C. Kaneko, M. Itoh, *J. Am. Chem. Soc.* 1980, 102, 5643–5647.
- [148] B. Kempf, H. Mayr, *Chemistry - A European Journal*, vol. 11, pp. 917–927, 2005.
- [149] M. Horn, L. H. Schappele, G. Lang-Wittkowski, H. Mayr and A. R. Ofial, “Towards a Comprehensive Hybrid donor ability scale”, *Chemistry - A European Journal*, vol. 19, pp. 249–263, 2013.
- [150] R. A. Marcus, “Chemical and Electrochemical Electron-Transfer Theory”, *Annual Review of Physical Chemistry*, vol. 15, pp. 155–196, 1964.
- [151] A. Albin and M. Alpegiani, “The photochemistry of the N-oxide function”, *Chemical Reviews*, vol. 84, pp. 43–71, 1984.
- [152] M. Besora, P. Vidossich, A. Lledos, G. Ujaque and F. Maseras, “Calculation of Reaction Free Energies in Solution: A Comparison of Current Approaches”, *The Journal of Physical Chemistry A*, vol. 122, pp. 1392–1399, 2018.
- [153] C. Micheletti, P. Minei, M. Carlotti, V. Mattoli, F. Muniz-Miranda, A. Perfetto, I. Ciofini, C. Adamo, G. Ruggeri, and A. Pucci, “Mechanochromic LLDPE Films doped with NIR Reflective Paliogen Black”, submitted in *Macromolecular Rapid Communications Journal*.
- [154] P. Bamfield and M. Hutchings, “Chromic Phenomena: Technological Applications of Colour Chemistry, 3rd Edition”, *Royal Society of Chemistry*, p. 782, 2018.
- [155] A. Pucci and G. Ruggeri, “Mechanochromic polymer blends”, *Journal of Materials Chemistry*, vol. 21, p. 8282, 2011.
- [156] F. Ciardelli, G. Ruggeri and A. Pucci, “Dye-containing polymers: methods for preparation of mechanochromic materials”, *Chemical Society Reviews*, vol. 42, p. 857 2013.
- [157] F. Würthner, T. E. Kaiser and C. R. Saha-Möller, “J-aggregates: from serendipitous discovery to supramolecular engineering of functional dye materials”, *Angewandte Chemie - International Edition*, vol. 50, p. 3376, 2011.
- [158] C. Lowe and C. Weder, “Oligo(p-phenylene vinylene) Excimers as Molecular Probes: Deformation-Induced Color Changes in Photoluminescent Polymer Blends”, *Advanced Materials*, vol. 14, p. 1625, 2002.
- [159] A. Pucci, “Mechanochromic Fluorescent Polymers with Aggregation-Induced Emission Features”, *Sensors*, vol. 19, p. 4969, 2019.
- [160] F. Donati, A. Pucci, C. Cappelli, B. Mennucci, G. Ruggeri, “Modulation of the Optical Response of Polyethylene Films Containing Luminescent Perylene Chromophores”, *Journal of Physical Chemistry B*, vol. 112, p. 3668, 2008.
- [161] G. Prampolini, F. Bellina, M. Biczysko, C. Cappelli, L. Carta, M. Lessi, A. Pucci, G. Ruggeri, V. Barone, “Computational design, synthesis, and mechanochromic properties of new thiophene-based π -conjugated chromophores”, *Chemistry - A European Journal*, vol.19, p. 1996, 2013.
- [162] D. W. R. Balkenende, S. Coulibaly, S. Balog, Y. C. Simon, G. L. Fiore, C. Weder, “Mechanochemistry with metallocsupramolecular polymers”, *Journal of the American Chemical Society*, vol. 136, p. 10493, 2014.

- [163] C. Calvino, E. Henriët, L. F. Muff, S. Schrettl and C. Weder, "Mechanochromic Polymers Based on Microencapsulated Solvatochromic Dyes", Macromolecular Rapid Communication, vol. 41, p. 1900654, 2020.
- [164] C. Calvino, Y. Sagara, V. Buclin, A. P. Haehnel, A. del Prado, C. Aeby, Y. C. Simon, S. Schrettl and C. Weder, "Mechanoresponsive, Luminescent Polymer Blends Based on an Excimer-Forming Telechelic Macromolecule", Macromolecular Rapid Communications, vol. 40, p. 1800705, 2019.
- [165] A. Pucci, R. Bizzarri and G. Ruggeri, "Polymer composites with smart optical properties", Soft Matter, vol. 7, p. 3689, 2011.
- [166] M. Zhang, L. Zhao, R. Zhao, Z. Li, Y. Liu, Y. Duan, T. Han, Spectrochim. Acta, Part A 2019, 220, 117125.
- [167] R. Zhao, L. Zhao, M. Zhang, Z. Li, Y. Liu, T. Han, Y. Duan, K. Gao, Dyes Pigm. 2019, 167, 181.
- [168] M. Karman, E. Verde-Sesto, C. Weder and Y. C. Simon, "Mechanochemical Fluorescence Switching in Polymers Containing Dithiomaleimide Moieties", ACS Macro Letters, vol.7, p. 1099, 2018.
- [169] C. Calvino, L. Neumann, C. Weder and S. Schrettl, "Approaches to polymeric mechanochromic materials", Journal of Polymer Science, Part A: Polymer Chemistry, vol. 55, p. 640, 2017.
- [170] G. I. Peterson, M. B. Larsen, M. A. Ganter, D. W. Storti and A. J. Boydston, "3D-Printed Mechanochromic Materials", ACS Applied Materials and Interfaces, vol. 7, p. 577, 2015.
- [171] Q. Wang, G. R. Gossweiler, S. L. Craig and X. Zhao, "Cephalopod-inspired design of electro-mechanochemically responsive elastomers for on-demand fluorescent patterning", Nature Communications, vol. 5, p. 4899, 2014.
- [172] D. R. T. Roberts and S. J. Holder, "Mechanochromic systems for the detection of stress, strain and deformation in polymeric materials", Journal of Materials Chemistry, vol. 21, p. 8256, 2011.
- [173] P. Zhang, X. Shi, A. P. H. J. Schenning, G. Zhou and L. T. de Haan, "A patterned mechanochromic photonic polymer for reversible image reveal", Advanced Materials Interfaces, vol. 7, p. 1901878, 2020.
- [174] K. Suenaga, K. Uemura, K. Tanaka and Y. Chujo, "Stimuli-responsive luminochromic polymers consisting of multi-state emissive fused boron ketoiminate", Polymer Chemistry, vol. 11, p.1127, 2020.
- [175] K. Kawasaki, D. Aoki and H. Otsuka, "Multicolor Mechanochromic Polymer Blends That Can Discriminate between Stretching and Grinding", Macromolecular Rapid Communications, vol. 41, p.1900460, 2020.
- [176] Y. Sagara, M. Karman, E. Verde-Sesto, K. Matsuo, Y. Kim, N. Tamaoki, C. Weder, Journal of the American Chemical Society 2018, 140, 1584.
- [177] C. Calvino, A. Guha, C. Weder and S. Schrettl, "Self-Calibrating Mechanochromic Fluorescent Polymers Based on Encapsulated Excimer-Forming Dyes", Advanced Materials, vol. 30, p. 1704603, 2018.
- [178] A. Nowak-Król and F. Würthner, "Progress in the synthesis of perylene bisimide dyes", Organic Chemistry Frontiers, vol. 6, p. 1272, 2019.
- [179] D. Görl, X. Zhang and F. Würthner, "Molecular Assemblies of Perylene Bisimide Dyes in Water", Angewandte Chemie - International Edition, vol. 51, p.6328, 2012.
- [180] Z. Chen, A. Lohr, C. R. Saha-Möller and F. Würthner, "Self-assembled π -stacks of functional dyes in solution: structural and thermodynamic features", Chemical Society Reviews, vol. 38, p. 564, 2009.
- [181] F. Donati, A. Pucci and G. Ruggeri, "Temperature and chemical environment effects on the aggregation extent of water soluble perylene dye into vinyl alcohol-containing polymers", Physical Chemistry Chemical Physics, vol. 11, p. 6276, 2009.
- [182] P. Minei, M. Lessi, L. Contiero, S. Borsacchi, F. Martini, G. Ruggeri, M. Geppi, F. Bellina and A. Pucci, "Structural order and NIR reflective properties of perylene bisimide pigments: Experimental evidences from a combined multi-technique study", Solar Energy, vol. 198, p.689, 2020.

- [183] M. Mazhar, M. Abdouss, K. Gharanjig, R. Teimuri-Mofrad and M. Zargaran, "Perylene-3,4,9,10-tetracarboxylic diimide and its derivatives: Synthesis, properties and bioapplications", Journal of Coatings Technology and Research, vol. 14, p. 207, 2017.
- [184] J. Qu, Z. N Zhang, W. D Shi, Y. X Zhang, T. Xue, X. Zhang, R. P Zhang, J. Qin, J. Song, Z. Song, W. Zhang, Y. Shi, T. Zhang, X. Xue, R. Zhang, Z. Hongqiang, Z. Zhang and X. Wu, "The Optical Properties of Black Coatings and Their Estimated Cooling Effect and Cooling Energy Savings Potential", Journal of Power and Energy Engineering, vol.2 ,pp. 68-75, 2014.
- [185] B. Kaur, S. N. Bhattacharya and D. J. Henry, "Interpreting the near-infrared reflectance of a series of perylene pigments", Dyes and Pigments, vol. 99, p. 502, 2013.
- [186] BASF, "Paint it cool! Pigments for solar heat management in paints".
- [187] F. Mahmoudi Meymand, M. Mazhar and M. Abdouss, "Investigation of substituent effect on cool activity of perylene bisimide pigments", Journal of Coatings Technology and Research, vol.16, p. 439, 2019.
- [188] F. Muniz-Miranda, P. Minei, L. Contiero, F. Labat, I. Ciofini, C. Adamo, F. Bellina and A. Pucci, "Aggregation Effects on Pigment Coatings: Pigment Red 179 as a Case Study", ACS Omega, vol. 4, p. 20315, 2019.
- [189] M. Mazhar, M. Abdouss, K. Gharanjig R. Teimuri-Mofrad, "Synthesis, characterization and near infra-red properties of perylenebisimide derivatives Prog Org Coating", Progress in Organic Coatings, vol. 101, p. 297, 2016.
- [190] F. Martini, M. Geppi, G. Barcaro, S. Monti, L. Contiero, G. Ruggeri, M. Lessi, A. Pucci, F. Bellina, S. Borsacchi, The Journal of Physical Chemistry C 2020.
- [191] F. Martini, P. Minei, M. Lessi, L. Contiero, S. Borsacchi, G. Ruggeri, M. Geppi, F. Bellina and A. Pucci, "Structural order and NIR reflective properties of perylene bisimide pigments: Experimental evidences from a combined multi-technique study", Dyes and Pigments, vol.179, p. 108401, 2020.
- [192] S. Grimme, S. Ehrlich and L. Goerigk, "Effect of the Damping Function in Dispersion Corrected Density Functional Theory", Journal of Computational Chemistry, vol. 32, p. 1456, 2011.
- [193] J. Tomasi, B. Mennucci and R. Cammi, "Quantum Mechanical Continuum Solvation Models", Chemical Reviews, vol. 105, pp. 2999- 3093, 2005.
- [194] R. Dovesi, A. Erba, R. Orlando, C. M. Zicovich-Wilson, B. Civalleri, L. Maschio, M. Rérat, S. Casassa, J. Baima, S. Salustro and B. Kirtman, "Quantum-mechanical condensed matter simulations with CRYSTAL", WIREs Computational Molecular Science, vol. 8, p. 1360, 2018.
- [195] M. C. R. Delgado, E.-G. Kim, D. A. d. S. Filho and J.-L. Bredas, "Tuning the Charge-Transport Parameters of Perylene Diimide Single Crystals via End and/or Core Functionalization: A Density Functional Theory Investigation", Journal of the American Chemical Society, vol. 132, p. 3375, 2010.
- [196] M. Klintonberg, S. E. Derenzo and M. J. Weber, "Accurate crystal fields for embedded cluster calculations", Computer Physics Communications, vol. 131, p.120, 2000.
- [197] L. Wilbraham, C. Adamo, F. Labat and I. Ciofini, "Electrostatic Embedding To Model the Impact of Environment on Photophysical Properties of Molecular Crystals: A Self-Consistent Charge Adjustment Procedure", Journal of Chemical Theory and Computation, vol. 12, p. 3316, 2016.
- [198] J. Mei, N. L. C. Leung, R. T. K. Kwok, J. W. Y. Lam and B. Z. Tang, "Aggregation-Induced Emission: Together We Shine, United We Soar!", Chemical Reviews, vol. 115, p. 11718, 2015.
- [199] F. Muniz-Miranda, M. C. Menziani and A. Pedone, "Assessment of Exchange-Correlation Functionals in Reproducing the Structure and Optical Gap of Organic-Protected Gold Nanoclusters", The Journal of Physical Chemistry C, vol. 118, p. 7532, 2014.

Résumé en français

Au cours des dernières années, il y a eu un intérêt croissant dans l'application de méthodes théoriques pour l'étude des phénomènes qui se produisent à l'état excité. Cet intérêt est principalement dû à une demande énorme de nouvelles classes de composés à appliquer dans différents domaines, tels que biologique et médical, de l'optoélectronique et le stockage d'énergie, dont les performances impliquent l'interaction lumière-matière. En effet, lors de l'interaction avec la lumière, ces matériaux sont capables d'obtenir une réponse observable sous forme de changement de couleur, de luminescence, d'altération des propriétés magnétiques, de réaction chimique induite ou de plusieurs d'entre elles, donc la raison pour laquelle ils sont appelés « molécules photo-actives ». Ainsi, l'élevage des technologies nécessite la synthèse de molécules avec des fonctions cibles très spécifiques, mais le manque de connaissances sur le mécanisme moléculaire des phénomènes induits par la lumière constitue un inconvénient majeur pour la conception de tels systèmes. Ces travaux de recherche montrent comment la mise en œuvre de nouvelles approches informatiques peut fournir une solution pour résoudre ce problème.

Lors de l'absorption d'un quantum de lumière, une molécule se déplace essentiellement de l'état fondamental à un état excité, qui à son tour prend part à une réaction photochimique. Les intermédiaires de ce processus préliminaire sont plus en énergie par rapport à ceux accessibles via les intermédiaires thermiques normaux et peuvent subir diverses réactions secondaires « sombres », ce qui donne les produits finaux. La compréhension de ces processus au niveau moléculaire exige une

description précise des états excités. En raison de la complexité de la caractérisation expérimentale des processus photochimiques et de l'exigence d'une image détaillée des états concernés, les méthodes théoriques peuvent jouer un rôle de plus en plus important dans ce contexte, en particulier pour les systèmes moléculaires complexes. Les développements récents de la théorie de la fonctionnelle de la densité (DFT), et en particulier de théorie de la fonctionnelle de la densité dépendant du temps (TD-DFT) permettent aujourd'hui d'obtenir une description complète d'un phénomène photo-induits, de l'absorption jusqu'à la formation de photo-produits finaux. La méthodologie la plus simple pour étudier un processus photochimique consiste à séquencer l'ensemble du parcours en différentes étapes de réaction sur des surfaces d'énergie potentielles avec une coordonnée de réaction représentative. De cette façon, il est possible d'identifier l'étape pertinente reliant la région de Franck Condon, qui est essentiellement l'endroit où le système absorbe la lumière, à la zone où les photo-produits sont formés. Néanmoins, l'identification des minima et des états de transition le long des surfaces d'énergie potentielle (SEP) et, par conséquent, la simple analyse énergétique s'en trouve insatisfaisante. En particulier, la présence de groupes donneurs et d'accepteurs d'électrons dans la structure moléculaire affecte fortement la nature de l'état excité, qui peut acquérir le caractère de transfert de charge (CT), et par conséquent les propriétés photophysiques du système. Pour cette raison, une quantité fondamentale supplémentaire qui peut également être considérée est la densité d'électrons et sa réorganisation tout au long du processus. De cette façon, l'analyse énergétique fournit les propriétés locales le long de la SEP, tels que les points de selle, minima et maxima, à travers lequel il est alors possible de calculer les barrières énergétiques, les énergies d'activation et ainsi de suite. D'autre part, l'analyse de la densité des électrons peut donner une image claire de la redistribution de la densité des électrons au cours du processus, ce qui permet de caractériser la nature des états électroniques, et ainsi obtenir d'autres informations sur les phénomènes induits par la lumière.

Dans ce contexte, DFT et TD-DFT se prêtent bien pour cette double analyse. Le principal avantage réside dans leur rapport coût-précision favorable et leur capacité à intégrer les effets environnementaux d'une manière computationnellement peu coûteuse. Néanmoins, il est bien documenté dans la littérature que les fonctionnelles

de la densité utilisée pour évaluer la contribution de l'énergie d'échange et de corrélation, essentiellement le seul terme approximatif dans l'expression de l'énergie totale, souffrent de différents inconvénients. Certains d'entre eux sont la description incorrecte de l'interaction électronique à longue portée et des énergies calculées erronées associées au transfert de charge (TC), conduisant à la prédiction d'états non physiques de faible altitude excités avec le caractère (TC), également connu sous le nom d'« états fantômes ».

De plus, la TD-DFT est incapable de reproduire les points de croisement entre deux ou plusieurs états excités, en raison de la nature intrinsèquement multi-déterminante de ce type de phénomène. Par conséquent, dans le contexte DFT et TD-DFT, il est nécessaire de développer de nouveaux outils pour traiter ou corriger les inconvénients des fonctionnelles de la densité, et en même temps pour explorer la SEP complète d'un état excité, donnant ainsi une meilleure description des phénomènes induits par la lumière. En effet, le but de ce travail de recherche est de développer et de tester des descripteurs théoriques *ad hoc* et innovants basés sur la densité électronique pour faire face à ces inconvénients. Ces descripteurs fournissent des informations sur les propriétés physiques importantes, traduisant les résultats computationnels en concepts chimiques et physiques simples. De cette façon, il est possible de définir efficacement les voies photo-physiques les plus importantes pour les processus complexes qui se déroulent simultanément à l'état excité (réorganisation électronique, décroissance radiative et non) à travers une description détaillée des surfaces d'énergie potentielle des états excités, non exclusivement dans la région de Frank-Condon. Le but ultime est la conception *in-silico* de nouveaux systèmes moléculaires photo-actifs intéressants avec des propriétés cibles pour résoudre des problèmes importants, y compris l'utilisation de matériaux durables et la crise énergétique mondiale.

Après un bref aperçu de la DFT et de la TD-DFT dans le Chapitre 2, le Chapitre 3 contient un excursus temporel des outils théoriques existants développés au cours des dernières décennies pour explorer les propriétés des états excités par la quantification de la redistribution de la densité de charge impliquée dans l'excitation, offrant ainsi une description concise de la transition électronique, non seulement dans la région de

Franck Condon, mais aussi dehors. Puisque l'information concernant la réponse du système à la perturbation induite par la lumière est contenue dans la densité électronique, nous avons basé la mise en œuvre de tels outils théoriques sur cet observable fondamental. Un exemple de ces descripteurs est représenté par le D_{CT} , qui donne des informations sur la force et l'étendue spatiale de la séparation de charges générée par une excitation électronique. Basée sur le calcul simple de la densité électronique dans une représentation de l'espace réel pour l'état fondamental et l'état excité, le D_{CT} mesure la distance entre le trou et la particule en référant les barycentres des charges négatives et positives (Figure 1).

$$D_{CT} = R^+ - R^- \quad (1)$$

Sa formulation simple et intuitive qui condense l'information sur la réorganisation des charges à la suite d'une excitation électronique rend le D_{CT} plus couramment utilisé entre les descripteurs pour mesurer une distance de transfert de charge.

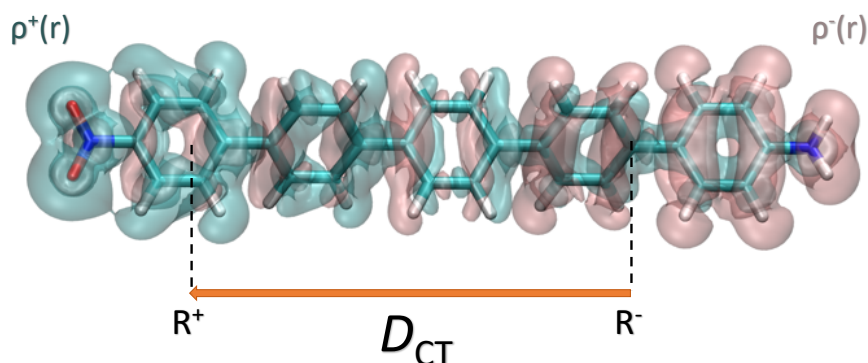


Figure 1 Représentation schématique de D_{CT} . L'accumulation (isosurface cyan) et l'épuisement (isosurface rose) de la charge électronique sont montrés avec les barycentres correspondants des deux densités d'électrons.

Cependant, dans sa formulation originale, ce descripteur n'a pas été en mesure de décrire le transfert de charge dans le cas de molécules symétriques étant par construction nulle indépendamment de la présence de phénomènes locaux de transfert de charge. D'où la nécessité de réviser la définition du D_{CT} pour élargir le champ d'application, permettant ainsi son utilisation pour n'importe quel système,

symétrique ou non. À cette fin, dans le Chapitre 4, nous avons présenté un nouvel indice basé sur la densité, le D_{CT} partiel (${}^P D_{CT}$), permettant de mesurer l'étendue du transfert de charge dans les conformations symétriques. Il a été essentiellement mis en œuvre en adaptant la formulation classique de l'indice D_{CT} sur le sous-ensemble des atomes composant le plus petit fragment asymétrique de la molécule symétrique d'intérêt. De cette façon, on calcule l'étendue de TC pour chaque fragment asymétrique en évitant le calcul de l'indice D_{CT} global, qui est égal à zéro par définition.

À cette fin, nous avons examiné trois familles de systèmes push-pull (Figure 2), caractérisés par un nombre croissant d'unités accepteurs et par une valeur de D_{CT} total égal ou non à zéro, et nous avons testé sur eux notre nouvel outil. En effet, nous avons montré qu'il était maintenant possible de surmonter l'incapacité de fournir des informations sur les excitations de transfert de charge dans les molécules symétriques pour lesquelles le TC global est nul. En outre, puisque le D_{CT} est calculé en ne tenant compte que de la contribution d'un sous-ensemble donné d'atomes, il est maintenant possible de disséquer la distance totale entre le trou et la particule le long de certaines directions d'intérêt, pour lesquelles il pourrait être intéressant d'avoir des informations indépendantes. Cependant, l'utilisation du ${}^P D_{CT}$ implique une définition *a priori* du sous-ensemble des atomes constituant le fragment asymétrique, ce qui pourrait ajouter des artefacts possibles, y compris le double (triple, etc.) comptage provenant de fragments moléculaires spécifiques.

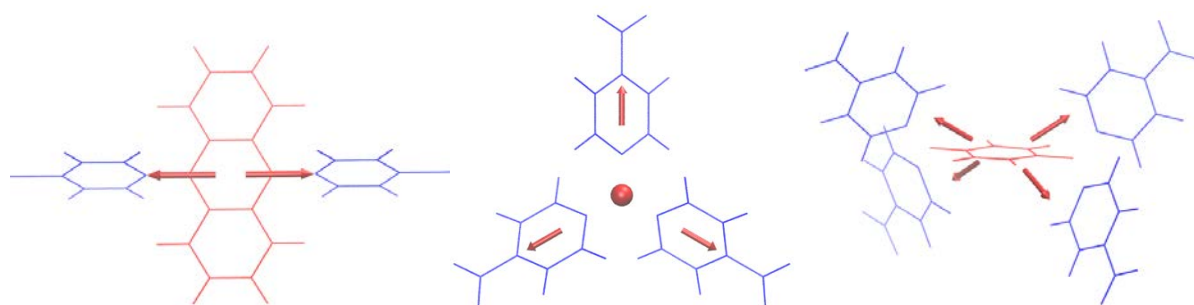


Figure 2 Représentation schématique des trois familles de systèmes push-pull considérées avec le ${}^P D_{CT}$ représenté sous la forme de flèches rouges.

Par conséquent, dans le Chapitre 5, nous avons fourni un autre descripteur basé sur la densité, l'indice D_{CT} moyen (${}^A D_{CT}$), qui peut être utilisé indistinctement pour toutes les conformations moléculaires, symétriques ou non, évitant ainsi toute manipulation de l'utilisateur. Contrairement au D_{CT} (et au ${}^P D_{CT}$), qui mesure l'étendue du TC comme la distance entre deux points de charge moyens, l' ${}^A D_{CT}$ pèse la moyenne des distances entre toutes les distributions possibles de trou et particule présentes dans le système d'intérêt, permettant ainsi une description indépendante de la topologie du système.

$${}^A D_{CT} = \frac{\int \int \rho^+(r) \rho^-(r') |r-r'| dr dr'}{\int \int \rho^+(r) \rho^-(r') dr dr'} \quad (2)$$

Afin de valider et comparer ${}^A D_{CT}$ avec les descripteurs déjà développés (D_{CT} et ${}^P D_{CT}$) nous avons d'abord envisagé un ensemble de molécules de cas d'essai, des prototypes de systèmes contenant des groupes donneur (D) et/ou accepteur (A) spectroscopiquement bien caractérisées (molécules 1a-3 dans la Figure 4), et puis des molécules push-pull réelles DA symétriques (molécules 4-11 dans la Figure 4). Nous avons vu que cet indice donne des étendues raisonnables de TC même pour la plupart des molécules symétriques et conserve les aspects positifs des descripteurs précédents basés sur la densité, à savoir qu'il a une charge de calcul particulièrement faible s'il est utilisé en conjonction avec les charges atomiques (par exemple celles de Mulliken) et il peut être appliqué indépendamment au niveau de la théorie adoptée. Comme son nom l'indique, il donne une valeur moyenne, il est donc intrinsèquement une quantité scalaire (et non vectorielle), contrairement aux précédents, et par conséquent il ne fournit pas une origine physiquement corrélée du déplacement de l'électron et du trou.

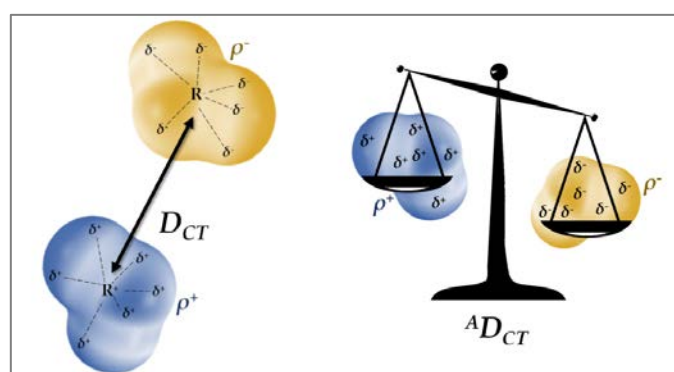


Figure 3 Représentation schématique de l'approche théorique D_{CT} et ${}^A D_{CT}$.

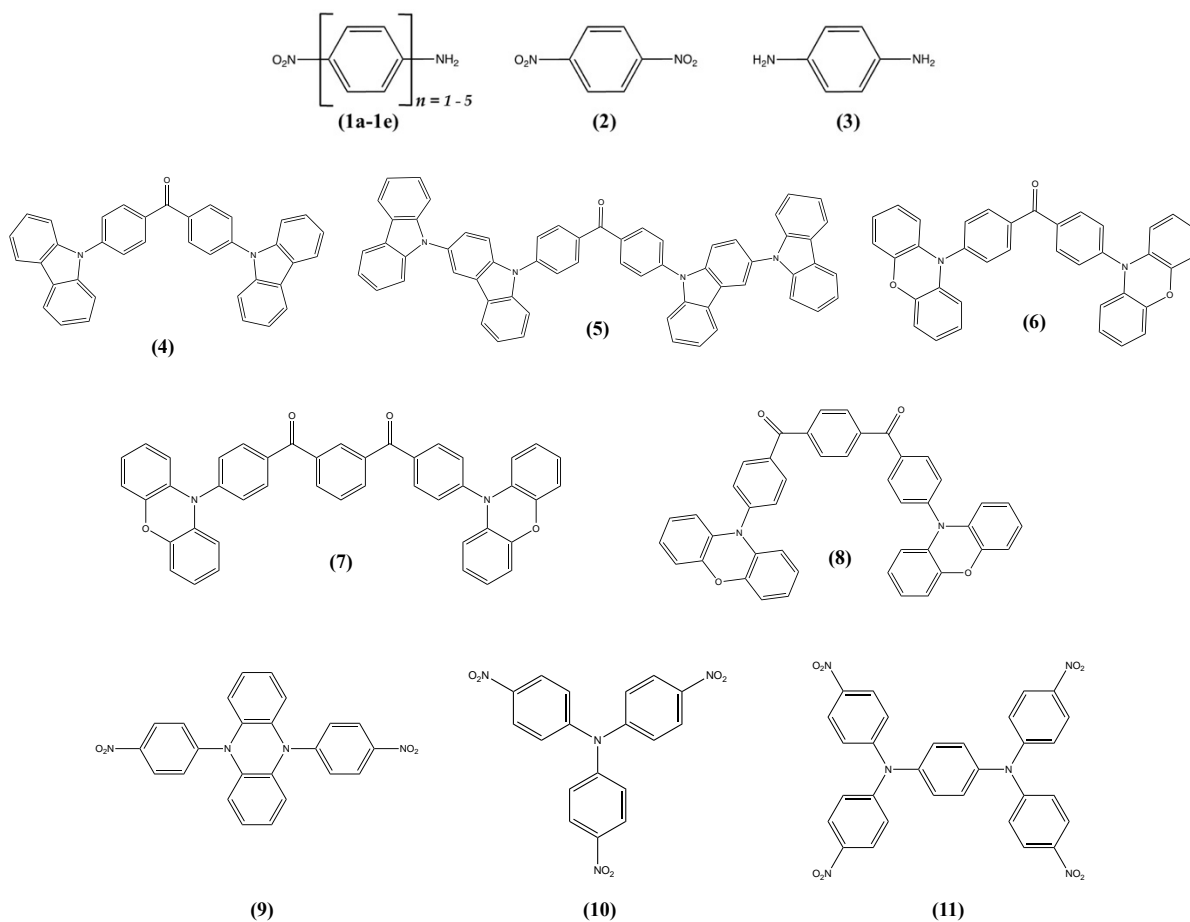


Figure 4 Représentation schématique des composés modèles utilisés comme donneur-accepteur (D-A, **1a-1e** pour $n=1,5$), accepteur-accepteur (A-A, **2**), et donneur-donneur (D-D, **3**) ainsi que les formules structurales des dérivés de benzophénone en forme de papillon (**4-8**) et des molécules DA_2-NO_2 , DA_3-NO_2 et DA_4-NO_2 (**9-11**).

Dans le contexte de la modélisation des profils des états excités et dans le but d'obtenir un aperçu des phénomènes complexes photo-induits, nous avons étendu notre cadre de calcul pour étudier comment le système évolue sur l'absorption de la lumière dans les Chapitres 6 et le Chapitre 7, en étudiant le réarrangement de densité d'électrons qui en résulte. En particulier, nous avons appliqué un indice de densité précédemment déjà défini, le Π , pour repérer la conversion interne entre l'états fondamental et les états excités afin de déterminer les régions possibles où la décroissance radiative ou non radiative est susceptible de se produire.

$$\Pi = \frac{1}{\Delta E \times D_{CT} \times q_{CT}} \quad (3)$$

Cela nous a permis de comprendre l'origine du comportement à double émission d'un dérivé de la phénantroline (Figure 5) (Chapitre 6), et d'appuyer des preuves expérimentales concernant la faisabilité d'un mécanisme de réaction hypothétique expliquant une réaction de désoxygénation métal-libre se produisant à l'état excité (Figure 6) (Chapitre 7). Par conséquent, cela nous a permis la description non seulement des propriétés d'état excités d'un seul système moléculaire, mais aussi de comprendre la complexe réactivité à l'état excité.

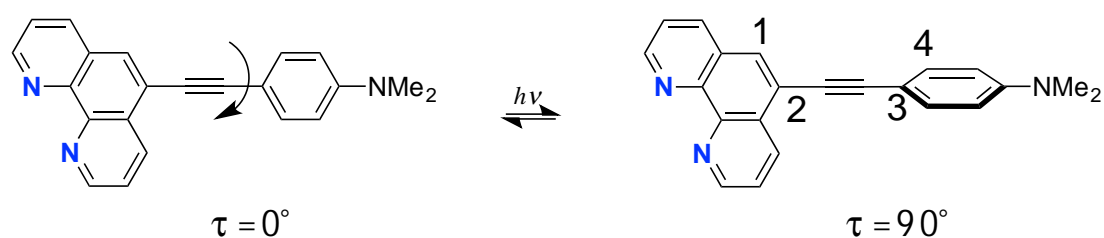


Figure 5 Structure schématique de la molécule Phen-PENMe2 dans son conformation planar ($\tau = 0^\circ$) et tordues ($\tau = 90^\circ$).

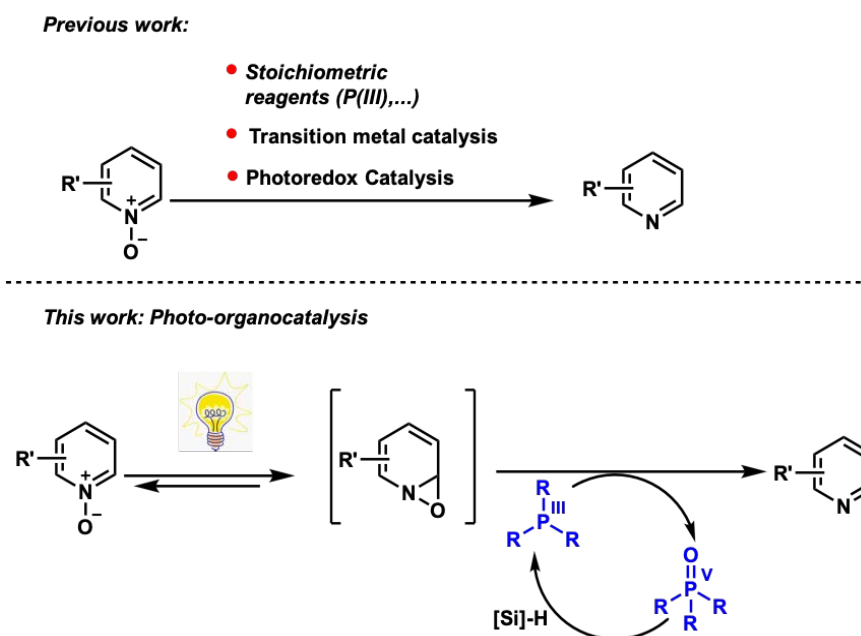


Figure 6 Désoxygénation des *N*-oxydes hétéroaromatiques.

L'une des caractéristiques les plus discutables de cette approche est que l'interprétation réelle de la voie photophysique dépend de la précision de la densité et plus particulièrement sur le niveau de théorie quantique choisi. De plus, le lecteur est invité à considérer le tableau d'ensemble obtenu par de telles approches plus qualitative qu'une caractérisation précise des régions de croisement. En effet, les indices basés sur la densité proposés ici devraient être conçus comme une méthode primaire peu coûteuse et efficace pour explorer et avoir une vue immédiate – *on the fly* – sur les SEPs et les trajectoires de réaction possibles. Un point de départ solide pour aider à la fois l'interprétation et la rationalisation des résultats expérimentaux, et pour soutenir la caractérisation classique de l'état excité par des méthodes quantiques coûteuses au niveau de calcul.

Certaines améliorations et suggestions pourraient être proposées pour utiliser efficacement ces descripteurs basés sur la densité sans avoir de problème d'application sur des molécules particulières. En effet, si l'on applique l'index Π *sic et simpliciter* pour les molécules symétriques pour lesquelles le D_{CT} est nul par définition, l'index divergerait incorrectement. Nous avons mis en œuvre le $^P D_{CT}$ pour mesurer l'étendue de TC dans le cas des molécules avec la configuration symétrique (voir Chapitre 4). Ainsi, une solution serait d'utiliser la définition de $^P D_{CT}$ dans l'index Π . Au contraire, l'utilisation du descripteur $^A D_{CT}$ (Chapitre 5) n'est pas recommandée puisqu'étant une quantité scalaire, elle ne contient pas l'information directionnelle, et n'est donc pas compatible avec l'index Π , qui est basé sur l'idée de suivre la trajectoire du changement de densité d'électrons. Le descripteur $^A D_{CT}$ pourrait être plutôt intégré dans le descripteur M_{AC} (Chapitre 3), qui tente essentiellement de remplacer la formulation de l'énergie de transition de Mulliken par une estimation moyenne pondérée sur les orbitales du potentiel d'ionisation et de l'affinité électronique ainsi qu'une distance efficace de TC (D_{CT}). En particulier, l' $^A D_{CT}$ pourrait être utilisé à la place du D_{CT} global, évitant ainsi l'inconvénient de prêter attention si la molécule est symétrique ou non.

Une répercussion possible de mes travaux de recherche pourrait être l'intégration de tous ces outils théoriques dans un protocole unique et efficace spécifiquement mis en œuvre pour simuler les spectres d'émissions visibles aux UV in-silico pour un large éventail de molécules. L'idée serait de développer un protocole prédictif efficace et

peu coûteux sur le plan informatique pour concevoir de nouveaux chromophores biocompatibles. En effet, l'Agenda 2030 pour le développement durable nous oblige à prendre la voie de la durabilité, les industries sont également appelées à prendre de nouvelles mesures pour atteindre les 17 fameux objectifs, tels que l'utilisation de matériaux durables. Les colorants chimiques courants sont inclus dans l'archive des matériaux à remplacer par des éco-matériaux. Par conséquent, l'idée est d'utiliser le protocole susmentionné pour prédire les chromophores possibles appropriés pour créer des colorants durables et naturels, évitant ainsi aux industries d'utiliser l'approche classique « trial and error » qui est très dispendieuse. Il s'agit de l'objectif du projet IRIS qui a reçu le financement du programme PSL-Pepite dans le cadre du concours « AAP Preuve de concept 2020 ».

La dernière étape logique a été d'essayer de reproduire l'effet de l'environnement dans la modulation des spectres à la fois dans la forme et l'énergie. En particulier, des efforts ont été consacrés à la modélisation de la phase solide afin de tenir compte des effets en phase condensée, d'une importance primordiale, en particulier lorsqu'il s'agit de processus d'agrégation. Dans ce contexte, dans le Chapitre 8, nous avons étudié les propriétés mécaniques, optiques et électroniques de la teinture Paliogen Black, un dérivé de perylène bis-imide avec conformation à haute symétrie qui favorise la formation d'assemblages supramoléculaires cristallins promus par les interactions intermoléculaires π - π parmi les noyaux de perylène.

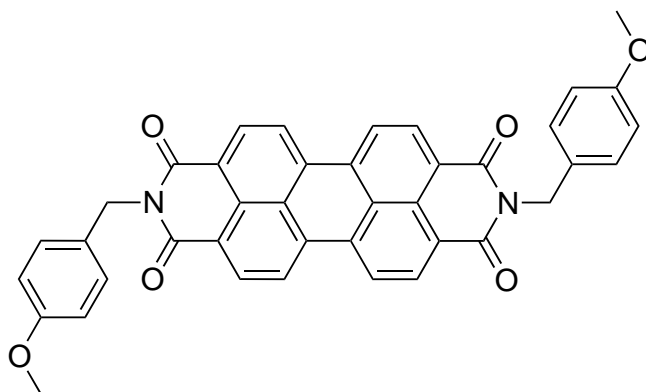


Figure 7 Structure chimique du Paliogen® Black L0086 (P-black).

Nous l'avons étudié par des moyens expérimentaux et computationnels : avec le premier, nous avons évalué ses propriétés comme un pigment « cool », c'est-à-dire sa haute réflexion au rayonnement proche infrarouge, et son comportement mécanochromique lorsqu'il est introduit dans une matrice de polyéthylène de faible densité et sujet à un stress directionnel. Avec des méthodes de calcul basées sur la TD-DFT, nous avons élucidé l'origine des transitions électroniques responsables de la couleur du colorant, et l'anisotropie dipolaire responsable des propriétés mécanochromiques.

Nous avons utilisé une simulation à plusieurs échelles précise pour mettre en évidence les caractéristiques structurales et optiques, et donc les différents comportements, en trois phases distinctes, à savoir la phase de gaz, la solution et l'état solide. Pour inclure correctement les effets électrostatiques à courte et longue portée et les interactions intermoléculaires possibles, nous avons d'abord étudié le monomère, puis le dimer et le trimer dans chaque phase. Cela pourrait représenter un protocole efficace qui peut être adopté pour étudier les mécanismes complexes impliquant des phénomènes à différentes échelles, où une très grande précision est nécessaire à chaque taille. Une sorte d'approche à grain grossier pour simuler des phénomènes complexes comme *aggregation induced emission* (AIE) ou *aggregation caused quenching* (ACQ). En effet, une idée future serait d'établir un protocole de calcul précis à plusieurs échelles pour une description approfondie du mécanisme sous-jacent aux phénomènes d'AIE. De cette façon, l'étude de la relation structure-propriété des systèmes pouvant produire des phénomènes d'AIE est essentielle pour guider la conception rationnelle de nouveaux AIEgènes avec une meilleure performance et une applicabilité améliorée.

RÉSUMÉ

L'interaction lumière-matière est la force motrice à l'origine de nombreux phénomènes et technologies allant de la photosynthèse artificielle à l'électronique moléculaire. Après absorption lumineuse, la matière peut émettre un rayonnement causé par une série de phénomènes, affectant les propriétés électroniques et structurales de l'objet irradié. La compréhension de ces processus au niveau moléculaire nécessite de caractériser les états excités et permet la prédiction du comportement photophysique de nouveaux systèmes moléculaires. En fait, le but de mon travail théorique est de développer et appliquer des outils théoriques permettant la description détaillée des surfaces d'énergie potentielle des états excités non exclusivement dans la région de Frank-Condon. À cette fin, des méthodes quantiques basées sur la théorie fonctionnelle de la densité dépendante du temps, en combinaison avec des descripteurs basés sur la densité électronique, sont utilisées. Le but final est l'interprétation du comportement photophysique des systèmes et la rationalisation des caractéristiques structurales et électroniques des états excités donnant lieu à des voies de décroissance radiatives et non. Cela permet la conception *in silico* de nouveaux composés permettant de résoudre des problèmes importants, notamment l'emploi de matériaux durables et la crise énergétique mondiale.

MOTS CLÉS

Photochimie - Transfert de charge - Index de la densité - Théorie de la fonctionnelle de la densité - États excités

ABSTRACT

Light-matter interaction is the driving force behind many phenomena and technologies ranging from artificial photosynthesis to molecular electronics. Upon light absorption, matter can emit radiation as a cause of a series of phenomena, affecting the electronic and structural properties of the irradiated object. Understanding these processes at the molecular level requires the characterization of excited states, thus allowing the prediction of the photophysical behavior of new molecular systems. Indeed, the purpose of my theoretical work is to develop and apply theoretical tools for the detailed description of the potential energy surfaces of excited states not exclusively in the Frank-Condon area. To this end, quantum methods based on time-dependent density functional theory (TD-DFT), in combination with descriptors based on the electronic density are used. The ultimate goal is the interpretation of the photophysical behavior of systems and the rationalization of the structural and electronic characteristics of excited states giving rise to radiative and non-radiative decay pathways. This allows the *in silico* design of new compounds to solve important problems, including the use of sustainable materials and the global energy crisis.

KEYWORDS

Photochemistry - Charge Transfer - Density based index - Density functional theory - Excited states